Forschungszentrum Karlsruhe
Technik und Umwelt

Wissenschaftliche Berichte
FZKA 6615

Experimental and Calculational Results of the QUENCH-05 Test

**L. Sepold, C. Homann, W. Leiling,
A. Miassoedov, D. Piel, G. Schanz,
L. Schmidt, U. Stegmaier, M. Steinbrück,
H. Steiner**

Institut für Materialforschung
Institut für Reaktorsicherheit
Programm Nukleare Sicherheitsforschung

Juni 2002

Forschungszentrum Karlsruhe

in der Helmholtz-Gemeinschaft

Wissenschaftliche Berichte

FZKA 6615

Experimental and Calculational Results of the QUENCH-05 Test

L. Sepold, C. Homann, W. Leiling, A. Miassoedov, D. Piel, G. Schanz,
L. Schmidt, U. Stegmaier, M. Steinbrück, H. Steiner

Institut für Materialforschung
Institut für Reaktorsicherheit
Programm Nukleare Sicherheitsforschung

Forschungszentrum Karlsruhe GmbH, Karlsruhe

2002

Forschungszentrum Karlsruhe GmbH
Postfach 3640, 76021 Karlsruhe

Mitglied der Hermann von Helmholtz-Gemeinschaft
Deutscher Forschungszentren (HGF)

ISSN 0947-8620

Zusammenfassung

Experimentelle und analytische Ergebnisse des Versuchs QUENCH-05

In den QUENCH-Versuchen soll der Wasserstoffquellterm bei der Einspeisung von Notkühlwasser in einen trockenen, überhitzten Reaktorkern eines Leichtwasserreaktors (LWR) ermittelt werden.

Das QUENCH-Testbündel ist mit 21 Brennstabsimulatoren bestückt und hat eine Gesamtlänge von ca. 2,50 m. 20 Brennstabsimulatoren sind auf einer Länge von 1024 mm beheizt, der Zentralstab ist unbeheizt. Als Heizer werden Wolfram-Stäbe von 6 mm Durchmesser verwendet, die im Zentrum der Brennstabsimulatoren angeordnet und von ZrO_2-Ringtabletten umgeben sind. Die Stabhüllen sind identisch mit LWR-Hüllrohren: Zircaloy-4, 10,75 mm Außendurchmesser und 0,725 mm Wanddicke. Testbündel und Shroud sind mit Thermoelementen instrumentiert. Sie sind auf 17 Messebenen im Abstand von je 100 mm angeordnet.

Der während des Versuchs durch die Zirkonium-Dampf-Reaktion gebildete Wasserstoff wird mit Hilfe von drei Messgeräten analysiert: zwei Massenspektrometer und ein „Caldos-7G“-Analysegerät (Wärmeleitfähigkeits-Messprinzip).

In diesem Bericht sind die Ergebnisse des Experiments QUENCH-05, das am 29. März 2000 in der QUENCH-Versuchsanlage des Forschungszentrums Karlsruhe durchgeführt wurde, beschrieben. Ziel des Versuchs QUENCH-05 war die Untersuchung des Verhaltens von voroxidierten LWR-Brennstäben während der Kühlung eines Brennstabbündels mit Dampf anstelle von Wasser im Vergleich zum Experiment QUENCH-04, das ohne Voroxidation durchgeführt wurde.

Das Experiment lief mit folgenden Versuchsphasen ab: einer Anfahr- oder Aufheizphase, um das Gesamtsystem bei ca. 900 K Bündeltemperatur ins thermische Gleichgewicht zu bringen, einer Voroxidations-Phase bei einer Temperatur von ca. 1473 K, einer transienten (Aufheiz-) Phase und einer Abschreck- bzw. Quench-Phase. In der transienten Phase wurde das Versuchsbündel mit einer Rate von 0,32 K/s (1445 - 1740 K, TCRC 13) aufgeheizt. Die maximale Stab-Hüllrohrtemperatur von 2272 K wurde in der Ebene 750 mm (TFS 5/11) gemessen. Zur Abschreckung des Versuchsbündels wurde Dampf einer mittleren Rate von 50 g/s von unten in die Teststrecke eingeleitet. Die Dampfeinspeisung führte zu einem unverzüglichen Abkühlen des Stabbündels; innerhalb einer Sekunde fielen alle Stabtemperaturen ab.

Die gesamte freigesetzte Wasserstoffmenge während des Versuchs QUENCH-05 wurde zu 26 g ermittelt. Davon wurden ca. 4 g während der ersten Aufheizphase, 12 g während der Voroxidation, ca. 9 g während der Transiente und nur etwa 1 g während der Kühlphase gebildet.

Nach dem Experiment konnte man zwischen 900 und 1010 mm Bündelhöhe eine deutlich ausgeprägte Shroudversagensstelle erkennen. Im Testbündel selbst gab es nur lokal auftretende Schmelzphasen.

Die maximale Oxidschichtdicke wurde bei Bündelkote 950 mm zu ~420 µm (mittlerer Wert aller Brennstabsimulatoren) bestimmt. Vor der Endphase der Transiente und dem Abkühlen mit Dampf betrug der Wert ~160 µm (auf der Grundlage des bei ~1620 K gezogenen Zircaloy-Eckstabs B).

Zum Oxidationsverhalten von Brennstabsimulatorhülle und Shroud wurden Rechnungen mit dem FZK-eigenen Rechenprogramm CALUMO durchgeführt. Um eine befriedigende Übereinstimmung zwischen den Ergebnissen mit dem CALUMO-Rechenprogramm (im Hinblick auf die Entwicklung der Oxidation) und den experimentellen Ergebnissen von QUENCH-05 zu bekommen, war es notwendig, die Wärmeübergangswerte Brennstabsimulatoren/Kühlmittel unterhalb 750 mm deutlich zu erhöhen.

Abstract

The QUENCH experiments are to investigate the hydrogen source term that results from the water injection into an uncovered core of a Light-Water Reactor (LWR).

The test bundle is made up of 21 fuel rod simulators with a length of approximately 2.5 m. 20 fuel rod simulators are heated over a length of 1024 mm, the one unheated fuel rod simulator is located in the center of the test bundle. Heating is carried out electrically using 6-mm-diameter tungsten heating elements installed in the center of the rods and surrounded by annular ZrO_2 pellets. The rod cladding is identical to that used in LWRs: Zircaloy-4, 10.75 mm outside diameter, 0.725 mm wall thickness. The test bundle is instrumented with thermocouples attached to the cladding and the shroud at 17 different elevations with an axial distance between the thermocouples of 100 mm.

The hydrogen that is produced during the experiment by the zirconium-steam reaction is analyzed by three different instruments: two mass spectrometers and a ”Caldos 7 G” hydrogen measuring device (based on the principle of heat conductivity).

This report describes the results of test QUENCH-05 performed in the QUENCH test facility at the Forschungszentrum Karlsruhe on March 29, 2000. The objective of the experiment QUENCH-05 was the investigation of pre-oxidized rod cladding on cooldown by steam. This experiment could be compared to test QUENCH-04 which was conducted without pre-oxidation.

The experiment consisted of a heatup phase to temperature plateau of around 900 K, a pre-oxidation phase at ~1473 K, a transient phase, and a cooldown phase. All phases were conducted in an argon/steam atmosphere. At the beginning of the transient phase the test bundle was ramped at around 0.32 K/s in the temperature range 1445 – 1740 K to the temperature excursion which led to a maximum rod cladding temperature of 2272 K at the 750 mm level (TFS 5/11). For cooling the test bundle, steam was injected at the bottom of the test section at a rate of 50 g/s. The steam injection led to undelayed cooling of the rods; all rod cladding temperatures began to drop within one second.

The total amount of hydrogen released during the QUENCH-05 experiment was 27 g. Of the 26 g, ~4 g is estimated for the first heatup phase, ~12 g for the pre-oxidation phase, ~9 g for the transient phase, and only ~1 g for the cooling phase.

After the test the shroud exhibited a localized failure zone between 900 mm and 1010 mm elevation. Only a limited local melt formation was observed in the test bundle itself.

The maximum oxide layer thickness measured at 950 mm elevation amounted to ~420 μm (mean value of all fuel rod simulators). Prior to the cooldown by steam, i.e. in the middle of the transient, the ZrO_2 layer thickness had a maximum of ~160 μm at the same level. The latter data were obtained from corner rod B which was withdrawn from the test bundle at ~1620 K.

Calculations with the FZK code CALUMO were performed to study the oxidation behavior of fuel simulator cladding and shroud. To achieve a satisfactory agreement between the calculational results of the CALUMO code (with respect to the evolution of the oxidation) and the experimental findings of QUENCH-05 it was necessary to considerably increase the heat transfer values of fuel rod simulator/coolant below 750 mm.

Contents

List of Tables

List of Figures

Introduction

The most important accident management measure to terminate a severe accident transient in a Light Water Reactor (LWR) is the injection of water to cool the uncovered degraded core. Analysis of the TMI-2 accident [1] and the results of integral out-of-pile (CORA [2, 3]) and in-pile experiments (LOFT [4], PHEBUS, PBF) have shown that before the water succeeds in cooling the fuel pins there could be an enhanced oxidation of the Zircaloy cladding that in turn causes a sharp increase in temperature, hydrogen production and fission product release.

Besides, quenching is considered a worst-case accident scenario regarding hydrogen release to the containment. For in- and ex-vessel safety analyses one has to prove that the hydrogen release rate and total amount do not exceed limits for the considered power plant. The hydrogen generation rate must be known to design appropriately accident mitigation measures for the following reasons.

- Passive autocatalytic recombiners require a minimum hydrogen concentration to start. Moreover, they work slowly, and their surface area and their position in the containment have to be quantified carefully.

- The air-steam-hydrogen mixture in the containment may be combustible for only a short time before detonation limits are reached. This limits the time period during which ignitors can be used.

The physical and chemical phenomena of the hydrogen release are, however, not sufficiently well understood. Presently it is assumed that new metallic surfaces are formed by cracking and fragmentation of the oxygen-embrittled cladding tubes as a result of the thermal shock during flooding leading to enhanced oxidation and hydrogen generation. Consequently, in most of the code systems describing severe fuel damage, the quench phenomena are either not considered or only modeled in a simplified empirical manner.

No models are yet available to predict correctly the thermal-hydraulic or the clad behavior of the quenching processes in the CORA and LOFT LP-FP-2 tests. No experiments have been conducted that are suitable for calibrating the existing models. The increased hydrogen production during quenching cannot be determined on the basis of the available Zircaloy/steam oxidation correlations. An extensive experimental database is needed as a basis for model development and code improvement.

The Forschungszentrum Karlsruhe has therefore started the QUENCH program on the determination of the hydrogen source term. The main objectives of this program are:

- The provision of an extensive experimental database for the development of detailed mechanistic fragmentation models,

- The examination of the physico-chemical behavior of overheated fuel elements under different flooding conditions,

- The provision of an improved understanding of the effects of water injection at different stages of a degraded core,

- The determination of cladding failure criteria, cracking of oxide layers, exposure of new metallic surfaces to steam which are currently supposed to result in renewed temperature escalation and hydrogen production, and

- The determination of the hydrogen source term.

The experimental part of the QUENCH program began with small-scale experiments with short Zircaloy fuel rod segments [5, 6]. On the basis of these results well-instrumented large-scale bundle experiments with fuel rod simulators under nearly adiabatic conditions are performed in the QUENCH facility at the Forschungszentrum Karlsruhe. The large-scale bundle experiments are more representative of prototypic reactor accident conditions than are the single-rod experiments. Important parameters of the bundle test program are (see Table 1): quench medium, i.e. water or steam, fluid injection rate, cladding pre-oxidation, and the temperature at onset of flooding. The results of the first experiments are documented in the following references: QUENCH-01 [7, 10, 16, 17], QUENCH-02 [8, 10, 16, 17], and QUENCH-03 [8, 18], and QUENCH-04 [9, 18].

The fifth bundle experiment, QUENCH-05, was performed at the Forschungszentrum Karlsruhe on 29 March, 2000. It was the second bundle experiment in the QUENCH series in which the bundle was cooled from high temperatures by steam (injected from the bottom), rather than being quenched by water. It differed from the first steam-cooled experiment QUENCH-04 only in that the bundle was pre-oxidized before the transient and the cooling phase began.

This report describes the test facility and the test bundle, and the main results of the QUENCH-05 experiment. In addition, one section is dedicated to the results of the calculations with the CALUMO (oxidation) computer code.

1 Description of the Test Facility

The QUENCH test facility consists of the following component systems:

- the test section with 21 fuel rod simulators
- the electric power supply for the test bundle heating
- the water and steam supply system
- the argon gas supply system
- the hydrogen measurement devices
- the process control system
- the data acquisition system.

A simplified flow diagram of the QUENCH test facility is given in Fig. 1, a three-dimensional schematic of the components in Fig. 2. The main component of the facility is the test section with the test bundle (Figs. 3 and 4). The superheated steam from the steam generator and superheater together with argon as the carrier gas for the hydrogen detection systems enter the test bundle at the bottom end. The steam that is not consumed, the argon, and the hydrogen produced in the zirconium-steam reaction flow from the bundle outlet through a water-cooled off-gas pipe to the condenser (Figs. 1 and 2). Here the steam is separated from the non-condensable gases argon and hydrogen. The cooldown phase with steam is initiated by turning off the superheated steam of 3 g/s whereas the argon gas remains unchanged. At the same time saturated steam of 50 g/s is injected at the bottom of the test bundle through the same line.

The design characteristics of the test bundle are given in Table 2. The test bundle is made up of 21 fuel rod simulators, each with a length of approximately 2.5 m, and of four corner rods (see cross section in Fig. 5). The fuel rod simulators are held in their positions by five grid spacers, four of Zircaloy, and one of Inconel in the lower bundle zone (Fig. 6). The cladding of the fuel rod simulators is identical to that used in PWRs with respect to material and dimensions, i.e. Zircaloy-4, 10.75 mm outside diameter, 0.725 mm wall thickness. The rods are filled with a mixture of 95 % argon and 5 % krypton to approx. 0.22 MPa, i.e. a pressure slightly above the system pressure. The gas filling of all rods is realized by a channel-like connection system inside the lower sealing plate. The krypton additive allows to detect fuel rod failure during the experiment with help of the mass spectrometer.

Twenty fuel rod simulators are heated electrically over a length of 1024 mm, the one unheated fuel rod simulator is located in the center of the test bundle. The unheated fuel rod simulator (Fig. 7) is filled with ZrO_2 pellets (bore size 2.5 mm ID). For the heated rods (Fig. 6) 6 mm diameter tungsten heating elements are installed in the center of the rods and are surrounded by annular ZrO_2 pellets. The tungsten heaters are connected to electrodes made of molybdenum and copper at each end of the heater. The molybdenum and copper electrodes are joined by high-frequency/high-temperature brazing performed under vacuum. For electrical insulation the surfaces of both types of electrodes are plasma-coated with 0.2 mm ZrO_2. To protect the copper electrodes and the O-ring-sealed wall penetrations against excessive heat they are water-cooled (lower and upper cooling chamber). The copper electrodes are connected to the DC electric power supply by means of special sliding contacts at the top and bottom. The total heating power available is 70 kW, distributed among the two groups of heated rods with 35 kW each. The first group consists of the inner eight rods (rod numbers 2 – 9), the second group consists of the outer twelve rods (rod numbers 10 – 21). The rod designation can be taken from Fig. 8.

The four corner positions of the bundle are occupied either by solid zircaloy rods with a diameter of 6 mm or by solid rods (upper part) and Zry tubes (lower part) of ∅ 6 x 0.5 mm for thermocouple instrumentation at the inside (Fig. 8). The positioning of the four corner rods avoids an atypically large flow cross section at the outer positions and hence helps to obtain a rather uniform radial temperature profile. A solid Zry rod can be pulled out to determine the axial oxide layer thickness at that time.

The lower boundary for the lower cooling chamber is a sealing plate made of stainless steel with plastic inlays for electrical insulation, sealed to the system by O-shaped rings. The upper boundary of the lower cooling chamber is a sealing plate of stainless steel. An insulation plate made of plastic (PEEK) forms the top of the upper cooling chamber, and a sealing plate of Al_2O_3, functioning as a heat-protection shield, is the lower boundary of the upper cooling chamber (see Fig. 6).

In the region below the upper Al_2O_3 plate the copper electrode is connected firmly to the cladding. This is done by hammering the cladding onto the electrode with a sleeve of boron nitride put between electrode and cladding for electrical insulation. The axial position of the fuel rod simulator in the test bundle is fixed by a groove and a locking ring in the top Cu electrodes. Referred to the test bundle the fixing of the fuel rod simulators is located directly above the upper edge of the upper insulation plate. So, during operation the fuel rod simulators are allowed to expand downwards. Clearance for expansion of the test rods is provided in the region of the lower sealing plate. Also in this region relative movement between cladding and internal heater/electrode can take place.

The test bundle is surrounded by a 2.38 mm thick shroud (80 mm ID) made of Zircaloy with a 37 mm thick ZrO_2 fiber insulation and an annular cooling jacket made of stainless steel (Figs. 4 and 5). The 6.7 mm annulus of the cooling jacket is cooled by an argon flow. Above the heated zone, i.e. above the 1024 mm elevation there is no ZrO_2 fiber insulation to allow for higher radial heat losses. This region of the cooling jacket is cooled by a water flow (Figs. 3 and 4). Both the lack of ZrO_2 insulation above the heated region and the water cooling force the axial temperature maximum downward.

2 Test Bundle Assembly

The test section consists of three subassemblies pre-assembled separately. One subassembly comprises the cooling jacket with the bundle head casing; the second subassembly includes the instrumented shroud with the bundle foot; and the third subassembly is composed of the instrumented test bundle with the bundle head. The test bundle and the shroud, including the respective thermocouples, must be replaced for each experiment. The instrumentation of the bundle head and the foot as well as the cooling jacket, however, remains unchanged.

3 Test Bundle Instrumentation

The test bundle was instrumented with sheathed thermocouples attached to the rod claddings at 17 different elevations between -250 mm and 1350 mm and at different orientations (Figs. 8 through 11). The elevations of the surface-mounted shroud thermocouples are from -250 mm to 1250 mm. In the lower bundle region, i.e. up to the 550 mm elevation, NiCr/Ni thermocouples (1 mm diameter) are used for temperature measurement of rod cladding and shroud as is illustrated in Fig. 9. The thermocouples of the hot zone are high-temperature thermocouples with W-5Re/W-26Re wires, HfO_2 insulation, and a duplex sheath of tantalum (internal)/Zircaloy with an outside diameter of 2.1 mm (Fig. 10). The leads of the thermocouples from -250 mm to 650 mm leave the test section at the bottom whereas the TCs above 650 mm penetrate the test section at the top. There is one exception, i.e. TFS 2/12 is penetrated from the bottom.

The thermocouple attachment technique for the surface-mounted high-temperature TCs is illustrated in Fig. 11. The TC tip is held in place by two clamps of zirconium. As these clamps are prone to oxidation and embrittlement in a steam environment an Ir-Rh wire of 0.25 mm diameter is additionally used in the experiments with pre-oxidation. So, in test bundle QUENCH-05 there were wires used for the additional fixing of the TCs.

The designations of the surface-mounted cladding and shroud thermocouples are “TFS” and “TSH”, respectively. The unheated fuel rod simulator of the QUENCH-05 bundle was especially instrumented to provide information on the accuracy of the temperature measurement with externally mounted thermocouples, particularly during cooldown. Therefore, two thermocouples were inserted in the center of the central rod (designation “TCRC”), two thermocouples at the rod cladding inner surface (designation “TCRI”, ∅ 0.5 mm), and two thermocouples at the rod cladding outer surface (designation “TCR”, ∅ 1 mm). These three thermocouple positions were realized at the 350 and 550 mm elevation (see Figs. 12 and 13).

The wall of the inner tube of the cooling jacket is instrumented between -250 mm and 1150 mm with 22 NiCr/Ni thermocouples (designation “TCI”). Five NiCr/Ni thermocouples are fixed at the outer surface of the outer tube of the cooling jacket (“TCO”). The designation of the thermocouples inside the Zircaloy instrumentation rods (corner positions) is “TIT” (Fig. 14). Three of the four corner rods of the QUENCH-05 test bundle were instrumented as follows:

- Rod A: W/Re, 2.1 mm diam., Zr/Ta duplex sheath, 950 mm elevation (TIT A/13)
- Rod C: NiCr/Ni, 1 mm diam., stainless steel sheath, 500 mm elevation (TIT C/9)
- Rod D: W/Re, 2.1 mm diam., Zr/Ta duplex sheath, 800 mm elevation (TIT D/12).

A list of the instruments for experiment QUENCH-05 installed in the test section and at the test loop is given in Table 3.

The following thermocouples failed during handling, prior to the experiment:

TIT A/13, TFS 2/13, TFS 5/14, TSH 4/270, and TCI 15/180.

All but two of the thermocouples survived the entire experiment:

TCR 13 with the failure at 5620 s (1719 K), and TFS 3/13 which failed at 5668 s (1646 K).

The internal thermocouples of the central rod, i.e. TCRI 7, TCRC 7, TCRI 9, and TCRC 9, worked during the entire experiment but resulted in too low temperatures (due to leakages of the TC sheath) so that the data were eliminated.

4 Hydrogen Measurement Devices

The hydrogen is usually analyzed by three different measurement systems: (1) a Balzers mass spectrometer (MS) “GAM 300” (Fig. 15) located at the off-gas pipe, approx. 2.7 m downstream from the test section outlet, (2) a hydrogen detection system ”Caldos 7 G” (Fig. 17) located in a bypass to the off-gas line behind the condenser, (3) a second, simpler mass spectrometer “Prisma” made by Balzers installed close to the Caldos device. So, the off-gas, i.e. the argon/hydrogen mixture, downstream the condenser passed at first the mass spectrometer “Prisma” and then the Caldos analyzer before it exited to the outside. Due to their different locations in the facility the mass spectrometer “GAM 300” responds almost immediately (less than 5 s) to a change in the gas composition in the bundle whereas the mass spectrometer “Prisma” and the Caldos device have a delay time of about 20 – 30 s.

The mass spectrometer “BALZERS GAM 300“ used is a completely computer-controlled quadrupole MS with an 8 mm rod system which allows quantitative measurement of gas concentrations down to about 10 ppm. For the MS measurement a sampling tube is inserted in the off-gas pipe. It has several holes at different elevations to guarantee that the sampling of the gas to be analyzed is representative (see Fig. 16). To avoid steam condensation in the gas pipes between the sampling position and the MS the temperature of the gas at the MS inlet is controlled by a heat exchanger to be between 110 °C and 150 °C (the upper operating temperature of the MS inlet valves). This allows the MS to analyze the steam production rate. Besides, the concentrations of the following species were continuously measured by the mass spectrometer during all test phases: argon, hydrogen, steam, nitrogen, oxygen, and krypton. As the fuel rod simulators are filled with krypton as a tracer gas in addition to the argon, i.e. a mixture of argon and 5% krypton, the measurement of krypton can be used as an indicator for a cladding failure. Additionally, the MS is used to control the atmosphere in the facility, e.g., to monitor the gas composition at the beginning of the test.

The temperature and pressure of the analyzed gas are measured near the inlet valve of the MS. The MS is calibrated for hydrogen with well-defined argon/hydrogen mixtures and for steam with mixtures of argon and steam supplied by the steam generator of the QUENCH facility. The MS off-gas is released into the atmosphere because the amount of hydrogen taken out of the system is negligible.

The principle of measurement of the Caldos system is based on the different heat conductivities of different gases. The Caldos device is calibrated for the hydrogen-argon gas mixture. To avoid any moisture in the analyzed gas a gas cooler, which is controlled at 296 K, is connected to the gas analyzer (Fig. 17). The response time of the gas analyzer is documented by the manufacturer to be 2 s, i.e. a time in which 90 % of the final value should be reached. In contrast to the mass spectrometer the Caldos device only measures the hydrogen content. Gases other than H_2 cannot be analyzed by this system.

For the Caldos device as well as for the MS the hydrogen mass flow rate is calculated by referring the measured H_2 concentration to the known argon mass flow rate according to equation (1):

$$\dot{m}_{H_2} = \frac{M_{H_2}}{M_{Ar}} \cdot \frac{C_{H_2}}{C_{Ar}} \cdot \dot{m}_{Ar} \tag{1}$$

with M representing the molecular masses, C the concentrations in vol-% and $\dot{m}$ the mass flow rates of the corresponding gases.

With an argon-hydrogen (two-component) mixture that in fact exists at the location of the Caldos analyzer equation (1) can be written as follows

$$\dot{m}_{H_2} = \frac{M_{H_2}}{M_{Ar}} \cdot \frac{C_{H_2}}{100 - C_{H_2}} \cdot \dot{m}_{Ar} \tag{2}$$

5 Data Acquisition and Process Control

A computer-based control and data acquisition system is used in the QUENCH facility. Data acquisition, data storage, online visualization as well as process control, control engineering and system protection are accomplished by three computer systems that are linked in a network.

The data acquisition system allows recording of about 200 measurement channels at a maximum frequency of 25 Hz per channel. The experimental data and the date and time of the data acquisition are stored as raw data in binary format. After the experiment the raw data are converted into SI units and stored as ASCII data.

For process control, a system flow chart with the most important actual measurement values is displayed on the computer screen. Furthermore, the operating mode of the active components (pumps, steam generator, superheater, DC power system, valves) is indicated. Blocking systems and limit switches ensure safe plant operation. Operating test phases, e.g. heatup or quenching phases, are pre-programmed and can be started on demand during the experiment. The parameter settings of the control circuits and devices can be modified online.

Online visualization allows to observe and to document the current values of selected measurement positions in the form of tables or plots. Eight diagrams with six curves each can be displayed as graphs. This means that altogether 48 measurement channels can be selected and displayed online during the course of the experiment.

The data of the main data acquisition system and of the mass spectrometers were stored on different computers. Both computers were synchronized by radio-controlled clocks.

The data of the main acquisition system were stored at frequencies of 0.25 Hz (pre-oxidation phase, i.e. 0 – 4860), and 5 Hz (from 4860 s on), respectively. The mass spectrometer data were recorded at a frequency of around 1 Hz during the entire test.

6 Test Conduct and General Results

In the QUENCH-05 experiment the bundle was heated from room temperature to ~900 K in an atmosphere of flowing argon (3 g/s) and steam (3 g/s). The bundle was stabilized at this temperature for about 2 hours, the electrical power being 4 kW (see Fig. 21, top). The test conduct is illustrated in Fig. 18, the duration of the test phases is defined in Fig. 19, bottom, on the basis of the TCRC 13 temperature history, and the sequence of events is summarized in Table 4.

At the end of the stabilization period the bundle was ramped by stepwise increases in power giving an average temperature rise of about 0.5 K/s between ~900 K and ~1500 K in the argon/steam mixture. Then the temperature was stabilized at the 1500 K level (axial maximum) with a power of about 11 kW (Fig. 21, top). The temperature was maintained constant by control of the electrical power in this pre-oxidation phase for 3500 s (The duration of this period was defined on the basis of the QUENCH-01 results [7] and on pre-test calculations performed with the SCDAP/RELAP5 computer code aiming at a maximum oxide layer thickness of about 200 μm at the end of the preoxidation phase). At the end of the pre-oxidation period the bundle was ramped at 0.3 W/s per rod to start the transient phase, in the same way as in test QUENCH-04. The heatup rate of the rod bundle during the transient phase evaluated on the basis of TCRC 13, level 950 mm, was 0.32 K/s between 1445 K and 1740 K (Fig. 19, top). During this period and prior to any temperature excursion corner rod B was withdrawn at about 1620 K to check the amount of oxidation at that time with help of an eddy-current device. This method resulted in a maximum oxide layer thickness of ~175 μm at the 950 mm elevation whereas the metallographic posttest examination resulted in a more accurate maximum oxide layer thickness of ~160 μm at the same elevation (see Fig. 80).

According to thermocouple TFS 2/1 at -250 mm the coolant inlet temperature was ~600 K from the beginning of the data acqisition to the onset of cooling as can be taken from Fig. 21, bottom. T 511 located upstreams is at a higher temperature due to heat radiation from the hot structure. During the steam injection the steam temperatures at the inlet of the test section as well as at the outlet (T 512) change continuously.

An oxidation excursion started in the rod bundle at 5985 s at 850 mm when the temperature there reached 1870 K (TFS 3/12, see Table 5). The pre-planned steam cooling sequence was initiated when two rod thermocouples (one each at 750 mm and 850 mm, i.e. TFS 2/11 and TFS 3/12) had exceeded 2000 K. Fig. 20 shows the temperature traces from these thermocouples together with the hydrogen concentration measured by the mass spectrometer and the first derivative of the hydrogen signal. From the diagram it can be seen that the temperature excursions and the slope of the hydrogen concentration correspond quite well. When the two thermocouples escalated the central rod centerline thermocouple TCRC 13 had reached ~1900 K, comparable to the cooldown initiation temperature for QUENCH-04. For cooling the test bundle, the flow of 3 g/s superheated steam (FM 401: 2.96 g/s) was turned off and steam of ~500 - 600 K was injected at the bottom of the test section at a nominal rate of 50 g/s (F 204 mean value: 47 – 48 g/s). The argon gas supply remained unchanged. 22 s after the begin of the cooldown the electrical power was reduced from ~17.95 kW to ~3.9 kW within 15 s, to simulate decay heat levels. Cooling of the test section to below 700 K was complete about 200 s later; the steam and electrical power were shut off 309 s after its initiation, terminating the experiment.

In Fig. 22, bottom, the cooldown steam injection (F 204 total input = 14722 g) is compared with the flow measurement F 601 with a total of 14838 g. The original F 601 data plotted vs. time in Fig. 22, top give a zero signal up to the onset of cooling so that one can assume that the increase of the signal at 6011 s is a result of the steam injection. So, with a known density the data can be converted to a mass flow rate. The spike at the onset of steam injection, however, is not real. This is because the F 601 is a standard orifice plate in the off-gas pipe and is designed for steady-state flow conditions. The total numbers, however, could be compared to learn if the F 601 data can be used for a steam balance which is of importance in the water injection tests to get information on the steaming rate and water/steam balance, respectively. Additionally, the steam flow rate determined on the basis of the L 701 data (condensed steam in the condensate collection tank) and by means of the mass spectrometer measurement (MS) is in accordance with the steam injection rate (F 204 + F 205) as demonstrated for the flow rates and for the integral values in Fig. 23, top and bottom, respectively. The original MS data, however, overestimate the steam flow rate. This is true particularly during the cooldown phase due to the fact that the MS was calibrated during the stabilization period by applying 3 g/s of steam plus 3 g/s argon. In separate calibration tests with a dummy test section it was realized that a portion of the steam condensed in the off-gas pipe at conditions which generally exist during the stabilization period, i.e. at ~900 K. The steam condensation leads to a wrong calibration factor for the MS steam data. With the test facility at temperature and the steam flow rate elevated during cooldown, the condensation is negligible. Therefore, the MS steam data had to be corrected.

The maximum rod temperature of 2272 K was measured with thermocouple TFS 5/11 (750 mm level) at 6012 s (see Table 7). In general, the maximum rod cladding temperatures coincide with the temperature at the onset of cooldown (strong temperature drop at 6011 s). There are only two exceptions, i.e. TFS 2/11 and TFS 3/12 show an earlier maximum. The onset of cooling as evaluated from the thermocouple data is given in Table 6.

The steam injection led to rapid cooling of the rods, i.e. within one second all rod cladding temperatures began to drop. Fig. 26 gives the cooldown behavior by the TFS, TCR, TCRC, TIT, and TSH thermocouples at three different axial levels, i.e. at 50, 550, and 950 mm. Within the first seconds after the onset of cooldown the temperature drop measured by the externally mounted cladding thermocouples (TFS and TCR) was more pronounced than that of the internal thermocouple TCRC 13 and of the shroud TCs (TSH). At some levels the signals of the external cladding thermocouples even dropped momentarily to the steam saturation temperature. One to four seconds later the externally mounted cladding thermocouples showed the usual cooldown behavior.

Different from the test rods the shroud has its real temperature maxima at the different elevations 1 - 2 s after the onset of cooling. In Fig. 27, top the temperature response of all shroud thermocouples during the quenching phase is given. Fig. 27, bottom compares the shroud thermocouples with the cladding surface thermocouples at elevation 1250 mm. At 6012 - 6013 s it appears as if the upper shroud experienced an excursion at the elevations from 750 to 1250 mm, above all in the 180 – 270° orientation (e.g. thermocouples TSH 13/270, TSH 14/270, TSH 15/180, TSH 16/180). The duration of the temperature excursions of the shroud of 1 - 2 s is, however, too short to justify a real excursion of the 2.38-mm thick shroud wall. It is possible that this effect is a thermocouple effect. Fig. 28 compares what is believed to be a real temperature excursion as seen in test QUENCH-04 with the one of test QUENCH-05 described above. So, these temperature peaks were not taken for the evaluation of the maximum temperatures presented in Table 8. The maximum rod cladding temperatures and shroud temperatures of each elevation are plotted in Fig. 33.

Shroud failure occurred at 1837 s, i.e. early in the pre-oxidation phase as is demonstrated in Fig. 34. At this time the pressure P 406 measured in the volume between inner cooling jacket and shroud drops to the bundle pressure level within a few seconds. In addition to the pressure trace the nitrogen concentration measured in the off-gas by the mass spectrometer reflects shroud failure by a spike that coincides with the pressure drop. Prior to the test the nitrogen as part of the air is still entrained in the void volume of the shroud insulation (ZrO_2 fiber). During heatup the air is released from the insulation into the volume between inner cooling jacket and shroud and enters the test section upon shroud failure.

A first rod failure can be indicated by a sudden drop in the rod internal pressure P 411 as well as in the sudden increase in the krypton concentration of the off-gas which can be measured by the mass spectrometer. The krypton is an additive of the rod filling gas so that it can be detected at the offgas measurement location upon rod failure. In the QUENCH-05 experiment rod failure does not occur before the onset of cooling takes place. In Fig. 25, top the P 411 history is given together with the system pressure at the inlet (P 511) and outlet of the test section (P 512). There is no clear indication from P 411 which shows no sharp drop but a slow decrease from around 6100 s. In Fig. 25, bottom a first increase in the krypton concentration can be seen at about 6225 s. This could be the time of a first rod failure which lies well in the cooldown phase.

In Figs. 31 through 33 the axial temperature profiles of the TFS 2-type (inner coolant channel), TFS 5-type (outer coolant channel), as well as of the shroud thermocouples are given for five different times within the transient and cooldown phase (see Fig. 30).

7 Hydrogen generation

The total hydrogen production is ~26 g. The peak production rate of ~0.3 g/s was measured by the main mass spectrometer as is shown in Fig. 24, top. There is a good agreement between the Caldos analyzer and the two mass spectrometers with respect to the total values. Of the 26 g, ~4 g is estimated for the heatup phase, ~12 g for the pre-oxidation phase, ~9 g for the transient phase, and ~1 g for the cooling phase. This compares with 10 g for the transient phase and 2 g for the cooling phase in the non-preoxidized test bundle QUENCH-04.

Fig. 29, top gives the time correlation of the electric bundle power input, the maximum measured temperature TFS 5/11, the cooldown steam flow rate, and the hydrogen release rate measured by the main mass spectrometer. It can be seen that the hydrogen release rate increases with the onset of the temperature excursion. It decreases promptly with the cooling steam injection indicating a very effective cooling.

A comparison of the chemical power poduced by the exothermal Zircaloy-steam reaction and the electric bundle power in Fig. 29, bottom shows that most of the heat generated is due to electrical heating almost during the entire test except for a period of a few seconds at the end of the transient phase and the beginning of the cooldown phase.

8 Posttest Examination

8.1 Sectioning of the Test Bundle

The mould for filling the bundle with epoxy resin mainly consists of a tube made of PMMA (∅133x6.5 mm, 2 m length) that surrounds the shroud over the entire bundle length. It is set up vertically. So, the bundle is filled from the bottom with approx. 20 kg of resin and hardener (epoxy system Rütapox 0273 with the hardener designated LC manufactured by Bakelite GmbH, Iserlohn). The epoxying process generally shows little heating during the curing stage due to the exothermal reaction. After epoxying the bundle the resin is allowed to harden for a minimum of one week. To obtain the cross sections a saw with a 2.0 mm-thick diamond blade (mean diamond grain size 138 µm) of 350 mm OD is used to cut the slabs at 1300 rpm. As an overview the sectioning map is given for test bundle QUENCH-05 in Fig. 39. The exact elevations are listed in Table 9. The 13-mm thick cross sections that were selected for metallographic examination (see also Table 9) were polished. For this purpose, the samples were infiltrated by "Araldit" resin to close up residual voids, then they were ground and polished. The work is performed using a semi-automatic machine with a closed water circuit for grinding and an automatic lubricant feeder for the polishing steps. In addition to the 13-mm thick sections, two cross sections of 5 mm thickness were cut to use their claddings for the analysis of the hydrogen absorption in the Zircaloy metal. The one 5 mm slice at 75 – 80 mm served as a reference sample.

8.2 General Observation

A local shroud failure was observed between the 900 mm and 1010 mm elevation (Figs. 35 – 38). In this region the shroud has ballooned (maximum radial deformation at around 280 - 290 ° orientation) and is severely oxidized. There are several longitudinal cracks which were caused by thermal stresses (hoop stress). The maximum crack length is 90 mm (from 915 to 1005 mm elevation). Besides this failure region the shroud is intact and so are the thermocouples which are still attached to the shroud surface.

Corner rod B which was withdrawn from the test bundle during the transient reveals gray ZrO_2 in the region between the 900 and 1000 mm level where the maximum oxide layer thickness was measured (~160 µm at the 950 mm elevation).

Test rod #15 was withdrawn from the test bundle prior to encapsulation. The rod cladding which was to determine the axial ZrO_2 layer profile and to analyze the hydrogen absorbed in the remaining Zircaloy-4 metal, however, broke during the pulling procedure due to severe embrittlement. So, the cladding remnants, i.e. from around 960 mm elevation upwards, fell back into the bundle and were lost for this analysis.

The cross sections can be viewed in the unpolished condition in Figs. 40 through 43. No melt had formed within the test bundle. The central rod is broken between 920 and 935 mm and between 985 and 1000 mm elevation. Cladding fragments at least, however, remained at all of these elevations.

The physico-chemical state of the Zircaloy cladding material was investigated and evaluated by light microscope and by scanning electron microscope examinations. Of special interest was the determination of the oxide layer thickness on the Zircaloy cladding tubes and the shroud, the formation of through-wall cracks in the cladding tubes and the oxidation of the crack surfaces.

8.3 Microstructural Analysis of Polished Cross Sections

8.3.1 Introductory remarks

More pretentious than describing the final bundle state is the effort of deducing the mechanisms of physico-chemical components' interaction and oxidation from the bundle state. It turned out to be helpful to proceed from the lower bundle elevations upward, in the direction of increasing temperatures, and thus increasing interaction. In this sense, the state of lower elevations can be understood to represent largely some interim states for the higher elevations. The cool-down related phenomena, which are of main concern here, deserve special attention.

For this bundle the final status of the thermocouples of the W-Re type was included in the main topics. As the test began with a pre-oxidation phase (after the usual stabilization period), relatively strong oxidative attack and mechanical loading was expected for them. It was decided to investigate the rod thermocouples systematically with the aim of finding out their degradation mechanisms.

8.3.2 Bundle elevation 73 mm

The polished cross section for this elevation is shown in Fig. 44 as a reference for the unchanged condition of the bundle arrangement relative to the lowest Zry spacer grid. As corner rod B had been pulled out during the transient test phase before the onset of escalation its previous south-west position is empty. The reason for missing pellets and tungsten heater rods in this and in higher elevations is simply the occasional loss during handling of the respective cross section slabs. This may occur before safe fixing of all loose pieces by additional resin impregnation, which is necessary before the metallographic preparation procedures. Several thermocouples are seen to cross the elevation, at which no measurements took place; the thinner ones of NiCr-Ni type can be distinguished from the thicker ones of W-Re type.

8.3.3 Bundle elevation 550 mm

Above mid-plane elevation of the heated zone of the bundle, at the position of the next Zry spacer grid, the overview of the cross section looks still intact, even in the bottom macrograph of Fig. 45.

In higher magnification the steam oxidation of the rod cladding and of the spacer structure can be studied (Fig. 46): Both components show a ZrO_2 scale, a relatively thick α-Zr(O) layer, a zone of duplex structure (α-Zr(O) within β-Zr) and the β-Zr matrix. The peak temperature at this elevation can be concluded to have exceeded the temperature range of 1093 to 1243 K (α-Zr + β-Zr), as the matrix shows β-Zr structure. However, the peak temperature was not much above 1243 K, as indicated by the adjacent oxygen diffusion zone of duplex (α-Zr(O) + β-Zr) structure, which is not observed at higher temperatures. Further indications for the moderate peak temperature are the low thickness ratio of ZrO_2 scale to α-Zr(O) layer and locally retarded scale growth behind pores. These observations are too complex to be further described and discussed in the present context. However, they are typical for the pre-transition regime of breakaway oxidation, according to experience from earlier studies on microstructure and kinetics related with this effect (see [11] and section on bundle elevation 1250 mm). The described bundle components are understood to have remained below 1330 °C, since the breakaway is restricted to that upper temperature limit. The above given temperature estimations on the basis of the oxidation morphology are in good agreement with the temperature measurements by thermocouples (1306 and 1326 K at onset of steam cooling, see Tab. 6).

8.3.4 Bundle elevation 750 mm

The shroud and the rod claddings are shown to be intact in the overview (Fig. 47). Most of the pellets and heater rod segments have been lost, which indicates that no interaction has occurred that could have tended to fix them. The oxidation status of the thermocouple TFS 5/11 and of the respective rod No. 13, to which it was attached by a spot-welded clamp, is depicted in Fig. 48. Growth of protective ZrO_2 scale is found on rod cladding, TC sheath and clamp, all with coarsely similar thickness. In none of the scale microstructures the cubic ZrO_2 modification is realised. This means that there is no indication for a temperature above 1800 K. This is in contrast to the result of evaluation of the reading of TFS 5/11 (see Tab. 6), for which a peak temperature of 2272 K is given. A slightly higher temperature for the heated rod compared to the TC (Fig. 48, left, bottom) could explain the thinner scale of the sheath, which shows the thicker α-Zr(O) layer. This can be due to the more advanced consumption of the external sheath or be due to differences in composition (Zry cladding, Zr sheath). Clamp oxidation itself or stress from extrinsic forces has resulted in crack formation across the embrittled metallic core of the clamp (right, top). According to the detectable crack surface oxidation (right, bottom) this cracking has occurred at higher a temperature than that during the late cool-down phase.

The other TCs of W-Re type are grouped in Fig. 49 according to the measurement elevation (No. 11, this elevation and No. 12, 850 mm) and to the extent of oxidation. TFS 2/11 is found outside the clamp and at distance from rod No. 8 for unknown reason. TFS 5/12, which is only slightly oxidised, and TFS 3/12, both inserted from above, were not expected to be seen at this position. They could have slipped downward in the bundle; but then one would expect them to show the more advanced oxidation gained at the original position. TFS 2/12 inserted from below, shows more advanced oxidation, in contradiction to the previous argument. More important is further that the TC oxidation status for this elevation in total does not correspond to the rather high peak temperature level deduced from TC measurements (1940 to 2272 K at onset of cooling, according to Tab. 6). It is important to try to resolve those discrepancies, which were especially realised for this elevation.

8.3.5 Bundle elevation 850 mm

The circular shroud and the bundle are still in quite intact condition at this elevation, according to the cross section overview (Fig. 50). Some fuel rod simulators show through-wall cracking (see macrograph). The oxidation status of the central and a peripheral fuel rod is given in Figs. 51 and 52, respectively. Independent from the position in the bundle the rod cladding shows the protective scale, indicating in both examples peak temperatures above 1800 K, the brittle α-Zr(O) layer, being strongly cracked (and further damaged in cross section preparation) and the β-Zr phase matrix. At some positions through-wall cracking has occurred, as already mentioned. The crack surfaces look non-oxidised and steam access to the internal cladding surface had no detectable effect. Locally some pellet/cladding interaction might have taken place; an oxygen uptake by the cladding is, however, not detectable. For this reason the spalled surface layer on the pellet, as shown in Fig. 51 is not understood as a product of interaction with the cladding. It might be the result of treatment of pellets in reducing atmosphere during manufacturing.

The status of thermocouples of the W-Re type is addressed in Figs. 53 and 54. Fig. 53 shows thermocouples for measurement level 750 mm, visible since inserted from above. The feature of wedge-shaped scale cracking of the partly oxidised external sheath will be treated for the subsequent elevations in the following sections. In Fig. 54, left column, a thermocouple is shown together with details of rather moderate oxidation. This TC was expected in north-east orientation from rod No. 9 fixed by a clamp. It has obviously lost this contact and this might be the reason for non-prototypical oxidation status. One has to take into account that TC detachment or rupture is inevitable during bundle dismantling, since the top plate has to be lifted by 5 to 7 cm in order to cut the TCs. This argument does not hold for TFS 2/12 which was not found. In contrast, TFS 3/13, not expected in the given elevation is found in form of a downward relocated fragment in seriously damaged condition: The outer sheath is completely oxidised and the inner sheath is partly oxidised. The sheath oxidation mechanisms will be described further on.

8.3.6 Bundle elevation 920 mm

At this elevation the axial splitting of the shroud is clearly visible in the cross section overview (Fig. 55). Compared to the considerable shroud oxidation on the internal side its external oxidation is concentrated to the split surfaces and the adjacent areas, where the penetrating steam was essentially consumed. This result is mentioned in advance, since no detailed documentation of the shroud oxidation will be given in the following description of the bundle status:

Whereas the central rod is found fragmented with respect to pellet and cladding, all peripheral rods are coarsely intact. Variations of the temperature history across the bundle and from rod to rod are illustrated in Fig. 56: Rod No. 16 described in the left column has retained β-Zr cladding matrix, whereas rod No. 21 in the right column, more advanced in cladding oxidation, shows complete conversion of the metallic part into α-Zr(O) phase, and correspondingly thicker scale. The scale microstructure, indicating a sub-layer of cubic ZrO_2 phase and thus a peak temperature clearly above 1800 K differs from that of rod No. 16, which just reached that level of temperature. The mechanical consequences of advanced oxidation can be compared as well: For rod No. 21 through-wall cracking of the embrittled cladding occurred, whereas only the brittle α-Zr(O) layer of rod No. 16 has developed cracks. (Despite all reasonable care in the metallographic preparation such cracked and correspondingly fragile structures or zones are often further damaged by formation of secondary cracks and loss of fragments. On the one hand this facilitates the detection of real cracks, but on the other hand, it is not always satisfactorily possible to distinguish artefacts from the pre-existing “real and typical” damage.)

Fig. 57 shows a rod which has reached a peak temperature above 1800 K without major mechanical degradation. Its partial coverage by a ceramic top layer with considerable porosity is illustrated. It can be assumed that melt, previously metallic, has relocated and got deposited on this rod, which re-solidified and got oxidised at place. This aspect will be further discussed in the next section, since this was observed at higher elevation as well. Fig. 58 is dedicated to the pellet/cladding interaction. At positions of solid state contact an interaction zone is formed in the course of oxygen diffusion along the concentration gradient from the pellet to the cladding. Under mechanical stress the interaction layer may separate from the pellet, from the cladding or split into two sub-layers. For another position where internal interaction with the pellet proceeded it can be argued that the integrity of a pellet fragment, found adherent to the interaction zone between pellet and cladding has been weakened subsequently (Fig. 59): With the formation of a through-wall crack an ingress of steam could have resulted in re-oxidation of the sub-stoichiometric interaction zone on the pellet. However, this zone looks unchanged and only the pellet itself shows grain de-cohesion tendencies at the fragment surface. Further, the surfaces of the breach through the α-Zr(O) phase layer appear non-oxidised as well as the other cracks do.

The following two figures deal with the condition in which the thermocouples (TCs) are found. (All TCs pertinent to this elevation are of the W-Re type and inserted from above.) The rod thermocouples TFS 2/13, TFS 5/12 and TFS 5/11 (dedicated for measurements at 950, 850 and 750 mm, respectively,) are found in unexpectedly slight extent of oxidation. Fig. 60 shows two others for which wedge-shaped cracks into the ZrO_2 scale of the external sheath were healed by localised oxidation. However, this self-healing tendency turns out to be detrimental to local wall consumption and splitting (Fig. 61, left column). Crack formation is understood to take place under stress related to oxide scale growth. Consequently, the tantalum internal TC sheath may suffer from premature steam exposure, as in Fig. 61, right column, where half of the circumference is already converted to a ceramic phase. In the next section the non-protective character of the tantalum oxide scale will be illustrated again.

8.3.7 Bundle elevation 950 mm

In the trial to pull rod No. 15 it broke at ca. 940 mm elevation, so that only the upper part could be removed from the bundle. This is why this rod is missing in the described elevation and the following ones. The arguments in the previous section concerning the shroud and its oxidation hold here as well. This cross section overview shows an intact central rod (Fig. 62). In general, the other observations obtained 30 mm below, are registered here in similar or more pronounced form. Fig. 63 combines the observation of the strong external steam oxidation, the cladding-internal pellet interaction, and the relocated metallic melt, found as a top layer on this and other rods. Fig. 64 illustrates the structure of such melt for two positions of the central rod. The contact area to the ZrO_2 scale of the cladding is either complete, and thus difficult to distinguish, or incomplete, and then similar to the case of poor wetting. The porosity shows often the character of gas bubble content. As tentative interpretation it is assumed that at some original positions cladding matrix material, i.e. Zry with low oxygen content and some tin enrichment, got molten at local temperatures above at least 2030 K. Escaping from its confinement through cladding breaches the melt got steam exposed and was able to relocate in a “candling” process determined by viscosity and wetting. As oxygen pick-up increases viscosity and re-solidification temperature, improves wetting, and converts the material to an immobile ceramic form, the observed melt distribution should be explained. However, the reason for the porosity is not clear. It may be speculated that dissolved hydrogen would be released during oxidative consumption of the metallic melt, or that the tin enrichment might have favoured the formation of a volatile product. Alternatively, the porosity could be only an apparent one: It cannot be excluded that tin-enriched metallic residues, which are known to be relatively oxidation resistant, have survived non-oxidised and fell out during the preparation procedure.

Even at this elevation prior β-Zr phase (α'-Zr) is found retained as matrix of some fuel rods after moderate temperature history, especially at positions where no oxygen pick-up from the pellet occurred (Fig. 65). Cracks, ending in the α-Zr(O) layer and even through-wall cracks show typically non-oxidised surfaces. This indicates the late occurrence of cracking during the steam cooling phase of the test.

In contrast, Fig. 66 depicts a rod at a position where pellet contact was provided. Oxygen diffusion from both sides has consumed the β-Zr cladding matrix, thus giving rise to the formation of some tin-rich residues, which are found distributed between both α-Zr(O) sub-layers. During further oxidation the oxygen solubility limit must have been reached, as ZrO_2 phase precipitation from α-Zr(O) is realised: The needle-shaped habit of ZrO_2 is interpreted by the filling of narrow crack volumes. The dendritic growth form is understood to facilitate oxygen supply from larger surrounding melt volumes. However, to the present knowledge, it has to be assumed that those forms of oxide precipitation have required conditions of decreasing temperature to occur. On the other hand such regular growth forms could not develop during the test phase of fast steam cooling. It is summarised that those forms of precipitation occurred during a local time window between peak temperature and onset of fast cooling. Fig. 67 supports the given observations and interpretations. In addition, growth of roundly-shaped ZrO_2 phase particles is found to decorate cracks. It is reasonable to assume that the presence of steam within the crack network has facilitated this form of oxide precipitation.

The following three figures help to describe the oxidation status of thermocouples, whereas the only slightly oxidised TCs TFS 2/13 and TFS 5/12 are not depicted. Fig. 68 compares the intact scale of the external sheath of one TC with the defective one of another TC, below which pronounced local scale growth is favoured by the trend towards spalling. Wedge-shaped cracks and resulting local scale growth are observed at this elevation as well (Fig. 69). For TFS 4/11 local attack of the tantalum sub-sheath proceeded obviously fast. This seems to be due to accompanying mechanical degradation of the tantalum oxide scale, for which poor protection even in intact form is known. Fig. 70 shows examples of more pronounced TC sheath degradation. The microstructure of the tantalum scale seems to have experienced periodic cracking events, similar to those observed typically during the breakaway oxidation of Zry. It is therefore reasonable to assume that the tantalum oxidation proceeded with linear time dependence. The described status is not yet serious enough to terminate functioning of the TCs at the given positions.

8.3.8 Bundle elevation 1000 mm

In the overview the outward bending of the broken shroud segments and the fracturing of the central and some peripheral rods is shown (Fig. 71). In higher magnification several coarser through-wall cracks are observed, but most claddings remain at place. The relocated metallic melt, already described, which is found on top of some fuel rods in completely oxidised condition is depicted in Fig. 72. By chance a through-wall crack it is found below. This crack was, however, not the path from the melt source, but formed after melt relocation and re-solidification. This is deduced from the microstructure of the crack with respect to orientation and absence of surface oxidation. Again the source of melt, molten cladding matrix material, which must have penetrated the scale at some defective positions, could not be directly studied. Fig. 72, bottom micrograph, also shows filling of previously formed cracks within the external part of the α-Zr(O) matrix by solid-state oxygen transfer due to oxygen super-saturation during cooling from peak temperature. The absence of crack surface oxidation is documented for two other fuel rods in Fig. 73. For both positions no steam penetration can be deduced, despite through-wall cracking.

The status of thermocouples is depicted in the next two figures. Fig.74 stresses the fact that the oxidation status is not determined by a locally averaged bundle temperature history, as TCs in close vicinity may show a rather different extent of sheath oxidation. In this case TFS 3/12 should have received more heat from the neighbouring rods Nos. 9 and 10 compared to TFS 2/13, which might have lost heat by transfer to the cooler fluid. Axial heat conduction along the rods might be an additional parameter in case of strong axial temperature gradients. Fig 75 depicts the other TCs of that elevation. Obviously the effect of sheath scale splitting and the advancing oxidation below wedge cracks, which is shown in different stages of development, dominates the oxidative consumption of the external part of the Zr/Ta duplex sheath. TFS 5/12, which is known to have slipped downward, most likely during pulling of rod No. 15, shows the only slightly oxidised condition gained at a position far higher than the final one.

8.3.9 Bundle elevation 1150 mm

Far above the heated length of the bundle the shroud and the rod arrangement are seen in good overall condition (Fig. 76). Whereas the pellet of the central rod is present, most of the heated rods have lost their Mo electrode during cutting of the slab. Fig. 77 compares the oxidation status of one heated rod with that of the central rod. Both rods have retained much β-Zr matrix. The growth of the α-Zr(O) layer and the ZrO_2 scale is advanced for the central rod.

8.3.10 Bundle elevation 1250 mm

For the general status, depicted in Fig. 78, the description given in the previous section is referred. In Fig. 79, the final figure illustrating the microstructural evaluation, some features of breakaway-related oxidation are depicted. The micrographs of the left column showing a heated rod, (unfortunately in poor preparation condition,) indicate the development of a scallopped growth front of the scale, instead of the normally observed smooth one. More advanced oxidation of the central rod, depicted in the right column, gave rise to the development of pores into voids, located between more advanced scale lobes. Similar features have been reported for the bundle elevation 550 mm. This growth form is accompanying, to the present understanding, the transformation of metastable tetragonal into stable monoclinic ZrO_2. Details of this interpretation are given in [11].

According to the referred earlier studies these growth features indicate the pre-transition phase of the breakaway-related kinetic transition towards linear time dependence of oxidation. Since linear rates would lead to dramatic oxidation it was important to realise that this breakaway phenomenon does not play any important role in the test. It was not ruled out in advance that breakaway-related scale defects formed during bundle pre-oxidation could have accelerated the oxidation during the subsequent transient phase of the experiment. In contrast, at no elevation above 550 mm such features were detected. This confirms the understanding that the breakaway effect cannot develop or continue to act above a threshold temperature of ca. 1330 K.

8.3.11 Lateral and axial oxidation profiles

Quantitative information on the extent of the steam oxidation of the bundle components was obtained by systematic and comprehensive oxide scale thickness measurement. The results may serve as basis for comparison with the final bundle status, the measured integral hydrogen release, the “chemical” heat evolution, as well as for comparison with respective results of code calculations.

In this context the measurements for corner rod B, withdrawn from the bundle during the transient before escalation, give valuable information as a “calibration” point for evaluation of time dependence. In the top part of Fig. 80 the axial oxide layer thickness profile along rod B is drawn in comparison of the independent methods of eddy current principle, drawn with an especially high axial resolution for this simple and fast procedure, and the destructive metallographic determination on prepared cross sections. The same convincing correspondence of the results of both determination methods is shown in the bottom half of the figure for the oxidation state of the simulator # 15, except for the strong oxidation at peak temperature elevation. Its upper part had been withdrawn as fragment from the bundle after the test, whereas its lower part remained there. So the continuous decrease of the extent of oxidation upward from the peak temperature elevation 950 mm is shown. Comparison of both graphs shows that the bundle oxidation has reached a coarsely two-fold extent during the escalation phase of the test.

The series of scale thickness measurements at different bundle elevations, comprising some measurements on both sides of the shroud and, mainly, the systematic determination of the scale thickness at four azimuthal positions of each rod, wherever feasible, are illustrated in Figs. 81 through 88. Up to the mid-elevation the oxidation remained unimportant and the lateral variation small (Fig. 81). For the elevation 750 mm the relatively weaker oxidation of shroud and corner rods compared to the fuel rod simulators can be seen in relation to temperature gradients (Fig. 82). Towards the upper elevations the variations of the extent of oxidation are found to increase, however to remain limited in terms of relative values. Comparison of different elevations shows frequently an axial correlation in the sense of preferred oxidation of some rods which were obviously hotter than neighbouring ones. However, no simple correlation to partial flow channels seems to exist. Moreover, relative lateral rod movement due to bending should have contributed to temperature variations, which must not have persisted during the whole test.

The described information for the individual elevations is collected and summarised in Fig. 89, the axial profiles of the oxide scale thickness distribution. It is given for the different rod types and the interior shroud surface, as well as for the common average and range of values for all the components.

8.3.12 Summary

The comprehensive metallographic investigation of the prepared bundle cross sections, the detailed photo documentation including high magnifications, the composition of selected photos into thematic illustrations and the microstructural analysis of the observed phenomena are the basis of the given description of the final state of the bundle and the discussion of its behaviour in time dependence and as result of simultaneous and competing mechanisms. The oxidation state of the bundle is quantified by systematic scale thickness measurement at all polished cross sections and along the removed bundle components, and is also documented in axial profiles.

The axial oxidation profile reflects the pronounced temperature dependence of Zircaloy-4 / steam oxidation. Generally, this reaction proceeded in the well-known kinetics controlled by growth of protective scale. Favourable conditions for breakaway-related growth anomalies during the pre-oxidation phase of the experiment at lowest and highest elevations did not influence the transient test phase. In the peak temperature range below the upper electrode zone strong oxidative conversion of the fuel rod simulator cladding was accompanied by chemical interaction with the ZrO_2 pellets at positions of solid-state contact. In total, however, the corresponding oxygen transfer to the cladding remained relatively unimportant in comparison to the effect of the external steam oxidation. No indications for early mechanical cladding failure at temperature were found.

Melting of cladding matrix volumes, melt confinement by the “crucible effect” of the oxygen-enriched surrounding structures, rod-internal melt relocation and resulting agglomeration and gap-filling at expense of void formation was observed in local variability at many positions. ZrO_2 precipitates of dendritic morphology support the existence of melt pools at temperature. Occasional cladding failure, which might be understood in terms of the “chemical thinning process” could not be observed. However, the limited amount of external melt, found in form of oxidised lumps on some rod surfaces, is interpreted to result from metallic cladding residues.

Cladding through-wall cracking, breach formation, steam ingress and internal steam oxidation under supply limitation conditions have to be correlated mainly to the cool-down phase of the experiment. Some ZrO_2 precipitation within the prior β-Zr phase matrix, some spot-wise scale growth from crack surfaces and crack-filling by ZrO_2 growth are attributed to oxidation at high temperature. However, the fact that most of the crack surface network remained non-oxidised, indicates its formation at a late stage, i.e. at low temperature. This interpretation of the oxidation state of the bundle supports the measured signal of hydrogen release.

The systematically documented state of the thermocouples reflects in general the influence of the strong steam oxidation during the pre-oxidation and the following test phases. The TC fixing procedure, using spot-welded Zr-clamps, is seen to provide safe rod contact until total clamp oxidation. The oxidation of the external part of the duplex TC sheath (Zircaloy / tantalum) is characterised by formation of some deep axial scale cracks and consequently premature rupture, which does not yet limit the TC function. However, tantalum oxidation proceeds extremely fast, so that the TC structure should have been degraded soon after steam exposure of the inner sheath. TC fragmentation and relocation of broken segments was observed, in relation to the experimental conditions and subsequent handling. Temperature escalations at 750 and 850 mm elevation, registered by TCs, are in contradiction to the oxidation state of the rods, and seem to be due to their thermal decoupling. This important discrepancy deserves further attention.

8.4 Hydrogen Absorption by Zircaloy

The hydrogen absorbed in the remaining Zircaloy-4 metal was analyzed by hot extraction in the so-called LAVA facility, which is an inductively heated furnace coupled to a mass spectrometer. Two-centimeter long cladding segments were taken from the rod cladding # 15, of corner rod B. (Corner rod B was withdrawn from the bundle after the pre-oxidation whereas rod # 15 was pulled out of the bundle after the test, prior to the encapsulation of the test bundle. As described above rod # 15 broke at ~950 mm elevation during handling so that only the upper part of the rod was available for this analysis as well.) In addition, two 5 mm thick cross-sectional slices of the embedded bundle, i.e. QUE-05-2 (elevation 75 - 80 mm, as reference) and QUE-05-8 (elevation 952 – 957 mm) were taken as samples. The segments were heated for 20 minutes to some 1800 K under a well-defined argon flow. The hydrogen released was measured by the mass spectrometer.

The axial profile of the hydrogen absorbed by the Zircaloy-4 metal is plotted in Fig. 90, the data of the cross section at 957 mm are given in Fig. 91. Obviously, almost no hydrogen was absorbed during the pre-oxidation phase according to the results from the corner rod. In the hot zone of the bundle a certain amount of hydrogen was absorbed by the cladding and shroud with measured maxima of 2 and 4 at-% for cladding and shroud, respectively. From Fig. 90 it can be seen that only a few data with a large scatter band exist. So, the integral values of the hydrogen absorbed in the metal phase were estimated to be ~0.4 g (assuming a mean hydrogen absorption of 0.5 at-% over a length of 1 m). The total amount is larger than that of test QUENCH-04 with ~0.1 g, but less than the results from tests QUENCH-01 and QUENCH-02 with 1 g and 5 g, respectively.

9 Calculational Support

9.1 Investigation of oxidation and hydrogen behavior with the FZK code CALUMO

Posttest calculations for QUENCH-05 have been done with the recently developed bundle code CALUMO [12] in order to simulate the oxidation behavior of the fuel rods and the shroud as well as the hydrogen production. The release of electrical power in the fuel rod simulators, the coolant inlet temperature, and the coolant mass flow are input data for the code. The oxidation correlation of Leistikow et al. [13] was used for the calculations of QUENCH-05 as was done in the calculations for QUENCH-01 [14], QUENCH-03, and QUENCH-04 [12]. In the overall, the calculations resulted in a satisfying simulation of the experimental results.

Results of code calculations in comparison to the respective experimental data are to be found in Figs. 92 to 96. These are temperature evolutions between 150 and 1350 mm, the axial profiles of oxide scales, and the hydrogen production rates. In Figs. 92 and 93 are plotted the average temperature in the bundle “trodz”, the average temperature in the inner cluster of 9 fuel rod simulators “tcenz” and the average shroud temperature “tshrz”. They are compared to the available thermocouple readings.

In the overall, the temperature evolution in the bundle and the shroud is simulated in a satisfactory way by the code. Most of the features of the temperature evolution are rather well reproduced, especially in the heated zone below 750 mm. The temperature rise to steady-state conditions, the pre-oxidation phase, the temperature transient, and the cooldown phase are quite well matched.

There is some serious difference between measured and calculated temperature values between 750 and 950 mm. The flat temperature evolution in the pre-oxidation phase could not be reproduced by the code.

Due to the implementation of radiation heat transfer in the model for axial heat transfer, the situation in the upper unheated zone was considerably improved compared to earlier calculations for QUENCH-01 and QUENCH-04. Except for the temperature escalations in the shroud thermocouples, which arise towards the end of the transient phase, the situation for the CALUMO code is not so bad.

These temperature escalations of the shroud thermocouples are observed in all QUENCH tests done so far, irrespective of the test conditions. The mechanism of heat transfer due to free convection in the Ar-filled annulus above the heated zone given in [15] can explain the experimental fact that only the respective shroud thermocouples show this effect but not the cladding thermocouples. Up to now there is no model for convective heat transfer in the Ar volume implemented in the CALUMO code.

The calculated profiles of axial scale thickness at the end of the test are plotted in Fig. 94 together with experimental values from posttest examinations, with “dox” denoting the oxide scales of the inner cluster of 9 fuel rods, “doxa” that of the outer ring of 12 fuel rods and “doxsh” the oxide scale of the shroud. The calculated profiles are similar to the experimental ones, although there is a downward shift by about 50 to 100 mm. The reason for this systematic discrepancy is not clear at the moment.

A comparison of measured and calculated hydrogen values (production rate and time integrated values) is to be seen in Fig. 95. The agreement is satisfactory. There is a very high peak in the experimentally measured hydrogen production rate towards the end of the transient which is not reproduced by the CALUMO code. As this peak starts well before the onset of quenching it is presumably no quench effect.

At the end of the test the overall produced hydrogen, as calculated by the code, is about 24 g, i.e. slightly lower than the measured values. The discrepancy might be a bit higher as the measured values deal only with the released hydrogen and not the hydrogen stored in the metallic phase. Also neglected in the code is the part of hydrogen that stems from the thermocouple sheaths, the spacers, and the lower unheated (cold) part of the test section.

The overall agreement between the calculational results and the experimental findings of QUENCH-05 is acceptable, although there are still some discrepancies. To achieve this agreement, it was necessay to considerably increase the heat transfer values below 750 mm. Without this change the oxidation peak would have been much lower and the profile more extended to the lower part, as was the case for QUENCH-04 [12].

The increase of the heat transfer from the fuel rod simulators to the coolant leads to higher coolant temperatures, to a “narrowing” of the oxidation profile, and to an increase of the maximum. Unfortunately, the coolant temperatures are not measured within the heated section. Only the coolant outlet temperature is measured.

Fig. 96 shows a comparison of the calculated coolant temperature at the uppermost node of CALUMO (ca. 1300 mm) and the evolution of the temperature T 512. The calculated values are high by about 100 – 150 K, but it is rather encouraging that the two curves evolve fairly in a parallel way. Of course, the uncertainties in heat transfer in the upper unheated section are considerable as there are convection phenomena in the Ar-volume that are not yet understood. Therefore it would be much better to have a measurement of the coolant temperature at the upper end of the heated zone.

References

[1] J.M. Broughton, P. Kuan, and D.A. Petti, “A Scenario of the Three Mile Island Unit 2 Accident,” Nuclear Technology, 87, 34, 1989.

[2] P. Hofmann, S. Hagen, V. Noack, G. Schanz, L. Sepold, “Chemical-Physical Behavior of Light Water Reactor Core Components Tested under Severe Reactor Accident Conditions in the CORA Facility,” Nuclear Technology, vol. 118, 1997, p. 200.

[3] S. Hagen, P. Hofmann, V. Noack, L. Sepold, G. Schanz, G. Schumacher, “Comparison of the Quench Experiments CORA-12, CORA-13, CORA-17,” FZKA 5679, Forschungszentrum Karlsruhe, 1996.

[4] S.M. Modro and M.L. Carboneau, “The LP-FP-2 Severe Fuel Damage Scenario; Discussion of the Relative Influence of the Transient and Reflood Phase in Affecting the Final Condition of the Bundle,” OECD/LOFT Final Event, ISBN 92-64-03339-4, 1991, p. 388.

[5] P. Hofmann, V. Noack, M.S. Veshchunov, A.V. Berdyshev, A.V. L.V. Matweev, A.V. Palagin, V.E. Shestak: „Physico-Chemical Behavior of Zircaloy Fuel Rod Cladding Tubes During LWR Severe Accident Reflood“, FZKA 5846, Forschungszentrum Karlsruhe, 1997.

[6] P. Hofmann, A. Miassoedov, L. Steinbock, M. Steinbrück, M. Veshchunov et al.: “Quench Behavior of Zircaloy Fuel Rod Cladding Tubes. Small-Scale Experiments and Modeling of the Quench Phenomena,” FZKA 6208, Forschungszentrum Karlsruhe, 1999.

[7] P. Hofmann, W. Hering, C. Homann, W. Leiling, A. Miassoedov, D. Piel, L. Schmidt, L. Sepold, M. Steinbrück, “QUENCH-01, Experimental and Calculational Results,” FZKA 6100, Forschungszentrum Karlsruhe, 1998.

[8] P. Hofmann, C. Homann, W. Leiling, A. Miassoedov, D. Piel, G. Schanz, L. Schmidt, L. Sepold, M. Steinbrück, “Experimental and Calculational Results of the Experiments QUENCH-02 and QUENCH-03,” FZKA 6295, Forschungszentrum Karlsruhe, 2000.

[9] “Investigation of an Overheated PWR-Type Fuel Rod Simulator Bundle Cooled Down by Steam,” Part I: L. Sepold, P. Hofmann, C. Homann, W. Leiling, A. Miassoedov, D. Piel, G. Schanz, L. Schmidt, U. Stegmaier, M. Steinbrück, H. Steiner, “Experimental and Calculational Results of the QUENCH-04 Test,” Part II: M.S. Veshchunov, A.V. Berdyshev, A.V. Boldyrev, A.V. Palagin, V.E. Shestak, “Application of SVECHA/QUENCH Code to the Analysis of the QUENCH-01 and QUENCH-04 Bundle Tests,” FZKA 6412, 2001.

[10] L. Sepold, P. Hofmann, W. Leiling, A. Miassoedov, D. Piel, L. Schmidt, M. Steinbrück, "Reflooding Experiments with LWR-Type Fuel Rod Simulators in the QUENCH Facility," Nuclear Engineering and Design 204 (2001), 205 - 220.

[11] G. Schanz, S. Leistikow, "Microstructural Reasons for Mechanical Oxide Degradation (Breakaway Effects) and Resulting Kinetic Anomalies of Zircaloy-4 / Steam- HT-Oxidation," Proc. 8th Intern. Congress Metallic Corrosion, Mainz, Germany, 6-11 Sept. 1981, Vol. II, pp. 1712-1717.

[12] H. Steiner, M. Heck, "The code CALUMO, a tool for the analysis for temperature transients in QUENCH tests," FZKA 6501, 2000.

[13] S. Leistikow, et al, "Kinetik und Morphologie der isothermen Dampfoxidation von Zircaloy-4 bei 700 bis 1300 °C," KFK 2587, 1978.

[14] H. Steiner, M. Heck, "Calculations to QUENCH-01 with the code CALUMO," contribution to FZKA 6653, 2001.

[15] G. Choi and S.T. Korpela, "Stability of the Conduction Regime of Natural Convection in a Tall Vertical Annulus," J. Fluid Mech. 99, 1980, pp. 725 – 738.

[16] L. Sepold, P. Hofmann, W. Leiling, A. Miassoedov, D. Piel, L. Schmidt, M. Steinbrück, "Reflood Behavior of PWR-Type Fuel Rod Simulator Bundles Used in the QUENCH Experiments," Proceedings (ASME, New York) of 33rd National Heat Transfer Conference, Aug. 15 - 17, 1999, Albuquerque, NM, USA.

[17] P. Hofmann, M. Steinbrück, A. Miassoedov, L. Schmidt, D. Piel, L. Sepold, W. Leiling, "Zircaloy Cladding Tube Behavior of PWR Fuel Rods During Quenching from High Temperatures (QUENCH Test Results)," Proceedings of the Annual Meeting on Nuclear Technology, 18 - 20 May 1999, Karlsruhe, Germany.

[18] A. Miassoedov, P. Hofmann, W. Leiling, D. Piel, L. Schmidt, L. Sepold, M. Steinbrück, W. Hering, C. Homann, "Flooding Experiments on the Investigation of the Hydrogen Source Term (QUENCH Test Results)," Proceedings of the Annual Meeting on Nuclear Technology, 23 - 25 May 2000, Bonn, Germany.

Acknowledgements

At the Karlsruhe Research Center the broad support needed for preparation, execution, and evaluation of the experiment is gratefully acknowledged. In particular, the authors would like to thank Messrs. L. Anselment and S. Horn for the assembly of the heated test rods and for the instrumentation of the central rod, Messrs. J. Moch and R. Vouriot for assembling and instrumenting the test bundle, Mr. S. Horn for the preparation of the hydrogen measurement with the “Caldos” analyzer and the support for the test data selection. Furthermore, the authors would like to express their gratitude to Dr. W. Krauss for the hydrogen measurement with the “Prisma” mass spectrometer, to Mr. L. Anselment for sectioning the epoxied bundle, to Mrs. J. Laier and Mrs. I. Werner for processing the test data, and to Mrs. M. Heck for processing the results of the metallographic examination.

Table 1: **QUENCH Test Matrix**

Test	Quench medium	Flooding rate[1)]	Heat-up rate	Max. ZrO_2 layer thickness[2)]	Temp. at onset of flooding[3)]	Remarks	Date of test conduct
QUENCH-00	water	2.8 cm/s from bottom	1.0 K/s	≈ 500 µm	≈ 1500 °C	COBE Project: commissioning tests	Oct. 9 - 16, 97
QUENCH-01	water	1.6 cm/s; from the bottom	0.5 K/s	≈ 300 µm	≈ 1600 °C	COBE Project: partial fragmentation of pre-oxidized cladding	February 26, 98
QUENCH-02	water	1.6 cm/s; from the bottom	0.5 K/s	completely oxidized	≈ 1900 °C	COBE Project: no additional pre-oxidation; quenching from high temperatures	July 7, 98
QUENCH-03	water	1.4 cm/s from the bottom	0.6 K/s	completely oxidized	≈ 2100 °C	delayed flooding; 240 s after temperature escalation has started	January 20, 99
QUENCH-04	steam	≈ 49 g/s; from the bottom	0.5 K/s	≈ 300 µm	≈ 1900 °C	cool-down behavior of slightly pre-oxidized cladding by injected cold steam	June 30, 99
QUENCH-05	steam	≈ 50 g/s from the bottom	0.5 K/s	≈ 200 µm at onset of excursion	≈ 1900 °C	cool-down behavior of pre-oxidized cladding by injected cold steam	March 29, 2000
QUENCH-06	water	1.4 cm/s from the bottom	0.5 K/s	≈ 250 µm	1600 – 1800 °C	OECD-ISP 45, prediction of H_2 source term by different code systems	December, 13 2000
QUENCH-07	steam	to be determined from the bottom	To be determined	determined by heat-up rate	1400 – 1600 °C	COLOSS Project: impact of B_4C absorber rod failure on H_2, CO, CO_2 and CH_4 generation.	2001

Revised: March, 2001

Table 2: Design characteristics of the QUENCH test bundle

Bundle type		PWR
Bundle size		21 rods
Number of heated rods		20
Number of unheated rods		1
Pitch		14.3 mm
Rod outside diameter		10.75 mm
Cladding material		Zircaloy-4
Cladding thickness		0.725 mm
Rod length	heated rod (levels)	2480 mm (-690 mm to 1790 mm)
	unheated rod (levels)	2842 mm (-827 mm to 2015 mm, incl. extension piece)
Heater material		Tungsten (W)
Heater length		1024 mm
Heater diameter		6 mm
Annular pellet	heated rod	ZrO_2; ∅ 9.15/6.15 mm; L=11 mm
	unheated rod	ZrO_2; ∅ 9.15/2.5 mm; L=11 mm
Pellet stack	heated rod	0 mm to ~ 1020 mm
	unheated rod	0 mm to 1553 mm
Grid spacer	material	Zircaloy-4, Inconel 718
	length	Zry 42 mm, Inc 38 mm
	location of lower edge	-200 mm Inconel 50 mm Zircaloy-4 550 mm Zircaloy-4 1050 mm Zircaloy-4 1410 mm Zircaloy-4
Shroud	material	Zircaloy-4
	wall thickness	2.38 mm
	outside diameter	84.76 mm
	length (extension)	1600 mm (-300 mm to 1300 mm)
Shroud insulation	material	ZrO_2 fiber
	insulation thickness	~ 37 mm
	elevation	-300 mm to ~1000 mm
Molybdenum-copper electrodes:		
length of upper electrodes		766 mm (576 Mo, 190 mm Cu)
length of lower electrodes		690 mm (300 Mo, 390 mm Cu)
diameter of electrodes:		
- prior to coating		8.6 mm
- after coating with ZrO_2		9.0 mm
Cooling jacket	material	1.4541 stainless steel
	inner tube	∅ 158.3 / 168.3 mm
	outer tube	∅ 181.7 / 193.7 mm

12/98

Table 3: List of instrumentation for the QUENCH-05 Test 24.5.2000

Chan-nel	Designation	Instrument, location	Output in
1	TFS 2/11	TC (W/Re) fuel rod simulator 8 (type 2), 750 mm, 135°	K
3	TFS 2/15	TC (W/Re) fuel rod simulator 4 (type 2), 1150 mm, 315°	K
4	TFS 2/17	TC (W/Re) fuel rod simulator 6 (type 2), 1350 mm, 45°	K
5	TSH 15/180	TC (W/Re)) shroud outer surface, 1150 mm, 206°	K
6	TFS 3/10	TC (W/Re) fuel rod simulator 7 (type 3), 650 mm, 135°	K
8	TFS 3/13	TC (W/Re) fuel rod simulator 3 (type 3), 950 mm, 315°	K
9	TFS 3/14	TC (W/Re) fuel rod simulator 5 (type 3), 1050 mm, 45°	K
10	TFS 4/11	TC (W/Re) fuel rod simulator 14 (type 4), 750 mm, 45°	K
11	TFS 4/13	TC (W/Re) fuel rod simulator 20 (type 4), 950 mm, 135°	K
12	TFS 5/10	TC (W/Re) fuel rod simulator 12 (type 5), 650 mm, 225°	K
13	TFS 5/11	TC (W/Re) fuel rod simulator 13 (type 5), 750 mm, 45°	K
15	TFS 5/13	TC (W/Re) fuel rod simulator 16 (type 5), 950 mm, 135°	K
17	TSH 16/180	TC (W/Re) shroud outer surface, 1250 mm, 206°	K
18	TSH 13/90	TC (W/Re) shroud outer surface, 950 mm, 116°	K
19	TSH 14/90	TC (W/Re) shroud outer surface, 1050 mm, 116°	K
20	TSH 11/0	TC (W/Re) shroud outer surface, 750 mm, 26°	K
21	TSH 12/0	TC (W/Re) shroud outer surface, 850 mm, 26°	K
22	TFS 2/5	TC (NiCr/Ni) fuel rod simulator 2 (type 2), 150 mm, 225°	K
23	TFS 2/7	TC (NiCr/Ni) fuel rod simulator 6 (type 2), 350 mm, 45°	K
24	F 902	Off-gas flow rate before Caldos (H_2)	Nm³/h
25	FM 401	Argon mass flow rate	g/s
33	TCRC 13	TC (W/Re) central rod, center, 950 mm	K
34	TFS 2/12	TC (W/Re) fuel rod simulator 2 (type 2), 850 mm, 315°	K
35	TSH 9/90	TC (NiCr/Ni) shroud outer surface, 550 mm, 116°	K
36	TSH 9/270	TC (NiCr/Ni) shroud outer surface, 550 mm, 296°	K
37	TFS 3/16	TC (W/Re) fuel rod simulator 7 (type 3), 1250 mm, 135°	K
38	TFS 5/9	TC (NiCr/Ni) fuel rod simulator 10 (type 5), 550 mm, 315°	K
39	TFS 2/9	TC (NiCr/Ni) fuel rod simulator 8 (type 2), 550 mm, 135°	K
40	TIT D/12	TC (W/Re) corner rod D, center, 800 mm	K
41	TCR 13	TC (We/Re) central rod cladding, 950 mm, 225°	K
42	TFS 5/8	TC (NiCr/Ni) fuel rod simulator 21 (type 5), 450 mm, 135°	K
43	TFS 3/8	TC (NiCr/Ni) fuel rod simulator 5 (type 3), 450 mm, 45°	K
45	TCRC 7	TC (NiCr/Ni) central rod, center, 350 mm	K
46	TIT C/9	TC (NiCr/Ni) corner rod C, center, 500 mm	K

Chan-nel	Designation	Instrument, location	Output in
47	TFS 5/15	TC (W/Re) fuel rod simulator 19 (type 5), 1150 mm, 225°	K
48	TFS 5/16	TC (W/Re) fuel rod simulator 21 (type 5), 1250 mm, 135°	K
49	TFS 5/17	TC (W/Re) fuel rod simulator 10 (type 5), 1350 mm, 315°	K
50	TFS 3/12	TC (W/Re) fuel rod simulator 9 (type 3), 850 mm, 225°	K
51	TFS 5/12	TC (W/Re) fuel rod simulator 15 (type 5), 850 mm, 315°	K
52	TSH 13/270	TC (W/Re) shroud outer surface, 950 mm, 296°	K
53	TSH 14/270	TC (W/Re) shroud outer surface, 1050 mm, 296°	K
54	TSH 11/180	TC (W/Re) shroud outer surface, 750 mm, 206°	K
55	TSH 12/180	TC (W/Re) shroud outer surface, 850 mm, 206°	K
58	TCRC 9	TC (NiCr/Ni) central rod, center, 550 mm	K
66	TSH 15/0	TC (W/Re) shroud outer surface, 1150 mm, 26°	K
67	TSH 16/0	TC (W/Re) shroud outer surface, 1250 mm, 26°	K
68	T 512	Gas temperature bundle outlet	K
71	Ref. T 01	Reference temperature 1	K
72	TFS 2/1	TC (NiCr/Ni) fuel rod simulator 4 (type 2), -250 mm, 315°	K
73	TFS 2/2	TC (NiCr/Ni) fuel rod simulator 6 (type 2), -150 mm, 45°	K
74	TFS 2/3	TC (NiCr/Ni) fuel rod simulator 8 (type 2), -50 mm, 135°	K
75	TCRI 7	TC (NiCr/Ni), central rod, cladding inner surface, 350 mm	K
76	TFS 2/6	TC (NiCr/Ni) fuel rod simulator 4 (type 2), 250 mm, 315°	K
77	TCRI 9	TC (NiCr/Ni), central rod, cladding inner surface, 550 mm	K
78	TFS 5/4/0	TC (NiCr/Ni) fuel rod simulator 15 (type 5), 50 mm, 315°	K
79	TFS 5/4/180	TC (NiCr/Ni) fuel rod simulator 21 (type 5), 50 mm, 135°	K
80	TFS 5/5	TC (NiCr/Ni) fuel rod simulator 16 (type 5), 150 mm, 135°	K
81	TFS 5/6	TC (NiCr/Ni) fuel rod simulator 18 (type 5), 250 mm, 45°	K
82	TFS 5/7	TC (NiCr/Ni) fuel rod simulator 19 (type 5), 350 mm, 225°	K
83	TSH 4/270	TC (NiCr/Ni) shroud outer surface, 50 mm, 296°	K
84	TSH 3/180	TC (NiCr/Ni) shroud outer surface, -50 mm, 206°	K
85	TSH 4/180	TC (NiCr/Ni) shroud outer surface, 50 mm. 206°	K
86	TSH 7/180	TC (NiCr/Ni) shroud outer surface, 350 mm, 206°	K
87	TSH 4/90	TC (NiCr/Ni) shroud outer surface, 50 mm, 116°	K
88	TSH 1/0	TC (NiCr/Ni) shroud outer surface, -250 mm, 26°	K
89	TSH 4/0	TC (NiCr/Ni) shroud outer surface, 50 mm, 26°	K
90	TSH 7/0	TC (NiCr/Ni) shroud outer surface, 350 mm, 26°	K
91	TCI 9/270	TC (NiCr/Ni) cooling jacket inner tube wall, 550 mm, 270°	K
92	TCI 10/270	TC (NiCr/Ni) cooling jacket inner tube wall, 650 mm, 270°	K
93	TCI 11/270	TC (NiCr/Ni) cooling jacket inner tube wall, 750 mm, 270°	K

Chan-nel	Designation	Instrument, location	Output in
94	TCI 13/270	TC (NiCr/Ni) cooling jacket inner tube wall, 950 mm, 270°	K
95	TCR 7	TC (NiCr/Ni) central rod, cladding outer surf., 350 mm, 315°	K
96	TCI 1/180	TC (NiCr/Ni) cooling jacket inner tube wall, -250 mm, 180°	K
97	TCI 4/180	TC (NiCr/Ni) cooling jacket inner tube wall, 50 mm, 180°	K
98	TCI 7/180	TC (NiCr/Ni) cooling jacket inner tube wall, 350 mm, 180°	K
99	TCI 11/180	TC (NiCr/Ni) cooling jacket inner tube wall, 750 mm, 180°	K
100	TCI 12/180	TC (NiCr/Ni) cooling jacket inner tube wall, 850 mm, 180°	K
101	TCI 13/180	TC (NiCr/Ni) cooling jacket inner tube wall, 950 mm, 180°	K
103	TCR 9	TC (NiCr/Ni) central rod, cladding outer surf., 550 mm, 315°	K
104	TCI 9/90	TC (NiCr/Ni) cooling jacket inner tube wall, 550 mm, 90°	K
105	TCI 10/90	TC (NiCr/Ni) cooling jacket inner tube wall, 650 mm, 90°	K
106	TCI 11/90	TC (NiCr/Ni) cooling jacket inner tube wall, 750 mm, 90°	K
107	TCI 13/90	TC (NiCr/Ni) cooling jacket inner tube wall, 950 mm, 90°	K
109	TCI 1/0	TC (NiCr/Ni) cooling jacket inner tube wall, -250 mm, 0°	K
110	TCI 4/0	TC (NiCr/Ni) cooling jacket inner tube wall, 50 mm, 0°	K
111	TCI 7/0	TC (NiCr/Ni) cooling jacket inner tube wall, 350 mm, 0°	K
112	TCI 11/0	TC (NiCr/Ni) cooling jacket inner tube wall, 750 mm, 0°	K
113	TCI 12/0	TC (NiCr/Ni) cooling jacket inner tube wall, 850 mm, 0°	K
114	TCI 13/0	TC (NiCr/Ni) cooling jacket inner tube wall, 950 mm, 0°	K
115	TCI 15/0	TC (NiCr/Ni) cooling jacket inner tube wall, 1150 mm, 0°	K
117	TCO 9/270	TC (NiCr/Ni) cooling jacket outer tube surface, 550 mm, 270°	K
118	TCO 4/180	TC (NiCr/Ni) cooling jacket outer tube surface, 50 mm, 180°	K
120	TCO 1/0	TC (NiCr/Ni) cooling jacket outer tube surface, -250 mm, 0°	K
121	TCO 7/0	TC (NiCr/Ni) cooling jacket outer tube surface, 350 mm, 0°	K
122	TCO 13/0	TC (NiCr/Ni) cooling jacket outer tube surface, 950 mm, 0°	K
123	T 601	Temperature before off-gas flow instrument F 601	K
128	T 104	Temperature quench water	K
129	T 201	Temperature steam generator heating pipe	K
130	T 204	Temperature before steam flow instrument location 50 g/s	K
131	T 205	Temperature before steam flow instrument location 10 g/s	K
132	T 301A	Temperature behind superheater	K
133	T 302	Temperature superheater heating pipe	K
134	T 303	Temperature before total flow instrument location	K
135	T 401	Temperature before gas flow instrument location	K
136	T 403	Temperature at inlet cooling gas	K

Chan-nel	Designation	Instrument, location	Output in
137	T 404	Temperature at outlet cooling gas	K
138	T 501	Temperature at containment	K
139	T 502	Temperature at containment	K
140	T 503	Temperature at containment	K
141	T 504	Temperature at containment	K
142	T 505	Temperature at containment	K
143	T 506	Temperature at containment	K
144	T 507	Temperature at containment	K
145	T 508	Temperature at containment	K
147	T 510	Temperature at containment	K
148	T 511	Gas temperature at bundle inlet	K
149	T 901	Temperature before off-gas flow instrument F 901	K
151	Ref. T 02	Reference temperature 2	K
152	P 201	Pressure steam generator	bar
153	P 204	Pressure at steam flow instrument location 50 g/s	bar
154	P 205	Pressure at steam flow instrument location 10 g/s	bar
155	P 303	Pressure before total flow instrument location	bar
156	P 401	Pressure before gas flow instrument location	bar
157	P 511	Pressure at bundle inlet	bar
158	P 512	Pressure at bundle outlet	bar
159	P 601	Pressure before off-gas flow instrument F 601	bar
160	P 901	Pressure before off-gas flow instrument F 901	bar
161	L 201	Liquid level steam generator	mm
162	L 501	Liquid level quench water	mm
163	L 701	Liquid level main condenser	mm
164	Q 901	H_2 concentration, off-gas (Caldos)	% H_2
165	P 411	Pressure Ar-Kr supply	bar
166	P 403	Pressure Ar cooling of cooling jacket	bar
167	P 406	Pressure insulation shroud/cooling jacket	bar
168	F 104	Flow rate quench water	l/h
169	F 204	Flow rate steam 50 g/s	g/s
170	F 205	Flow rate steam 10 g/s	g/s
171	F 303	Flow rate at bundle inlet (steam + argon), orifice	mbar
172	F 401	Argon gas flow rate	Nm^3/h

Chan-nel	Designation	Instrument, location	Output in
173	F 403	Flow rate cooling gas	Nm³/h
174	F 601	Flow rate off-gas (orifice)	mbar
175	F 901	Off-gas flow rate before Caldos (H_2)	m³/h
176	E 201	Electric current steam generator	A
177	E 301	Electric current superheater	A
178	E 501	Electric current inner ring of fuel rod simulators	A
179	E 502	Electric current outer ring of fuel rod simulators	A
180	E 503	Electric voltage inner ring of fuel rod simulators	V
181	E 504	Electric voltage outer ring of fuel rod simulators	V
182	Hub_V302	Steam supply valve lift	%
183	Ref. T 03	Reference temperature 3	K
250	E 505	Electric power inner ring of fuel rod simulators	W
251	E 506	Electric power outer ring of fuel rod simulators	W

Note: Tip of thermocouple TFS 2/1 bent into flow channel to measure the fluid temperature; F 901 and F 902 were not activated

Table 4: QUENCH-05; Sequence of events

Time [s]	Event
0	Start of data recording, test bundle at ~873 K, data acquisition frequency 0.25 Hz
60	Start of heatup from ~873 K to ~1473 K
1368	Start of pre-oxidation phase at ~1473 K
1837	Shroud failure
4860	Start of transient phase, data acquisition frequency 5 Hz
5490	Begin to withdraw corner rod B (T ~1620 K)
5518	Corner rod B pulled
5985	Begin of temperature escalation at the 850 mm level (TFS 3/12: ~ 1870 K)
6003	Begin of significant H_2 production, based on the mass spectrometer data
6009	Indication of start of steam flow (3 g/s) shutoff and of cooldown steam injection at F 204
6010	Start of cooldown steam injection into the test section, end of power transient, steam flow (3 g/s) at zero
6011	Cooldown steam in the test section, strong temperature decrease at all axial levels (6011 s: 42 g/s; maximum at 6150 s: 48 g/s)
6033	Start of electric power reduction from 17.95 kW to 3.9 kW
6048	Electric power at 3.9 kW
6317	Electric power and steam flow shutoff
6318	Electric power at zero
6320	Steam flow at zero
6426	End of data recording

0 s = 13:40:00 h on March 29, 2000

Table 5: QUENCH-05; Excursion temperatures

Elevation [mm]	Thermocouple	Time at excursion [s]	Excursion temperature [K]
750	TFS 2/11	6000	1923
750	TFS 5/11	6011	1999
750	TSH 11/180	6012	1564
850	TFS 3/12	5985	1870
850	TFS 5/12	6010	1972
850	TSH 12/0	6012	1673
850	TSH 12/180	6012	1728
950	TFS 5/13	6011	1912
1050	TSH 14/90	6012	1625
1050	TSH 14/270	6012	1653

Table 6: QUENCH-05; Onset of cooling based on cladding TCs (TFS), central rod TC (TCRC 13), corner rod TCs (TIT), and shroud TCs (TSH)

Thermocouple	Elevation [mm]	Onset of cooling Time [s]	Onset of cooling Temp. [K]	Mean value per elevation Time [s]	Mean value per elevation Temp. [K]
TFS 2/1	- 250	6011	625	6011	625
TFS 2/2	- 150	6011	709	6011	709
TFS 2/3	- 50	6011	783	6011	783
TFS 5/4/0	50	6010	844	6011	841
TFS 5/4/180	50	6011	838		
TFS 2/5	150	6011	982	6011	959
TFS 5/5	150	6011	935		
TFS 2/6	250	6010	1090	6011	1061
TFS 5/6	250	6011	1032		
TFS 2/7	350	6010	1158	6011	1151
TFS 5/7	350	6011	1143		
TFS 3/8	450	6011	1238	6011	1242
TFS 5/8	450	6010	1245		
TFS 2/9	550	6011	1326	6011	1316
TFS 5/9	550	6011	1306		
TFS 3/10	650	6011	1418	6011	1441
TFS 5/10	650	6011	1464		
TFS 2/11	750	6011	2103	6011	2105
TFS 4/11	750	6011	1940		
TFS 5/11	750	6012	2272		

Thermocouple	Elevation	Onset of cooling		Mean value per elevation	
	[mm]	Time [s]	Temp. [K]	Time [s]	Temp. [K]
TFS 2/12	850	6011	1871	6012	2036
TFS 3/12	850	6012	2040		
TFS 5/12	850	6012	2197		
TFS 4/13	950	6010	2028	6011	2022
TFS 5/13	950	6011	2016		
TFS 3/14	1050	6010	1707	6011	1707
TFS 2/15	1150	6011	1575	6011	1488
TFS 5/15	1150	6011	1400		
TFS 3/16	1250	6011	1354	6011	1301
TFS 5/16	1250	6011	1248		
TFS 2/17	1350	6011	1181	6011	1123
TFS 5/17	1350	6011	1064		
TCR 7	350	6011	1143	6011	1143
TCR 9	550	6011	1297	6011	1297
TCRC 13	950	6015	1914	6015	1914
TIT C/9	500	6012	1227	6012	1227
TIT D/12	800	6012	1707	6012	1707
TSH 1/0	- 250	6011	587	6011	587
TSH 3/180	- 50	6011	706	6011	706
TSH 4/0	50	6011	750	6011	756
TSH 4/90	50	6011	750		
TSH 4/180	50	6011	767		

Thermocouple	Elevation	Onset of cooling		Mean value per elevation	
	[mm]	Time [s]	Temp. [K]	Time [s]	Temp. [K]
TSH 7/0	350	6011	1089	6011	1106
TSH 7/180	350	6011	1123		
TSH 9/90	550	6012	1232	6012	1255
TSH 9/270	550	6011	1277		
TSH 11/0	750	6013	1516	6013	1611
TSH 11/180	750	6013	1705		
TSH 12/0	850	6013	1710	6013	1785
TSH 12/180	850	6013	1860		
TSH 13/90	950	6013	1939	6013	1967
TSH 13/270	950	6013	1994		
TSH 14/90	1050	6013	1847	6013	1999
TSH 14/270	1050	6013	2151		
TSH 15/0	1150	6013	1806	6013	1937
TSH 15/180	1150	6013	2068		
TSH 16/0	1250	6013	1786	6013	1910
TSH 16/180	1250	6013	2034		

Table 7: QUENCH-05; Maximum measured test rod temperature of each elevation

Elevation [mm]	Thermocouple	Time [s]	Maximum temperature [K]
- 250	TFS 2/1	6011	625
- 150	TFS 2/2	6011	709
- 50	TFS 2/3	6011	783
50	TFS 5/4/180	6010	844
150	TFS 2/5	6011	982
250	TFS 2/6	6010	1090
350	TFS 2/7	6010	1158
450	TFS 5/8	6010	1245
550	TFS 2/9	6010	1326
650	TFS 5/10	6011	1464
750	TFS 5/11	6012	2272
850	TFS 5/12	6012	2197
950	TFS 4/13	6010	2028
1050	TFS 3/14	6010	1707
1150	TFS 2/15	6011	1575
1250	TFS 3/16	6011	1354
1350	TFS 2/17	6011	1181

Table 8: **QUENCH-05; Maximum measured shroud temperature of each elevation**

Elevation [mm]	Thermocouple	Time [s]	Maximum temperature [K]
- 250	TSH 1/0	6011	587
- 50	TSH 3/180	6011	706
50	TSH 4/180	6011	767
350	TSH 7/180	6011	1123
550	TSH 9/270	6011	1277
750	TSH 11/180	6013	1705
850	TSH 12/180	6013	1860
950	TSH 13/270	6013	1994
1050	TSH 14/270	6013	2151
1150	TSH 15/180	6013	2068
1250	TSH16/180	6013	2034

Table 9: **QUENCH 05; Cross sections** 15.06.00

Sample	Sample length (mm)	Axial position Bottom (mm)	Top (mm)	Remarks
QUE-05-a			58	Remnant
Cut	2	58	60	
QUE-05-1	13	60	73	Reference, 73 mm polished
Cut	2	73	75	
QUE-05-2	5	75	80	Sample for H_2 absorption
Cut	2	80	82	
QUE-05-b	453	82	535	
Cut	2	535	537	
QUE-05-3	13	537	550	Elevation 9, 550 mm polished
Cut	2	550	552	
QUE-05-c	183	552	735	
Cut	2	735	737	
QUE-05-4	13	737	750	Elevation 11, 750 mm polished
Cut	2	750	752	
QUE-05-d	83	752	835	
Cut	2	835	837	
QUE-05-5	13	837	850	Elevation 12, 850 mm polished
Cut	2	850	852	
QUE-05-e	53	852	905	
Cut	2	905	907	
QUE-05-6	13	907	920	920 mm polished
Cut	2	920	922	
QUE-05-f	13	922	935	
Cut	2	935	937	
QUE-05-7	13	937	950	Elevation 13, 950 mm polished
Cut	2	950	952	
QUE-05-8	5	952	957	Sample for H_2 absorption
Cut	2	957	959	
QUE-05-g	26	959	985	
Cut	2	985	987	
QUE-05-9	13	987	1000	1000 mm polished
Cut	2	1000	1002	
QUE-05-h	133	1002	1135	
Cut	2	1135	1137	

Sample	Sample length (mm)	Axial position Bottom (mm)	Top (mm)	Remarks
QUE-05-10	13	1137	1150	Elevation 15, 1150 mm polished
Cut	2	1150	1152	
QUE-05-i	83	1152	1235	
Cut	2	1235	1237	
QUE-05-11	13	1237	1250	Elevation 16, 1250 mm polished
Cut	2	1250	1252	
QUE-05-j		1252		Remnant

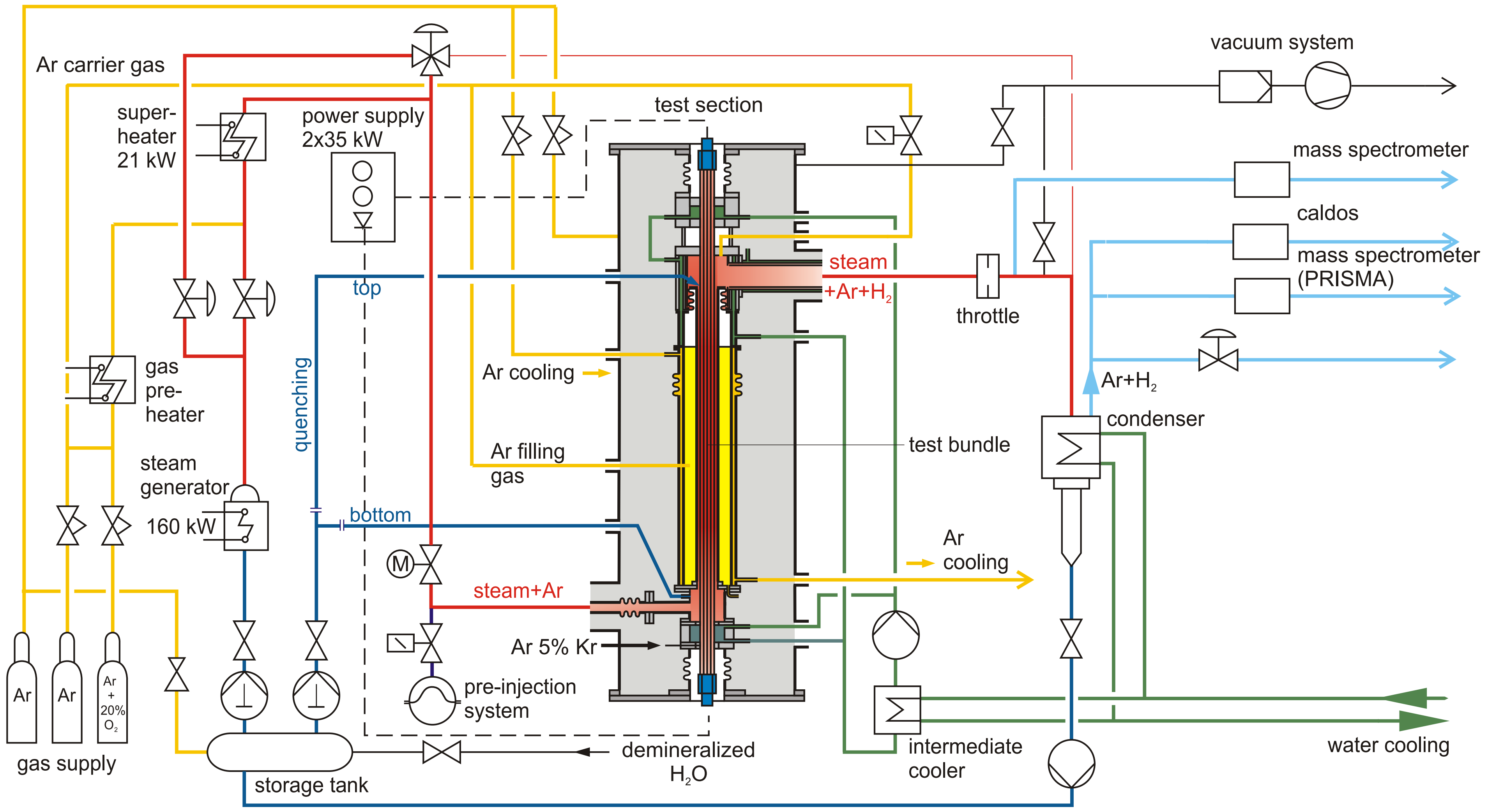

Fig. 1: Flow diagram of the QUENCH test facility

Fig.1-QUE05-Flow diagram.cdr
21.12.01 - IMF

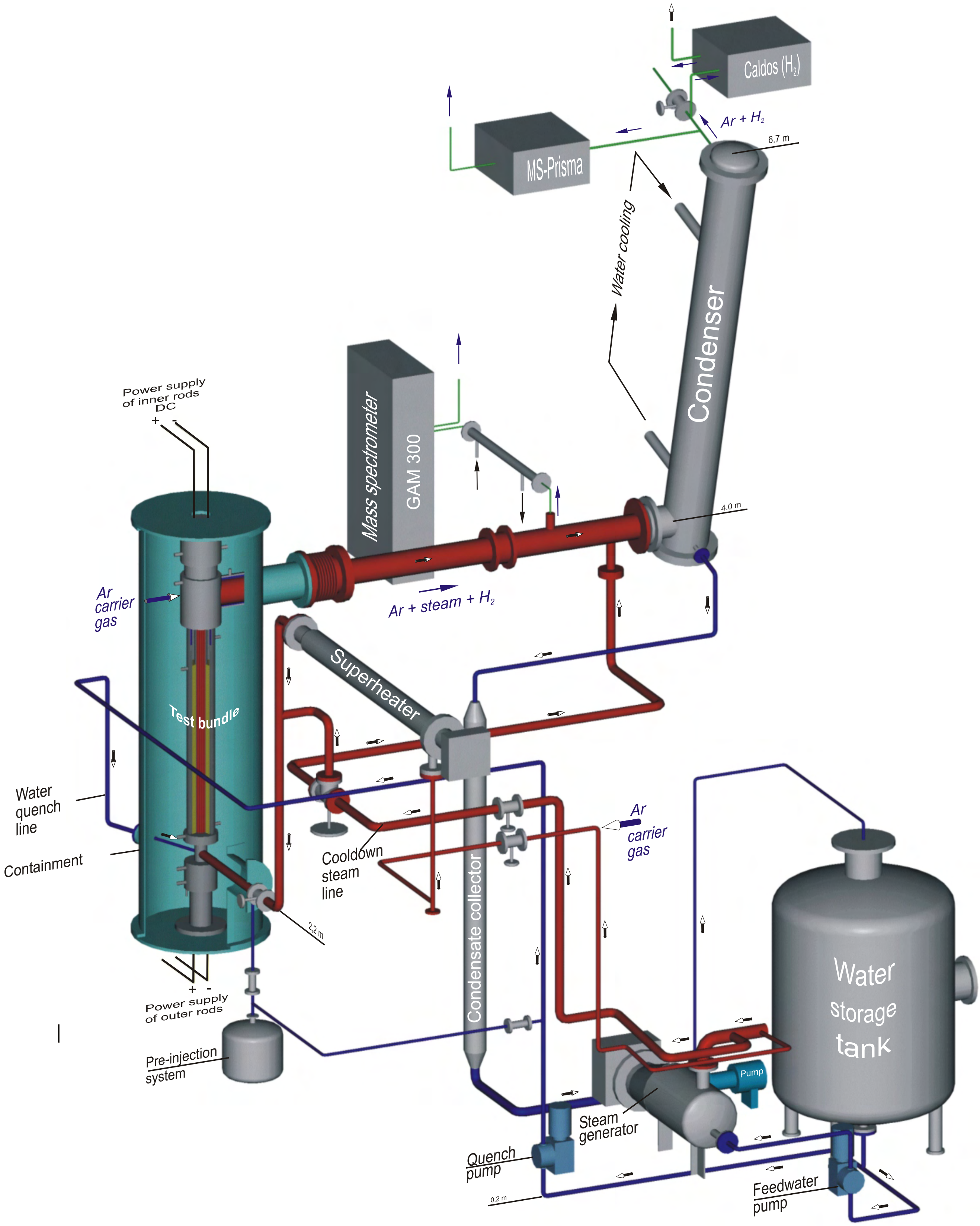

Fig. 2: QUENCH Facility; main components

Fig.2-QUE04 Gesamtanlage 3D.cdr
10.03.02 - IMF

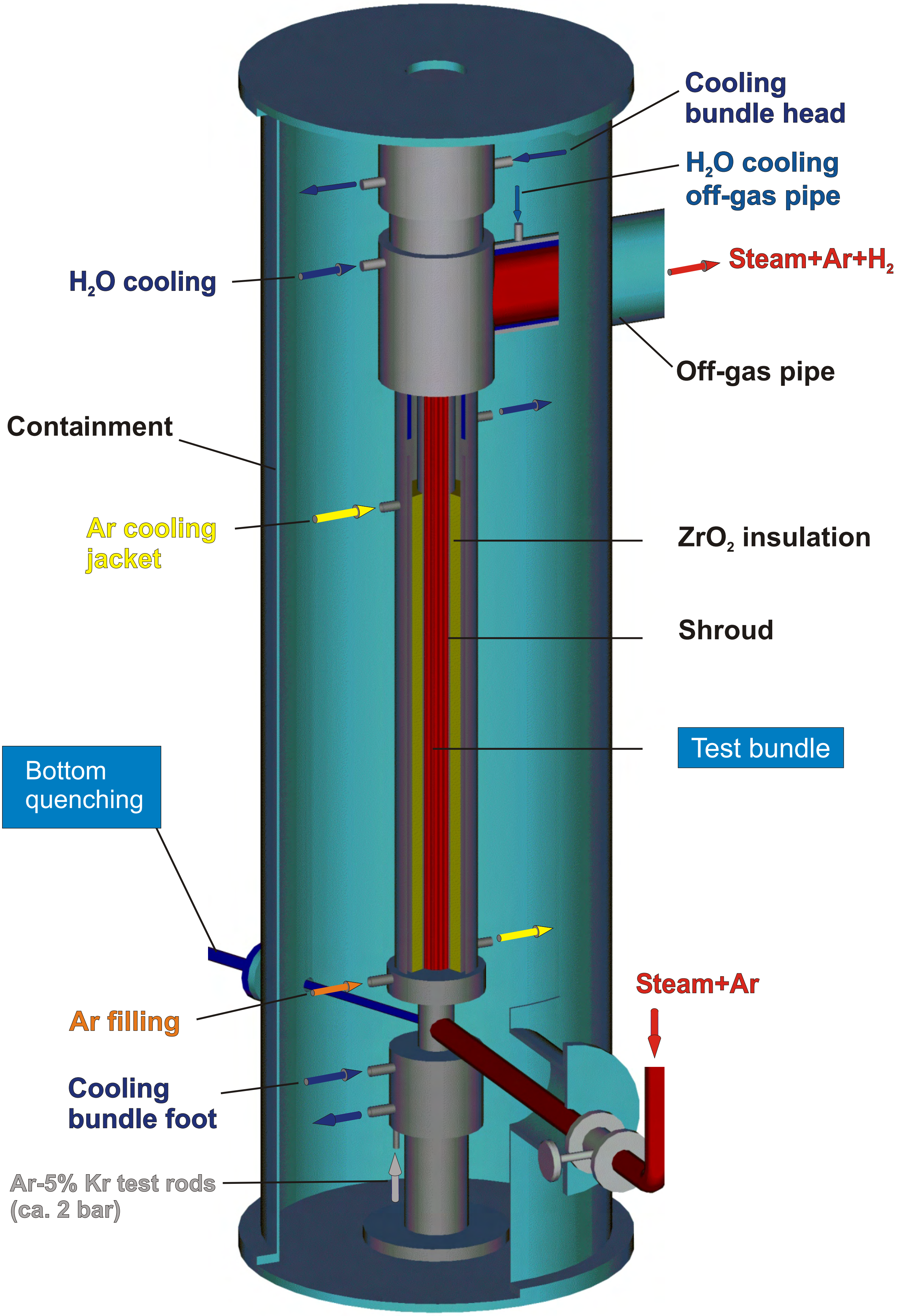

Fig. 3: QUENCH Facility; containment and test section

Fig.3-QUE05 Containment 3D.cdr
20.12.01 - IMF

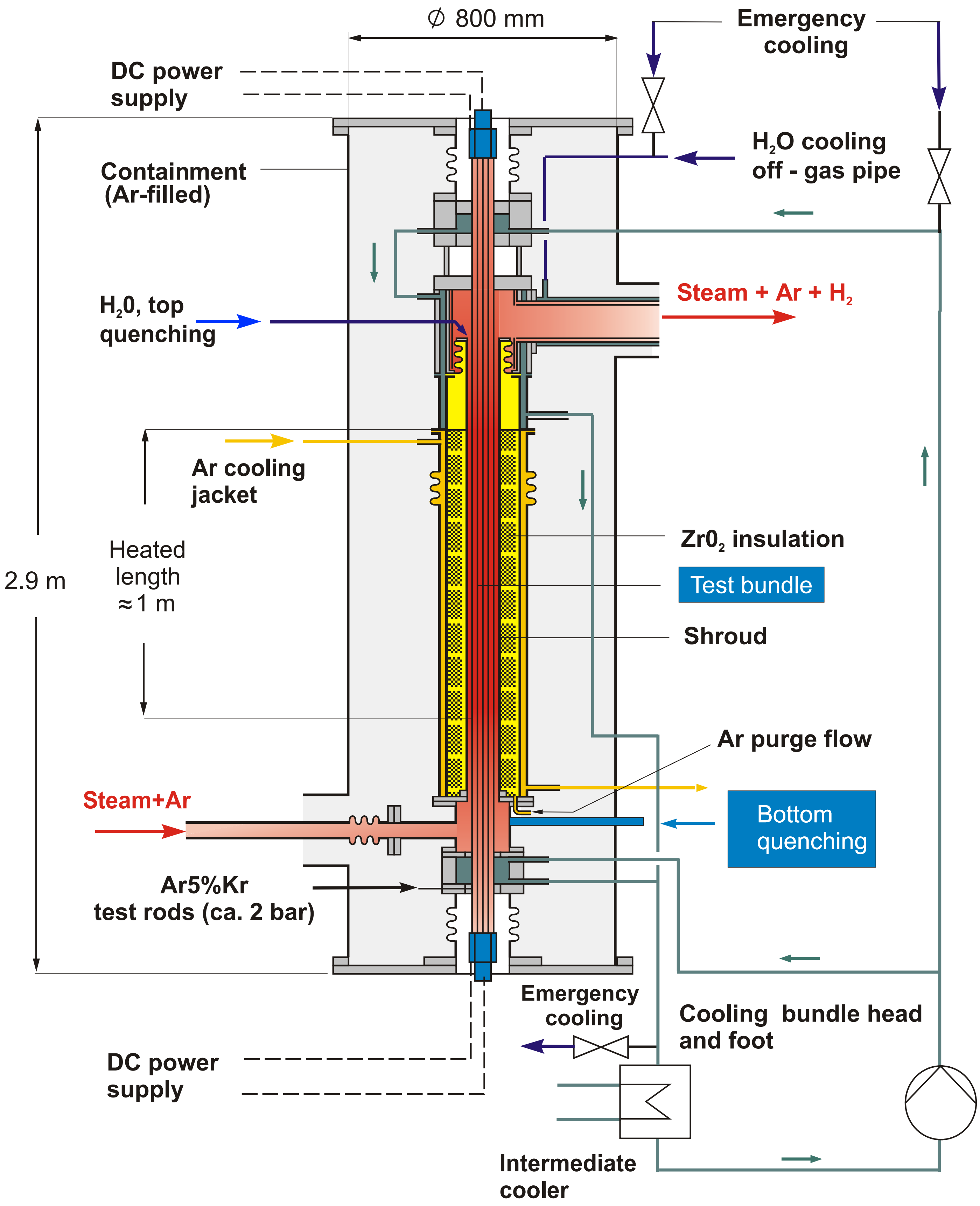

Fig. 4: QUENCH Test section; flow lines

Fig.4-QUE05 Flow lines.cdr
20.12.01 - IMF

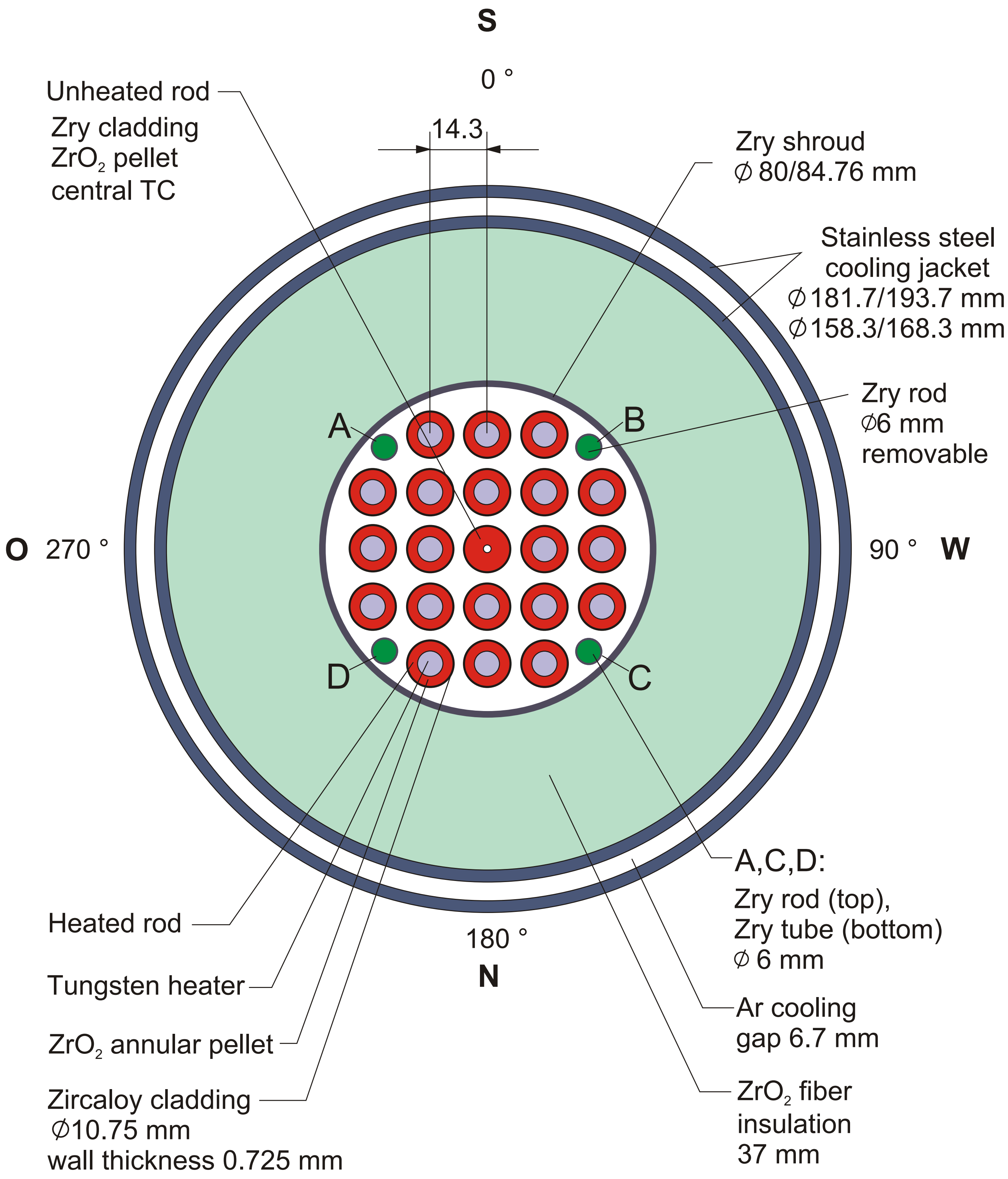

Fig. 5: QUENCH-05; Fuel rod simulator bundle (Top view)

Fig.5-QUE05 Cross section.cdr
13.02.02 - IMF

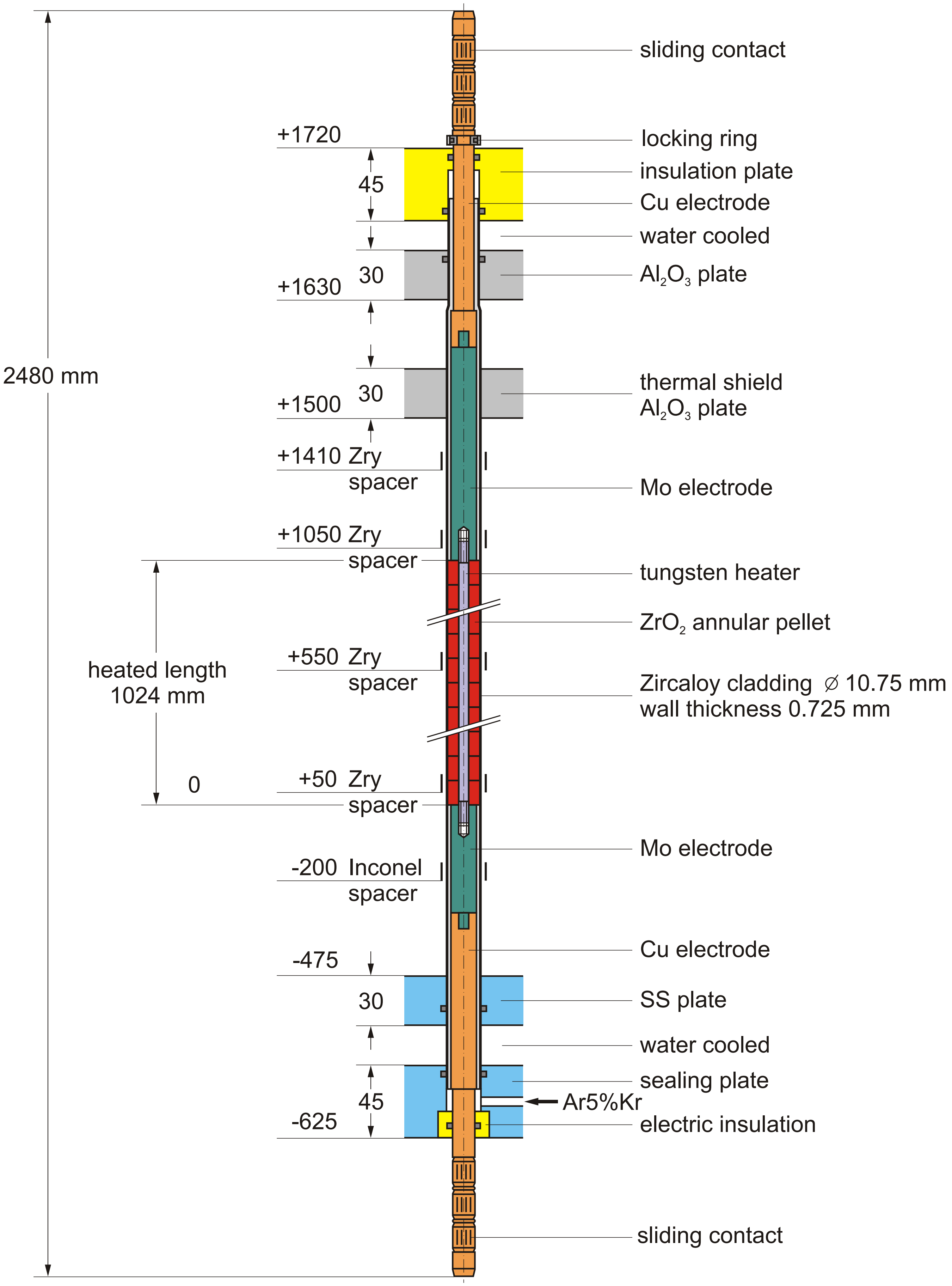

Fig. 6: Heated fuel rod simulator

Fig.6-QUE05 Heated fuel rod sim.cdr
20.12.01 - IMF

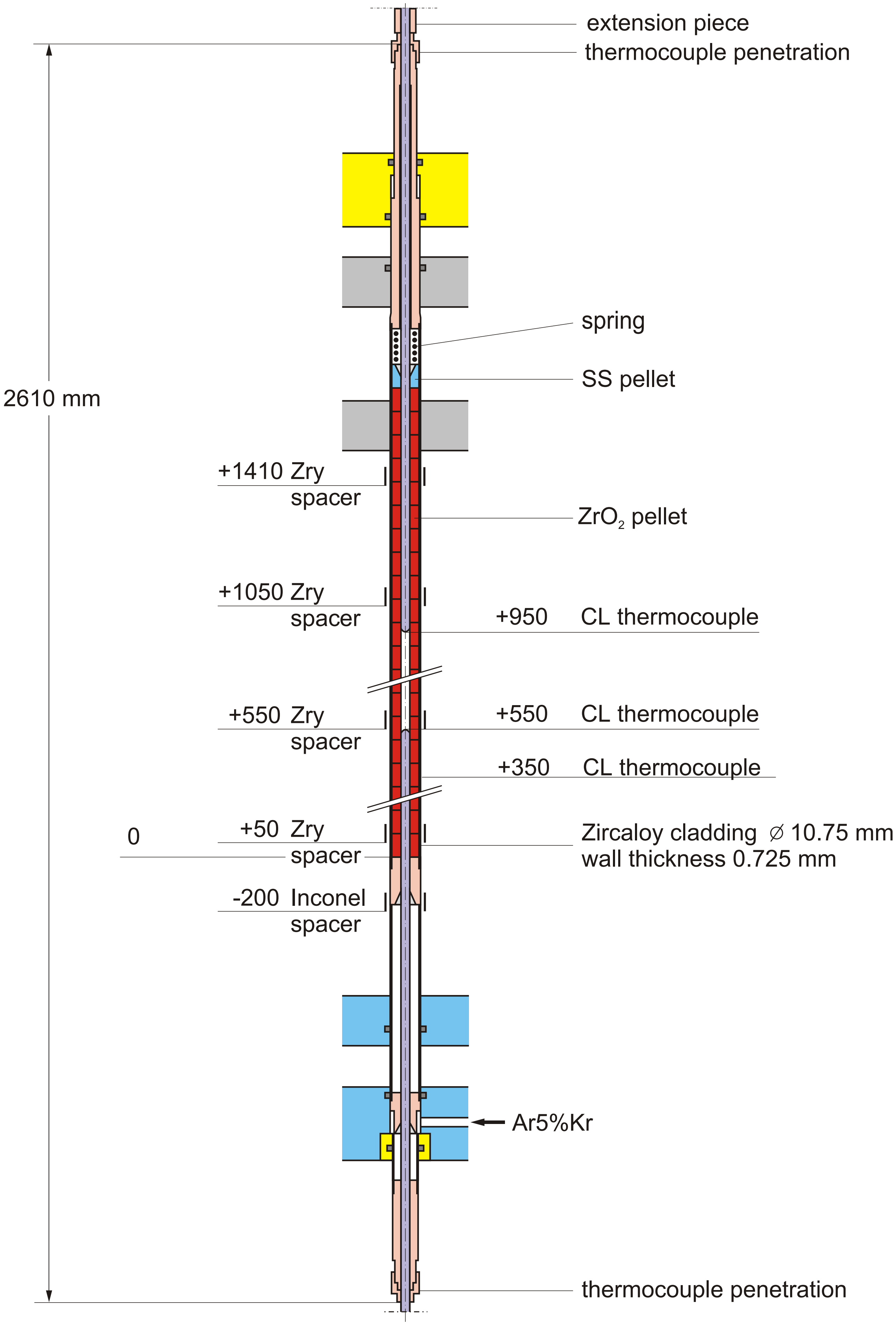

Fig. 7: Unheated fuel rod simulator

Fig.7-QUE05 Unheated fuel rod sim.cdr
20.12.01 - IMF

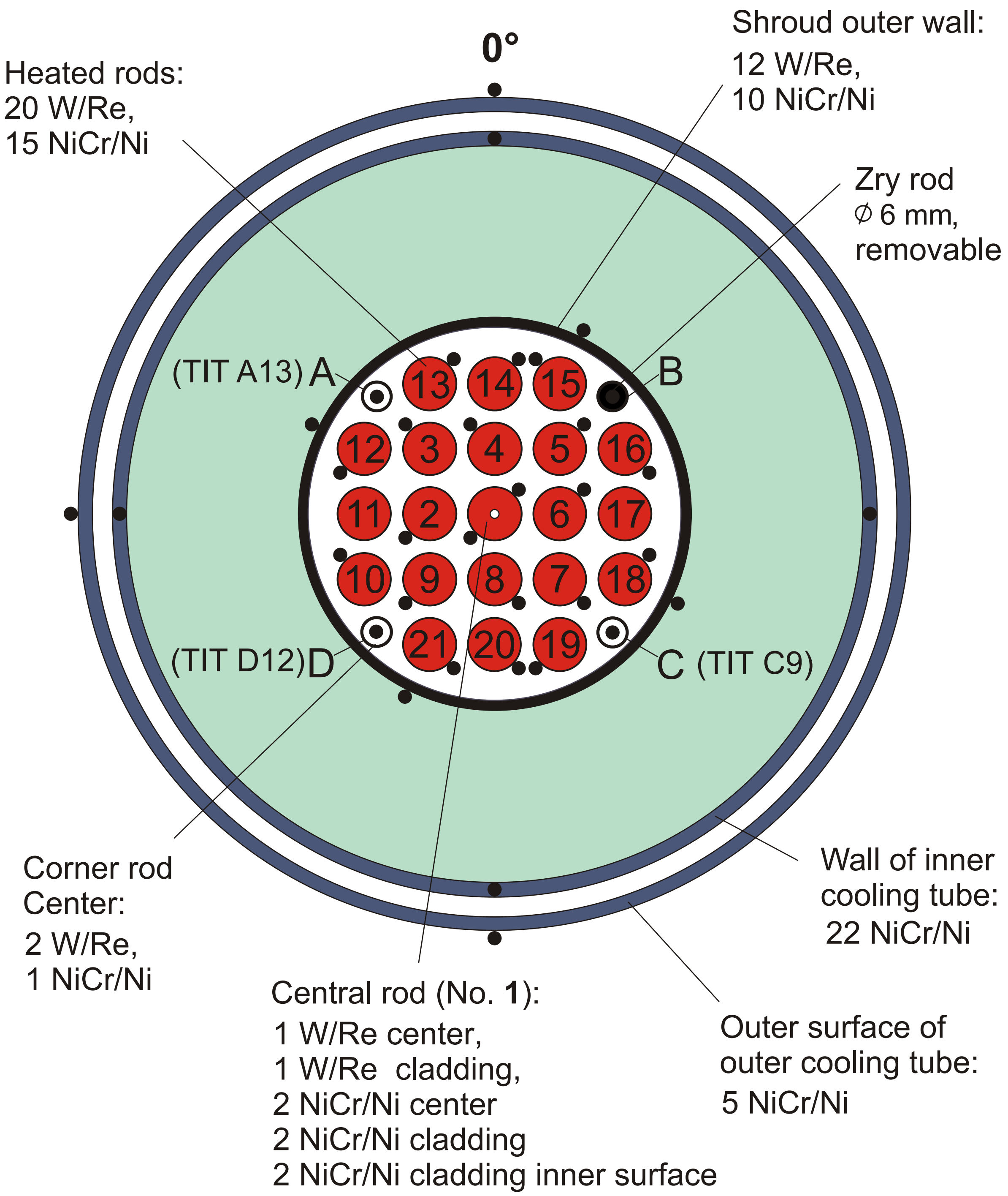

Fig. 8: QUENCH-05; Test bundle; TC instrumentation and rod designation (top view)

Fig.8-QUE05 TC instr.cdr
13.02.02 - IMF

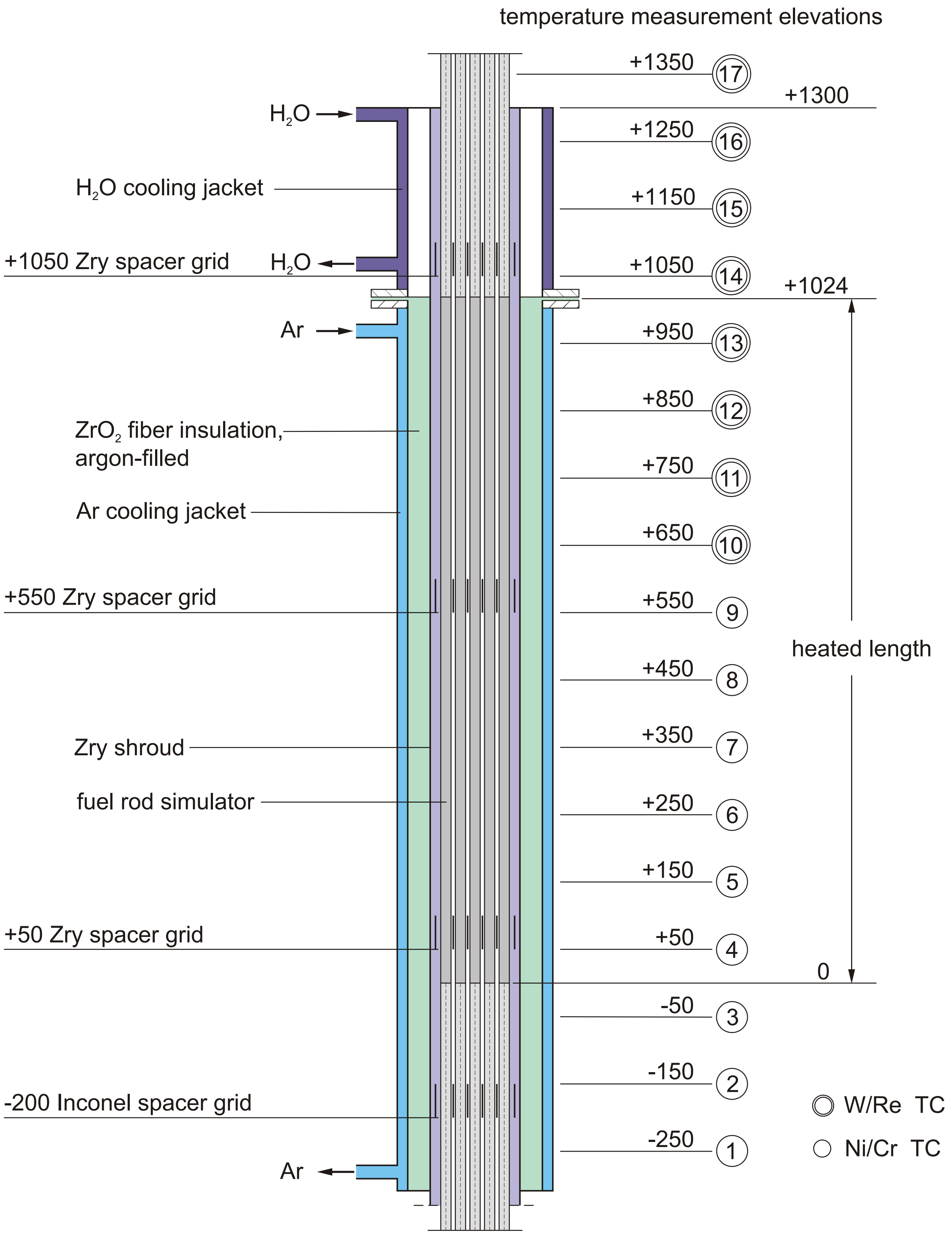

Fig. 9: QUENCH; Test section instrumentation

Fig.9-QUE TC elevations.cdr
20.12.01 - IMF

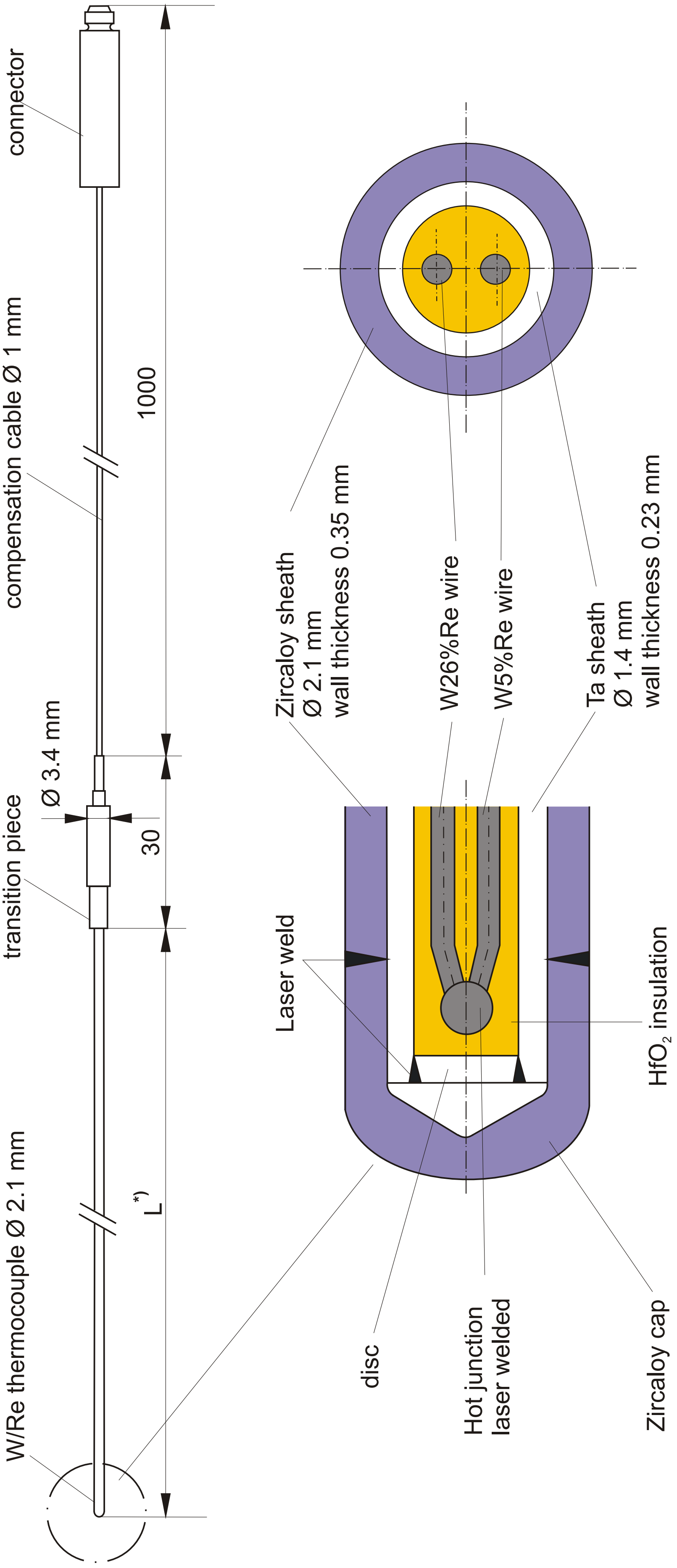

*) L: high-temperature section length dependent on the TC position in the test bundle 500 mm - 1700 mm

Fig. 10: QUENCH; High-temperature thermocouple

Fig.10-QUE05 High-temp thermocouple.cdr
20.12.01 - IMF

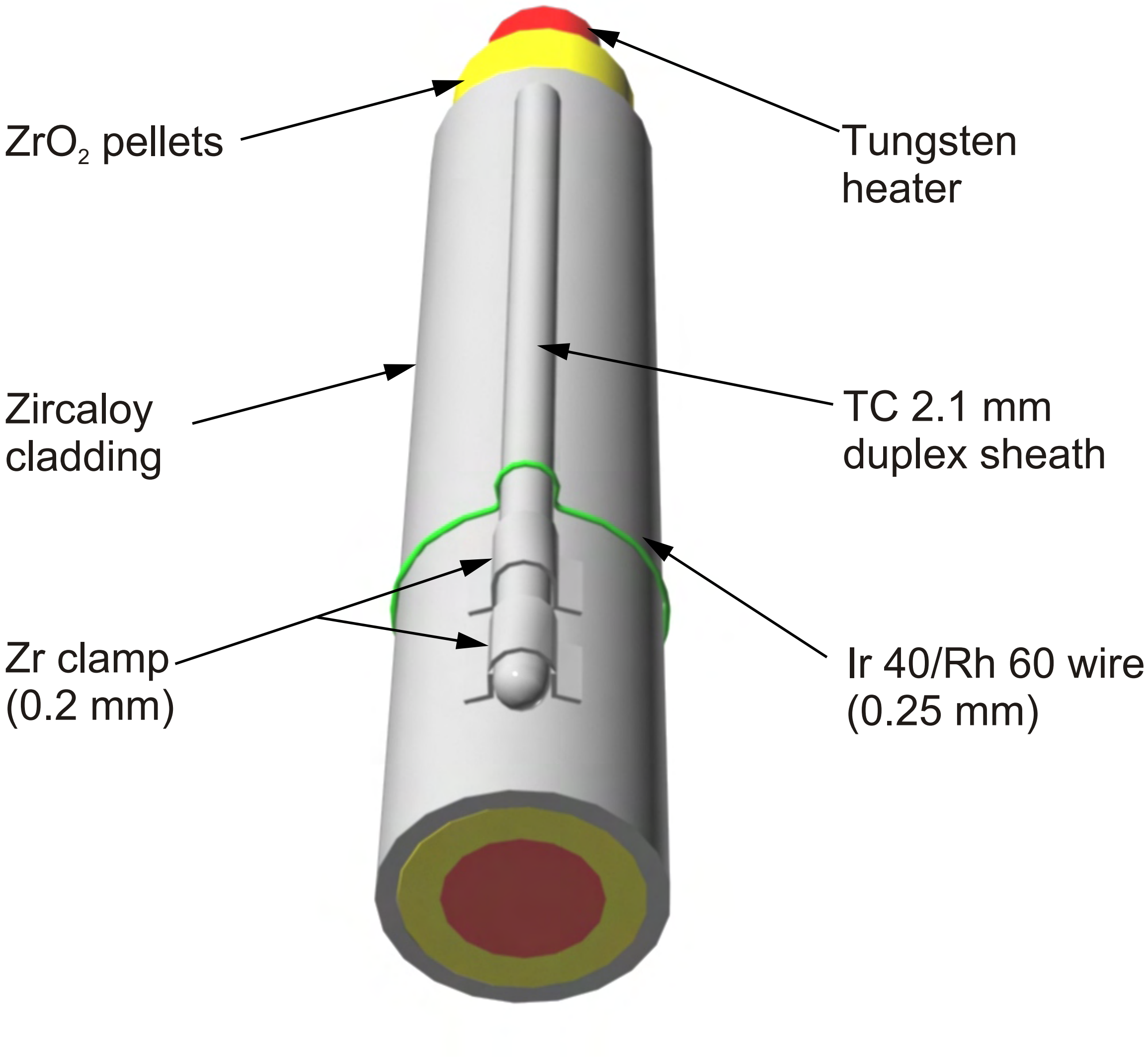

Tests with pre-oxidation: Zr clamp + wire

Tests without pre-oxidation: Zr clamp

Fig. 11: TC fastening concept for the QUENCH test rod

Fig 11QUE05 TC Fastening3.cdr
20.12.01 - IMF

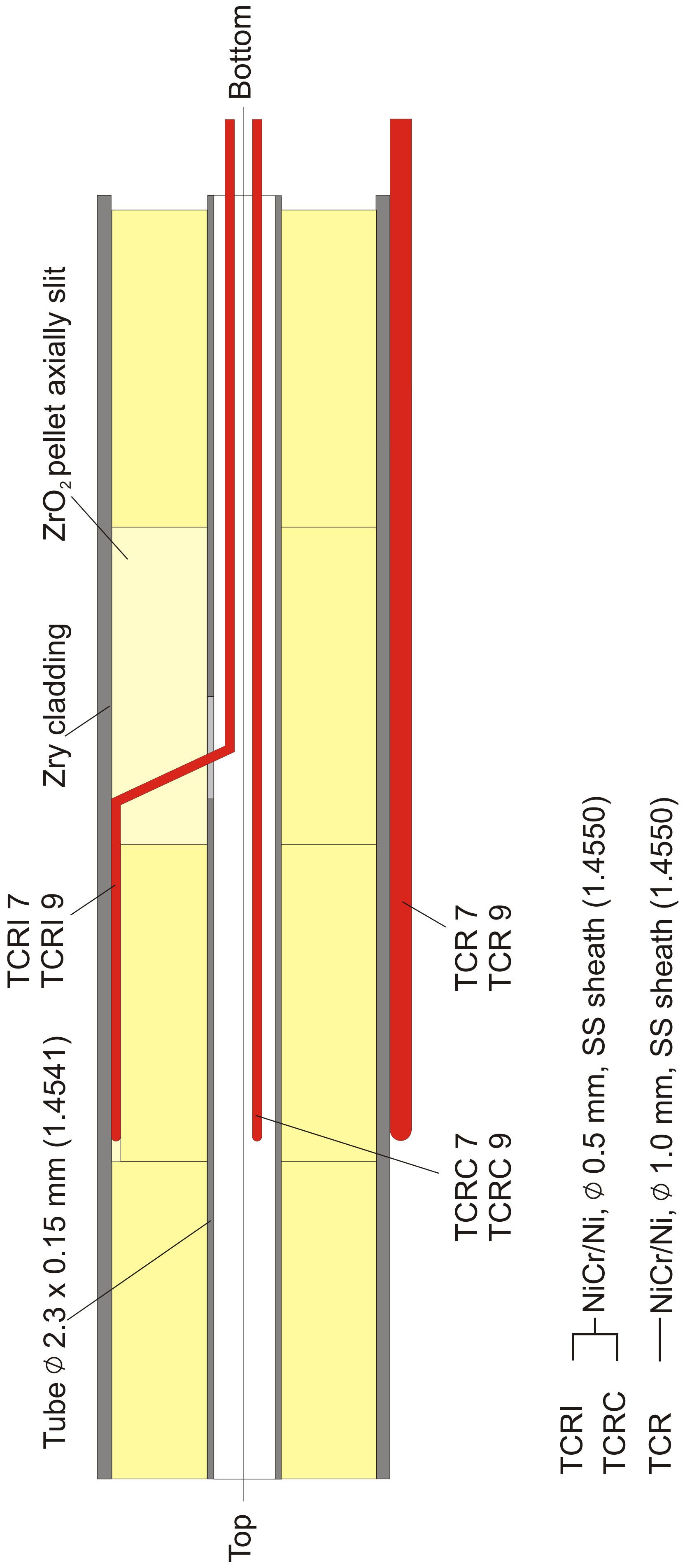

Fig. 12: QUENCH-05; TC instrumentation of the unheated fuel rod simulator at levels 7 (350 mm) and 9 (550 mm)

Fig 12 QUE05 Zentralstab.cdr
07.01.02 - IMF

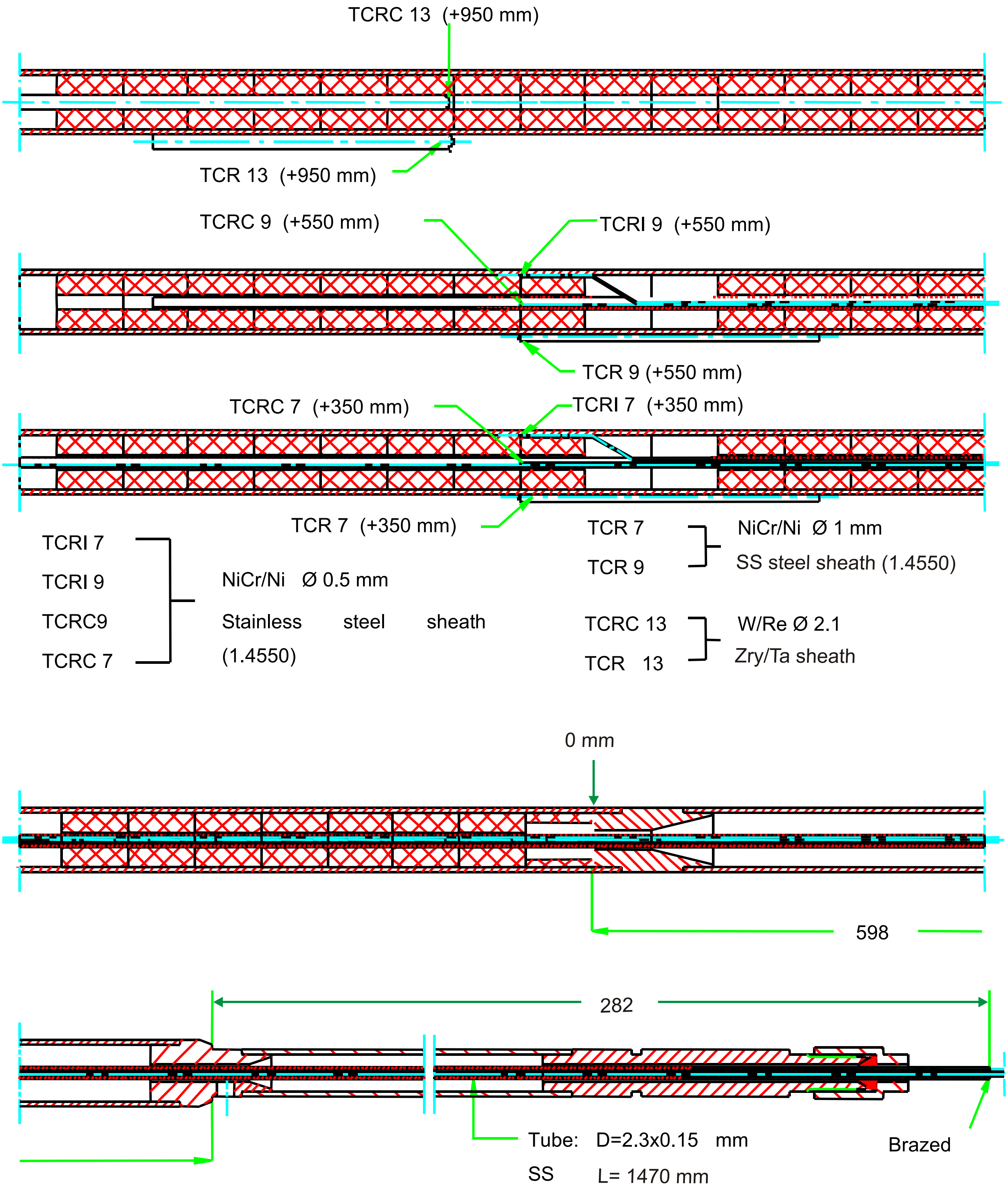

Fig. 13: QUENCH-05; TC instrumentation of the unheated fuel rod simulator

Fig 13 QUE05-Stab unbeheizt.cdr
18.03.02 - IMF

(TIT A13, TIT D12, TIT C9)

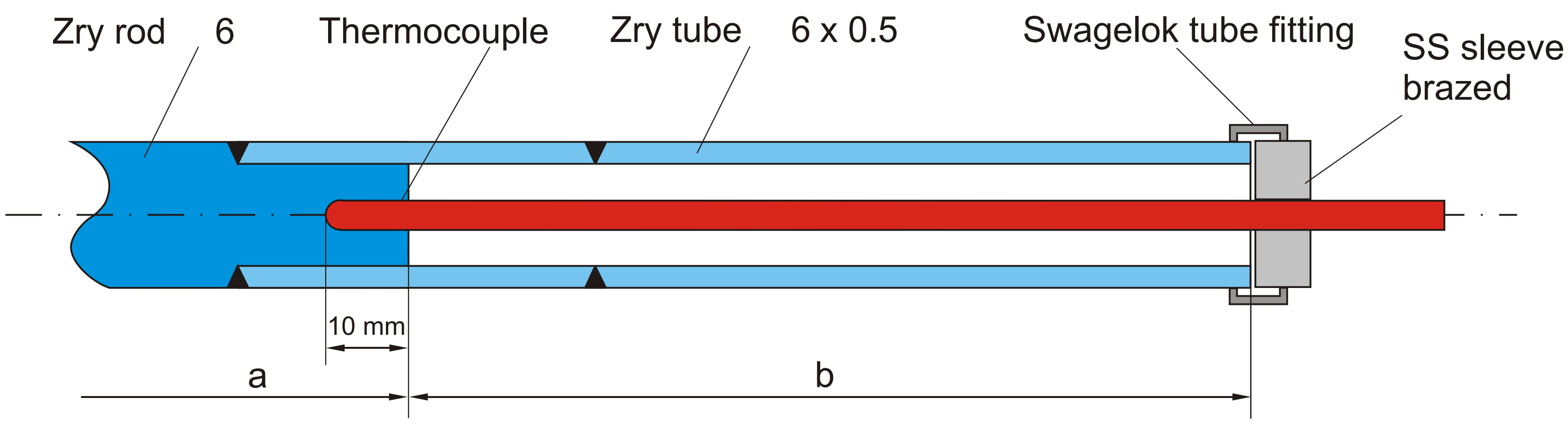

Rod A: TIT A13 (950 mm), W/Re, 2.1 mm, a = 360 mm, b = 2080 mm

Rod D: TIT D12 (850 mm), W/Re, 2.1 mm, a = 460 mm, b = 1980 mm

Rod C: TIT C 9 (550 mm), NiCr/Ni, 1 mm, a = 760 mm, b = 1680 mm

(Rod B: Zry-4 rod, 6 mm, removable)

Fig. 14: QUENCH-05; Schematic of the arrangement of the thermocouples inside the corner rods

Fig 14 QUE05 TC in Zry-rod.cdr
07.01.02 - IMF

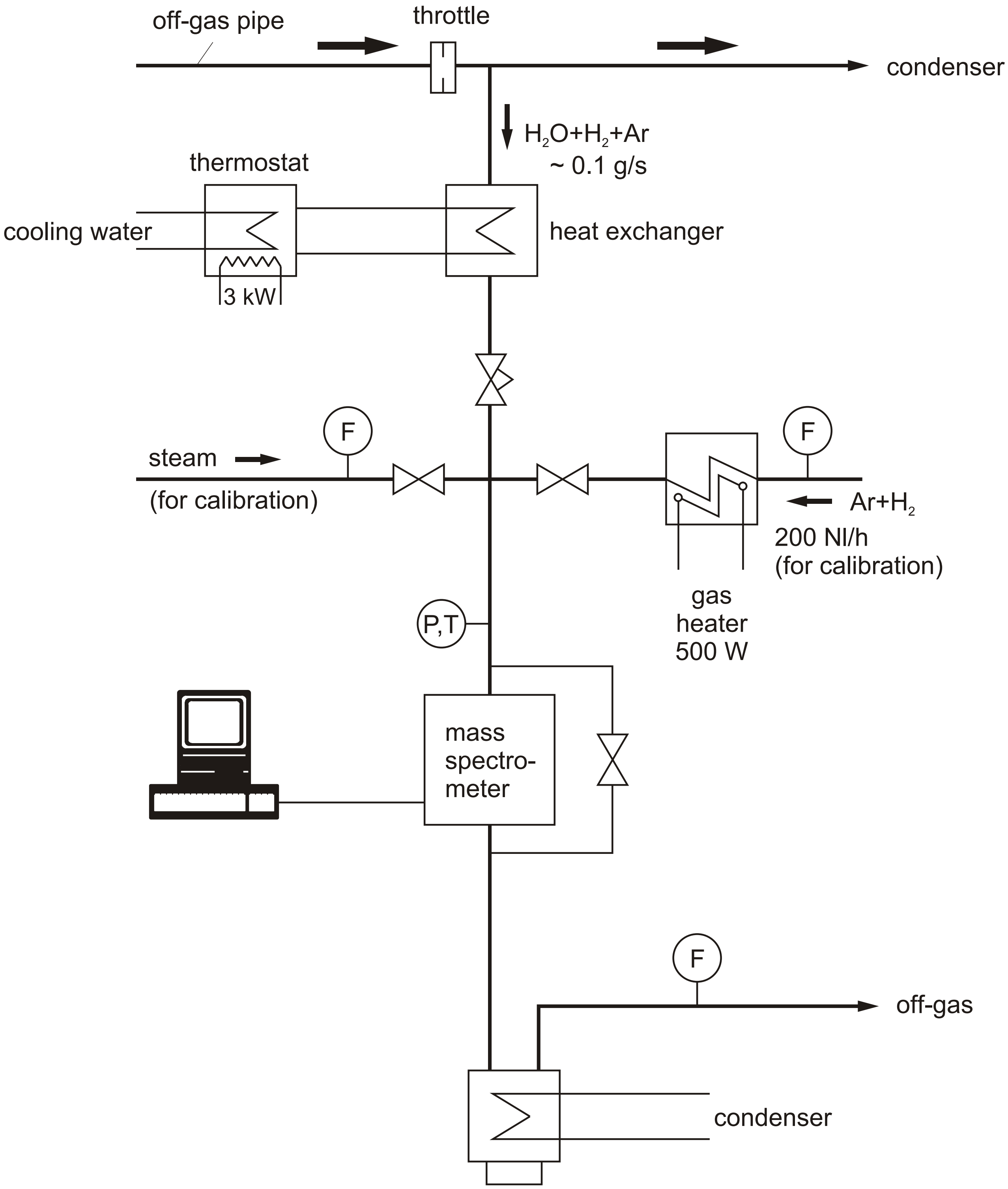

Fig. 15: QUENCH-Facility; H_2 measurement with the mass spectrometer

Fig 15 QUE05 MS QUENCH-Facility.cdr
08.01.02 - IMF

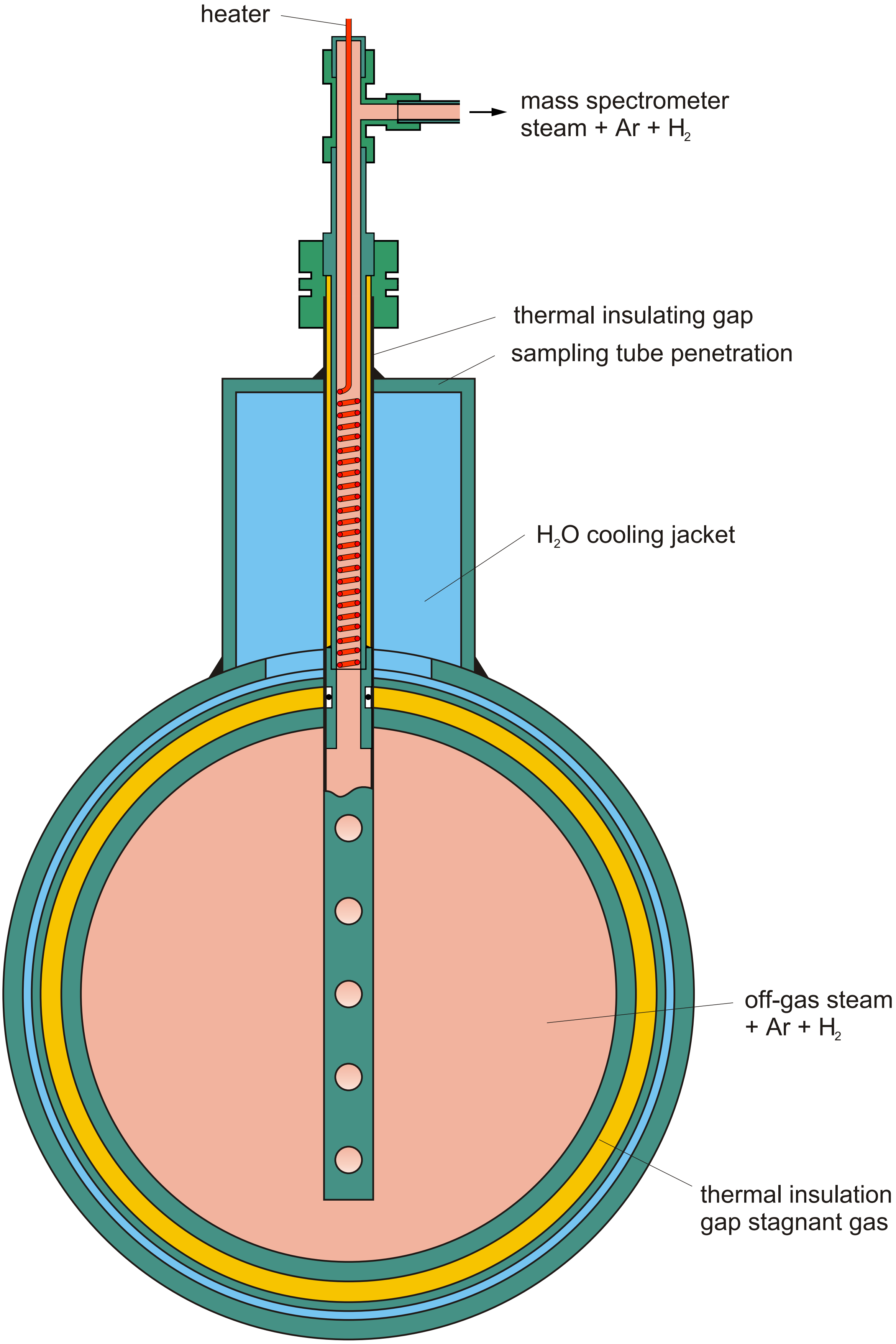

Fig. 16: QUENCH; Mass spectrometer sampling position at the off-gas pipe

Fig 16 QUE05 MS sampling position new.cdr
08.01.02 - IMF

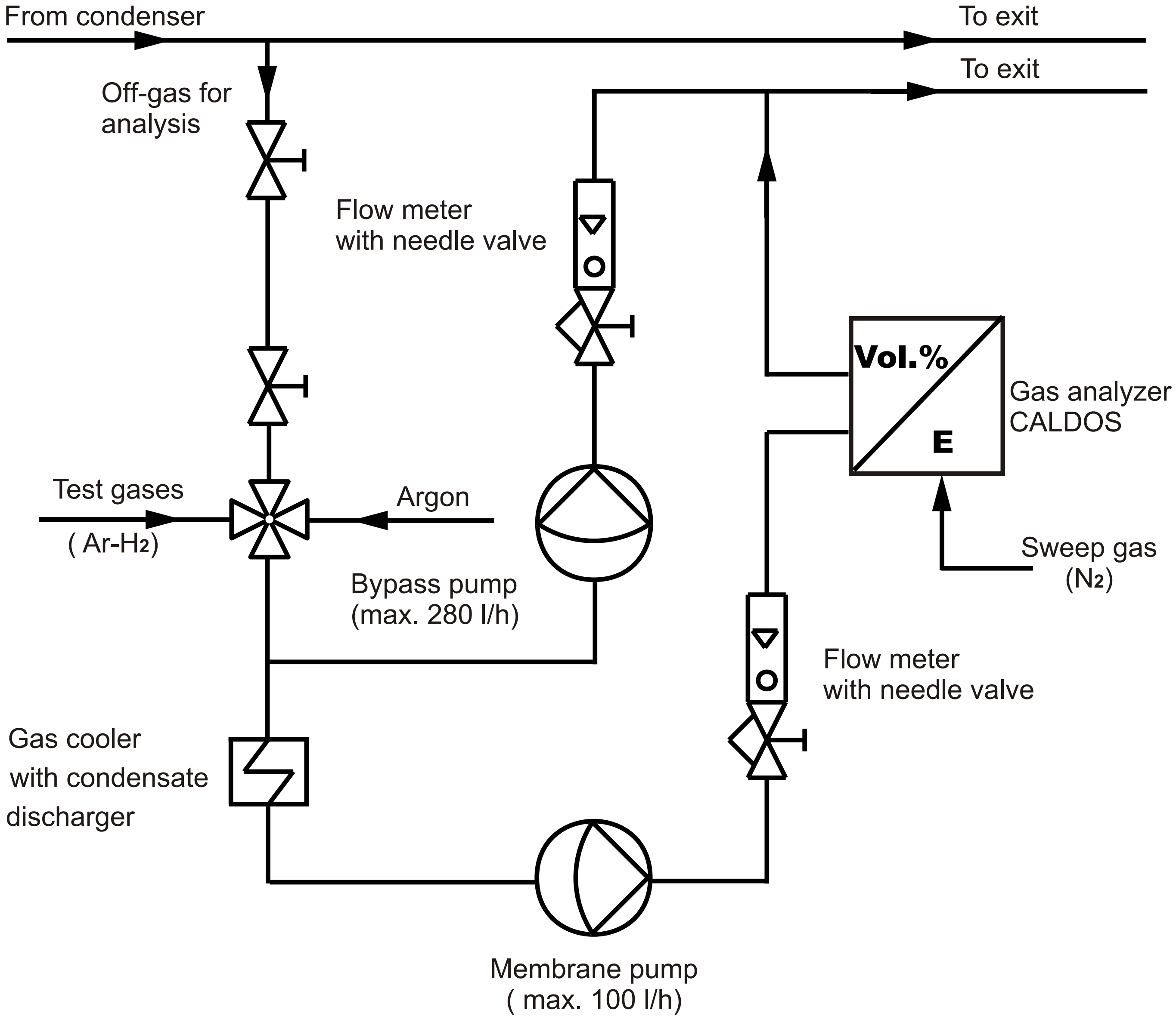

Fig. 17: QUENCH-05; Hydrogen measurement with the CALDOS analyzer

Fig 17 QUE05 Caldos Schema (ab QUE04).cdr
08.01.02 - IMF

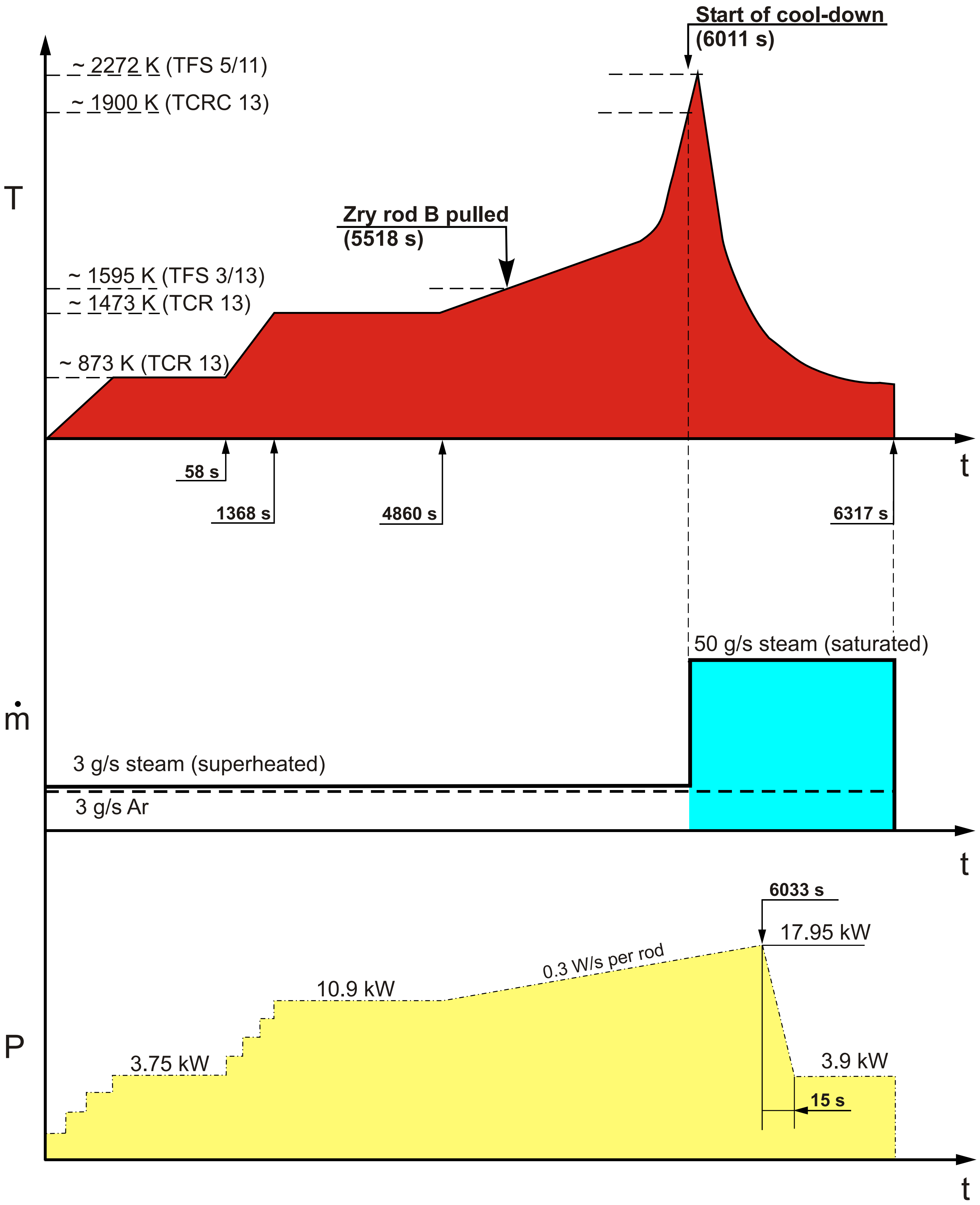

Fig. 18: Test conduct QUENCH-05 (schematic)

Fig 18 QUE05 Test conduct.cdr
13.02.02 - IMF

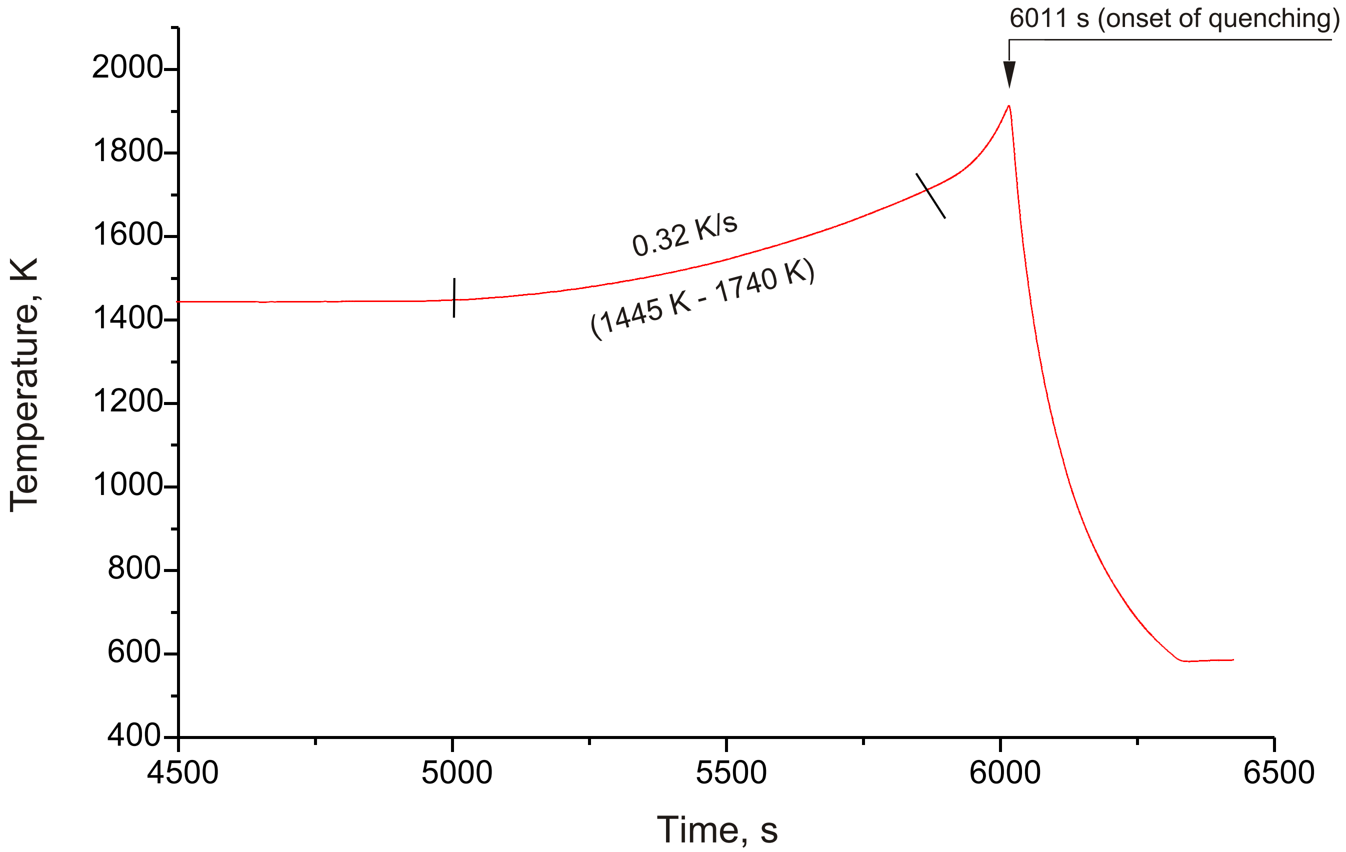

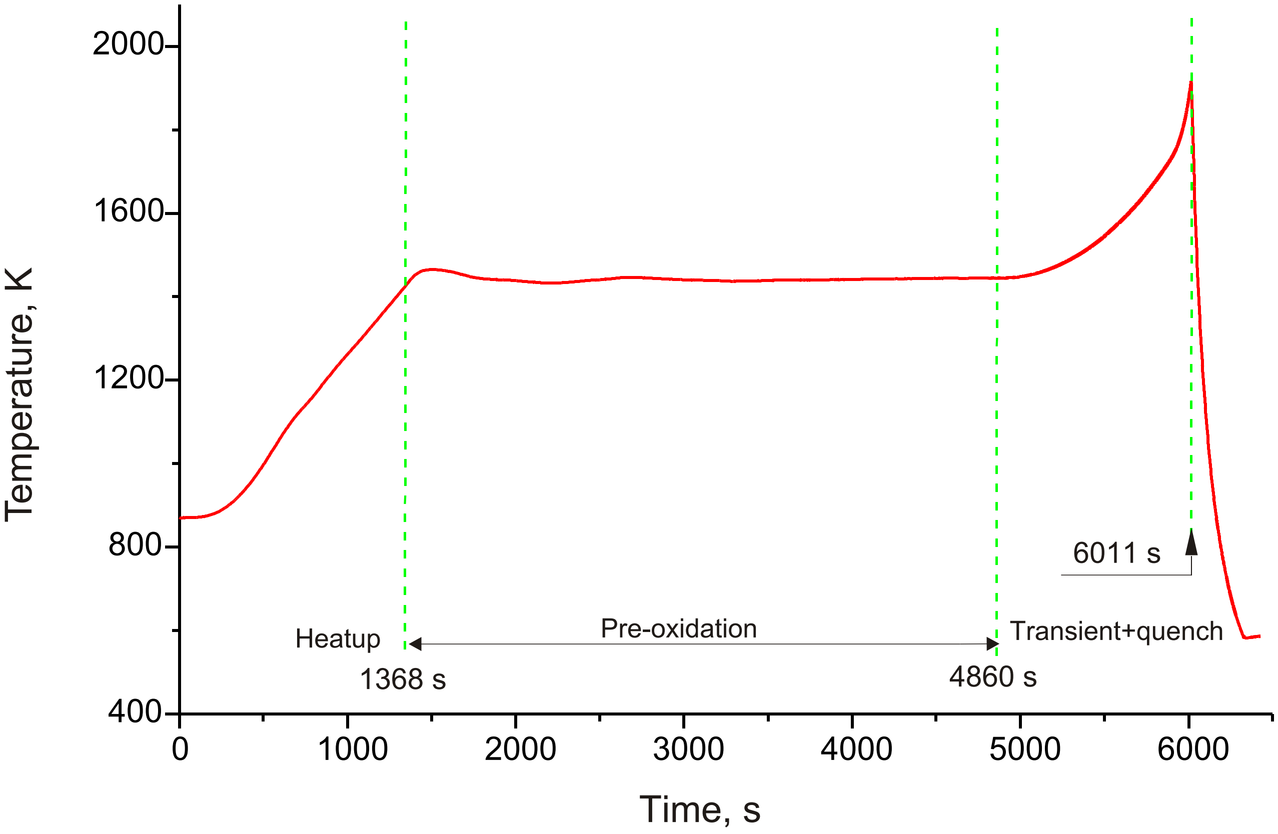

Fig. 19: QUENCH-05; Heatup rate determined on the basis of TCRC 13 (centerline thermocouple), top, together with the test phase definitions, bottom

Fig.19 QUE05 Temp-Zeit-TCRC13.cdr
13.02.02 - IMF

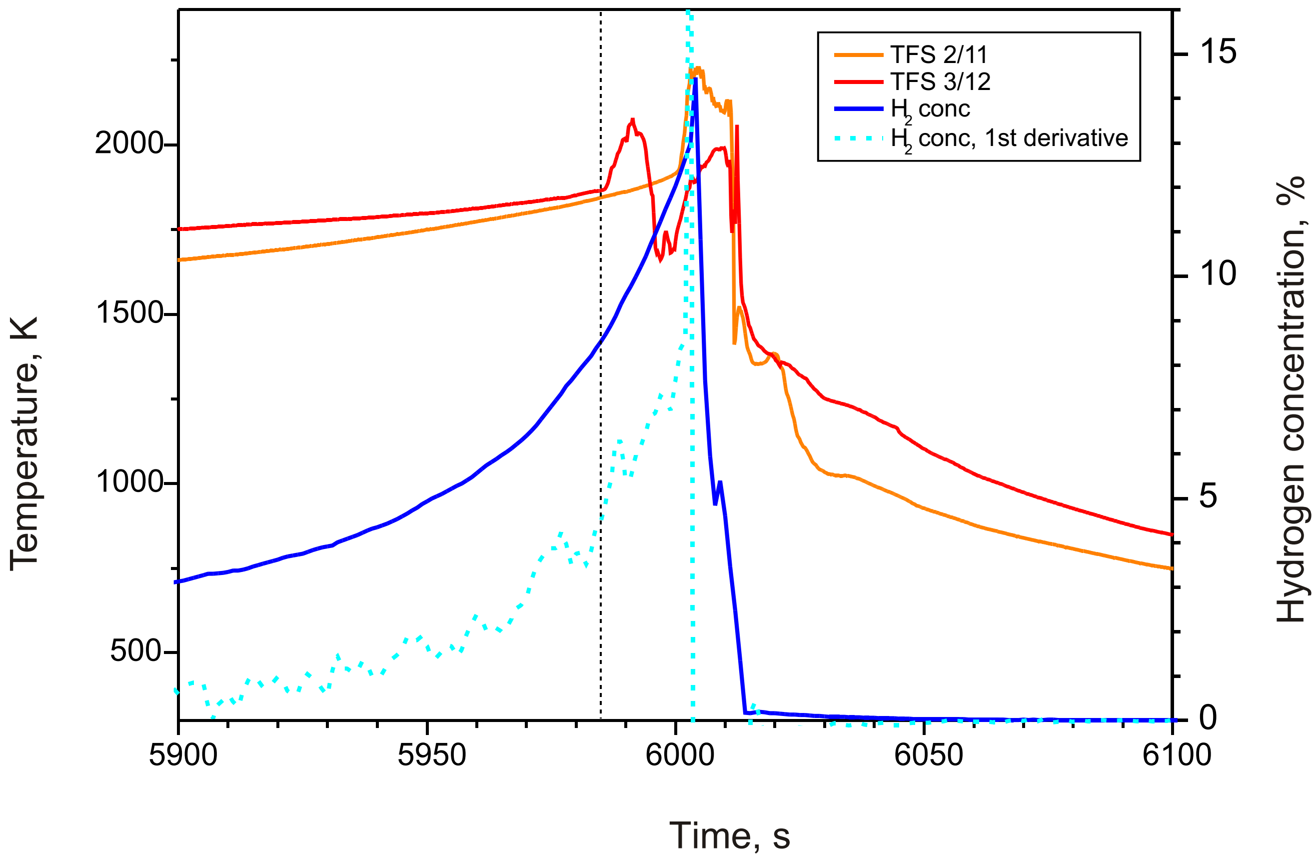

Fig. 20: QUENCH-05; Temperature excursion at levels 750 and 850 mm during the transient phase together with the hydrogen concentration in the off-gas

Fig.20 QUE05 MS all G8.cdr
10.01.02 - IMF

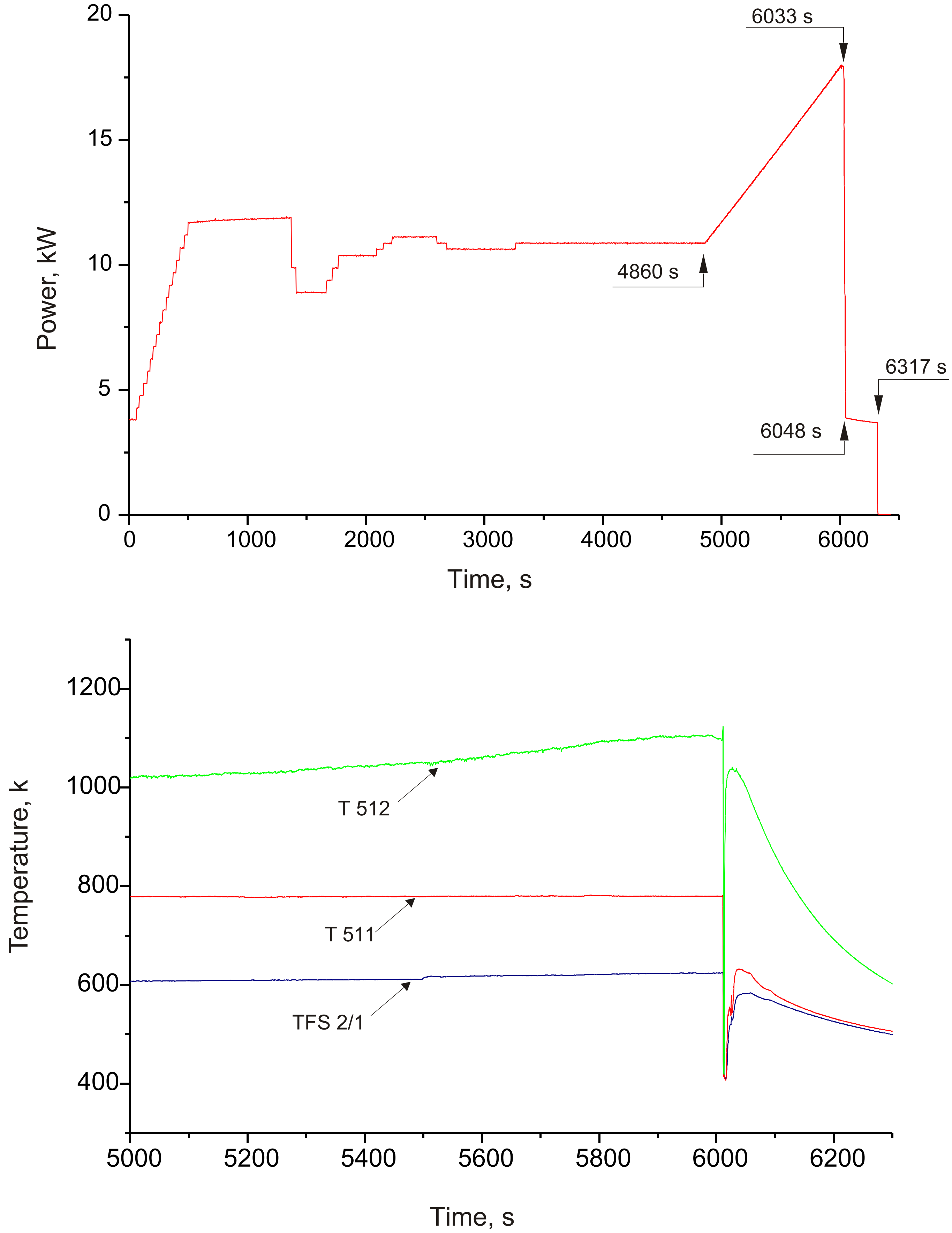

Fig.21: QUENCH-05; Total electric power, top, and coolant temperatures T 511 at bundle inlet, T 512 at bundle outlet, TFS 2/1 at -250 mm, bottom

Fig.21-QUE05-Leistung.cdr
15.01.02 - IMF

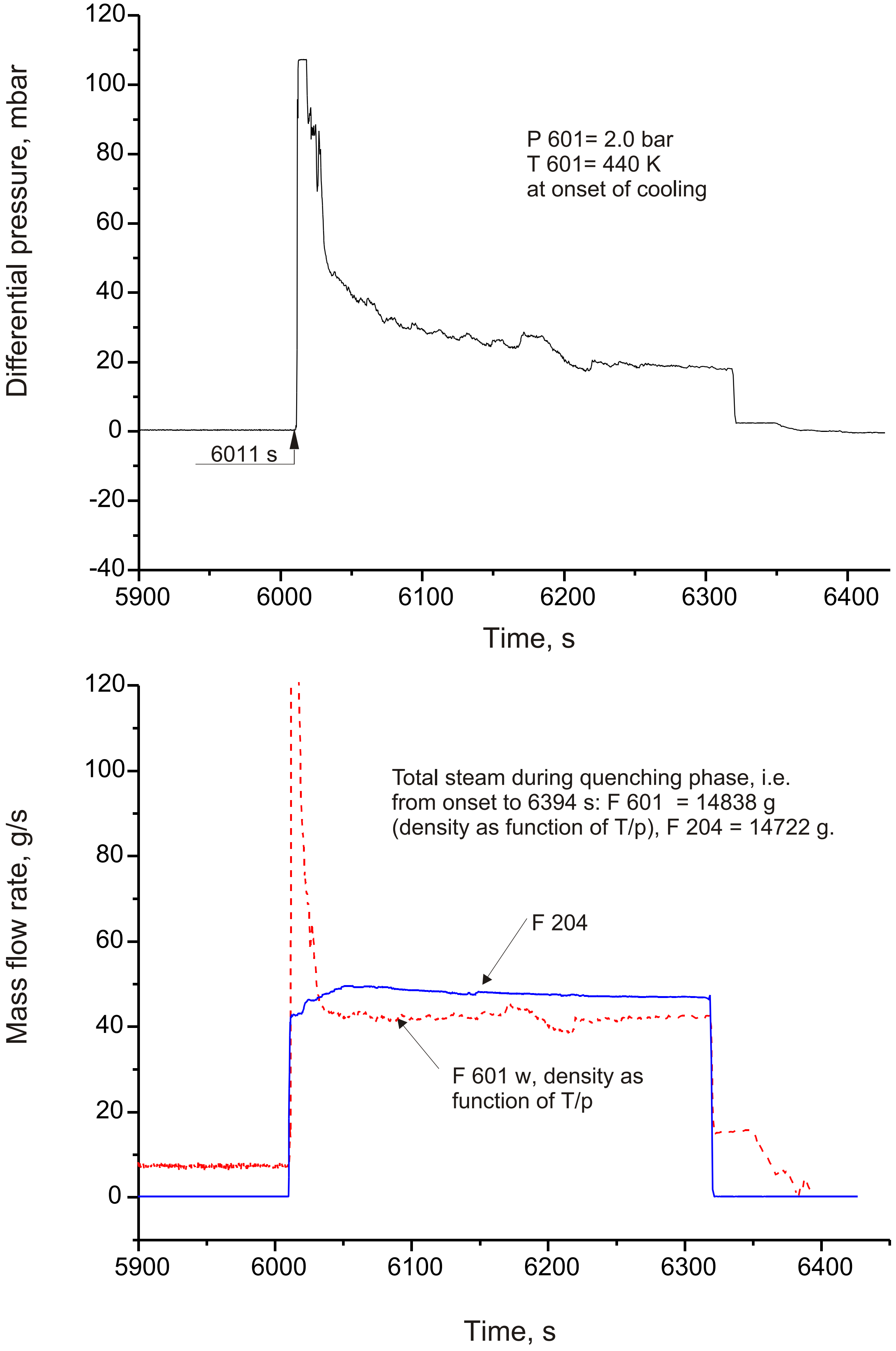

Fig.22: QUENCH-05; Flow measurement in the off-gas pipe F 601, top, and comparison of F 601 with the steam injection flow rate F 204, bottom

Fig.22-QUE05 F601 rho approx.cdr
13.02.02 - IMF

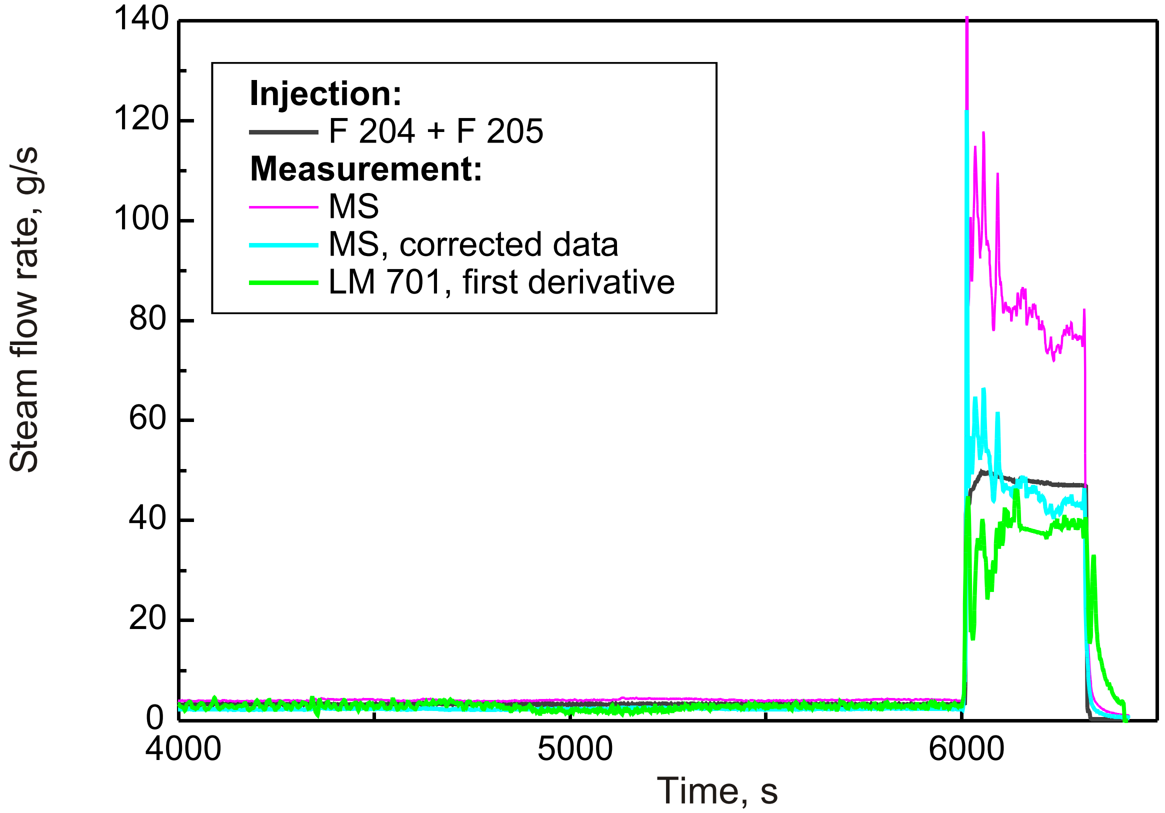

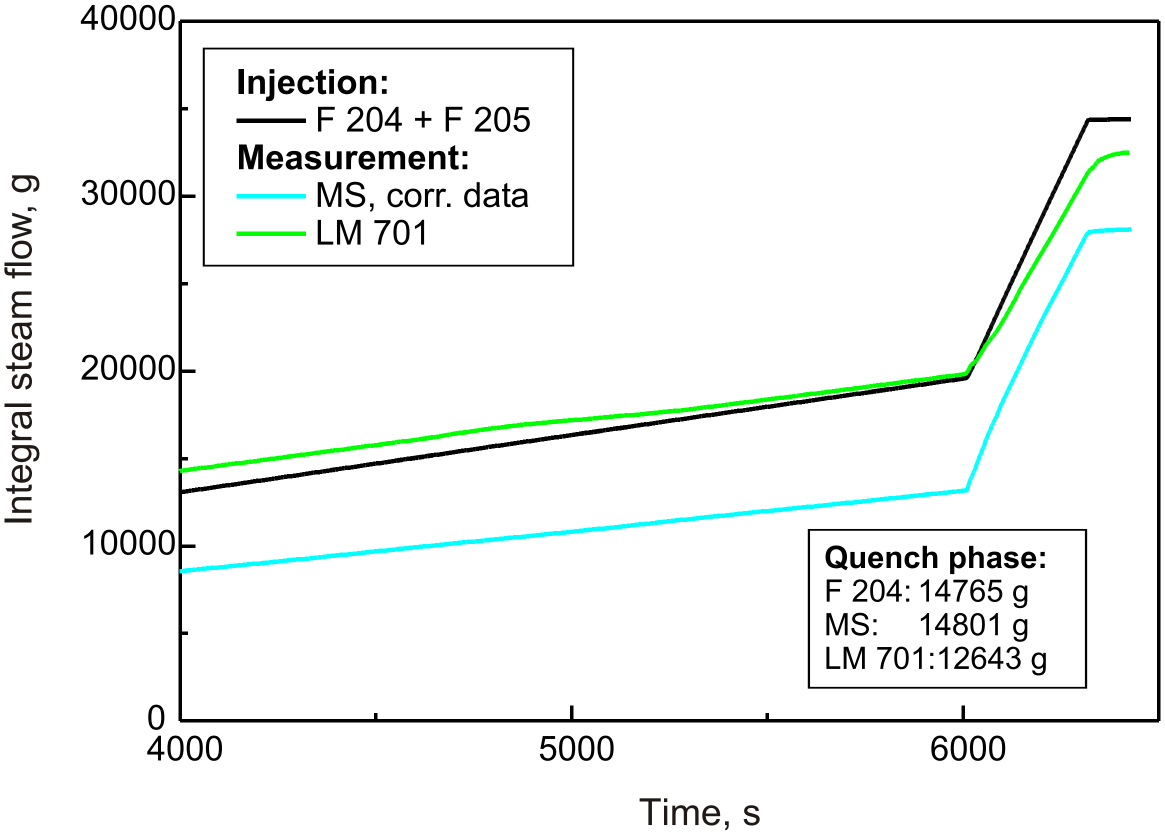

Fig. 23: QUENCH-05; Comparison of cooldown steam input (F 204 + F 205) and steam flow rates measured by the MS, top, and of integral values of F 204 + F 205, MS steam, and LM 701, bottom

Fig. 23 QUE05 MS all G17+12.cdr
11.03.02 - IMF

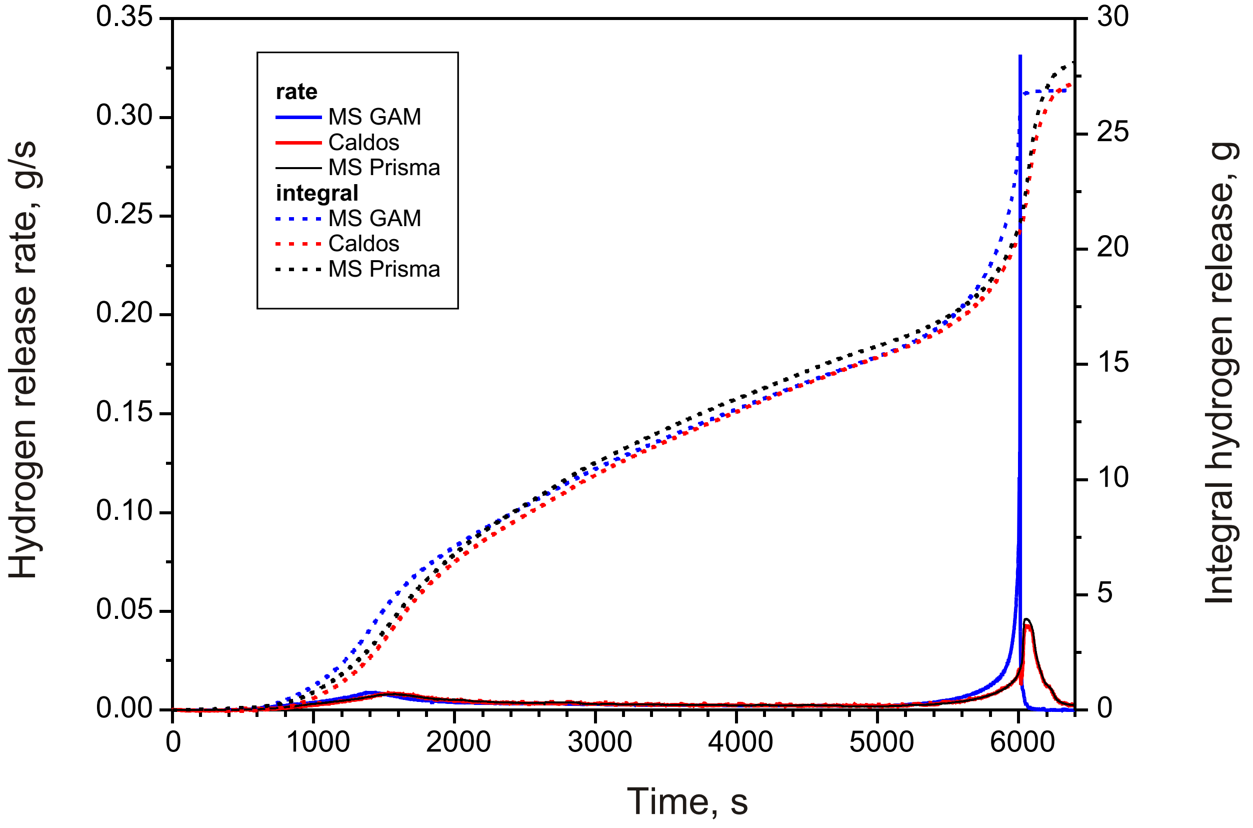

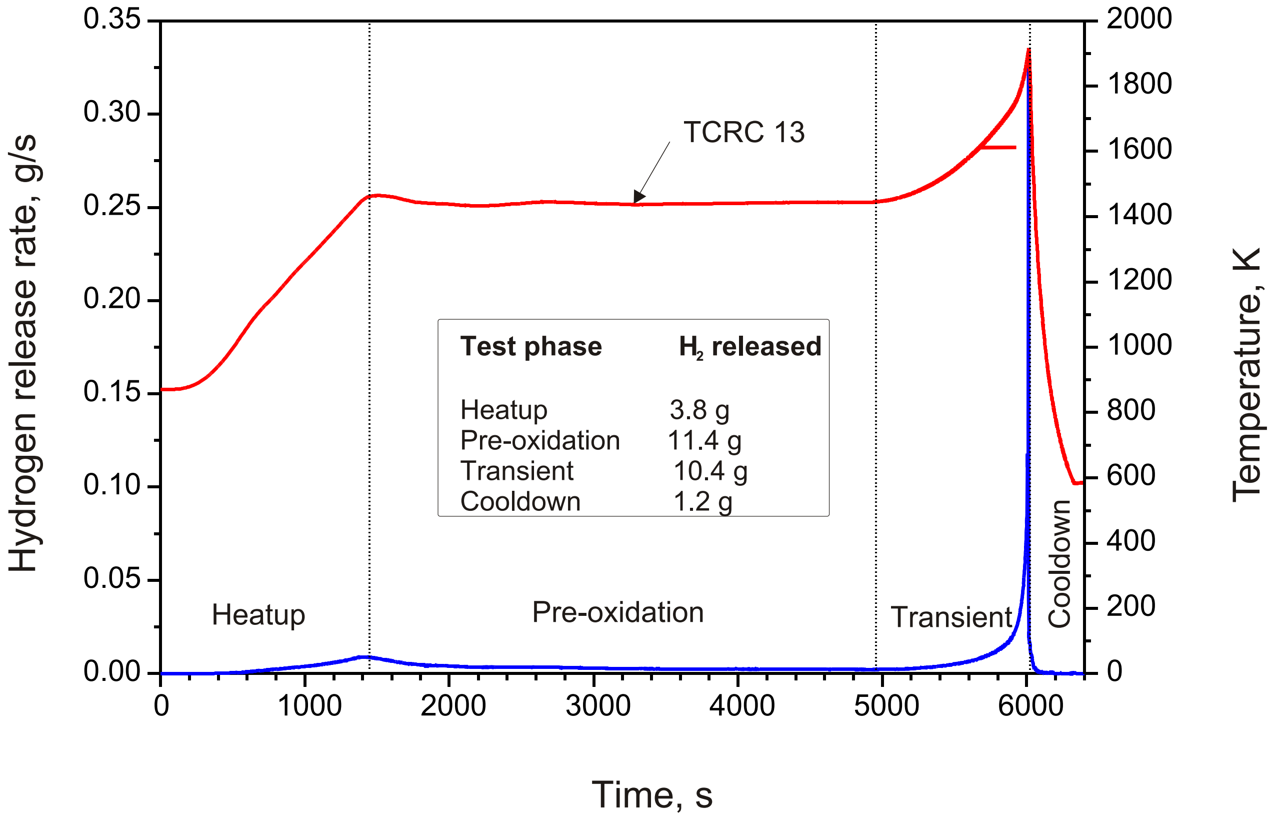

Test phase	H_2 released
Heatup	3.8 g
Pre-oxidation	11.4 g
Transient	10.4 g
Cooldown	1.2 g

Fig.24: QUENCH-05; Hydrogen release measured by MS and Caldos, top, and comparison of hydrogen release measured by MS with the TCRC 13 temperature history, bottom

Fig.24-QUE05 MS&Caldos.cdr
13.02.02 - IMF

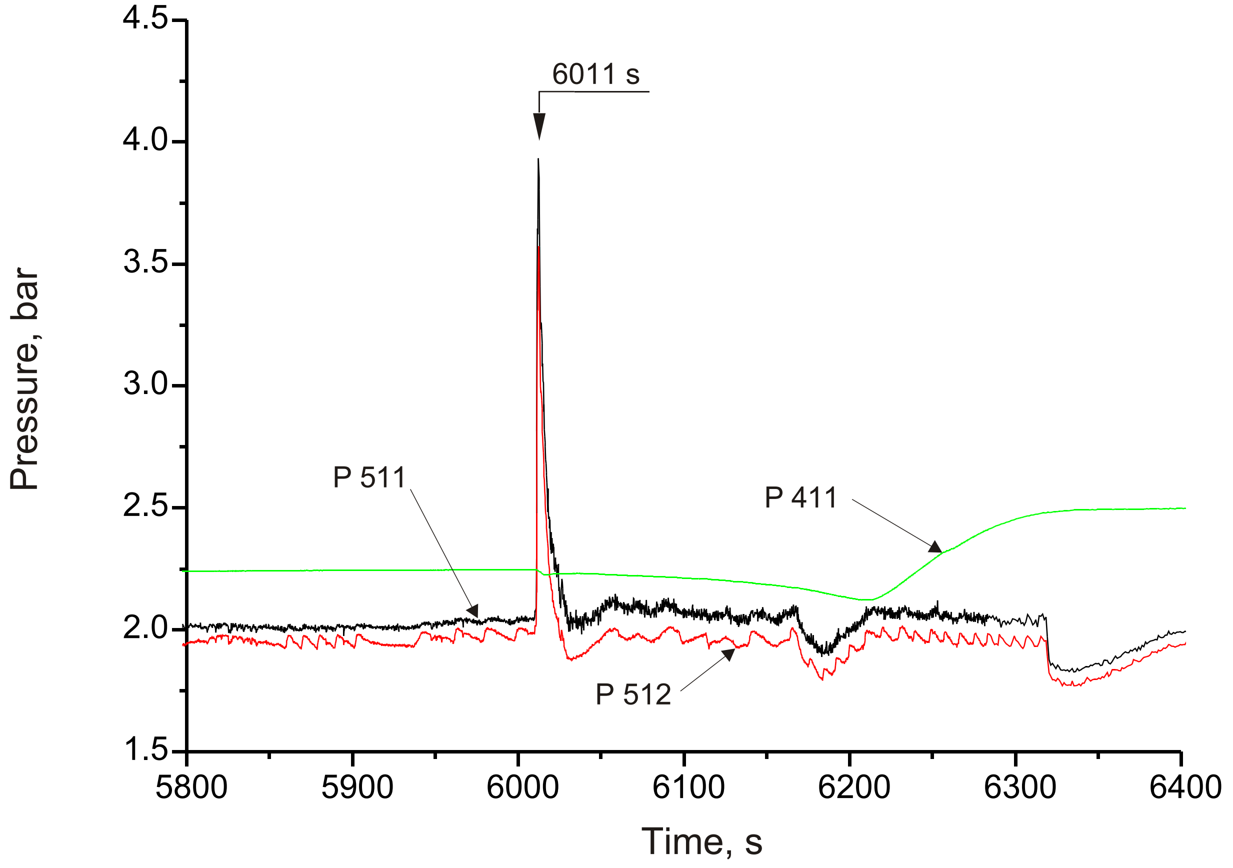

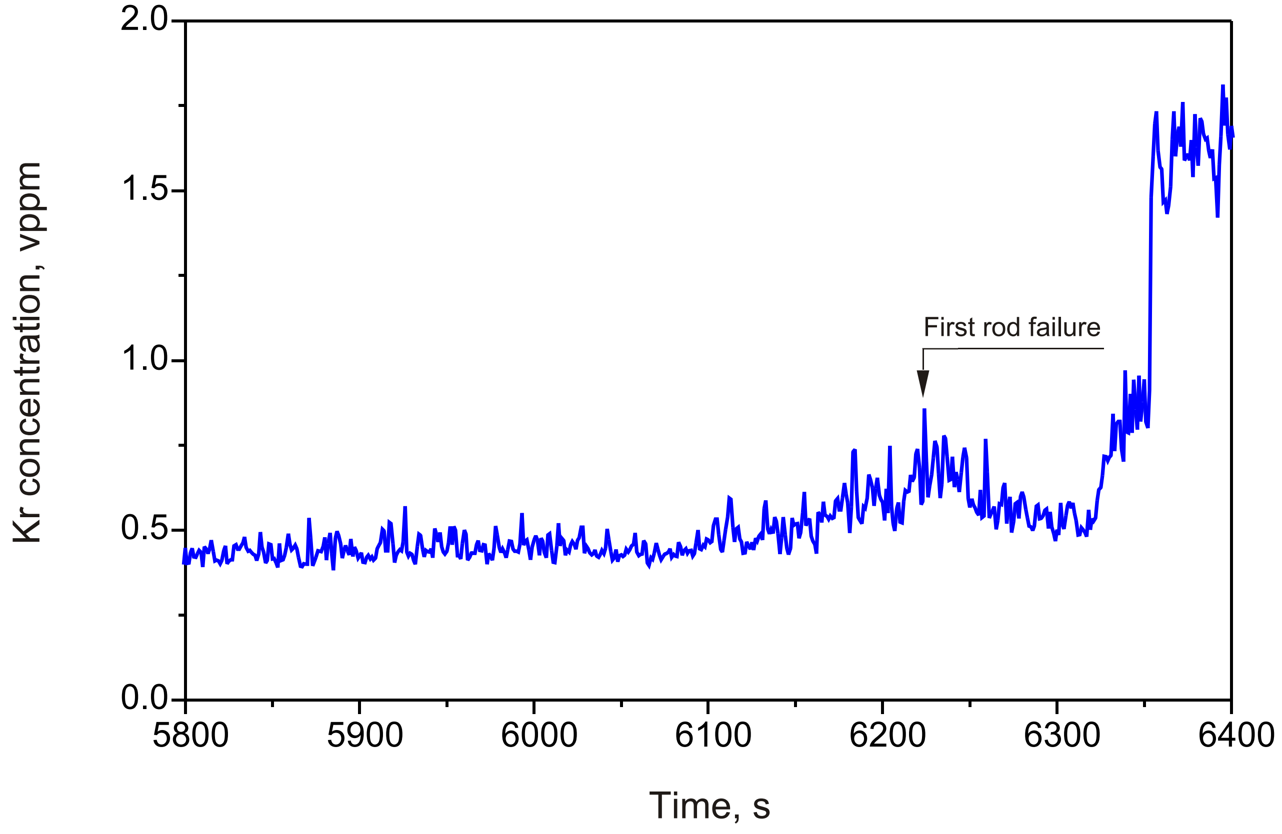

Fig.25: QUENCH-05; System pressure P 511 at the test section inlet, P 512 at the test section outlet, P 411 rod internal pressure, top, and krypton concentration in the off-gas measured by the mass spectrometer, bottom

Fig.25-QUE05 P511+512+411+krypton.cdr
11.03.02 - IMF

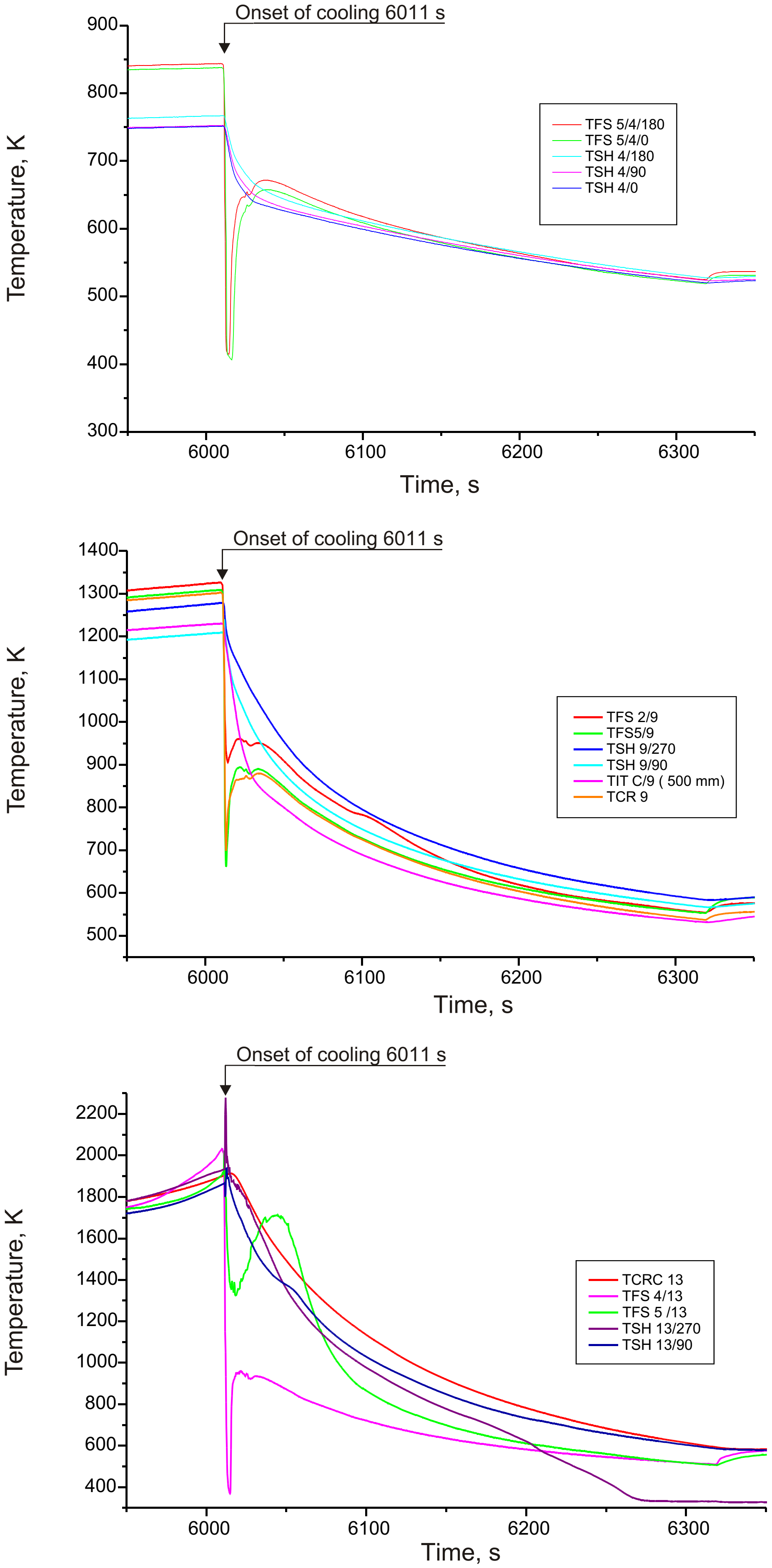

Fig.26: QUENCH-05; Typical temperature response of the TFS, TCR, TCRC, TIT, and TSH thermocouples during cooldown with steam at three different levels (50, 550, and 950 mm)

Fig.26-QUE05 Temperature response.cdr
22.01.02 - IMF

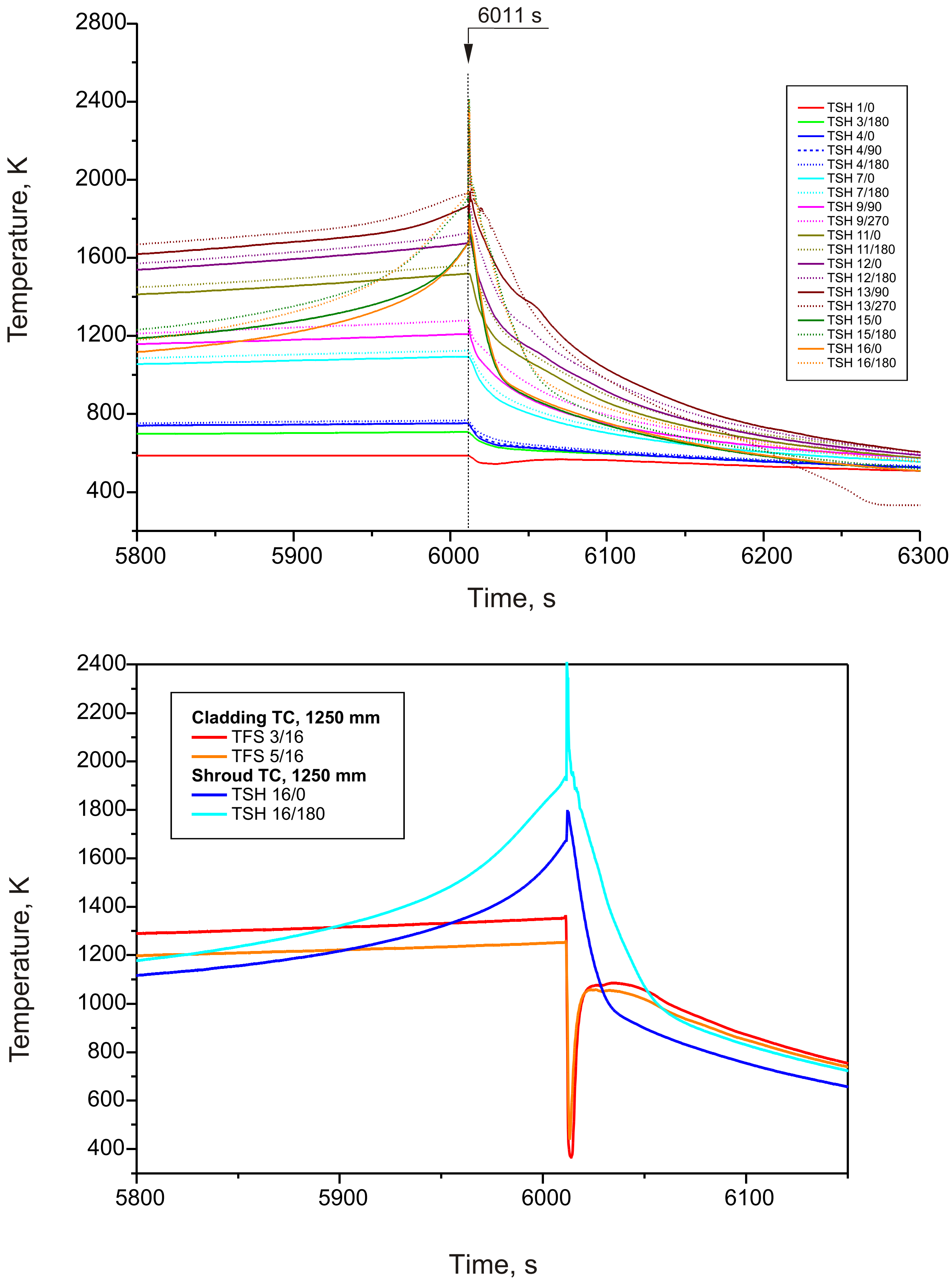

Fig. 27: QUENCH-05; Temperature response of the shroud thermocouples during cooldown with steam, top, and excursion of the shroud temperatures at the 1250 mm elevation, bottom

Fig.27-QUE05 alleTSH.cdr
28.01.02 - IMF

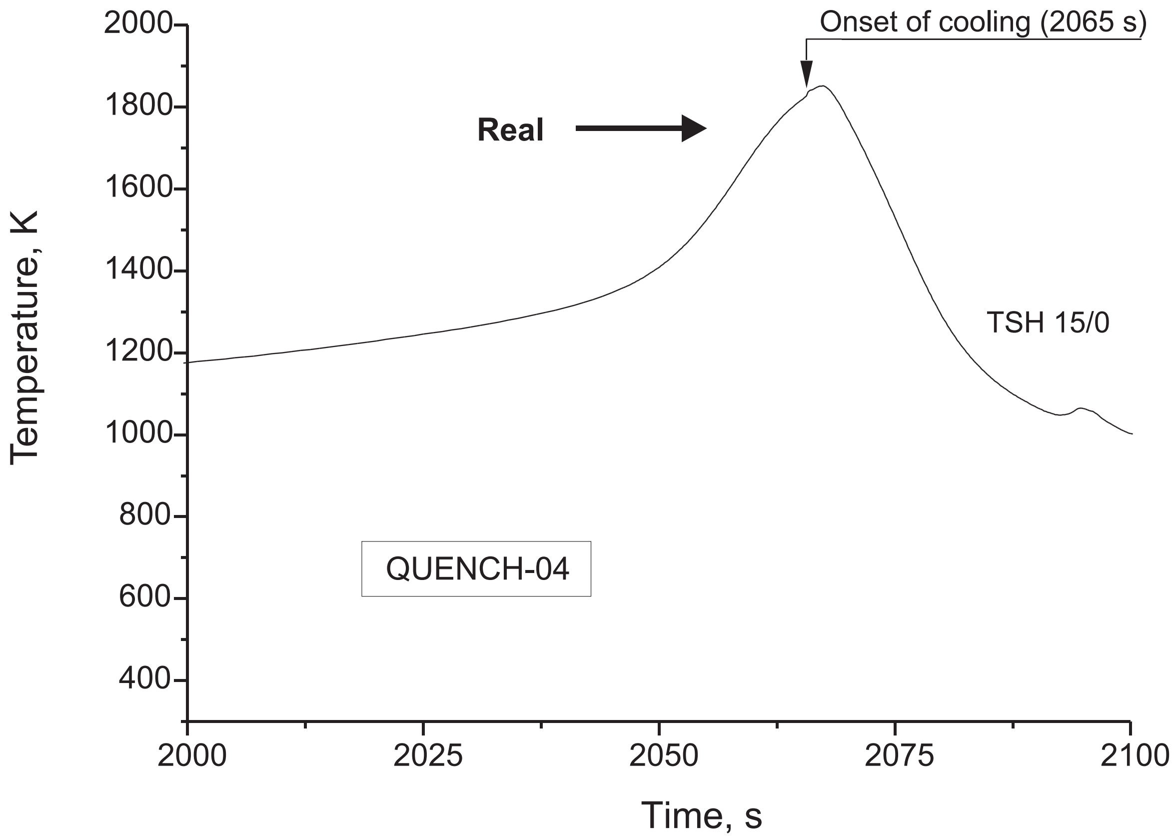

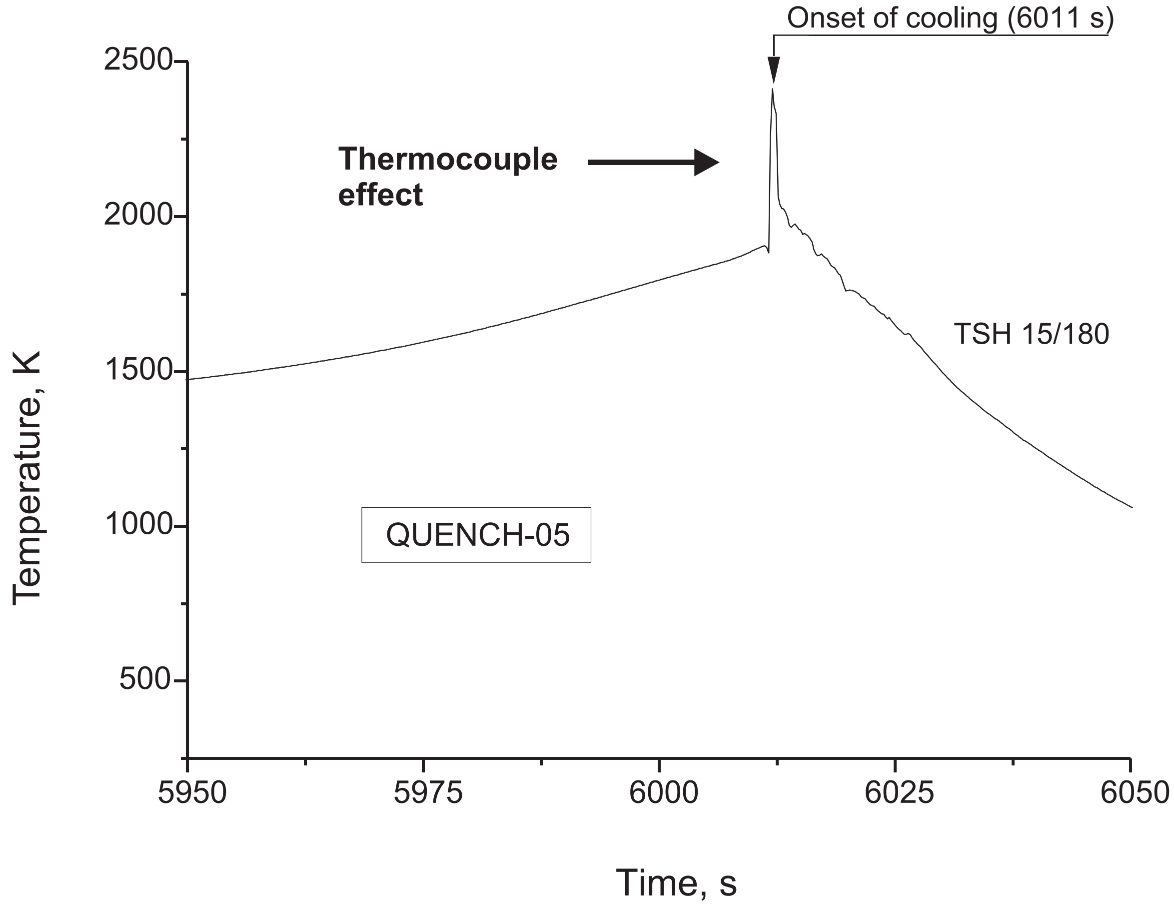

Fig.28: Temperature excursions of the shroud during the QUENCH-04 and QUENCH-05 experiments

Fig.28-QUE04+05 ebe15 shroud.cdr
17.04.02 - IMF

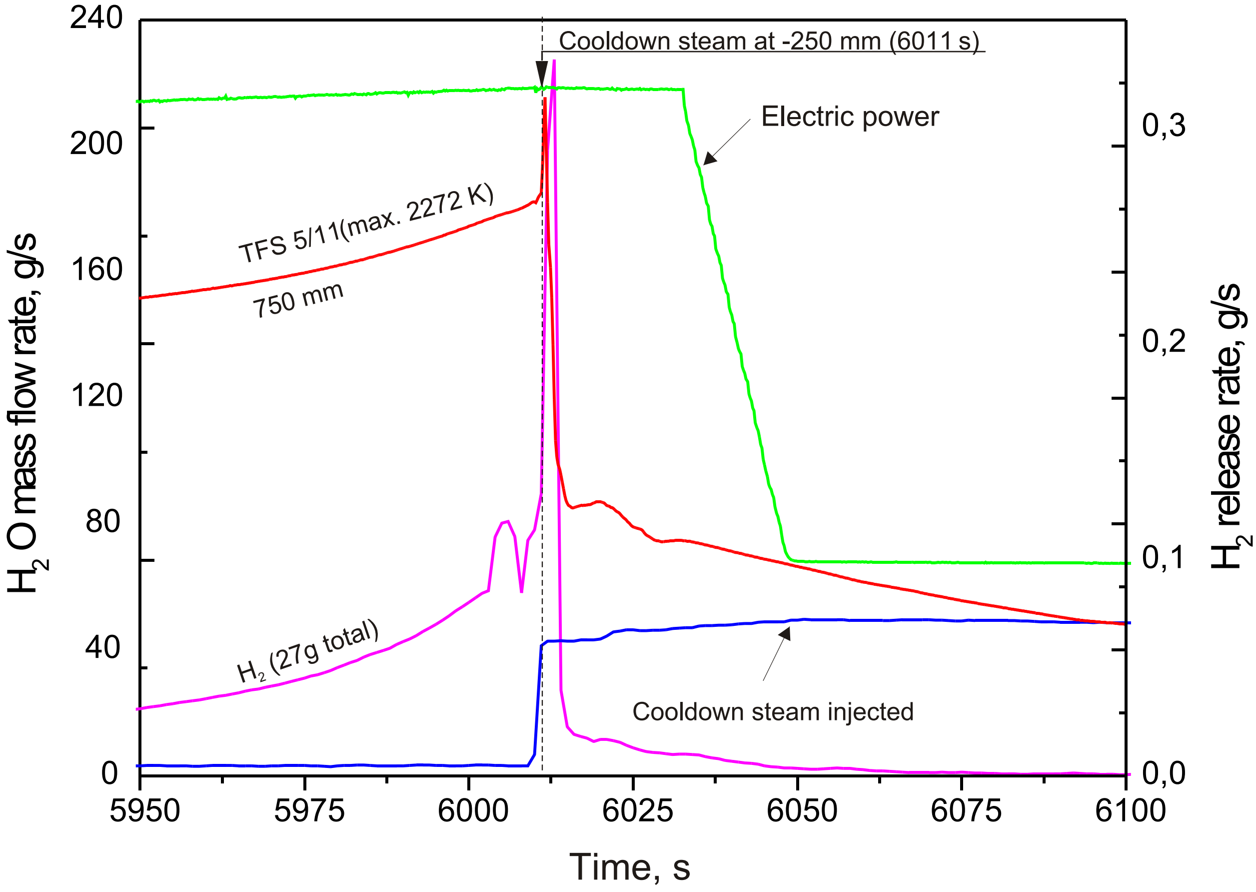

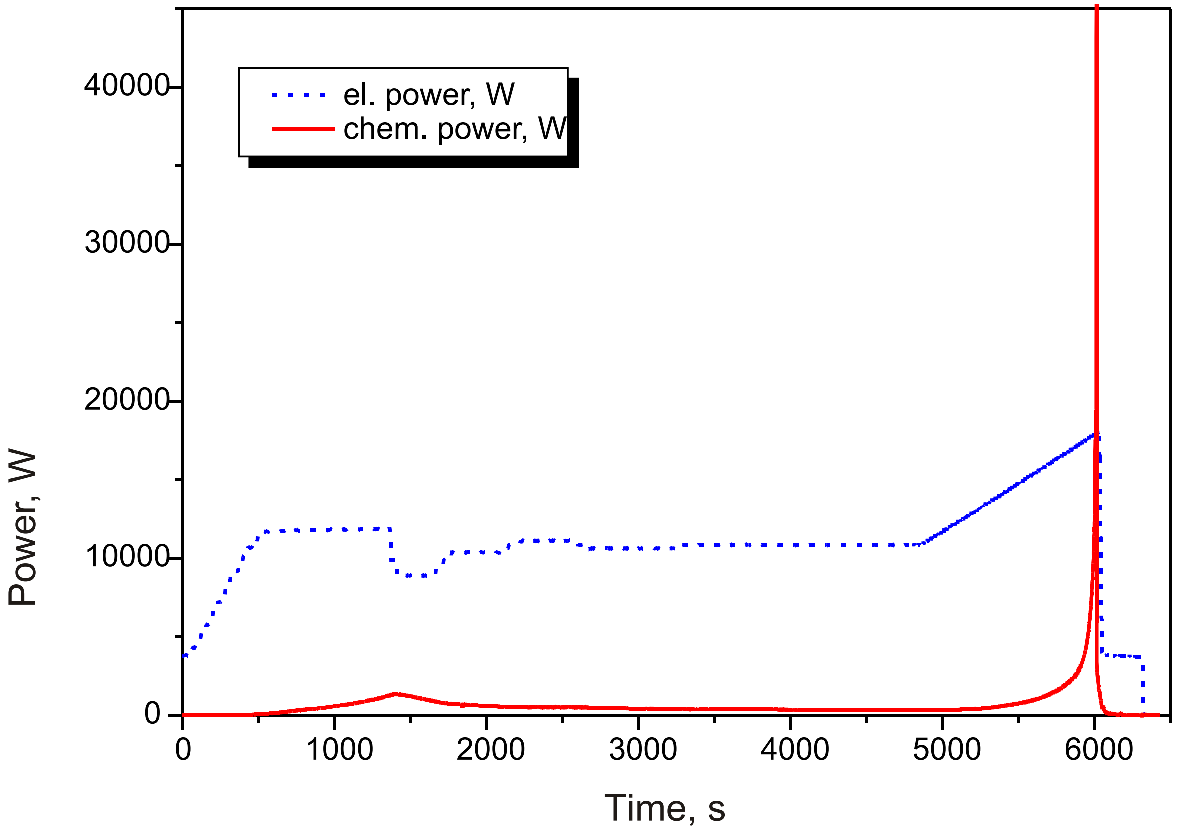

Fig. 29: QUENCH-05; Synopsis of the electric bundle power input, characteristic bundle temperature, cooldown steam flow, and of the hydrogen release rate measured by the mass spectrometer, top, and chemical power (produced by the exothermal Zircaloy-steam reaction) together with the electric power, bottom

Fig.29-QUE05 Zeitbezug.cdr
13.02.02 - IMF

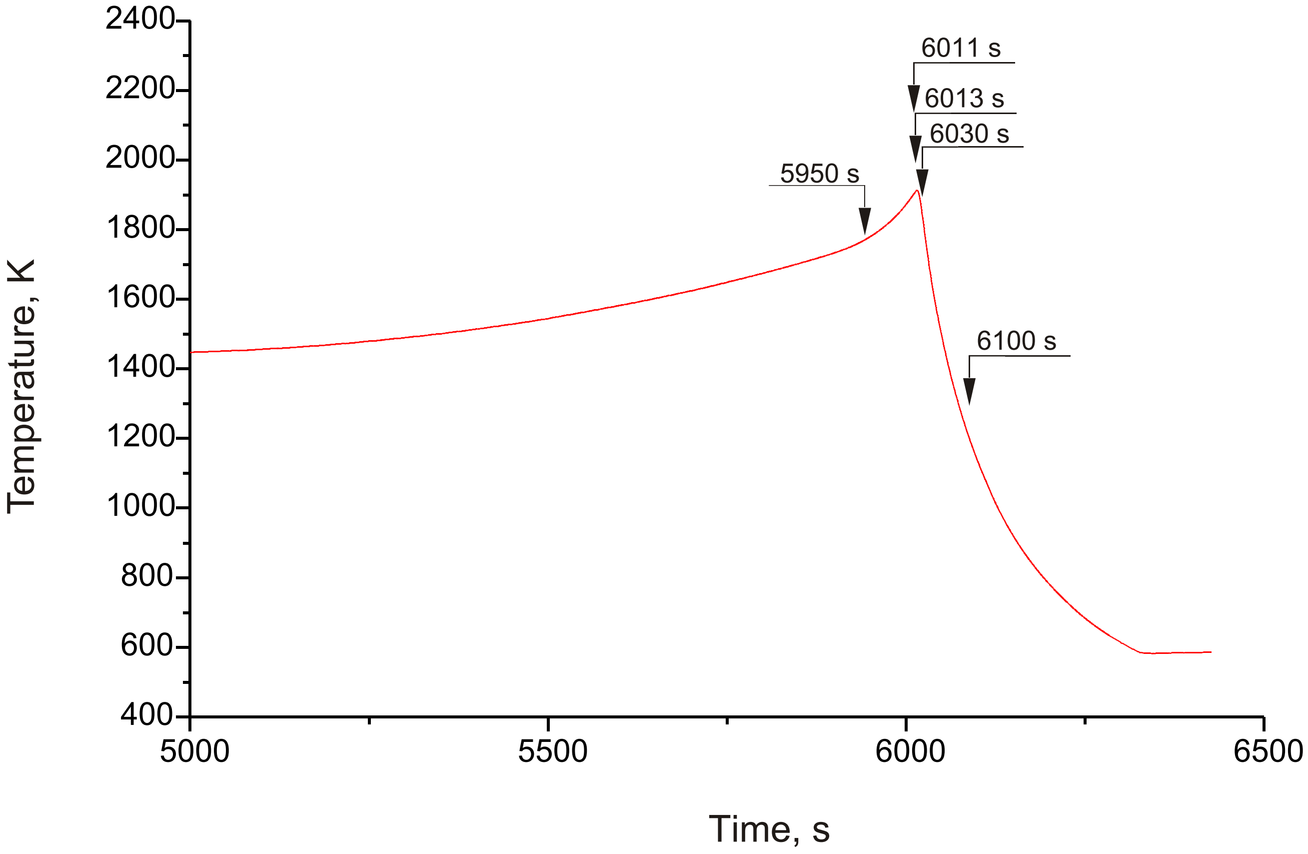

Fig.30: QUENCH-05; Selected times for the axial temperature profiles

Fig 30-QUE05 TCRC 13 Time.cdr
13.02.02 - IMF

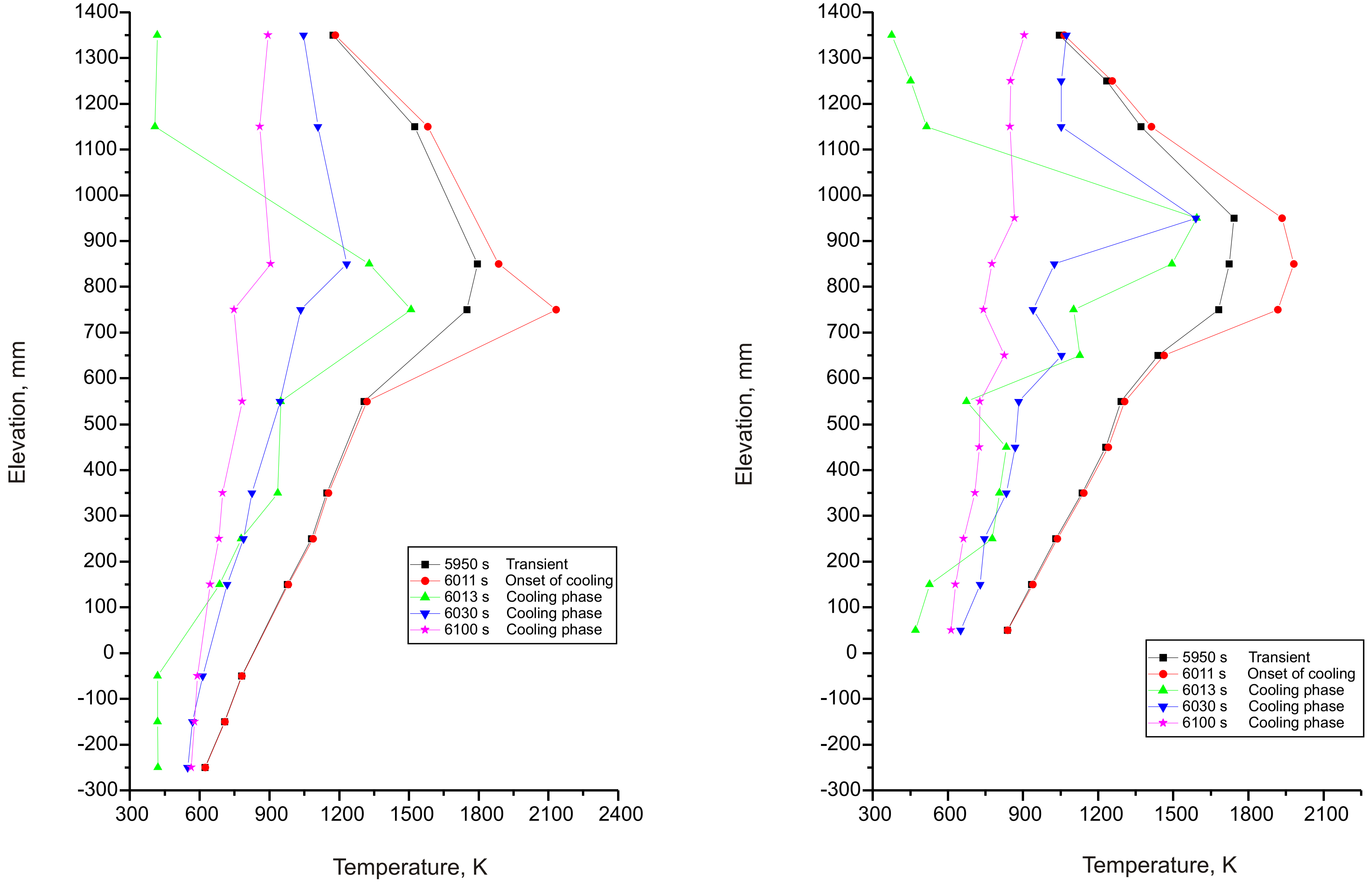

Fig. 31: QUENCH-05; Axial temperature profile TFS 2 , left, and TFS 5, right, at 5950 s, 6011 s, 6030 s, 6100s

Fig 31-QUE05 Axial TFS2+TFS5.cdr
24.01.02 - IMF

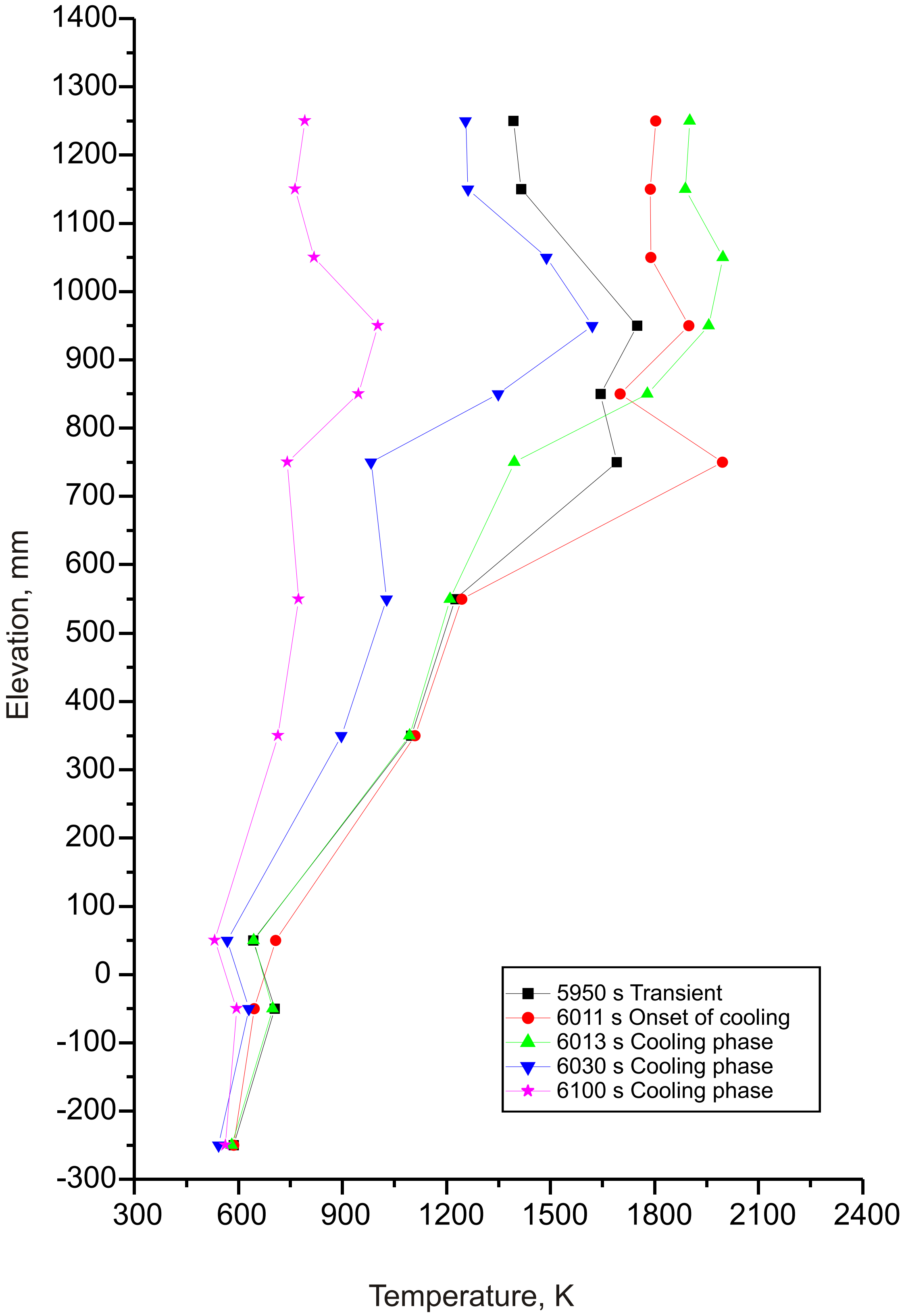

Fig.32: QUENCH-05; Axial profile of the shroud temperature at 5950 s, 6011 s, 6013 s, 6030 s, 6100 s

Fig 32-QUE05 Axial TSH.cdr
11.03.02 - IMF

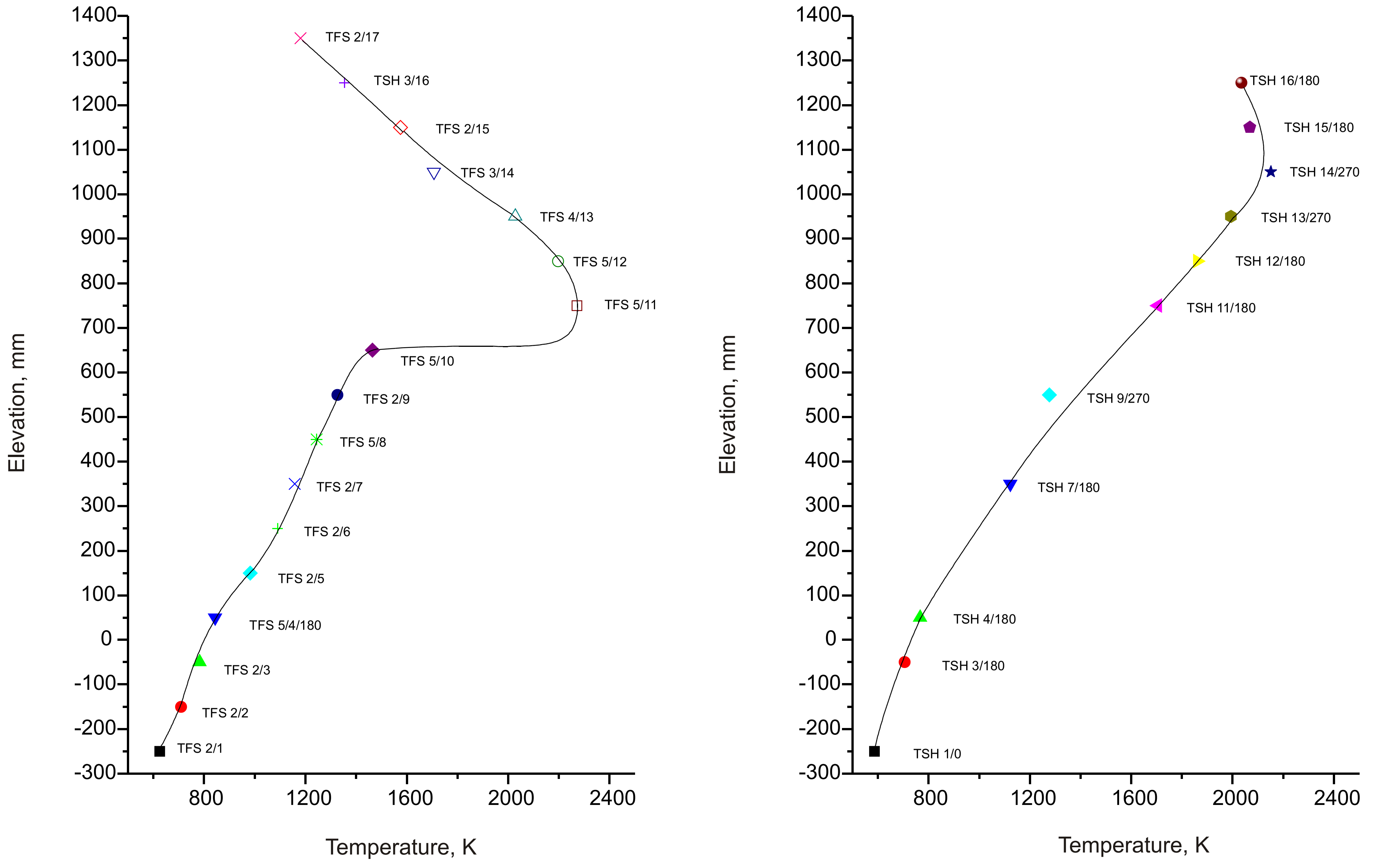

Fig. 33: QUENCH-05; Maximum rod cladding, left, and shroud temperature, right, of each elevation

Fig 33-QUE05 maxT-TSH.cdr
24.01.02 - IMF

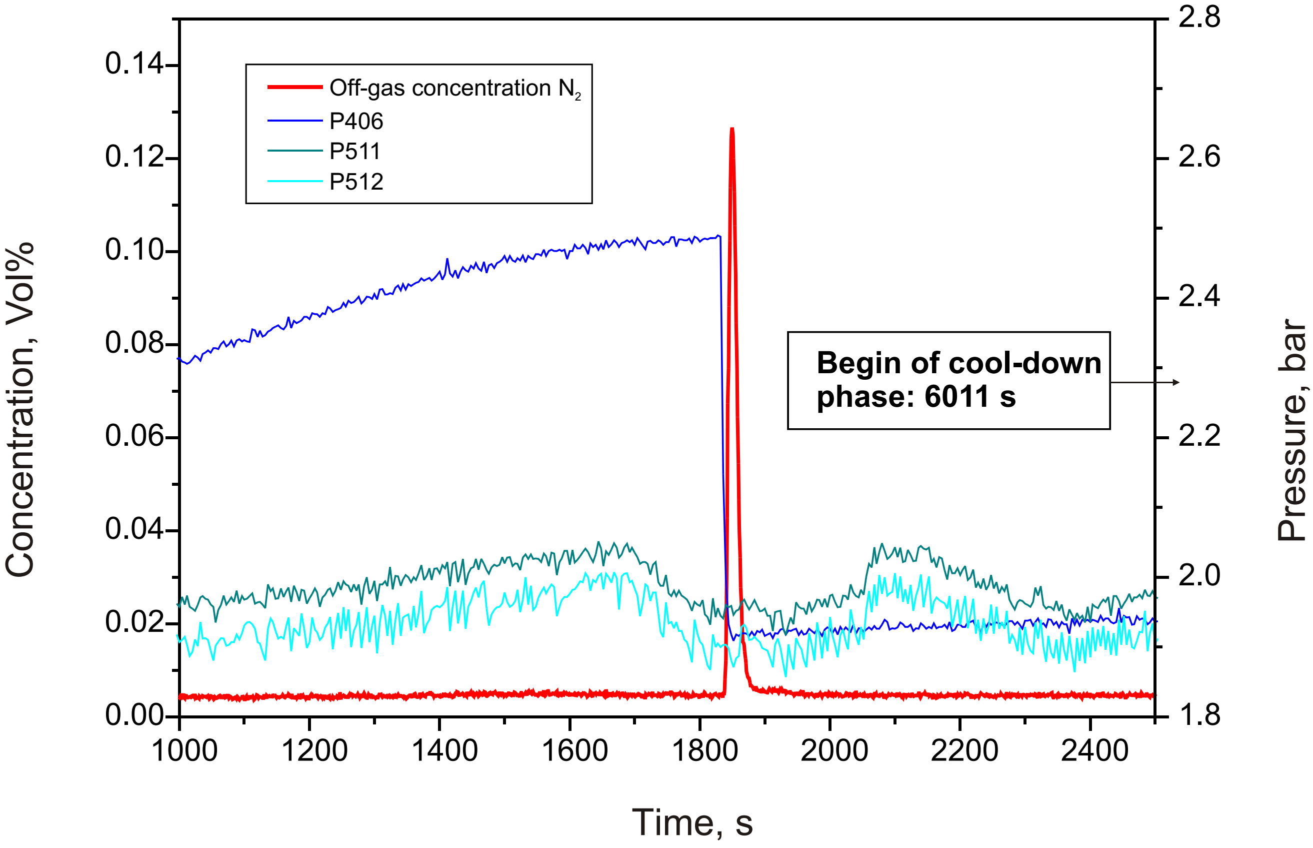

Fig.34: QUENCH-05; Shroud failure during the pre-oxidation phase (1837 s) as indicated by the pressure P 406 measured in the space between shroud and inner cooling jacket and by the nitrogen concentration measured in the off-gas by the mass spectrometer

Fig 34-QUE05 shroud failure.cdr
14.02.02 - IMF

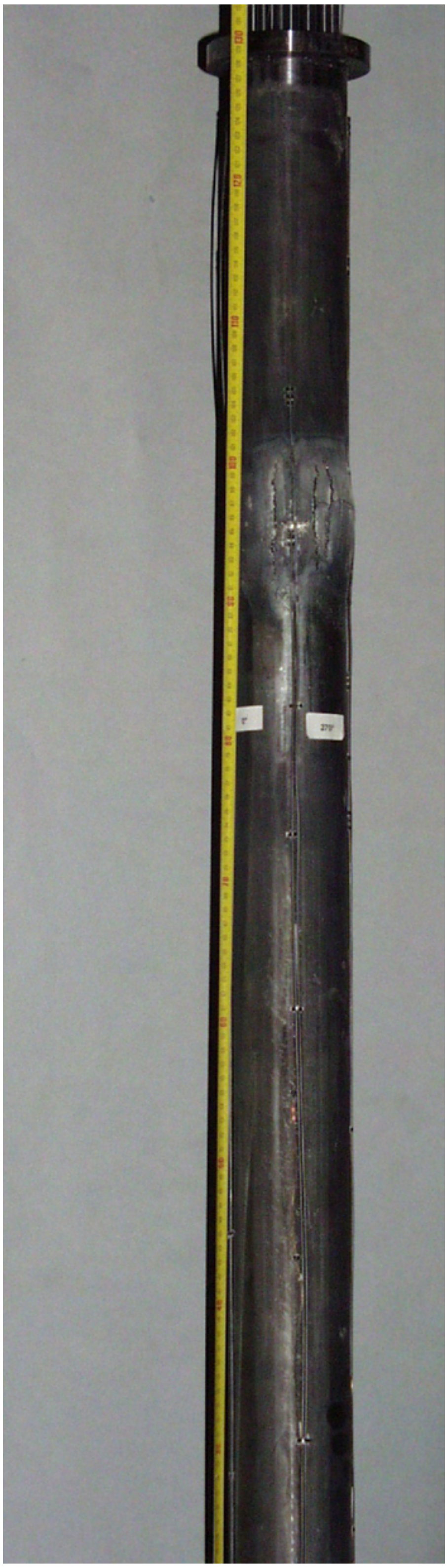

Fig.35: QUENCH-05; Posttest appearance of the shroud

Fig 35-QUE05 Posttest f.cdr
28.01.02 - IMF

Fig. 36: QUENCH-05; Posttest appearance of the shroud at the upper end of the heated zone, 180° orientation

Fig 36-QUE05 Posttest e.cdr
14.02.02 - IMF

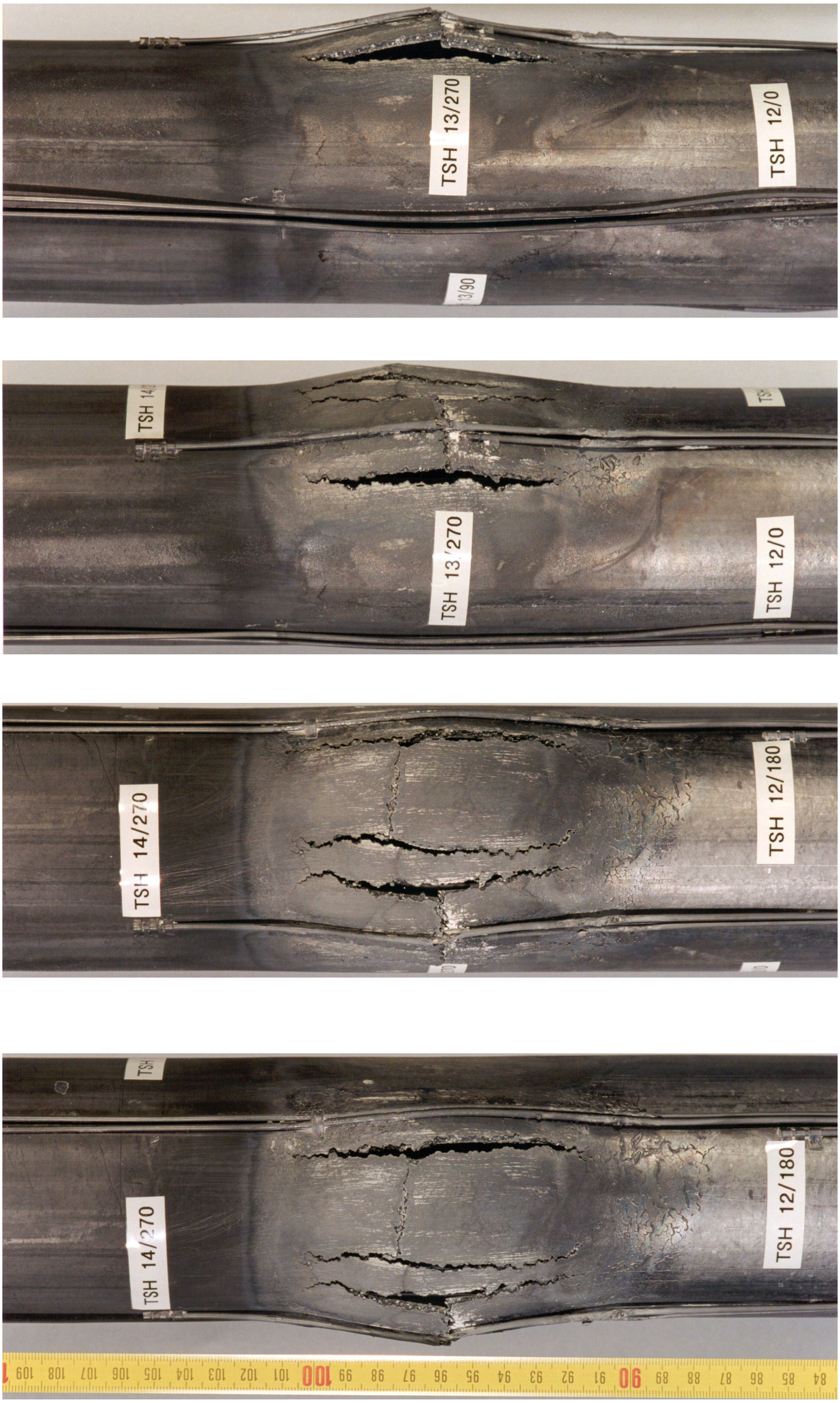

Fig. 37: QUENCH-05; Posttest appearance of the shroud at different orientations

Fig 37-QUE05 Posttest 1.cdr
11.03.02 - IMF

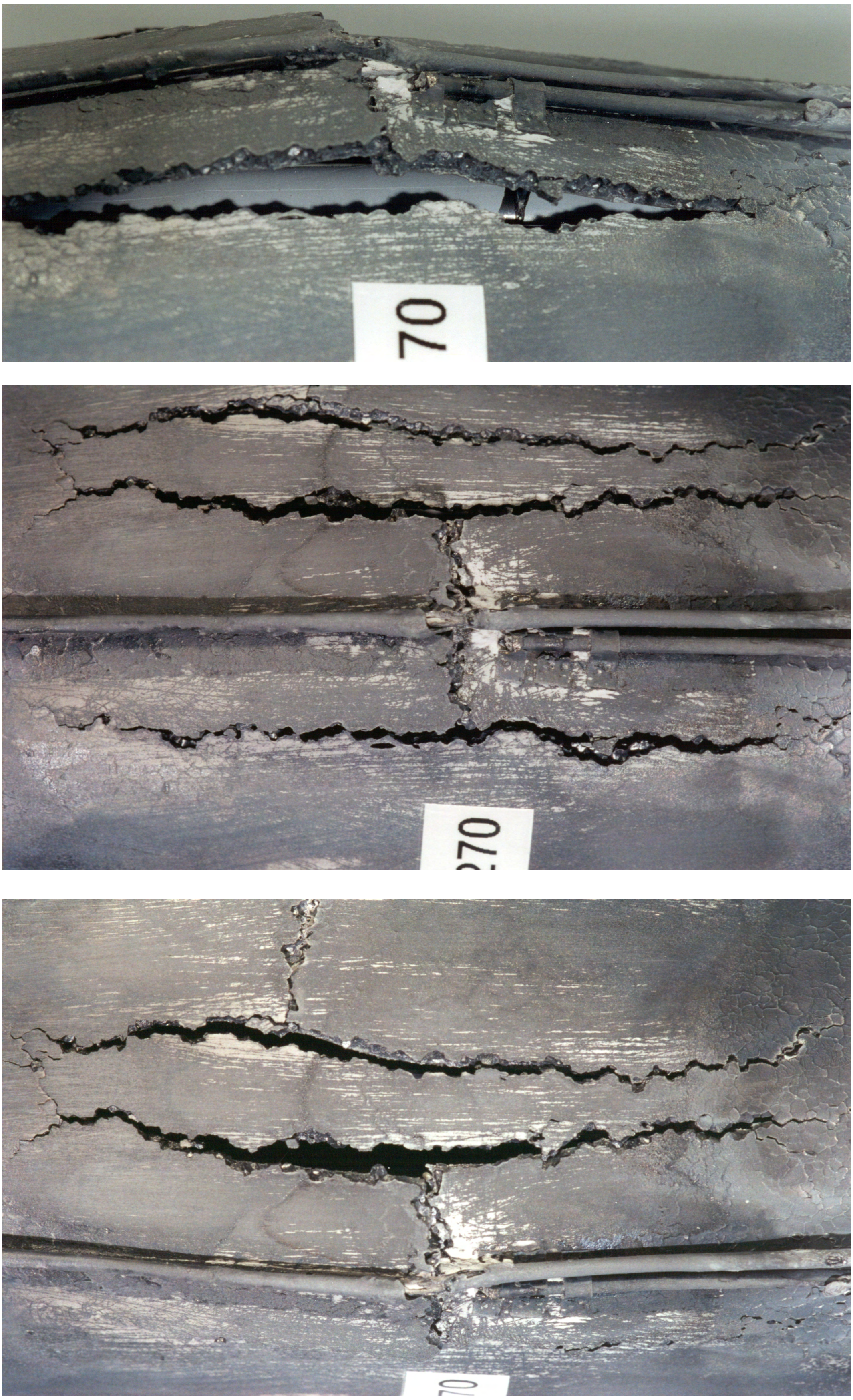

Fig.38: QUENCH-05; Posttest appearance of the shroud, fissures in detail

Fig 38-QUE05 Posttest 2.cdr
11.03.02 - IMF

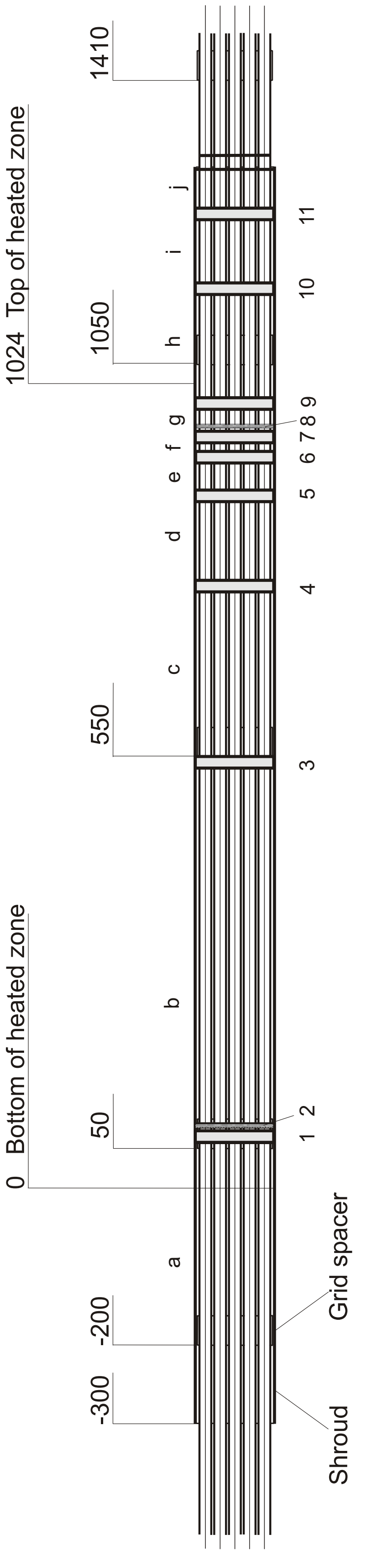

Fig.39: QUENCH-05; Sectioning of test bundle

Fig 39-QUE05 Schnittplan.cdr
30.01.02 - IMF

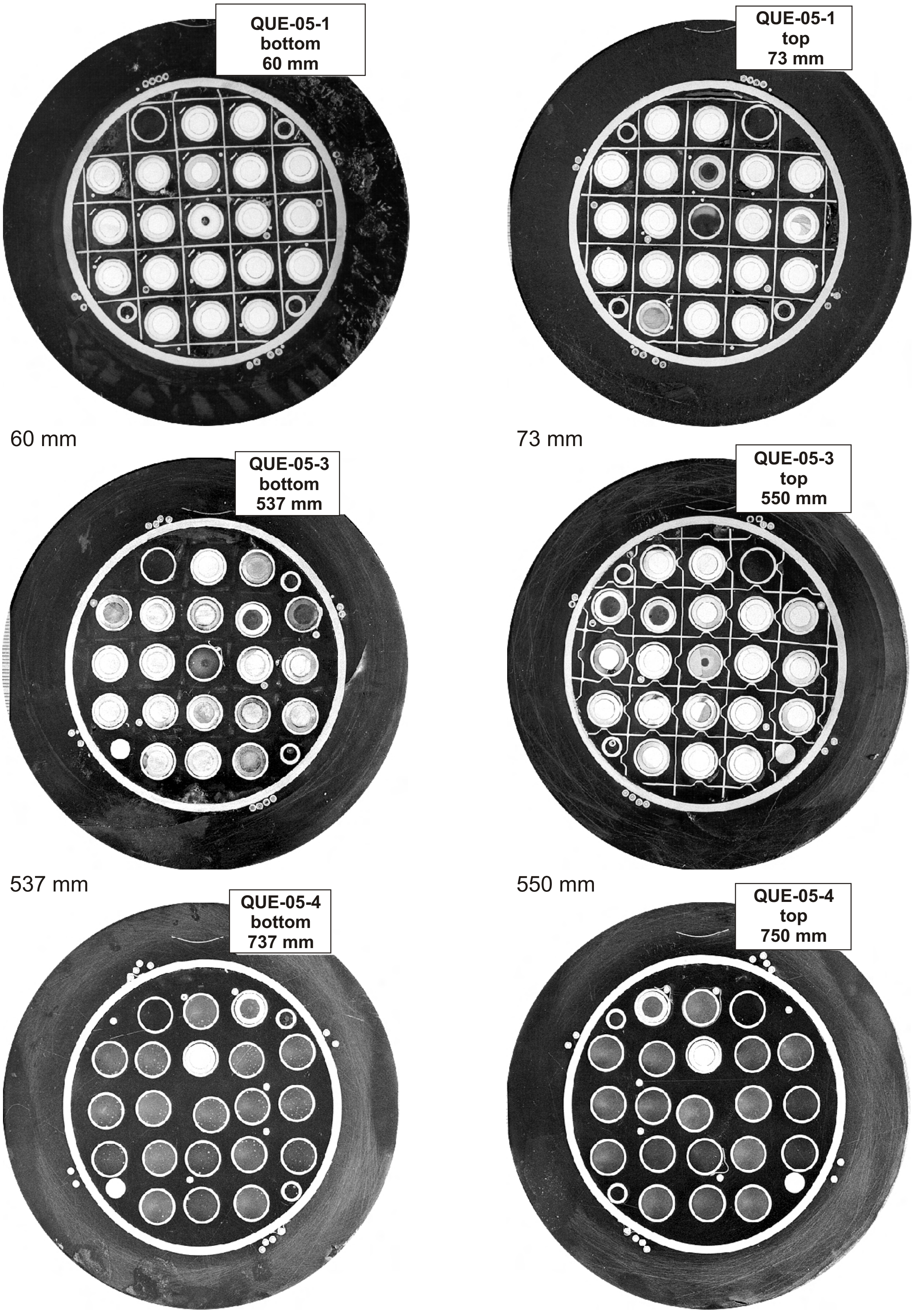

60 mm

73 mm

537 mm

550 mm

737 mm

750 mm

Fig. 40: QUENCH-05; Cross sections at 60 - 750 mm elevation

Fig 40-QUE05 cross section1.cdr
14.02.02 - IMF

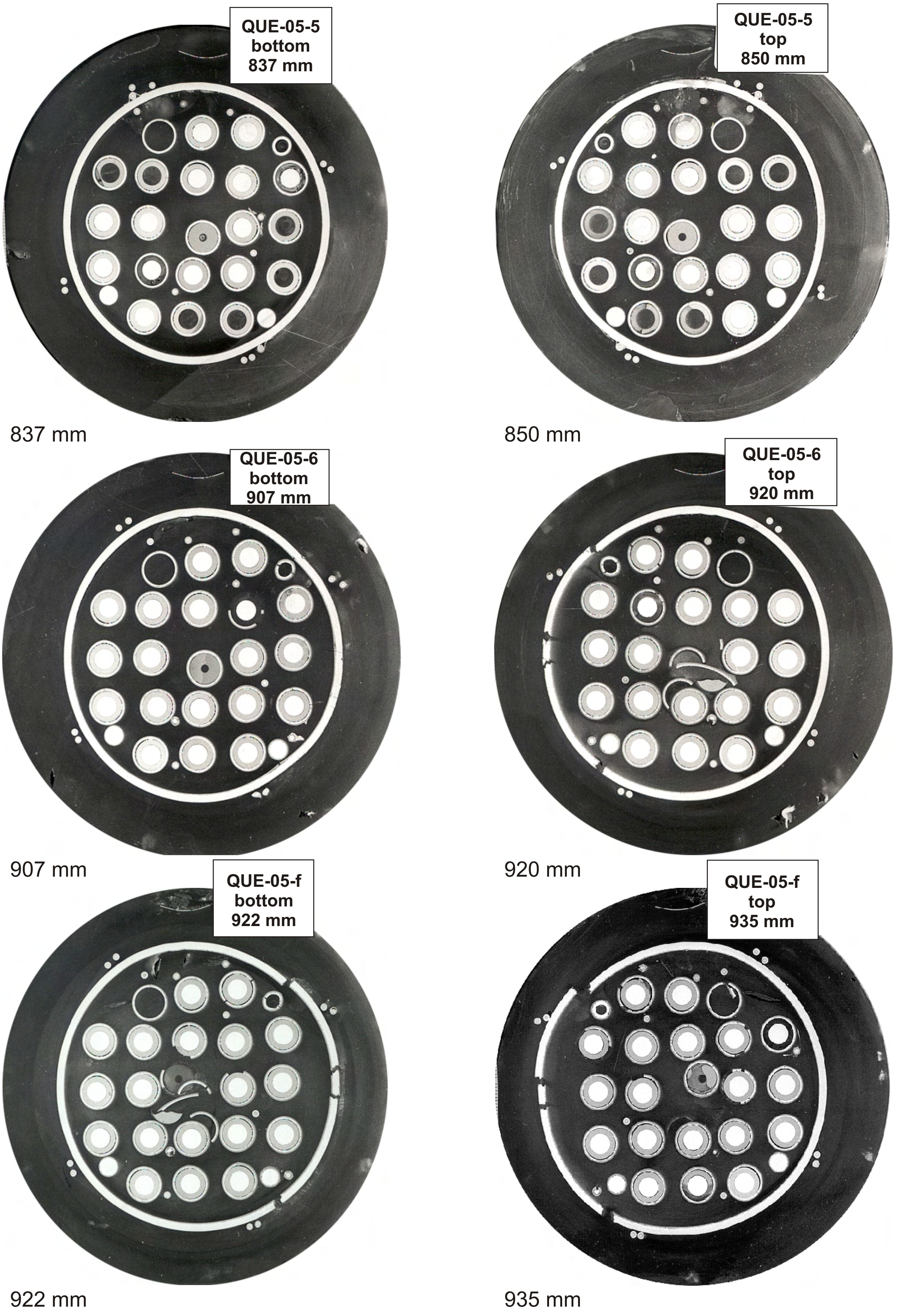

837 mm

850 mm

907 mm

920 mm

922 mm

935 mm

Fig. 41: QUENCH-05; Cross sections at 837 - 935 mm elevation

Fig 41-QUE05 cross section2.cdr
14.02.02 - IMF

937 mm

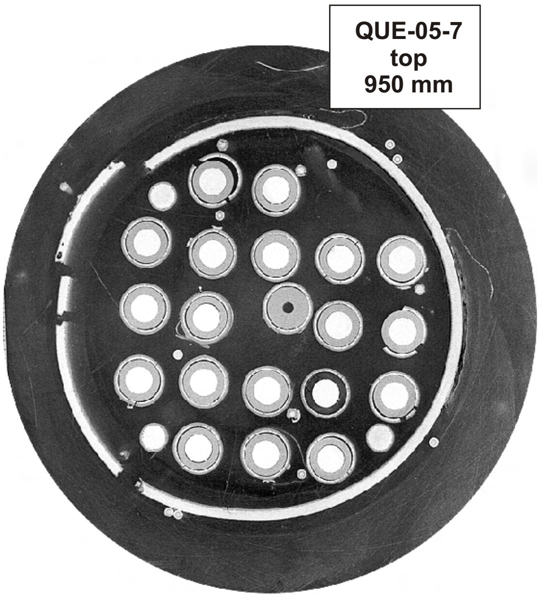

950 mm

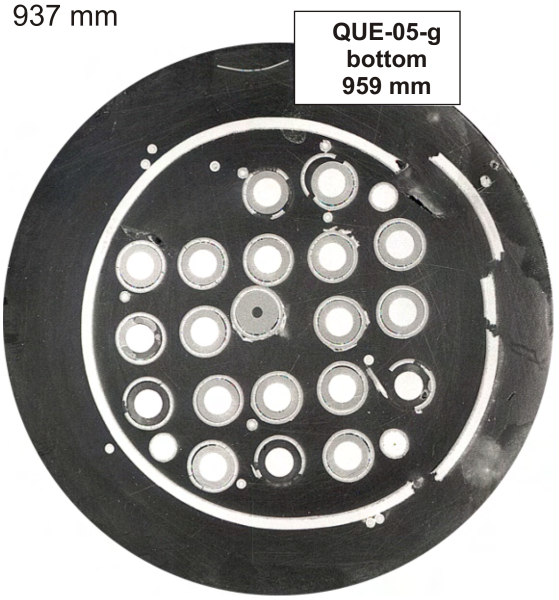

959 mm

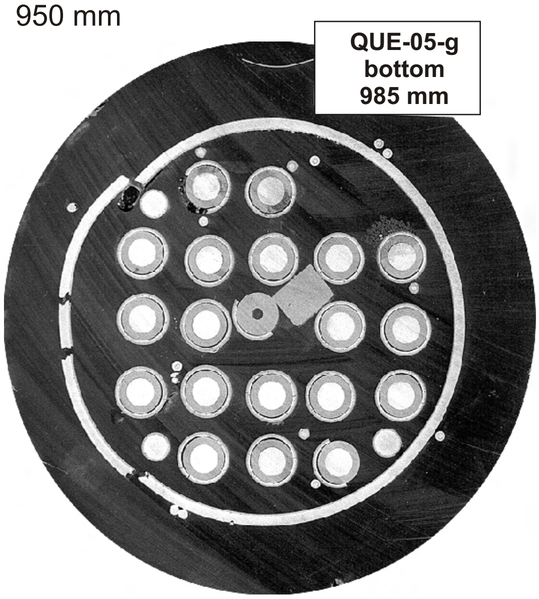

985 mm

987 mm

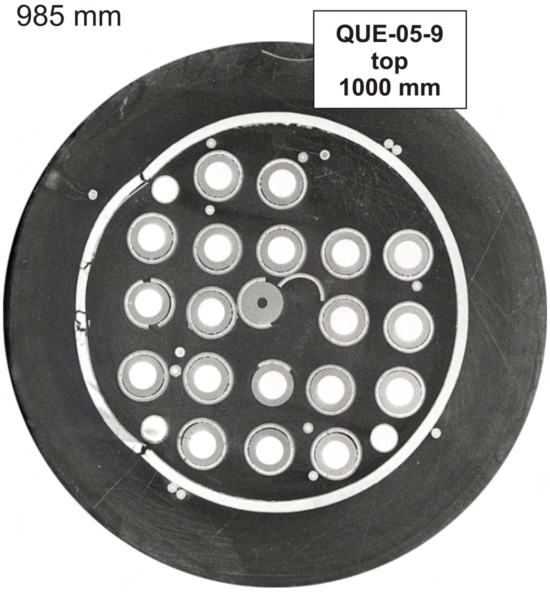

1000 mm

Fig. 42: QUENCH-05; Cross sections at 937 - 1000 mm elevation

Fig 42-QUE05 cross section3.cdr
14.02.02 - IMF

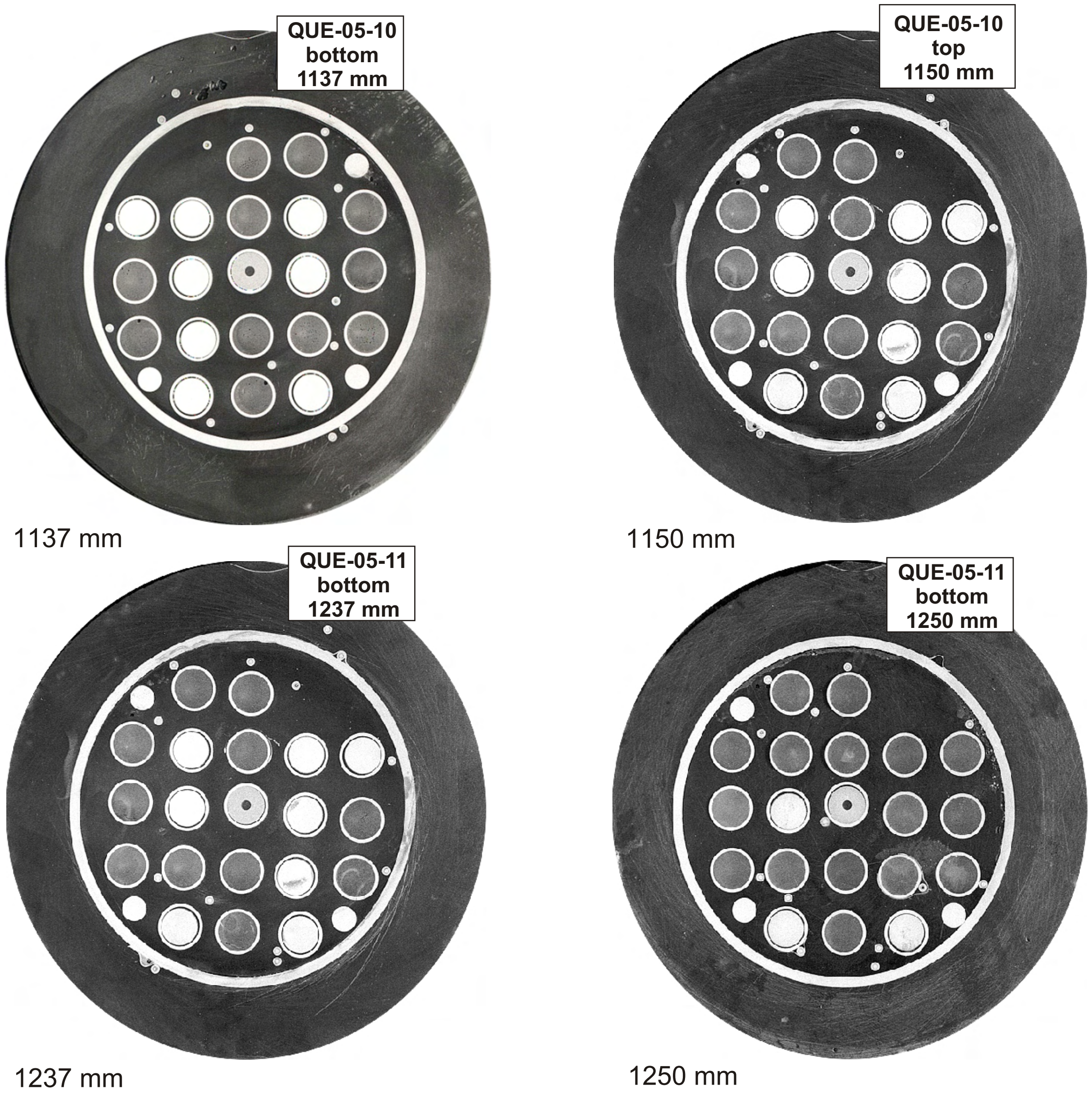

1137 mm

1150 mm

1237 mm

1250 mm

Fig. 43: QUENCH-05; Cross sections at 1137 - 1250 mm elevation

Fig 43-QUE05 cross section4.cdr
14.02.02 - IMF

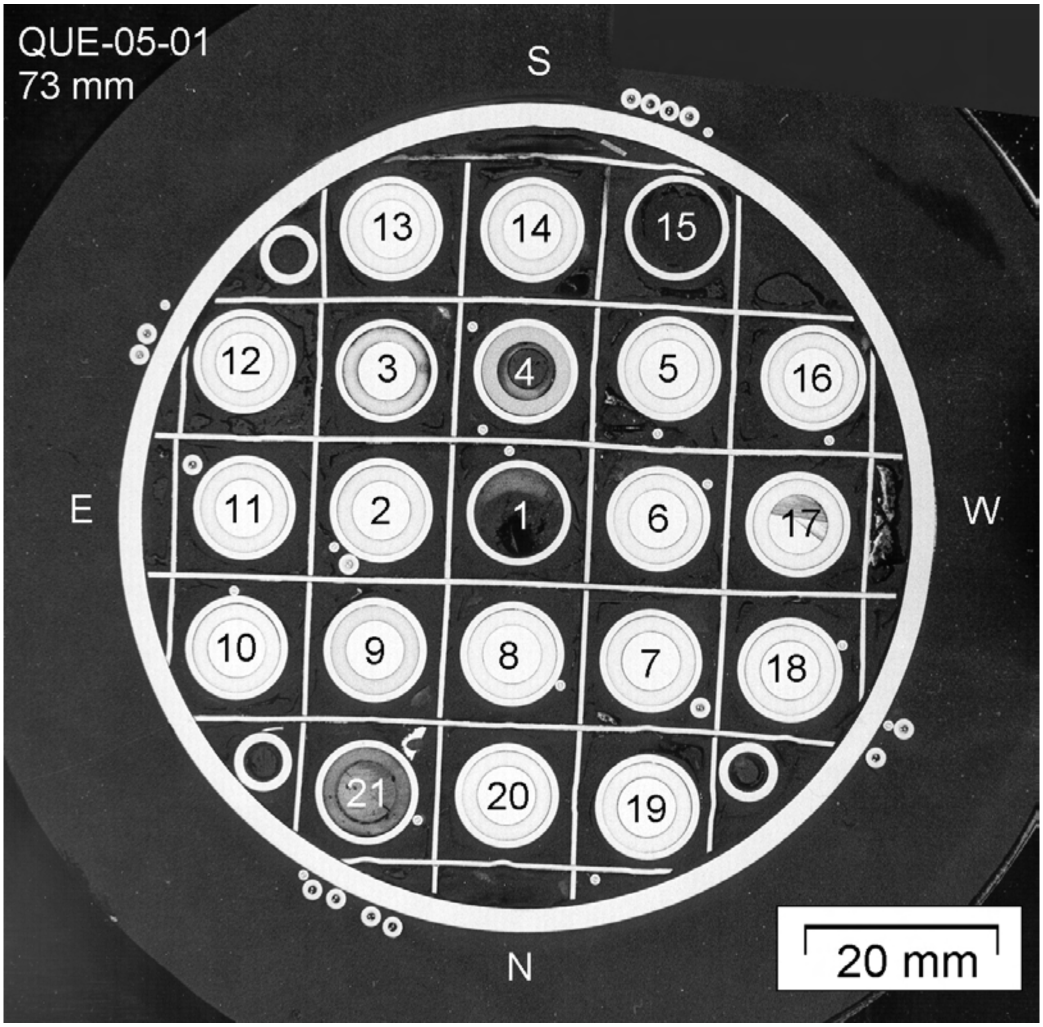

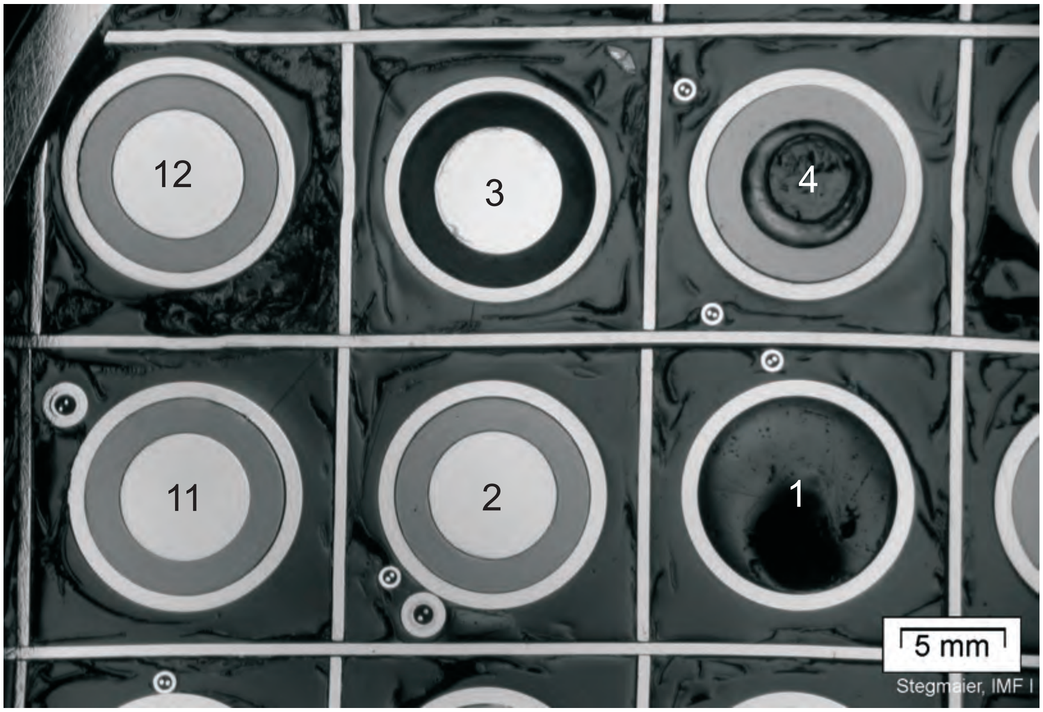

Fig 44:QUE05-01(73mm)F73-1.cdr
18.04.02 - IMF

Fig. 44: QUENCH-05; Cross section at bundle elevation 73 mm (QUE-05-01, top); reference overview.

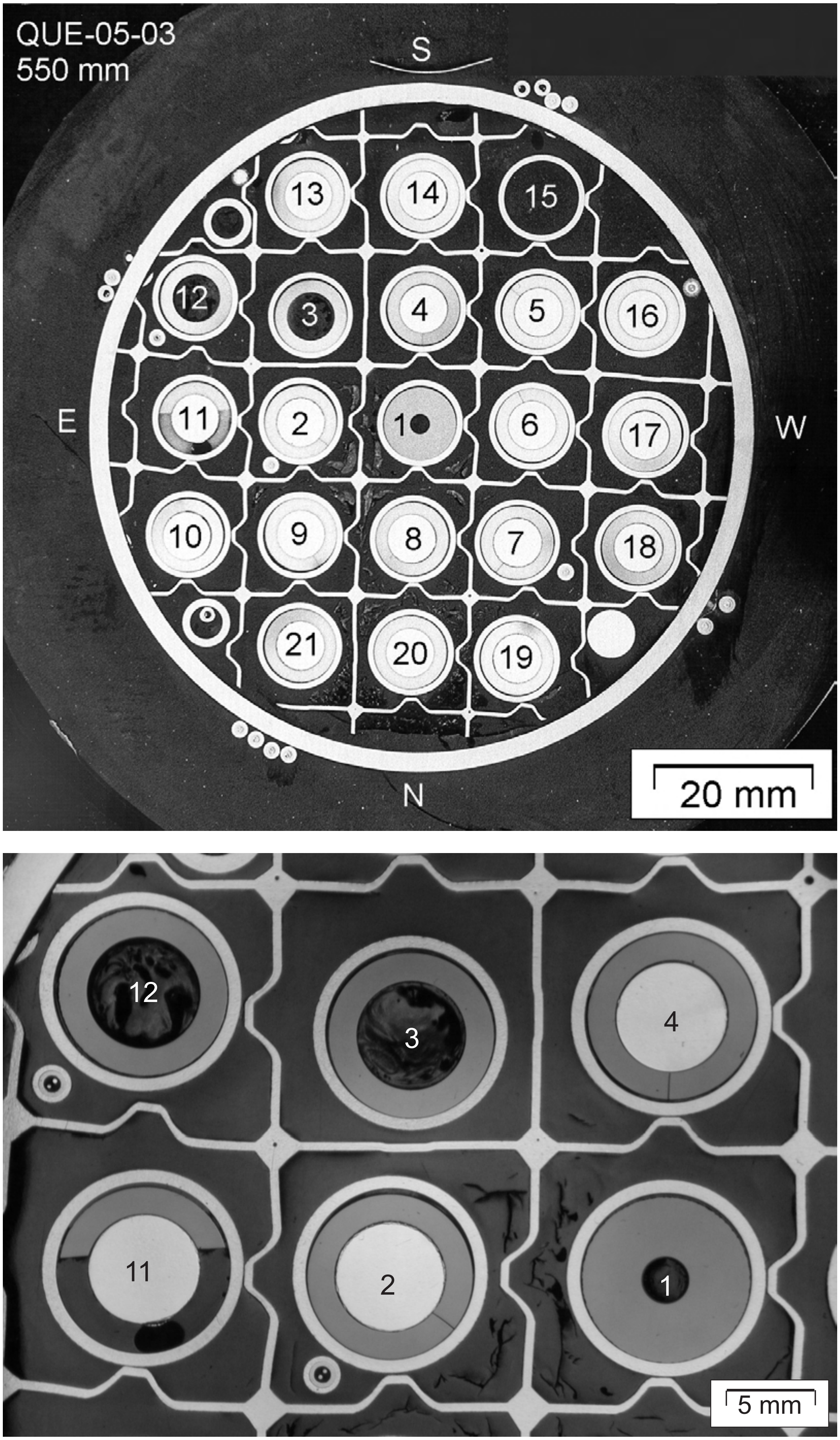

Fig 45:QUE05-03(550mm)F550-1.cdr
18.04.02 - IMF

Fig. 45: QUENCH-05; Cross section at bundle elevation 550 mm (QUE-05-03, top); overview.

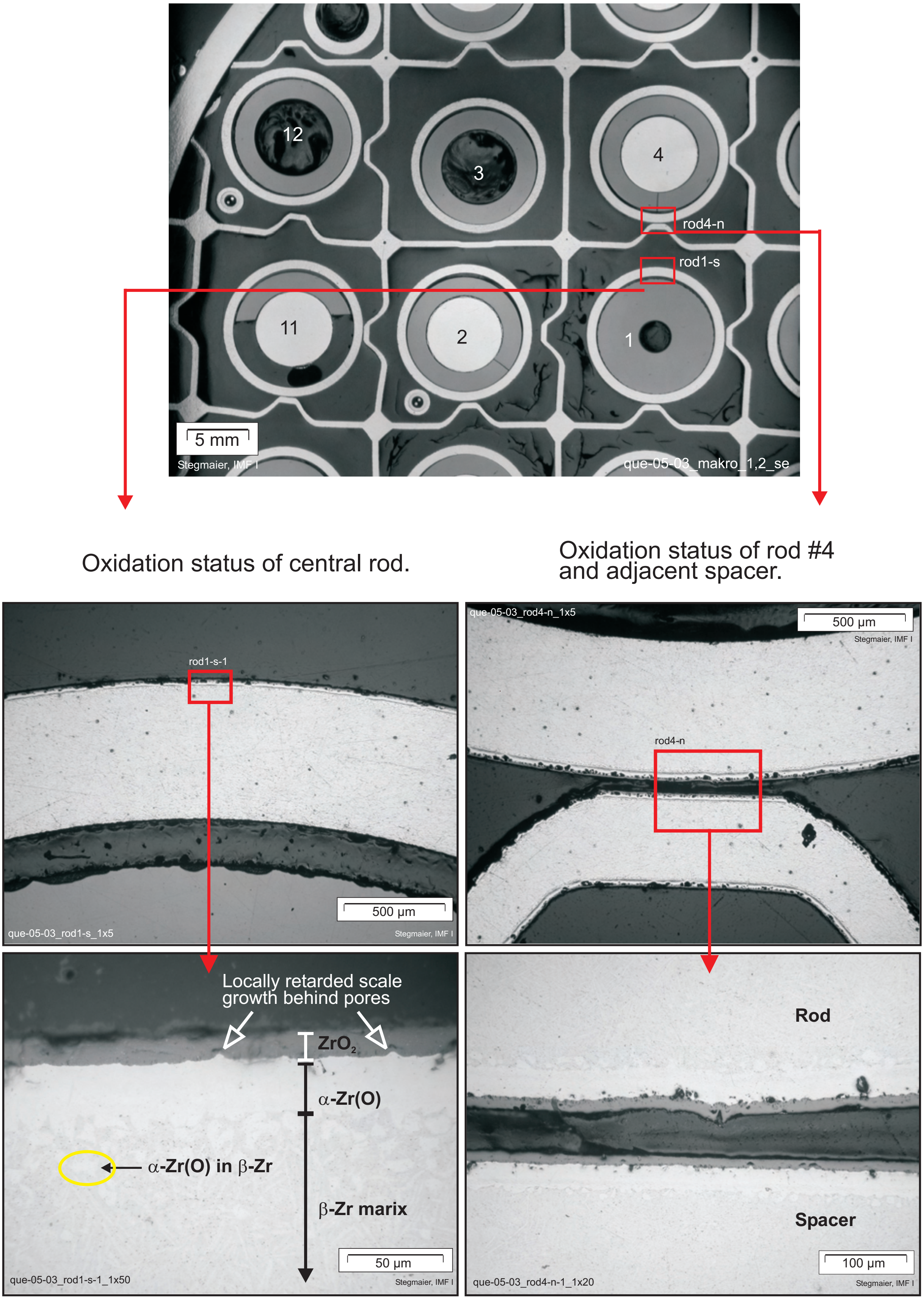

Fig 46:QUE05-03(550mm)F550-2.cdr
06.03.02 - IMF

Fig. 46: QUENCH-05: Cross section at bundle elevation 550 mm (QUE-05-03, top); rod and spacer grid oxidation.

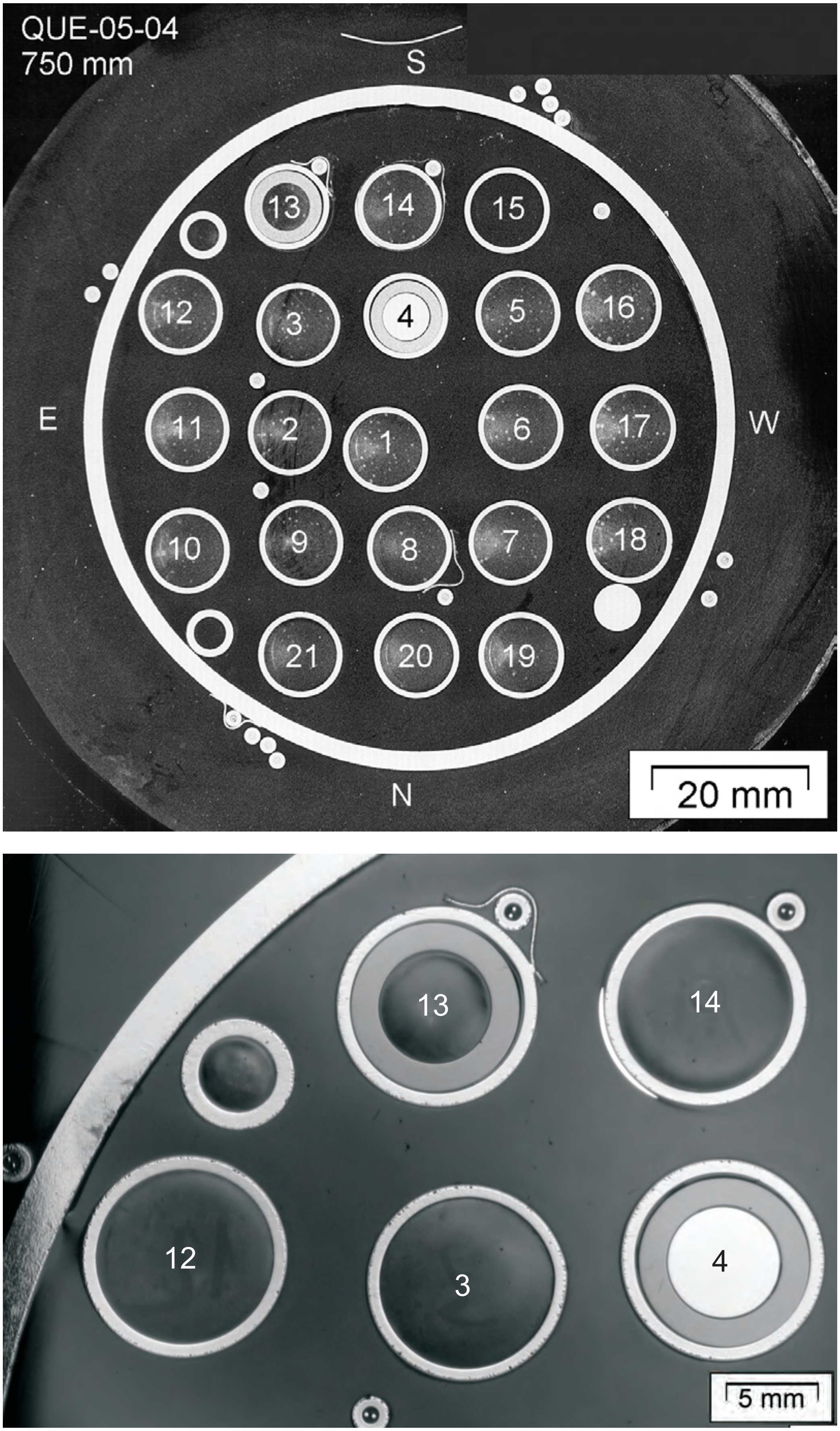

[redacted]

Fig 47:QUE05-04(750mm)F750-1.cdr
06.03.02 - IMF

Fig. 47: QUENCH-05: Cross section at bundle elevation 750 mm (QUE-05-04, top); overview.

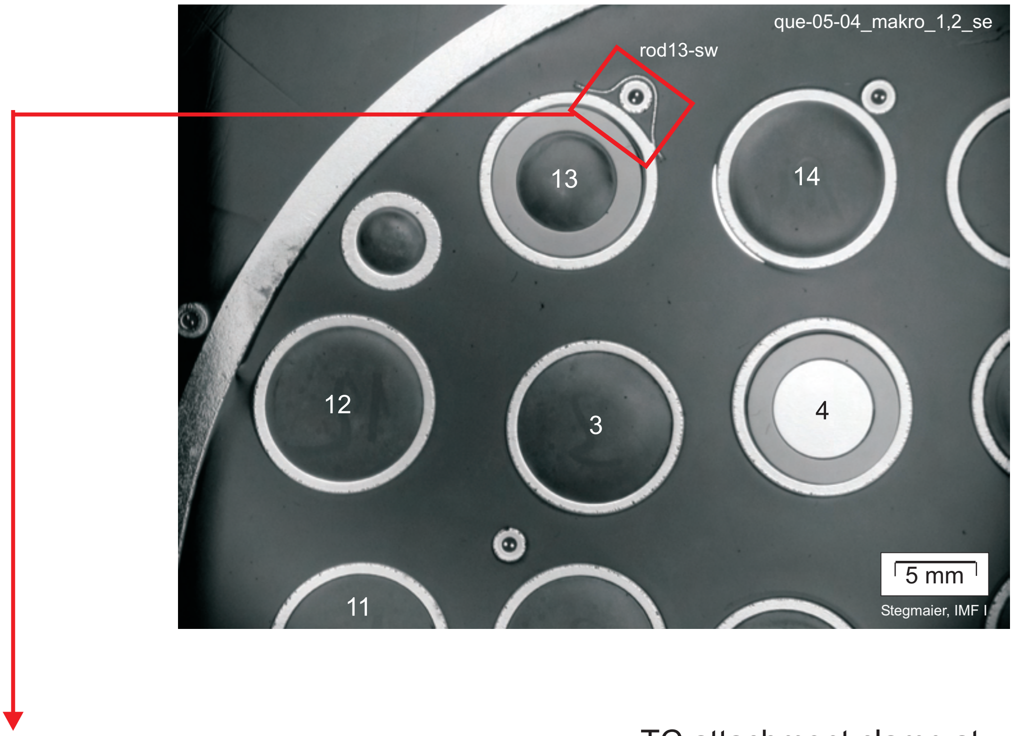

Thermocouple TFS 5/11

TC attachment clamp at welding position; crack surfaces oxidized.

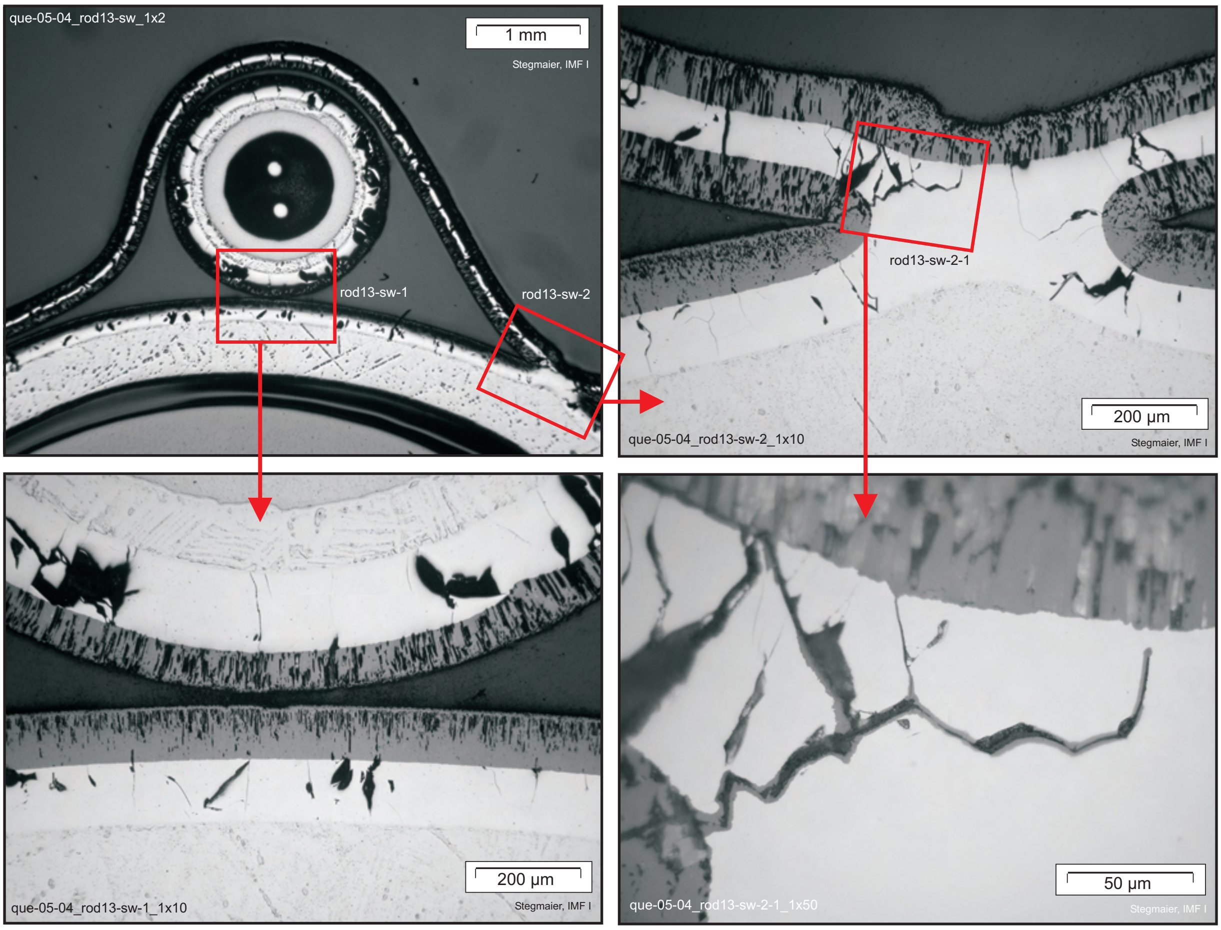

Fig 48:QUE05-04(750mm)F750-2.cdr
06.03.02 - IMF

Fig. 48: QUENCH-05; Cross section at bundle elevation 750 mm (QUE-05-04, top); oxidation and thermocouple status.

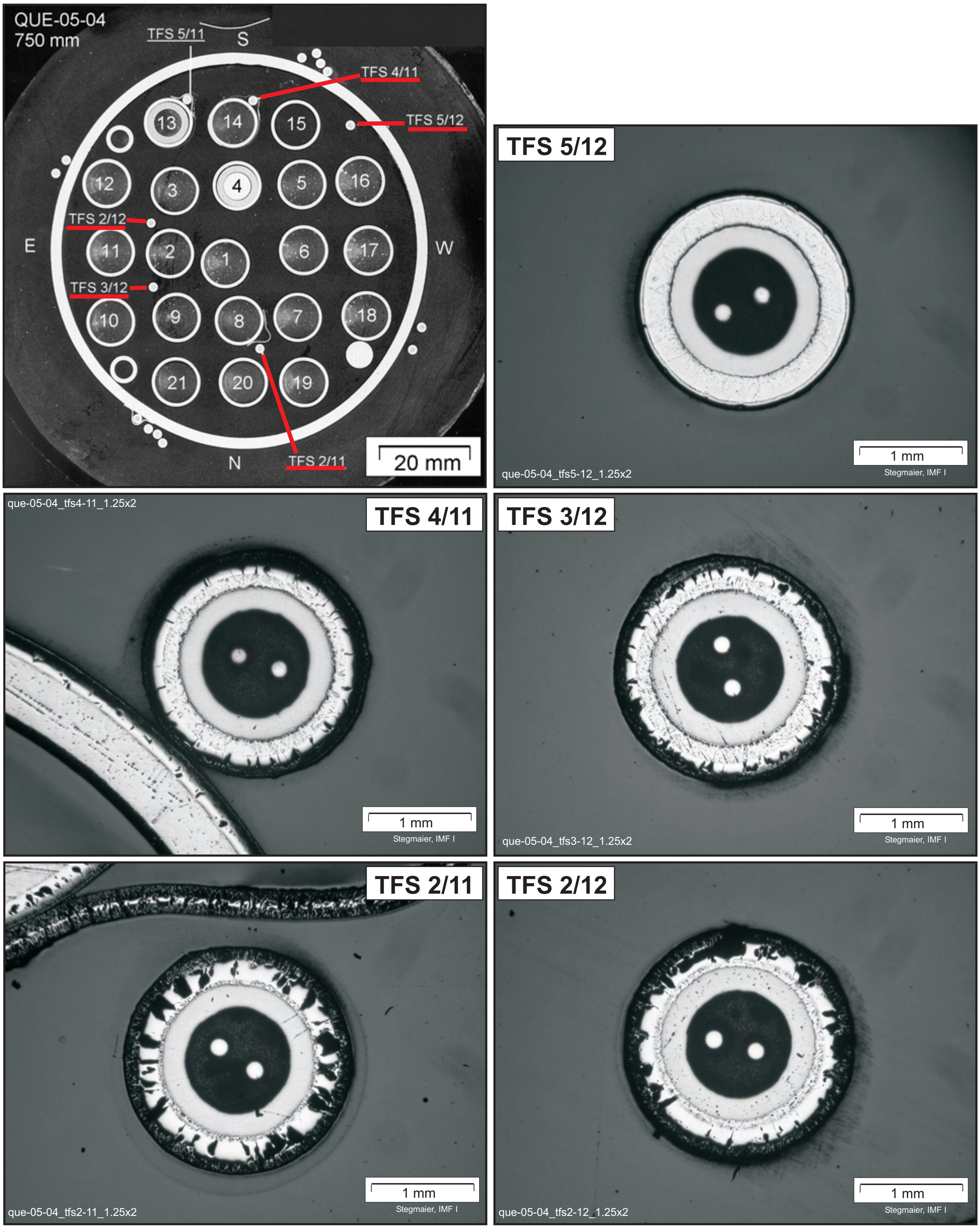

Fig 49:QUE05-04(750mm)F750-3.cdr
06.03.02 - IMF

Fig. 49: QUENCH-05; Cross section at bundle elevation 750 mm (QUE-05-04, top); status of W-Re thermocouples.

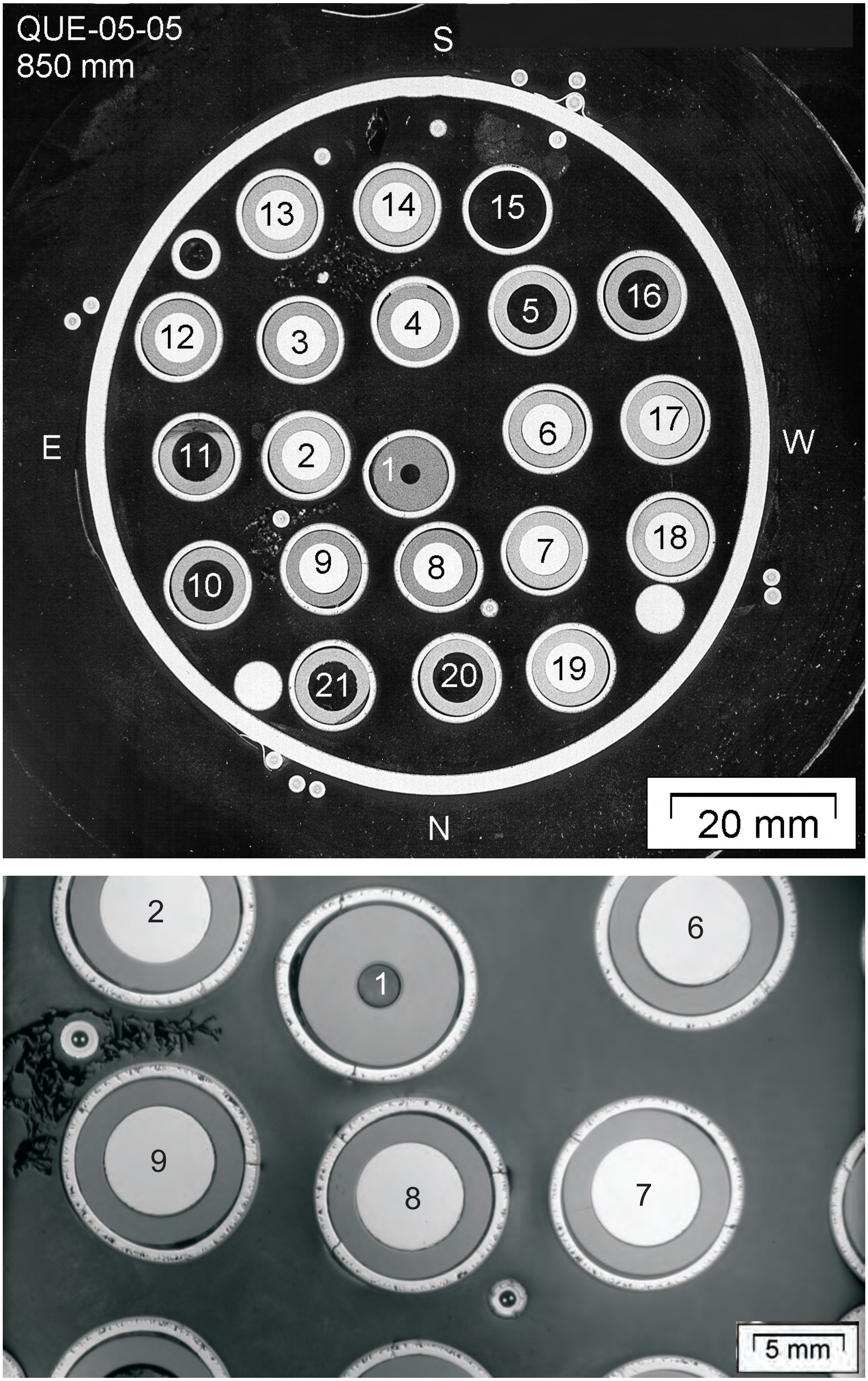

Fig 50:QUE05-05(850mm)F850-1.cdr
18.04.02 - IMF

Fig. 50: QUENCH-05; Cross section at bundle elevation 850 mm (QUE-05-05, top); overview.

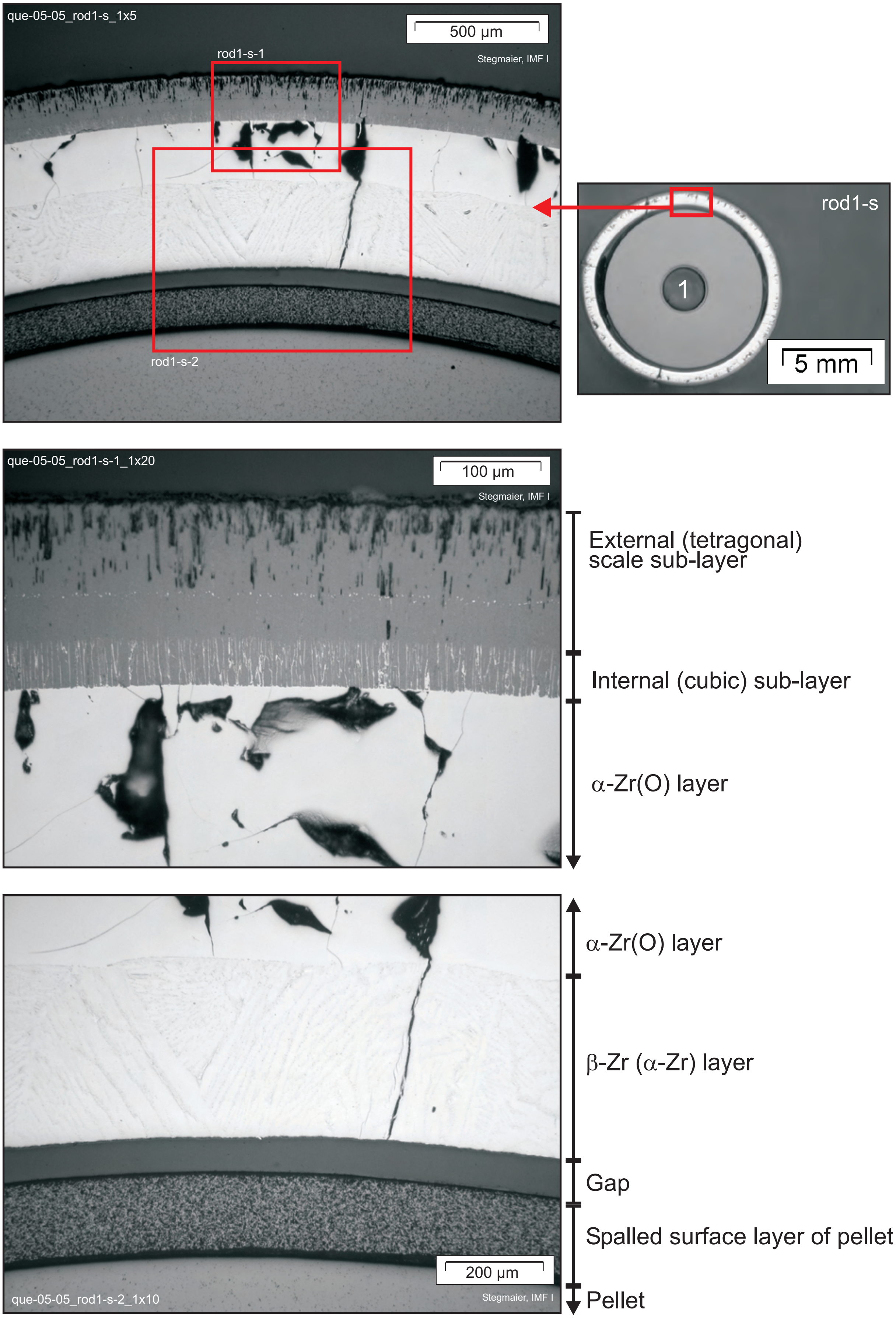

Fig 51:QUE05-05(850mm)F850-2.cdr
18.04.02 - IMF

Fig. 51: QUENCH-05; Cross section at bundle elevation 850 mm (QUE-05-05, top); oxidation status of the central rod.

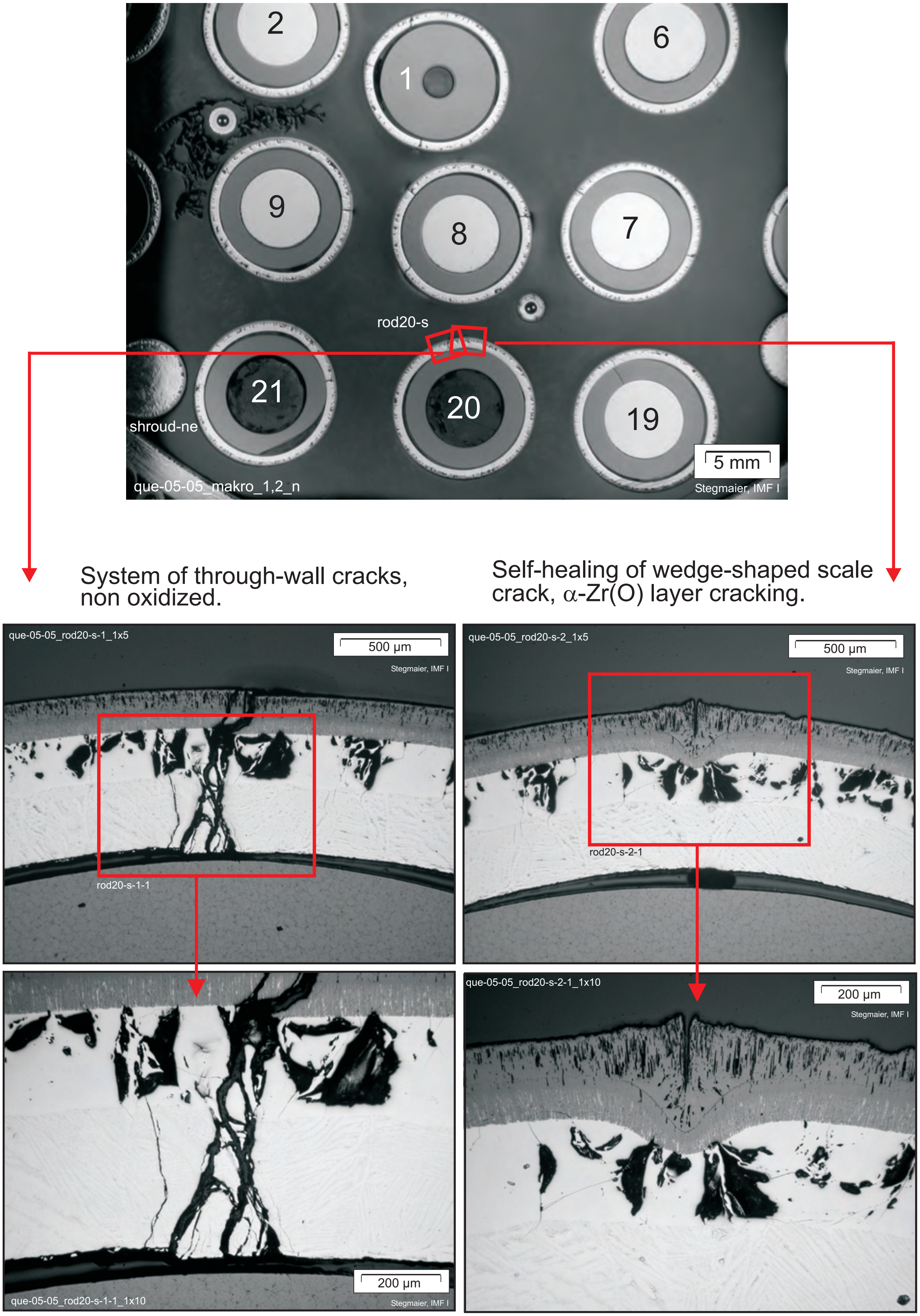

System of through-wall cracks, non oxidized.

Self-healing of wedge-shaped scale crack, α-Zr(O) layer cracking.

Fig 52:QUE05-05(850mm)F850-3.cdr
18.04.02 - IMF

Fig. 52: QUENCH-05; Cross section at bundle elevation 850 mm (QUE-05-05, top); details of rod oxidation status.

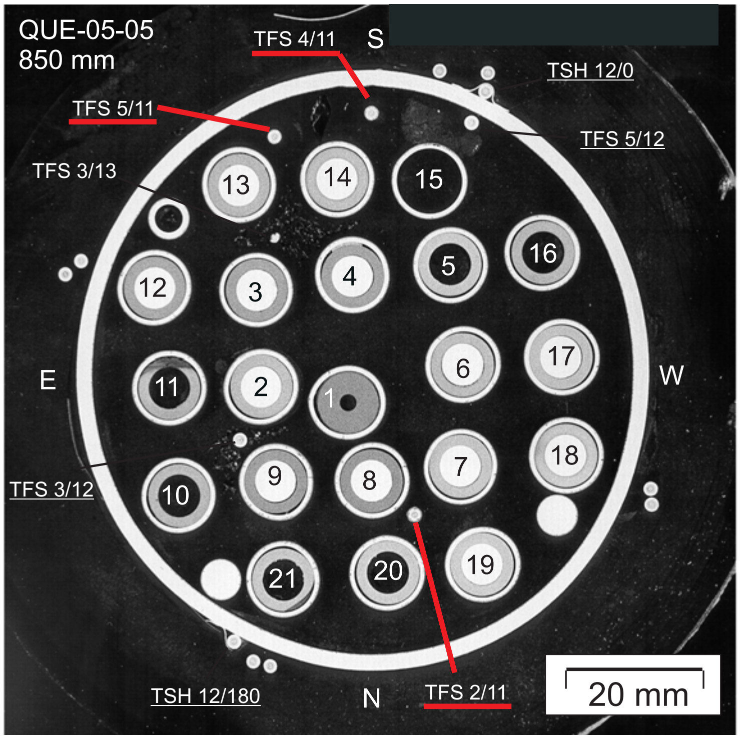

TCs for measurement at 750 mm bundle elevation.

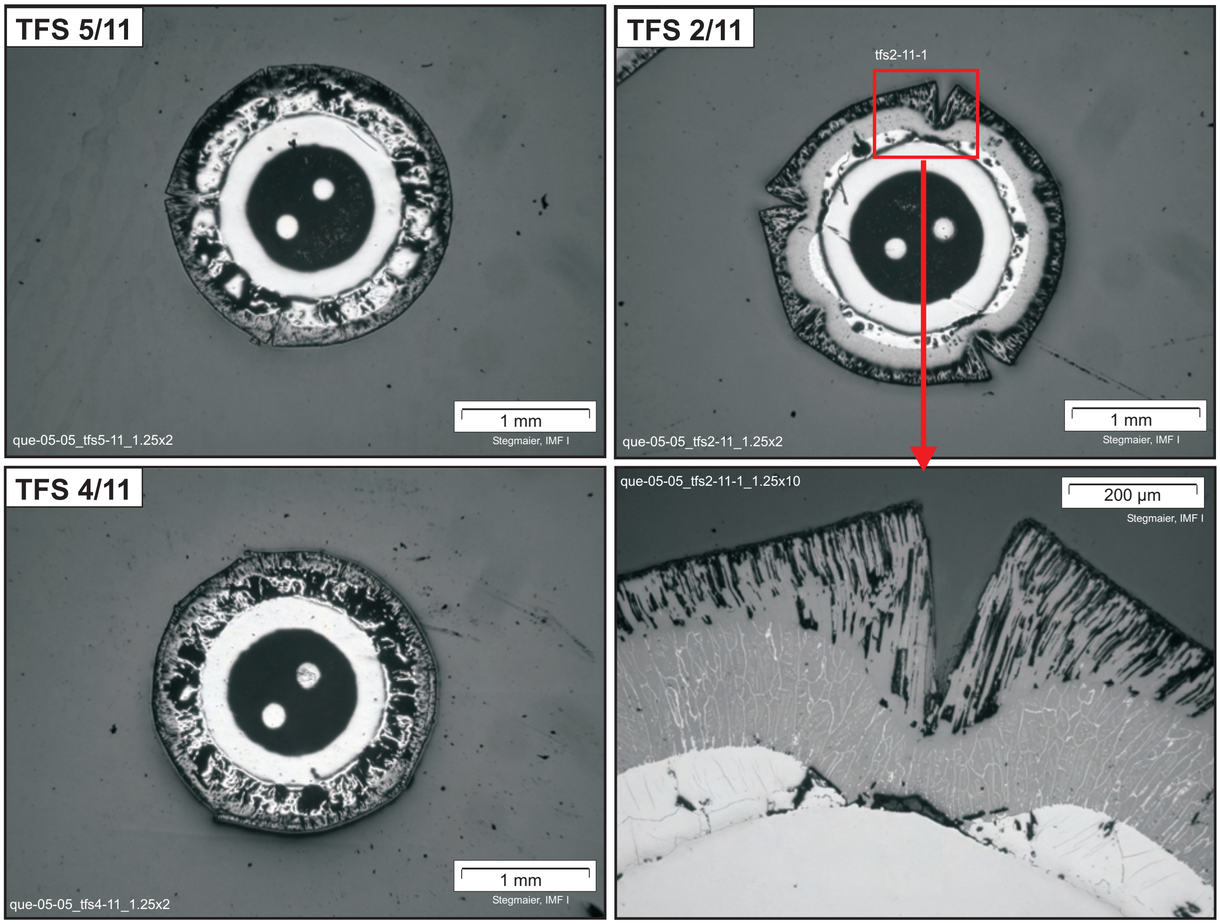

Fig 53:QUE05-05(850mm)F850-4.cdr
18.04.02 - IMF

Fig. 53: QUENCH-05; Cross section at bundle elevation 850 mm (QUE-05-05, top); status of W-Re thermocouples.

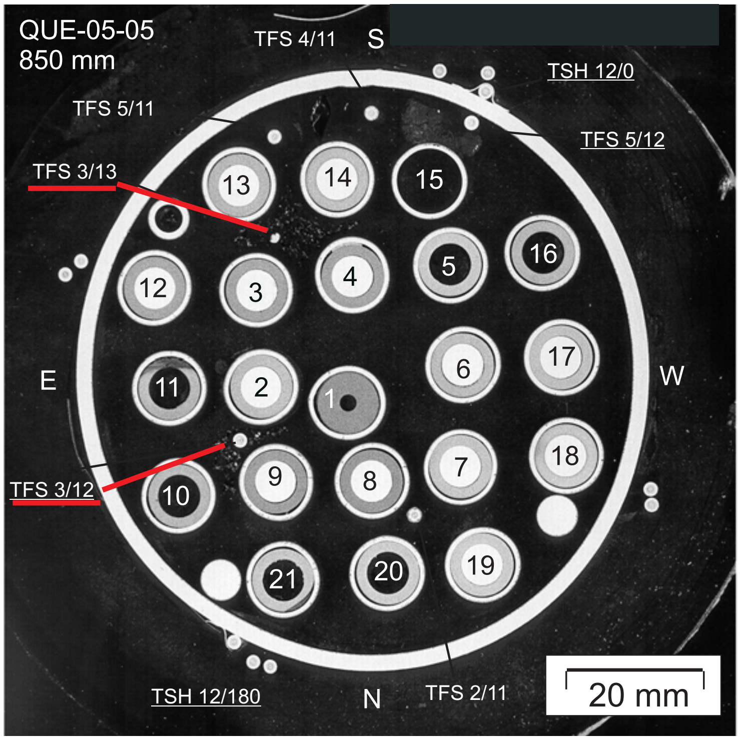

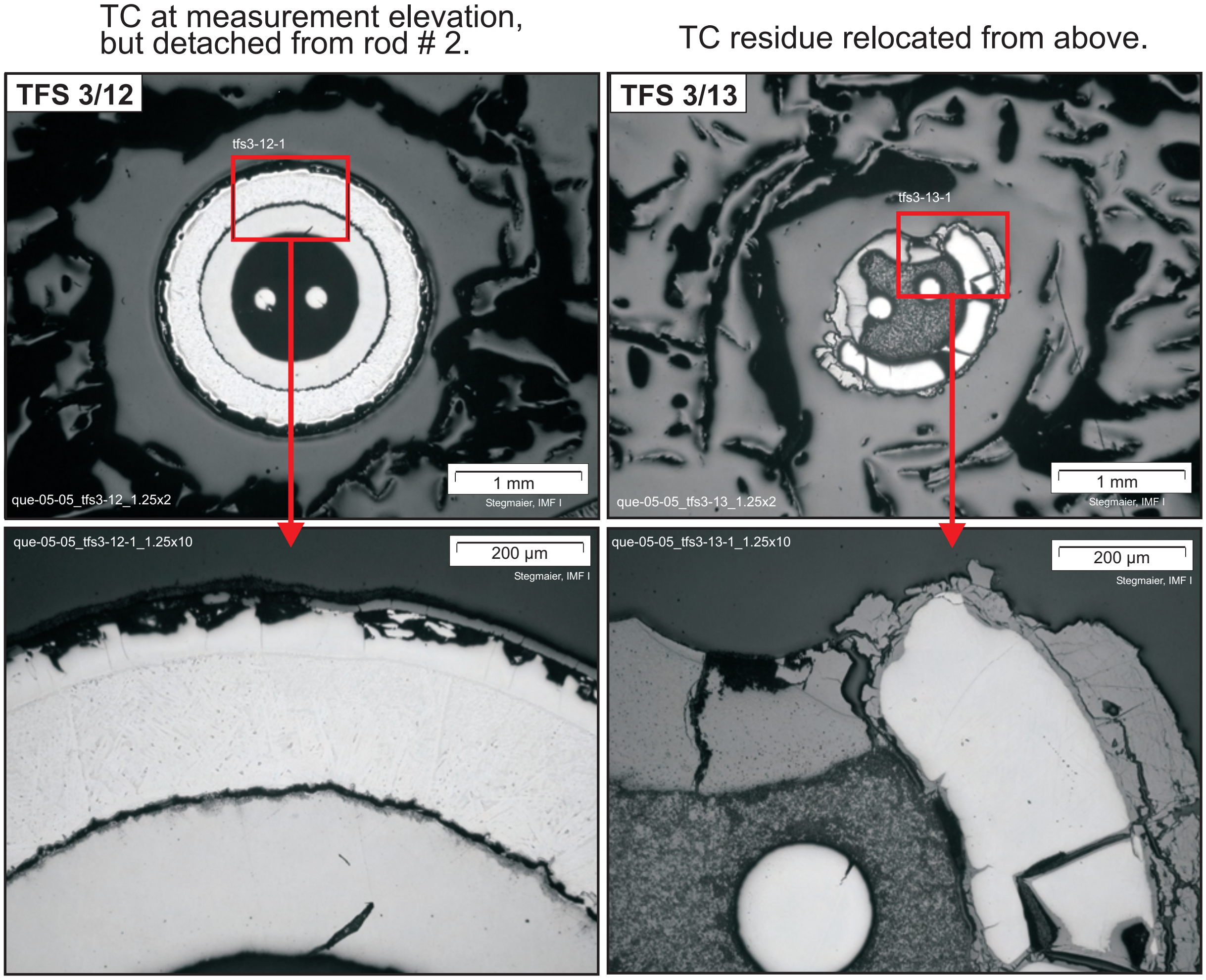

TC at measurement elevation, but detached from rod # 2.

TC residue relocated from above.

Fig 54:QUE05-05(850mm)F850-5.cdr
18.04.02 - IMF

Fig. 54: QUENCH-05; Cross section at bundle elevation 850 mm (QUE-05-05, top); status of W-Re thermocouples.

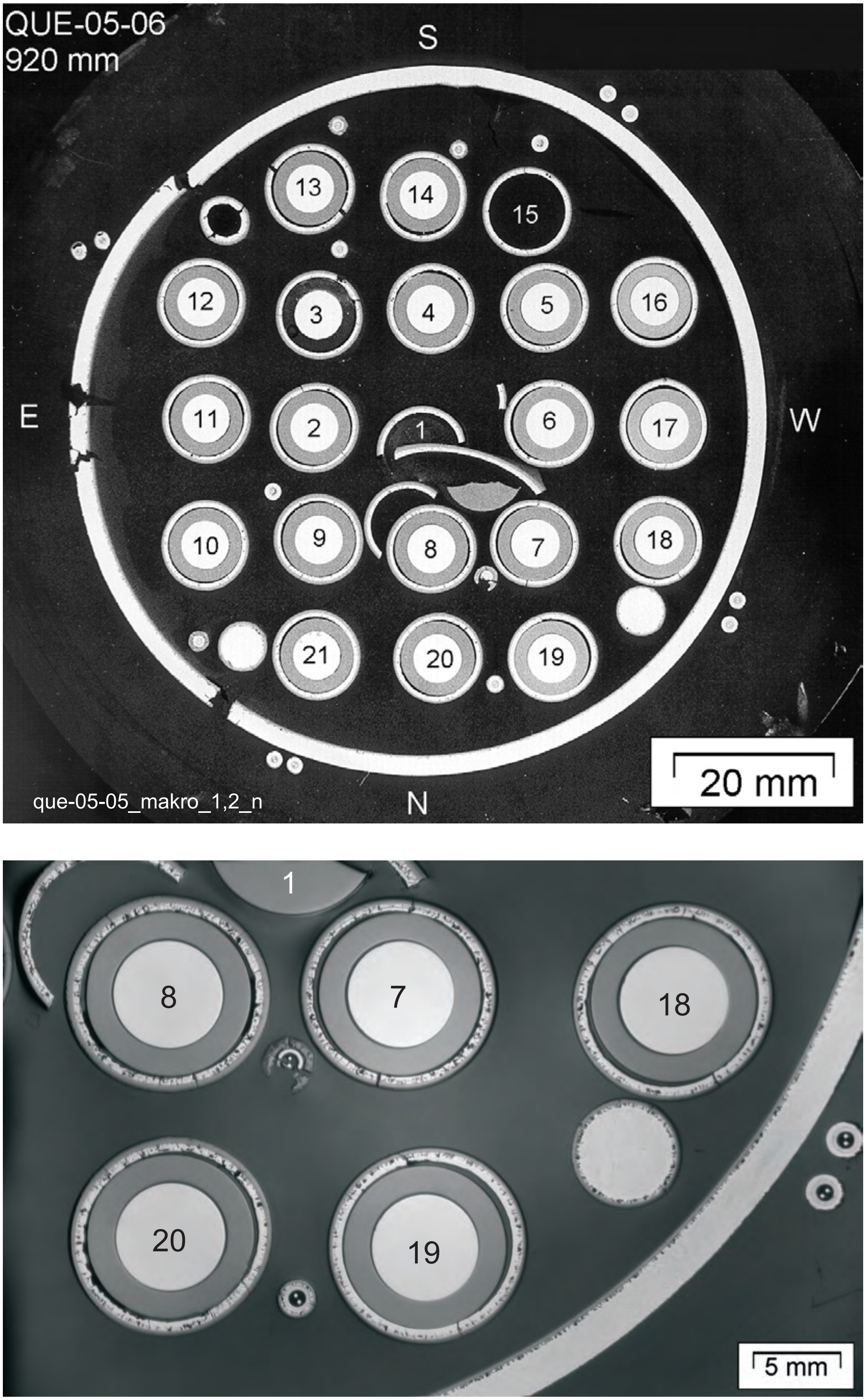

Fig 55:QUE05-06(920mm)F920-1.cdr
18.04..02 - IMF

Fig. 55: QUENCH-05; Cross section at bundle elevation 920 mm (QUE-05-06, top); overview.

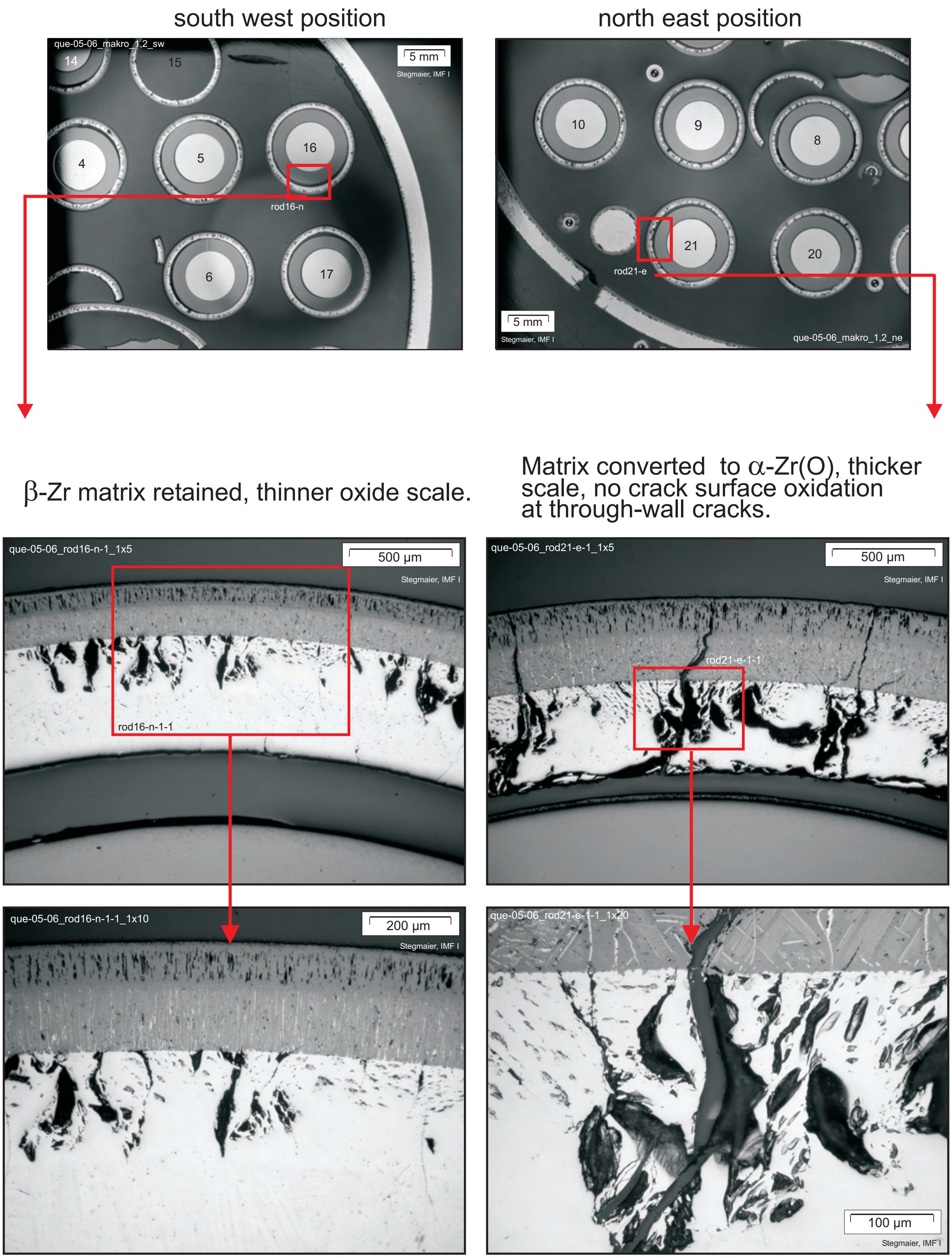

south west position

north east position

β-Zr matrix retained, thinner oxide scale.

Matrix converted to α-Zr(O), thicker scale, no crack surface oxidation at through-wall cracks.

Fig 56:QUE05-06(920mm)F920-2.cdr
22.04.02 - IMF

Fig. 56: QUENCH-05; Cross section at bundle elevation 920 mm (QUE-05-06, top); comparison of the rod oxidation status for opposite positions in the bundle.

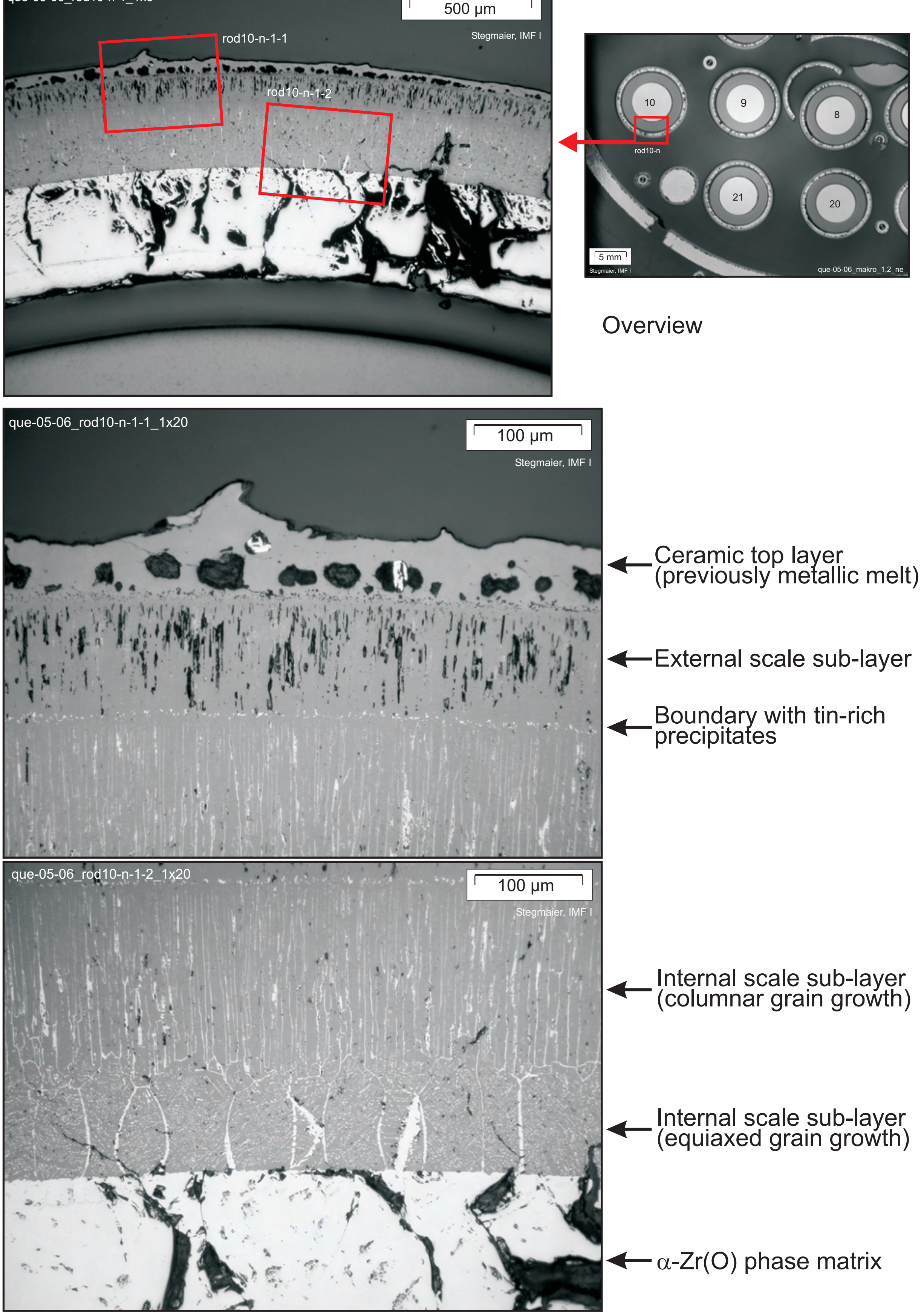

Fig 57:QUE05-06(920mm)F920-3.cdr
22.04.02 - IMF

Fig. 57: QUENCH-05; Cross section at bundle elevation 920 mm (QUE-05-06, top); microstructure of cladding scale and ceramic top layer.

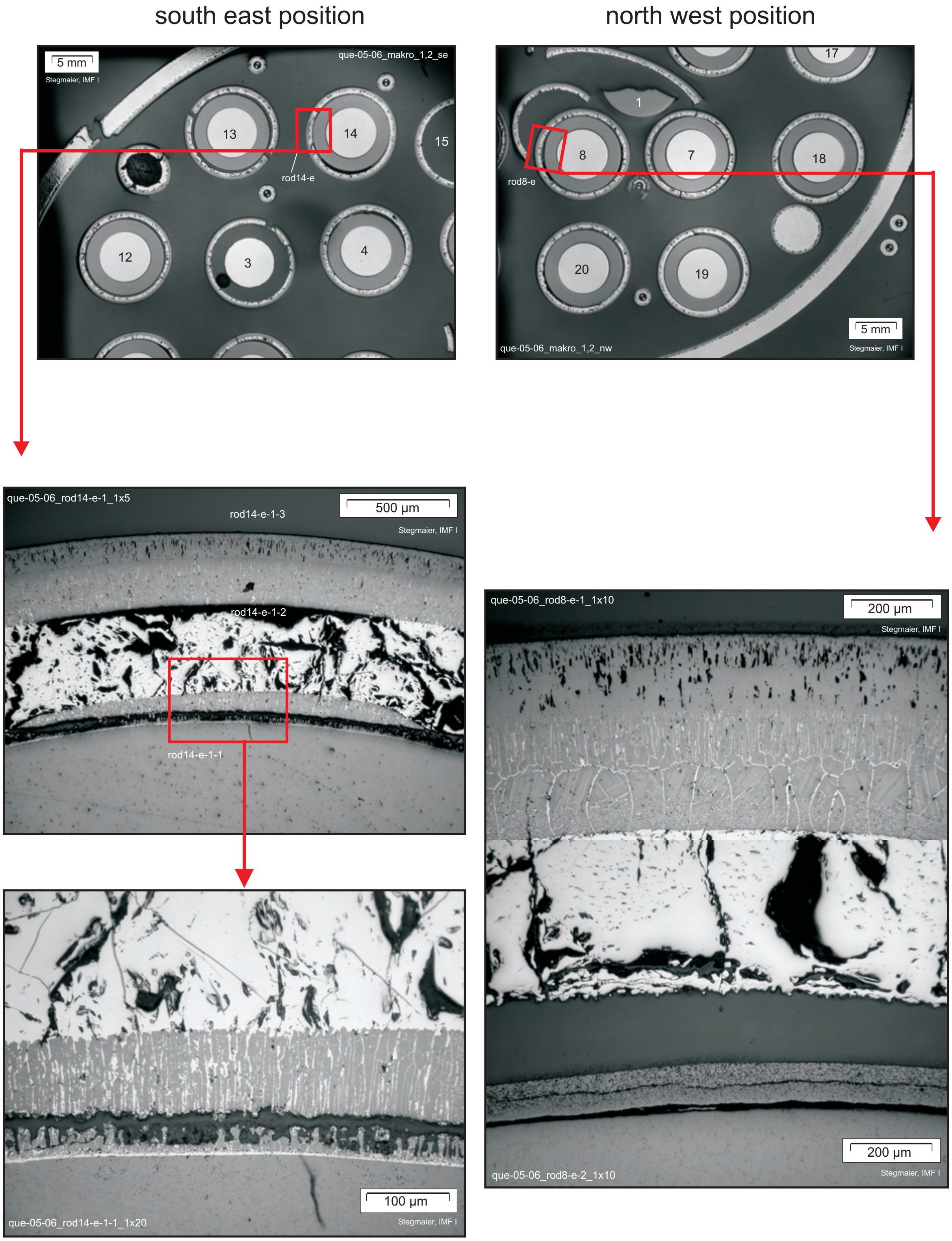

Fig 58:QUE05-06(920mm)F920-4.cdr
22.04.02 - IMF

Fig. 58: QUENCH-05; Cross section at bundle elevation 920 mm (QUE-05-06, top); external steam oxidation and internal pellet interaction of rod claddings.

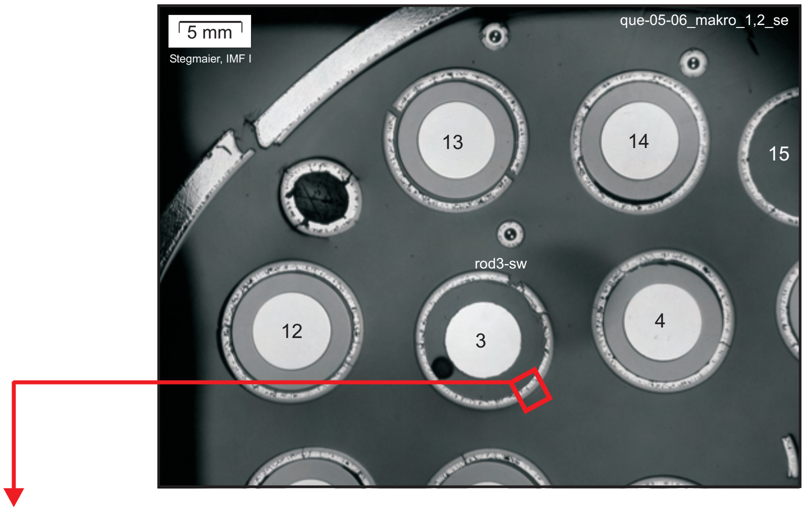

Overview on position of breach; no indication of steam penetration.

Crack within scale and α-Zr(O).

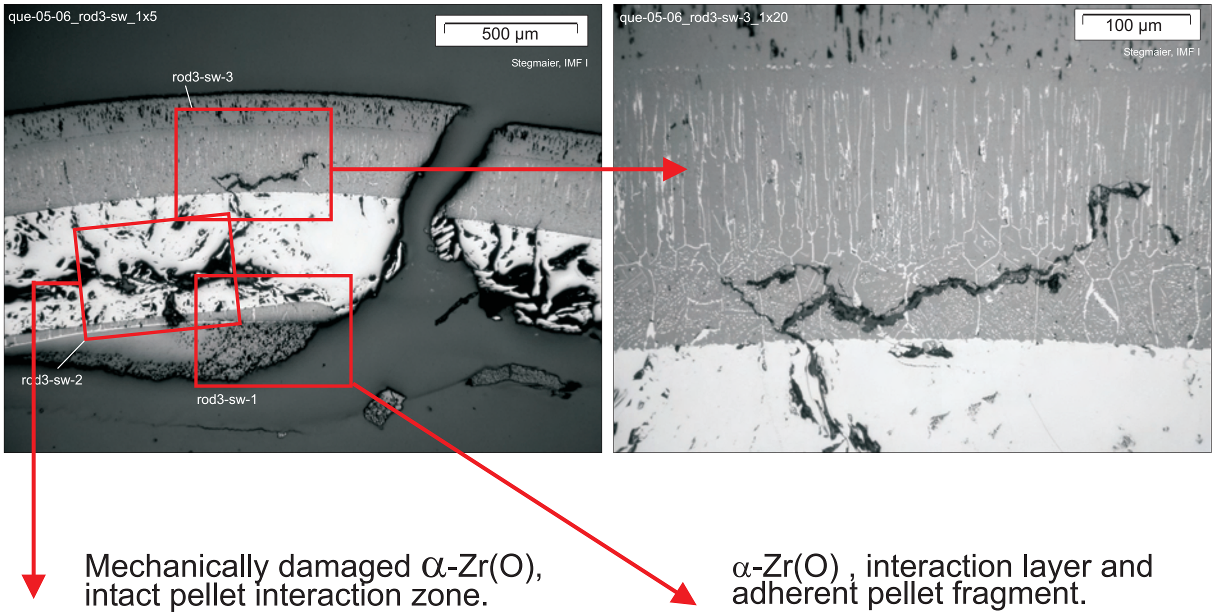

Mechanically damaged α-Zr(O), intact pellet interaction zone.

α-Zr(O) , interaction layer and adherent pellet fragment.

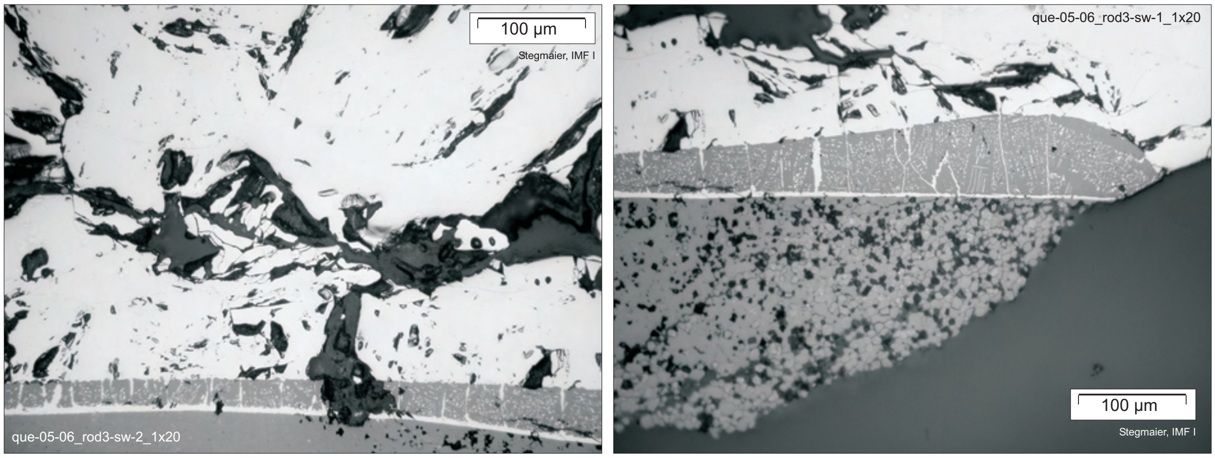

Fig 59:QUE05-06(920mm)F920-5.cdr
22.04.02 - IMF

Fig. 59: QUENCH-05; Cross section at bundle elevation 920 mm (QUE-05-06, top); microstructures of a broken rod, indicating late breach formation by absence of steam penetration effects.

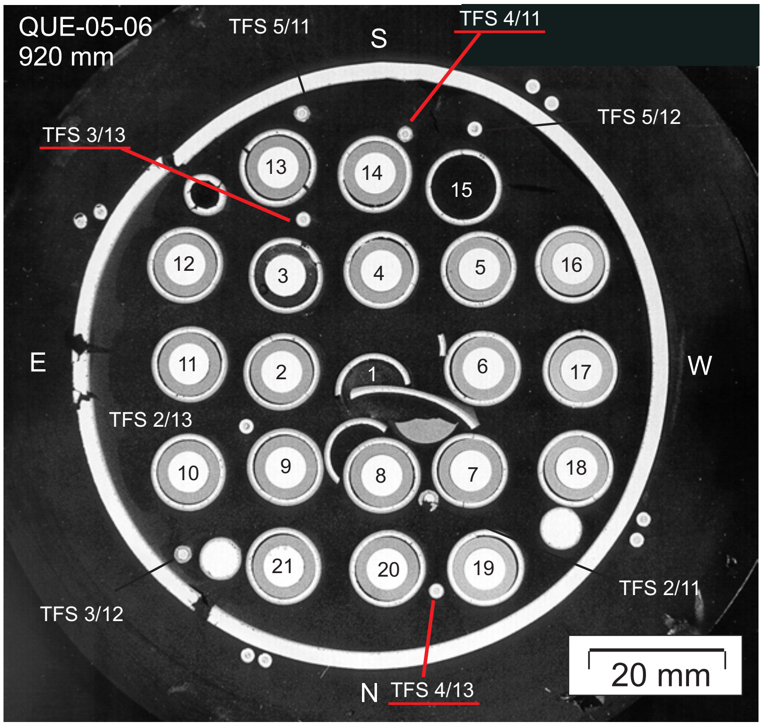

TCs with wedge-cracked outer sheath

TC with detail of wedge crack

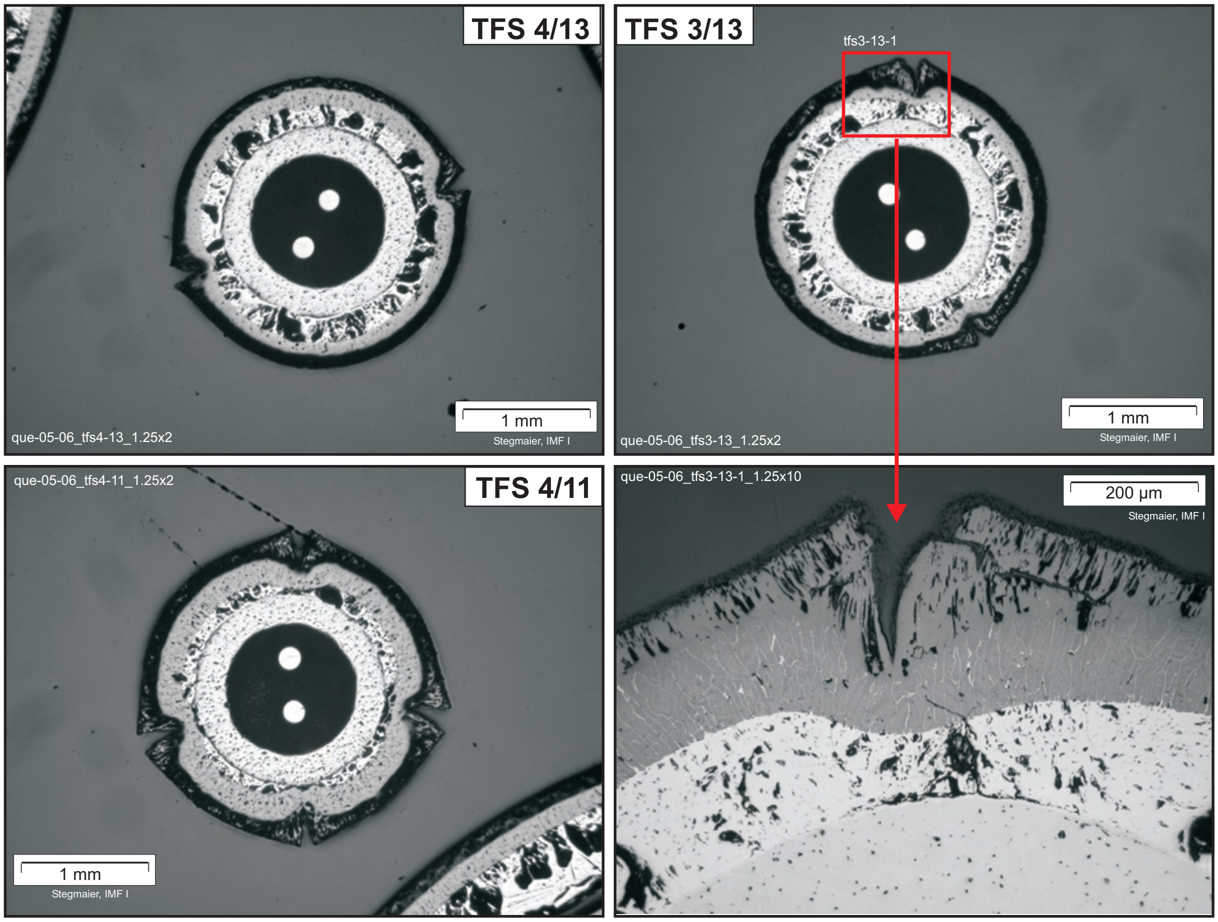

Fig 60:QUE05-06(920mm)F920-6.cdr
22.04.02 - IMF

Fig. 60: QUENCH-05; Cross section at bundle elevation 920 mm (QUE-05-06, top); status of W-Re thermocouples.

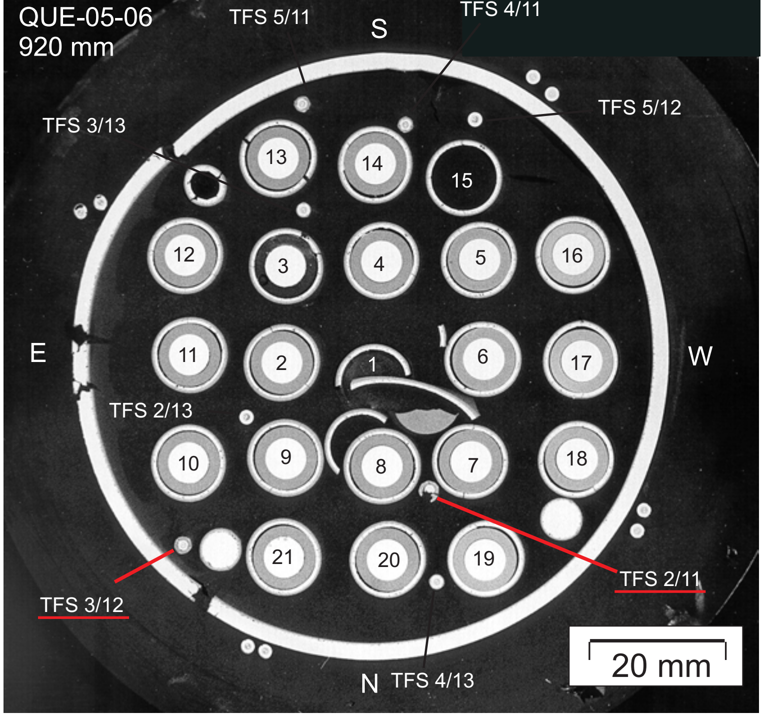

External sheath converted to ZrO_2 and cracked, internal Ta-sheath intact.

External sheath converted to ZrO_2, internal Ta-sheath half destroyed.

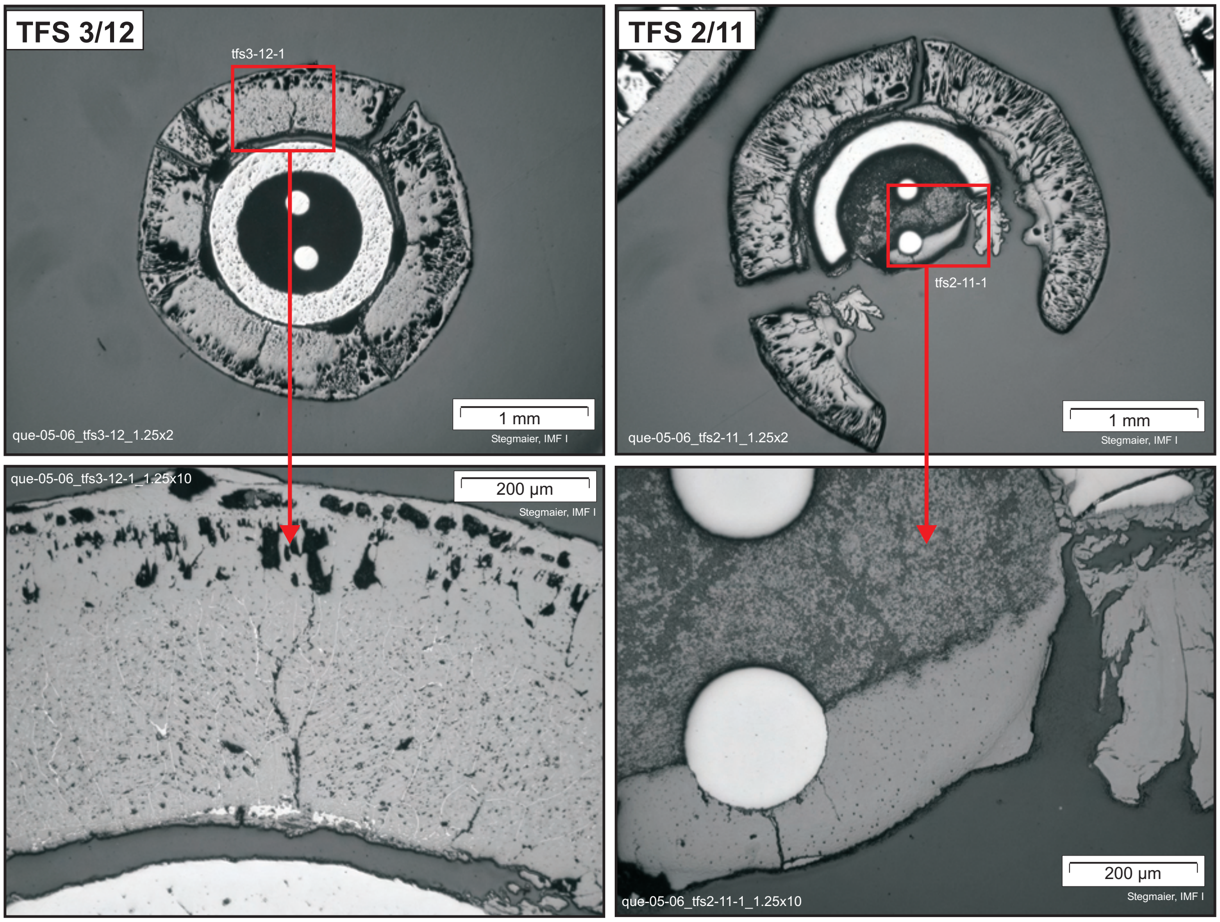

Fig 61:QUE05-06(920mm)F920-7.cdr
22.04.02 - IMF

Fig. 61: QUENCH-05; Cross section at bundle elevation 920 mm (QUE-05-06, top); status of W-Re thermocouples.

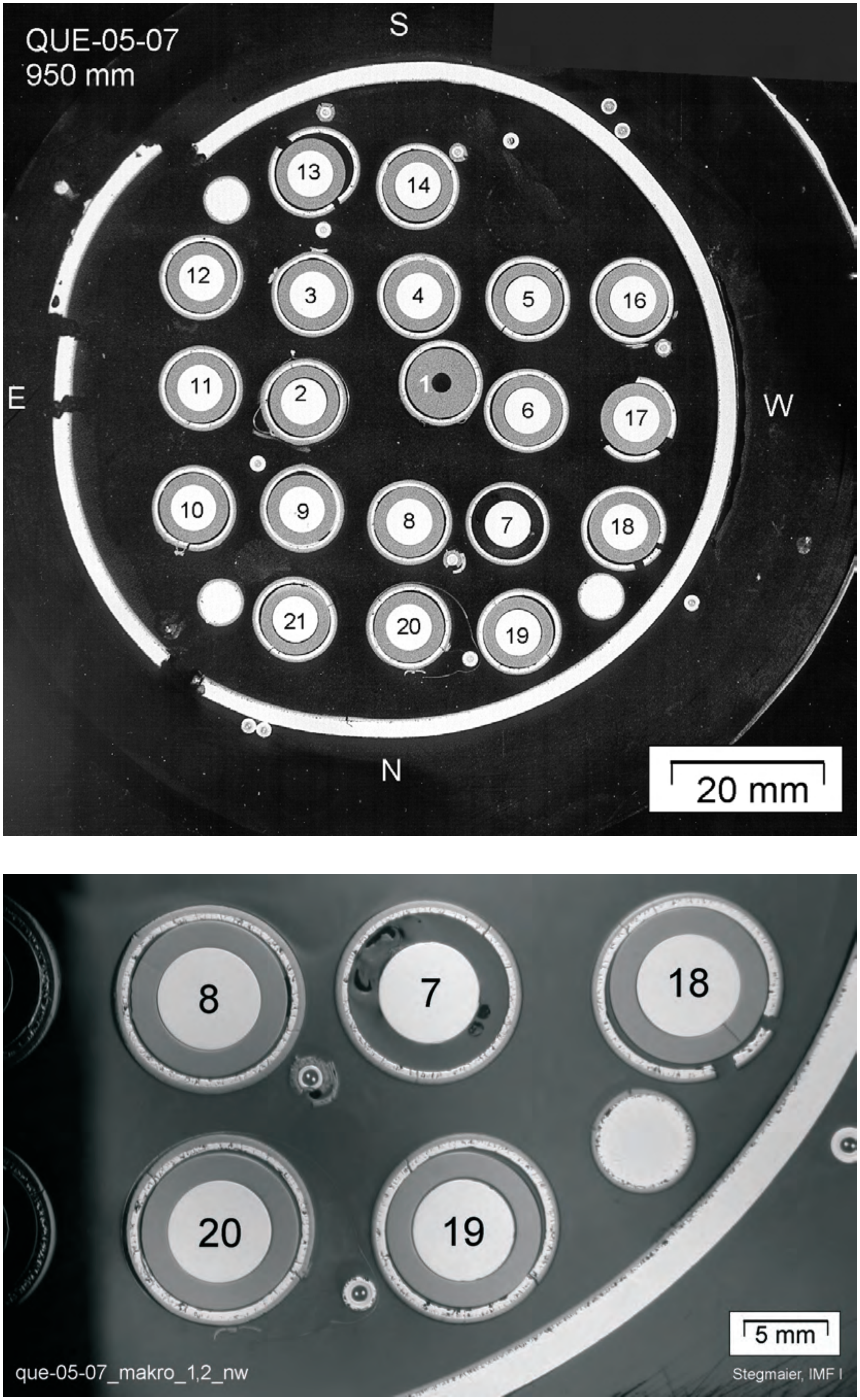

Fig 62:QUE05-07(950mm)F950-1.cdr
22.04.02 - IMF

Fig. 62: QUENCH-05; Cross section at bundle elevation 950 mm (QUE-05-07, top); overview.

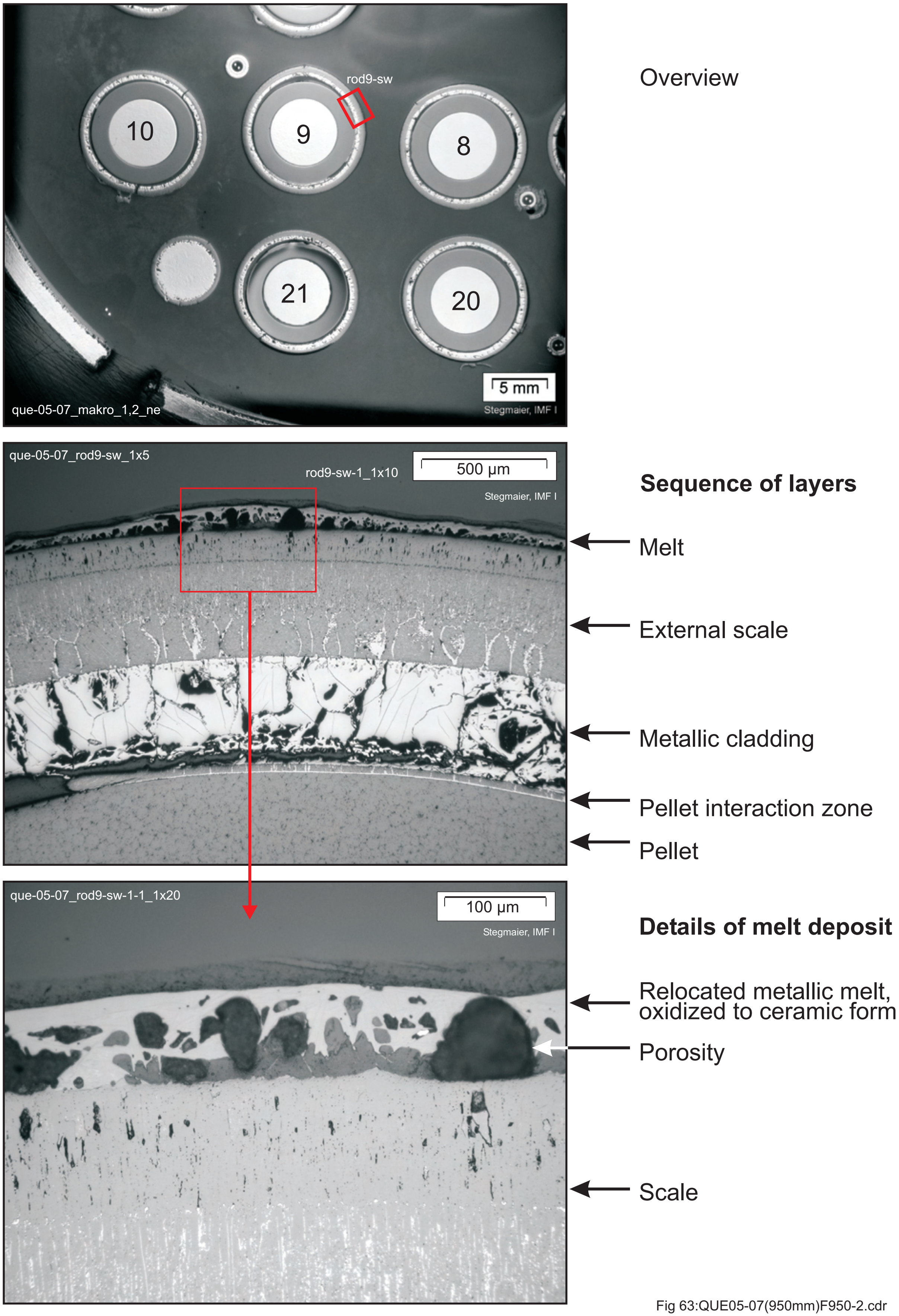

Overview

Sequence of layers

Melt

External scale

Metallic cladding

Pellet interaction zone

Pellet

Details of melt deposit

Relocated metallic melt, oxidized to ceramic form

Porosity

Scale

Fig 63:QUE05-07(950mm)F950-2.cdr
22.04.02 - IMF

Fig. 63: QUENCH-05; Cross section at bundle elevation 950 mm (QUE-05-07, top); relocated melt, external scale and internal interaction layer on rod cladding.

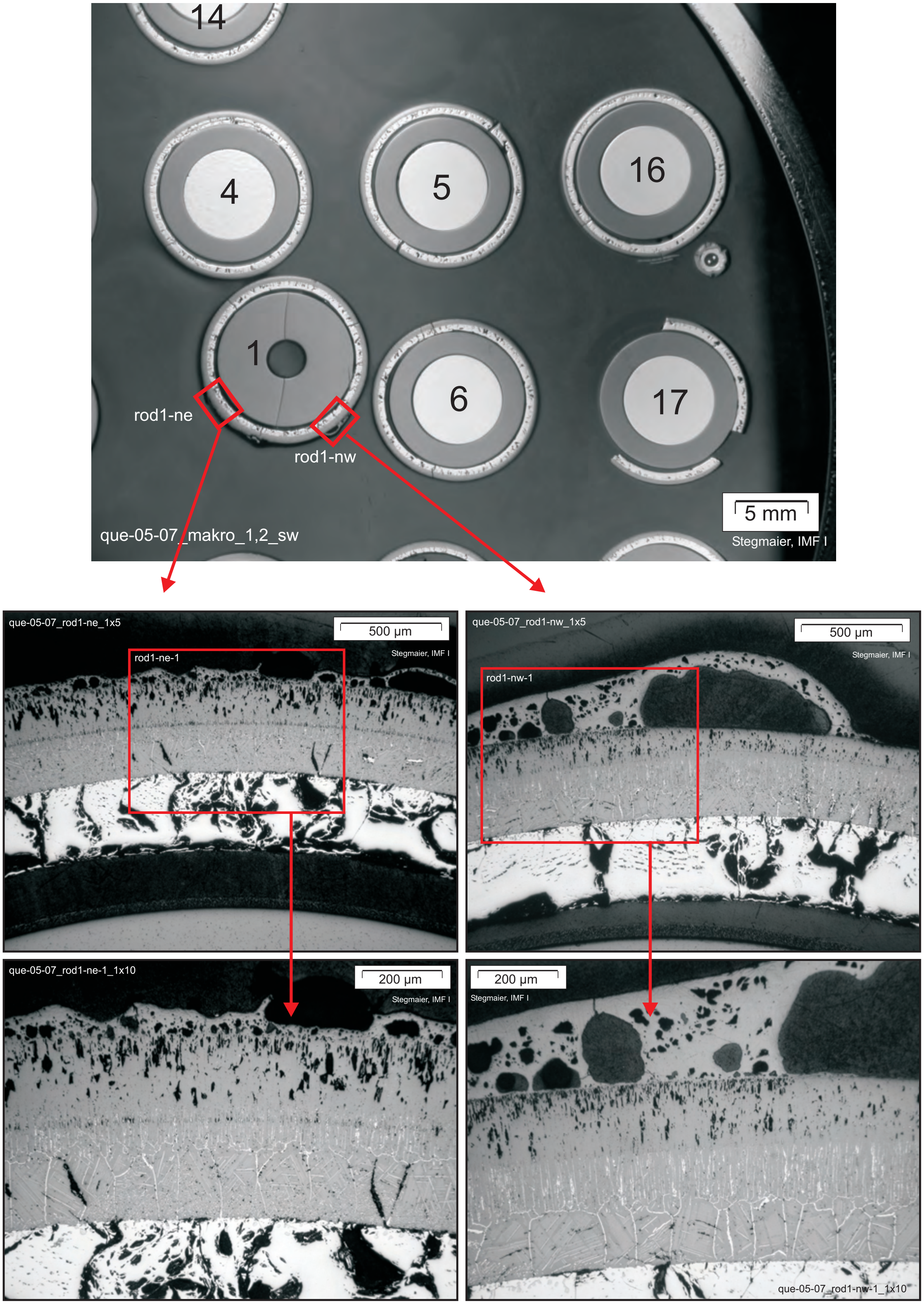

Fig 64:QUE05-07(950mm)F950-3.cdr
22.04.02 - IMF

Fig. 64: QUENCH-05; Cross section at bundle elevation 950 mm (QUE-05-07, top); relocated metallic melt on central rod, completely oxidized to ceramic product.

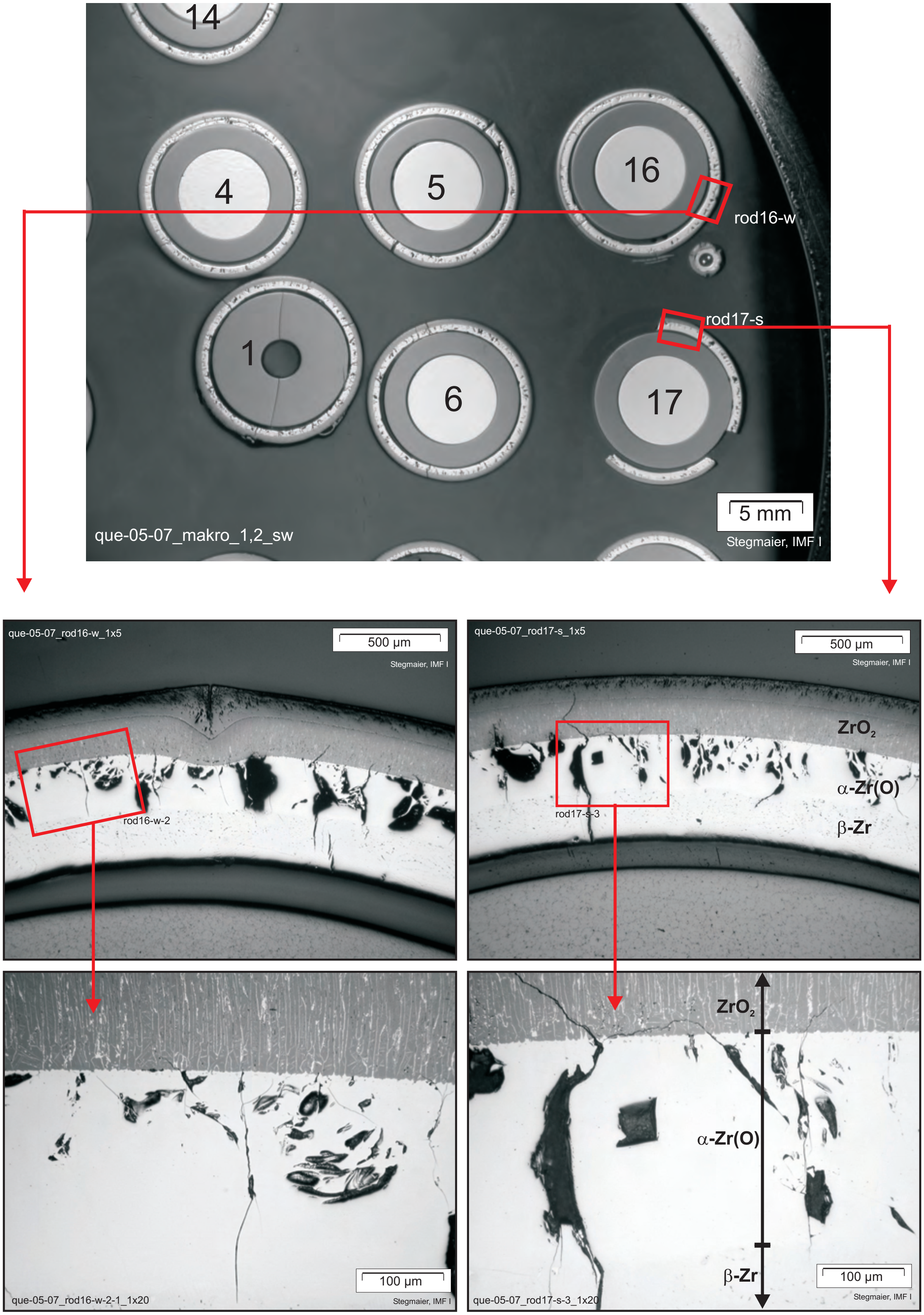

Fig 65:QUE05-07(950mm)F950-4.cdr
22.04.02 - IMF

Fig. 65: QUENCH-05; Cross section at bundle elevation 950 mm (QUE-05-07, top); rods with residual β-Zr phase (α'-Zr), crack surfaces non oxidized.

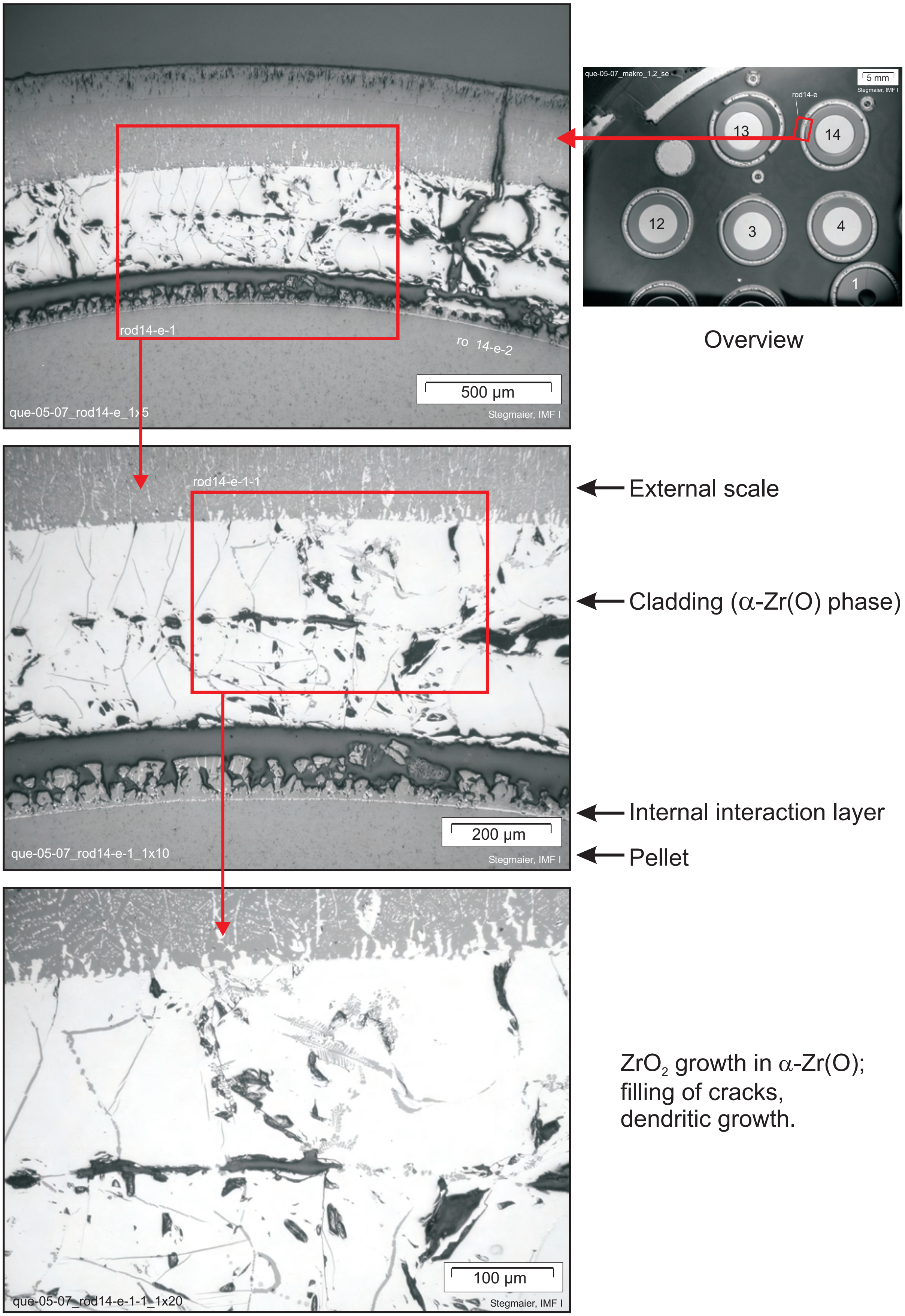

ZrO_2 growth in α-Zr(O);
filling of cracks,
dendritic growth.

Fig 66:QUE05-07(950mm)F950-5.cdr
22.04.02 - IMF

Fig. 66: QUENCH-05; Cross section at bundle elevation 950 mm (QUE-05-07, top); ZrO_2 phase growth in α-Zr(O) cladding.

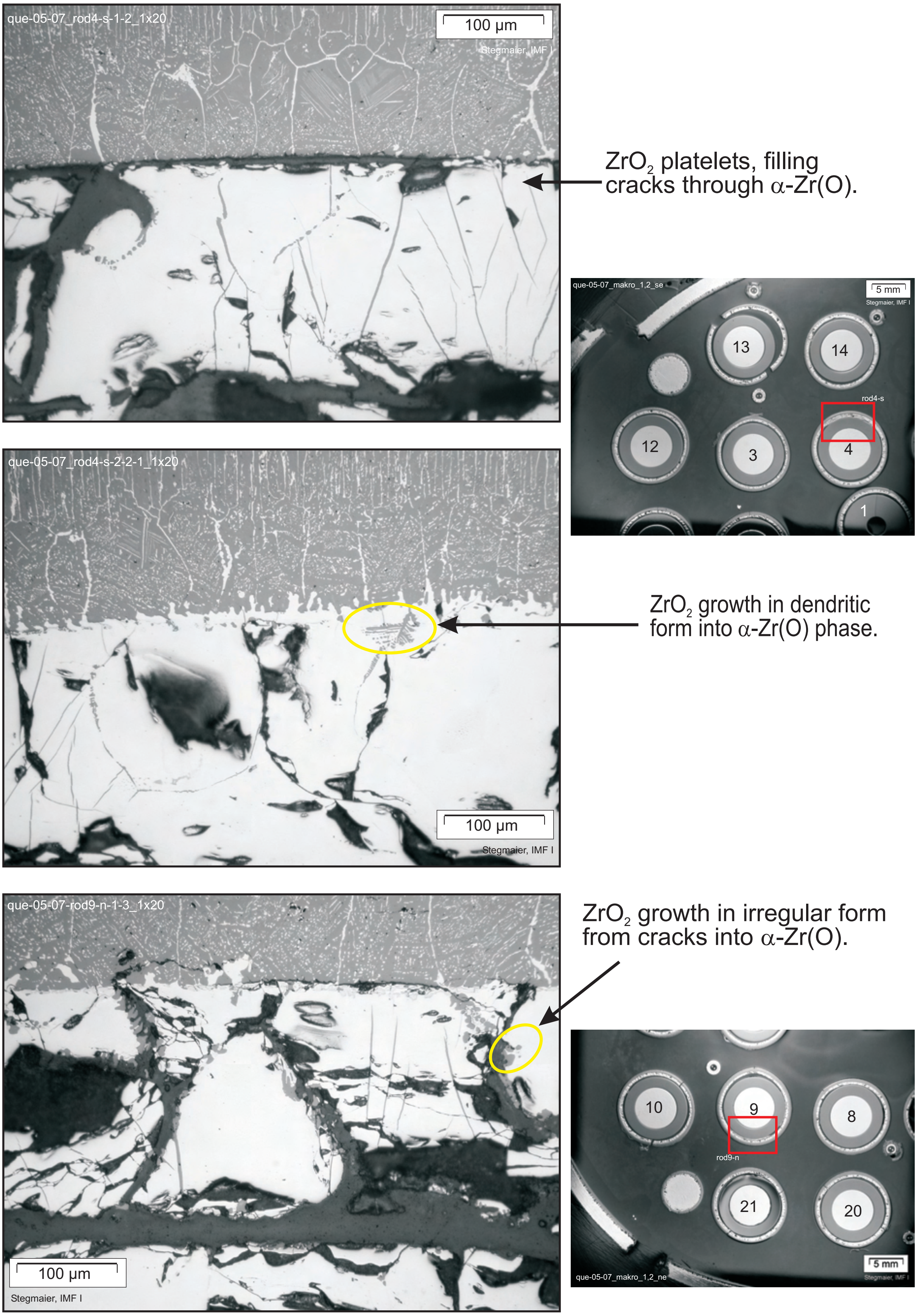

ZrO_2 platelets, filling cracks through α-Zr(O).

ZrO_2 growth in dendritic form into α-Zr(O) phase.

ZrO_2 growth in irregular form from cracks into α-Zr(O).

Fig 67:QUE05-07(950mm)F950-6.cdr
22.04.02 - IMF

Fig. 67: QUENCH-05; Cross section at bundle elevation 950 mm (QUE-05-07, top); details of ZrO_2 phase growth in α-Zr(O) layer.

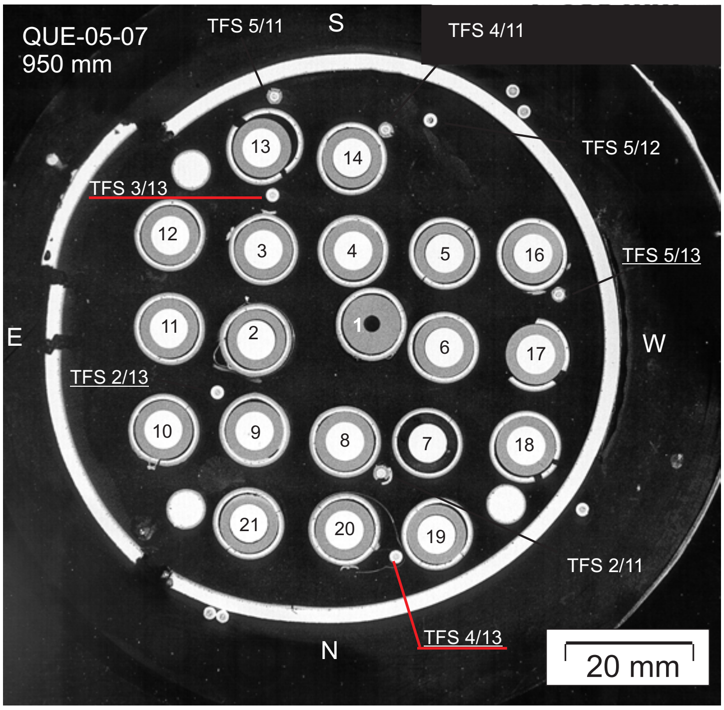

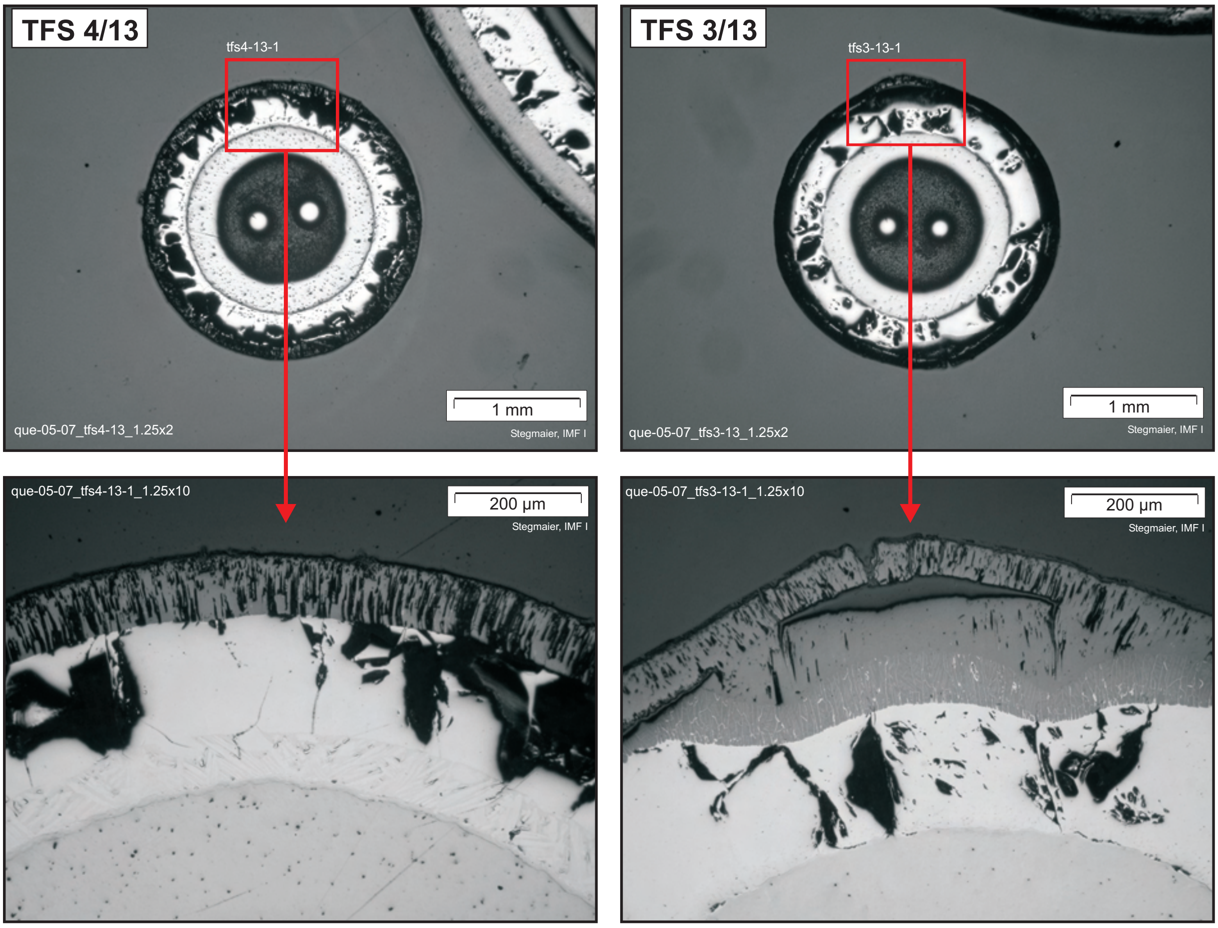
External sheath partly oxidized,
β-Zr phase retained.

External sheath partly oxidized,
no residual β-Zr phase.

Fig 68:QUE05-07(950mm)F950-7.cdr
22.04.02 - IMF

Fig. 68: QUENCH-05; Cross section at bundle elevation 950 mm (QUE-05-07, top); status of W-Re thermocouples.

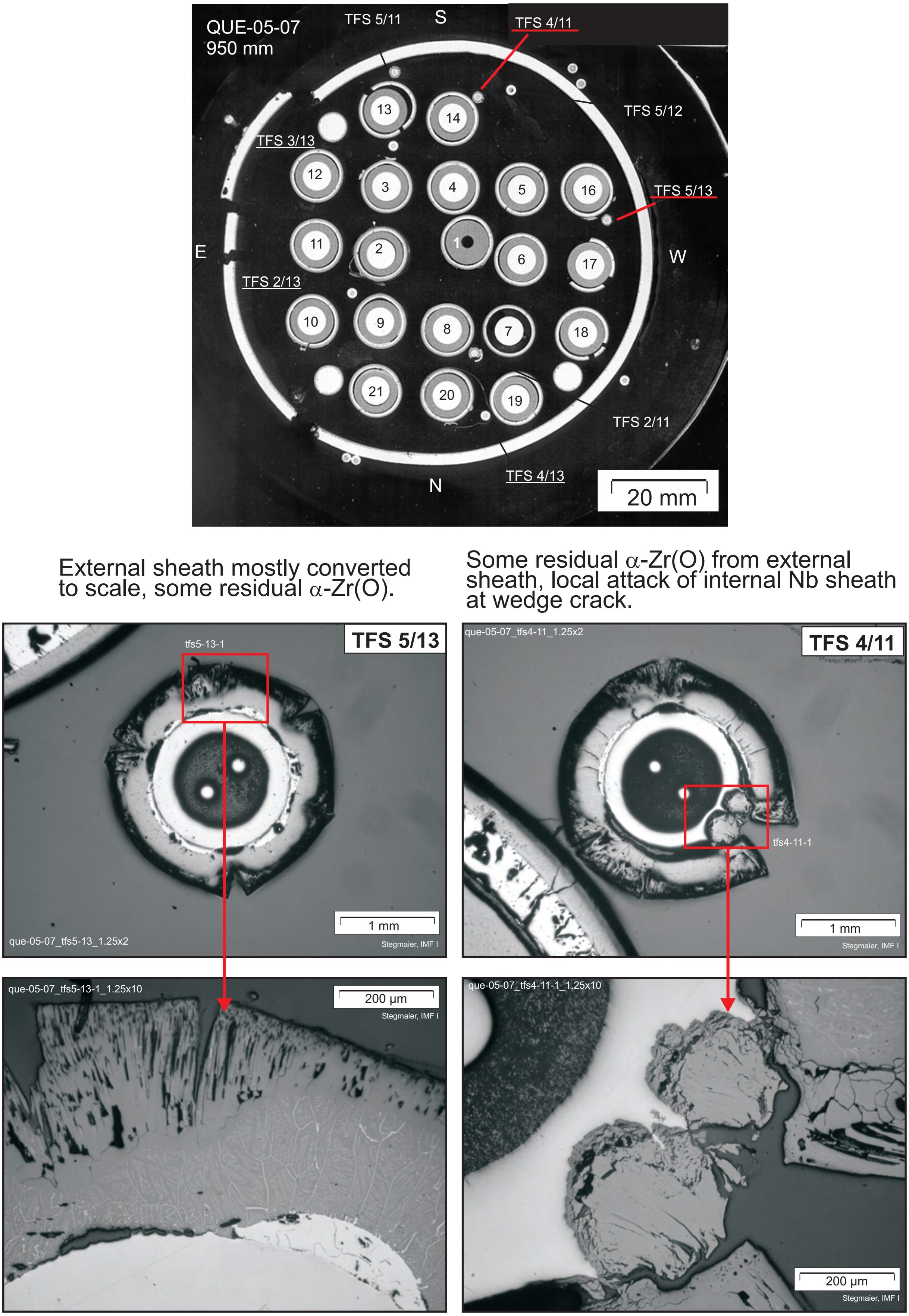

External sheath mostly converted to scale, some residual α-Zr(O).

Some residual α-Zr(O) from external sheath, local attack of internal Nb sheath at wedge crack.

Fig 69:QUE05-07(950mm)F950-8.cdr
22.04.02 - IMF

Fig. 69: QUENCH-05; Cross section at bundle elevation 950 mm (QUE-05-07, top); status of W-Re thermocouples.

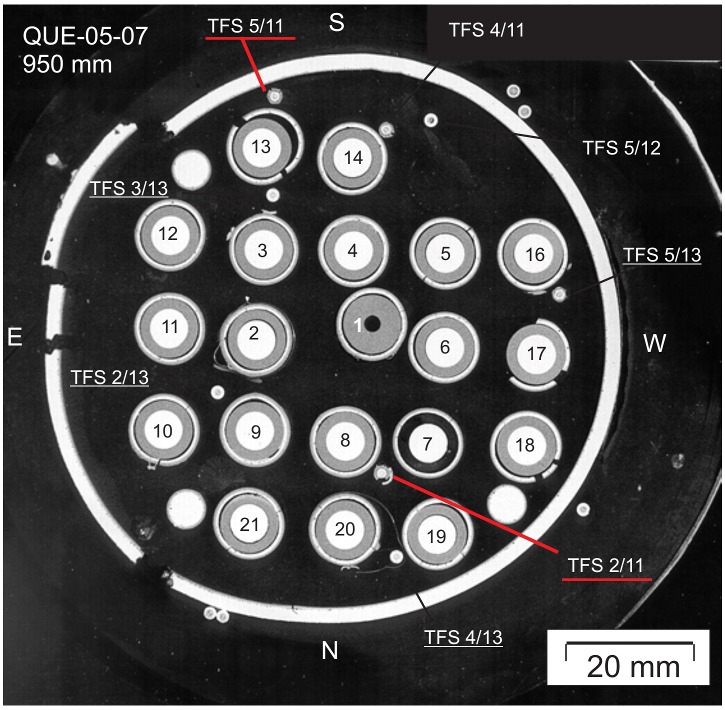

External sheath converted to ZrO_2 and wedge cracked, local Nb oxidation attack.

External sheath and clamp converted to ZrO_2, internal Nb sheath in advanced penetration.

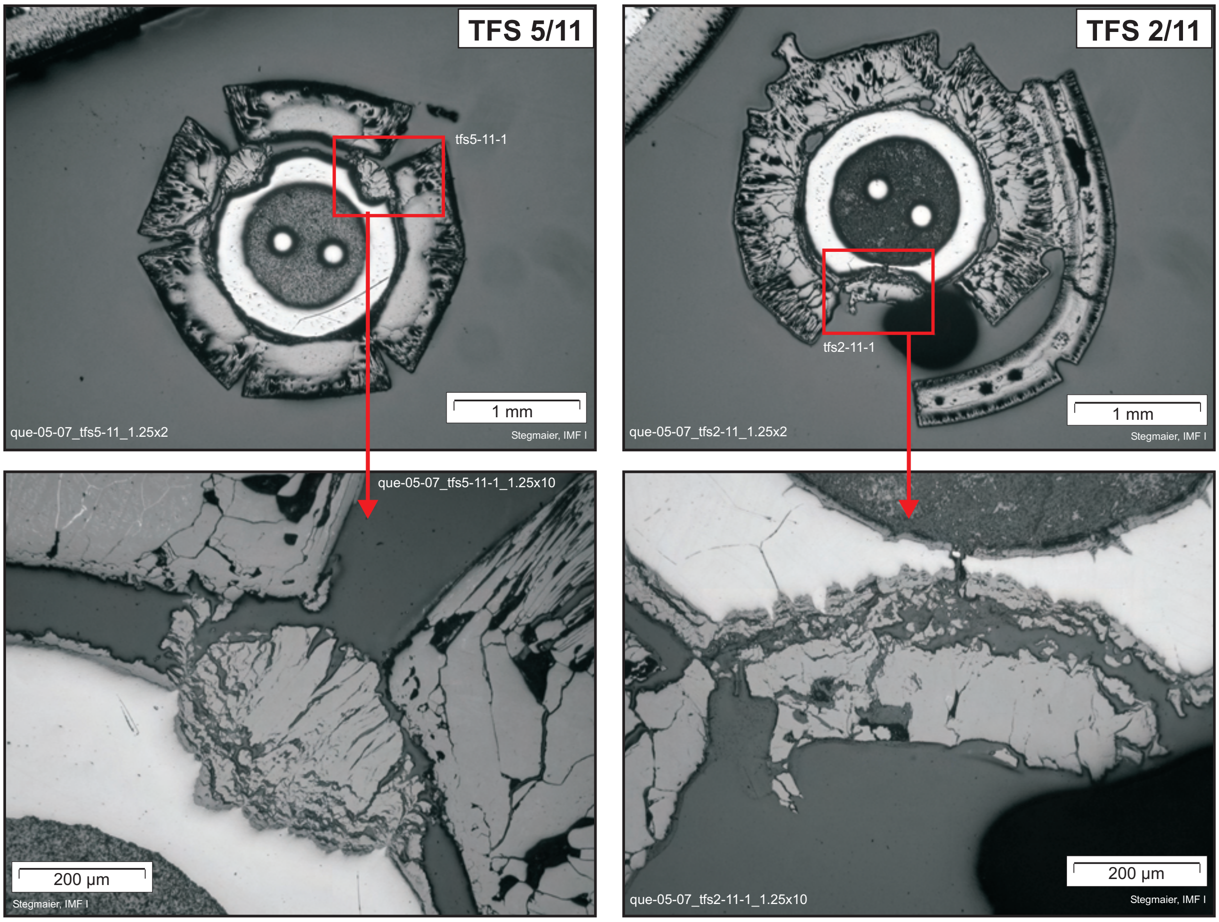

Fig 70:QUE05-07(950mm)F950-9.cdr
22.04.02 - IMF

Fig. 70: QUENCH-05; Cross section at bundle elevation 950 mm (QUE-05-07, top); status of W-Re thermocouples.

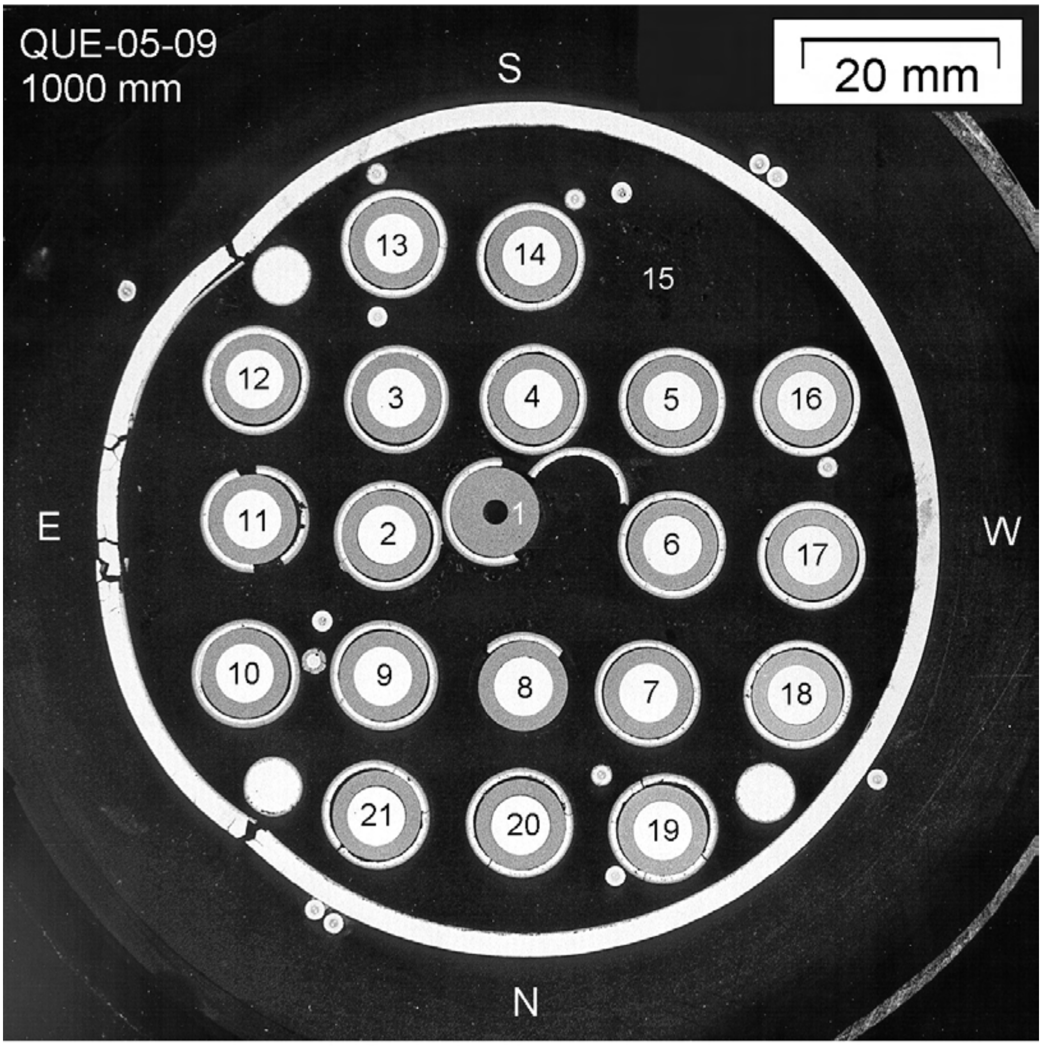

Fig71:QUE05-09(1000mm)F1000-1.cdr
23.04.02 - IMF

Fig. 71: QUENCH-05; Cross section at bundle elevation 1000 mm (QUE-05-09, top); overview.

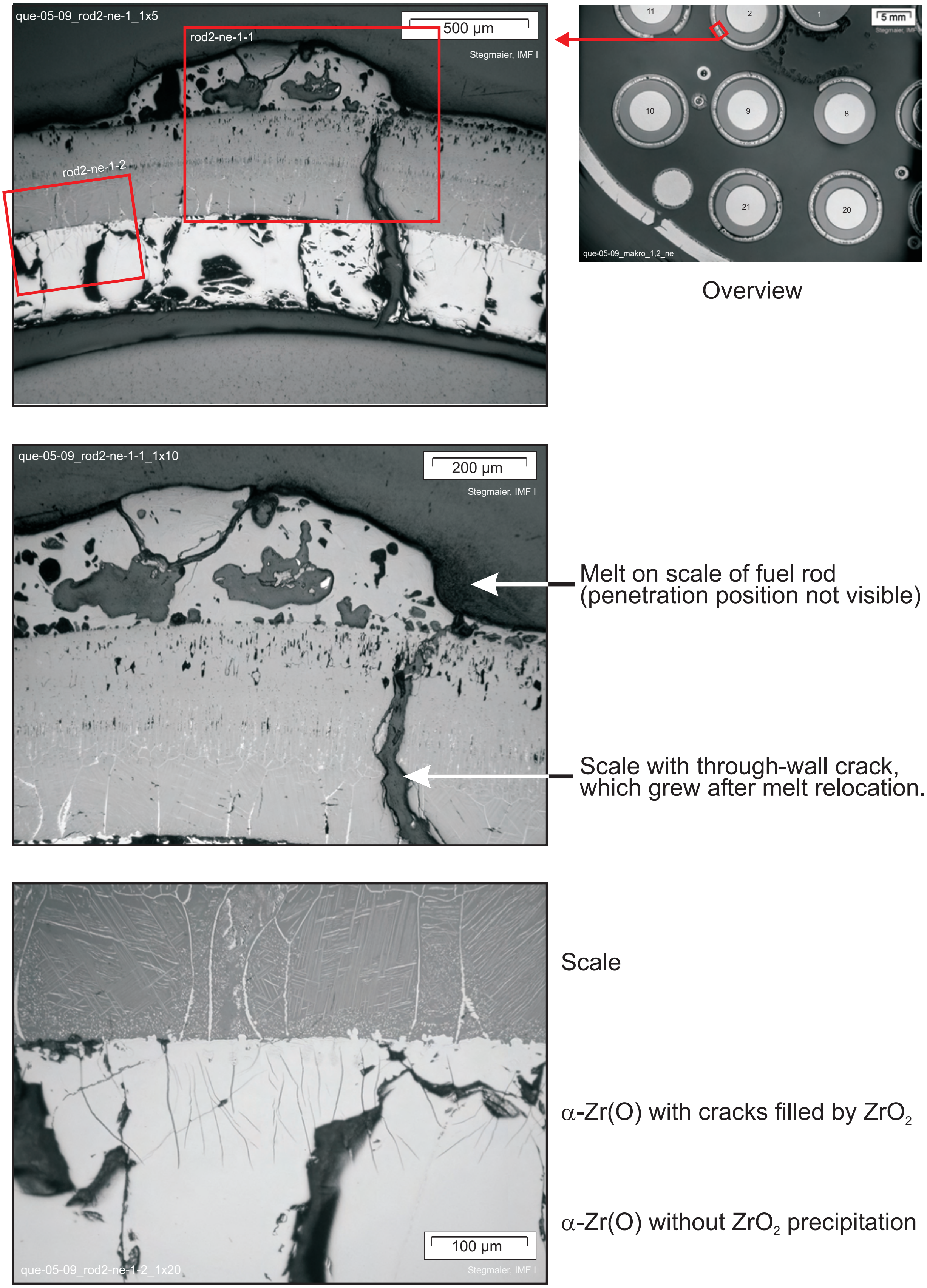

Overview

Melt on scale of fuel rod (penetration position not visible)

Scale with through-wall crack, which grew after melt relocation.

Scale

α-Zr(O) with cracks filled by ZrO_2

α-Zr(O) without ZrO_2 precipitation

Fig72:QUE05-09(1000mm)F1000-2.cdr
23.04.02 - IMF

Fig. 72: QUENCH-05; Cross section at bundle elevation 1000 mm (QUE-05-09, top); final status of rod and relocated melt.

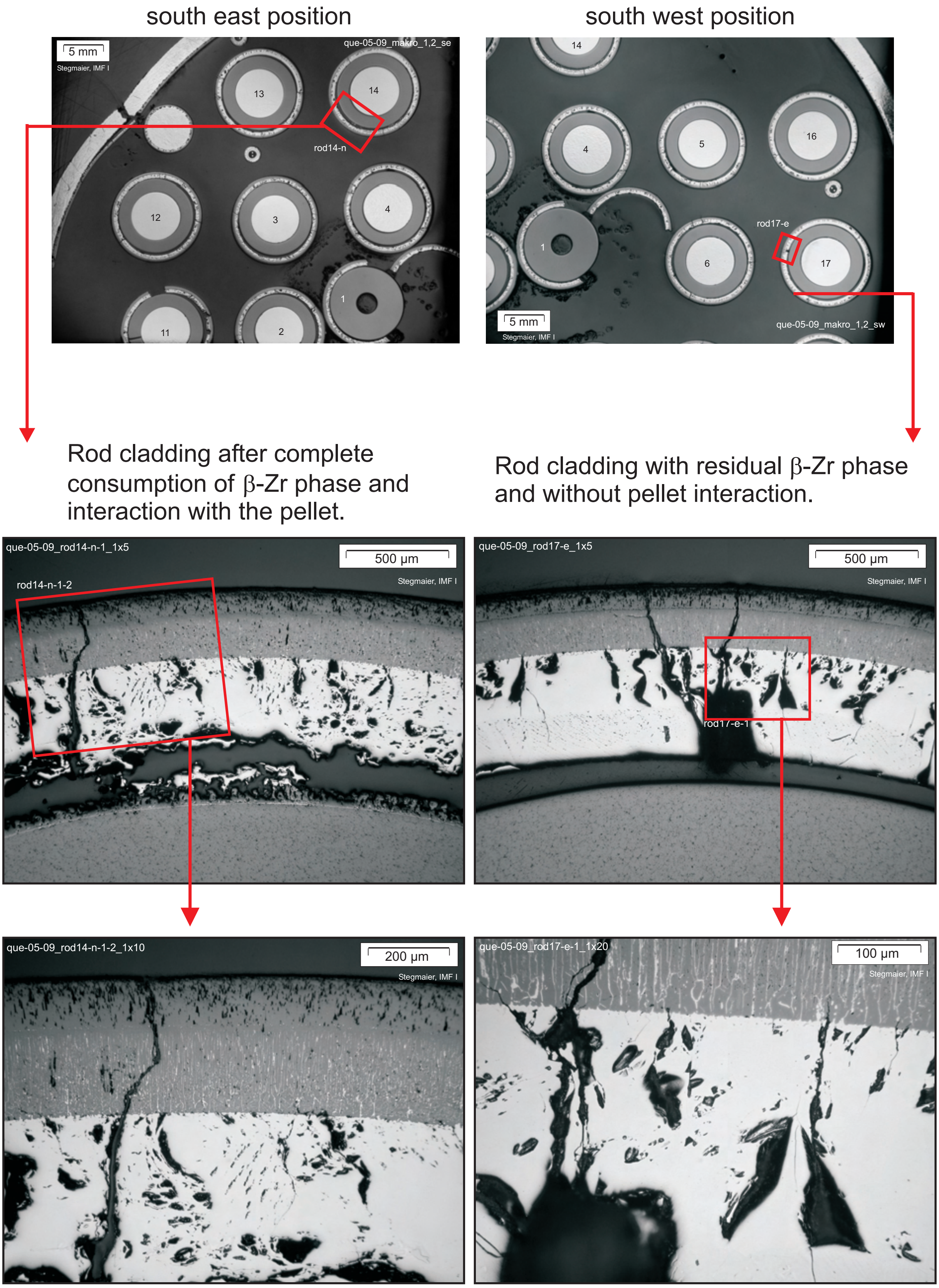

Fig73:QUE05-09(1000mm)F1000-3.cdr
23.04.02 - IMF

Fig. 73: QUENCH-05; Cross section at bundle elevation 1000 mm (QUE-05-09, top); non-oxidized through-wall crack surfaces.

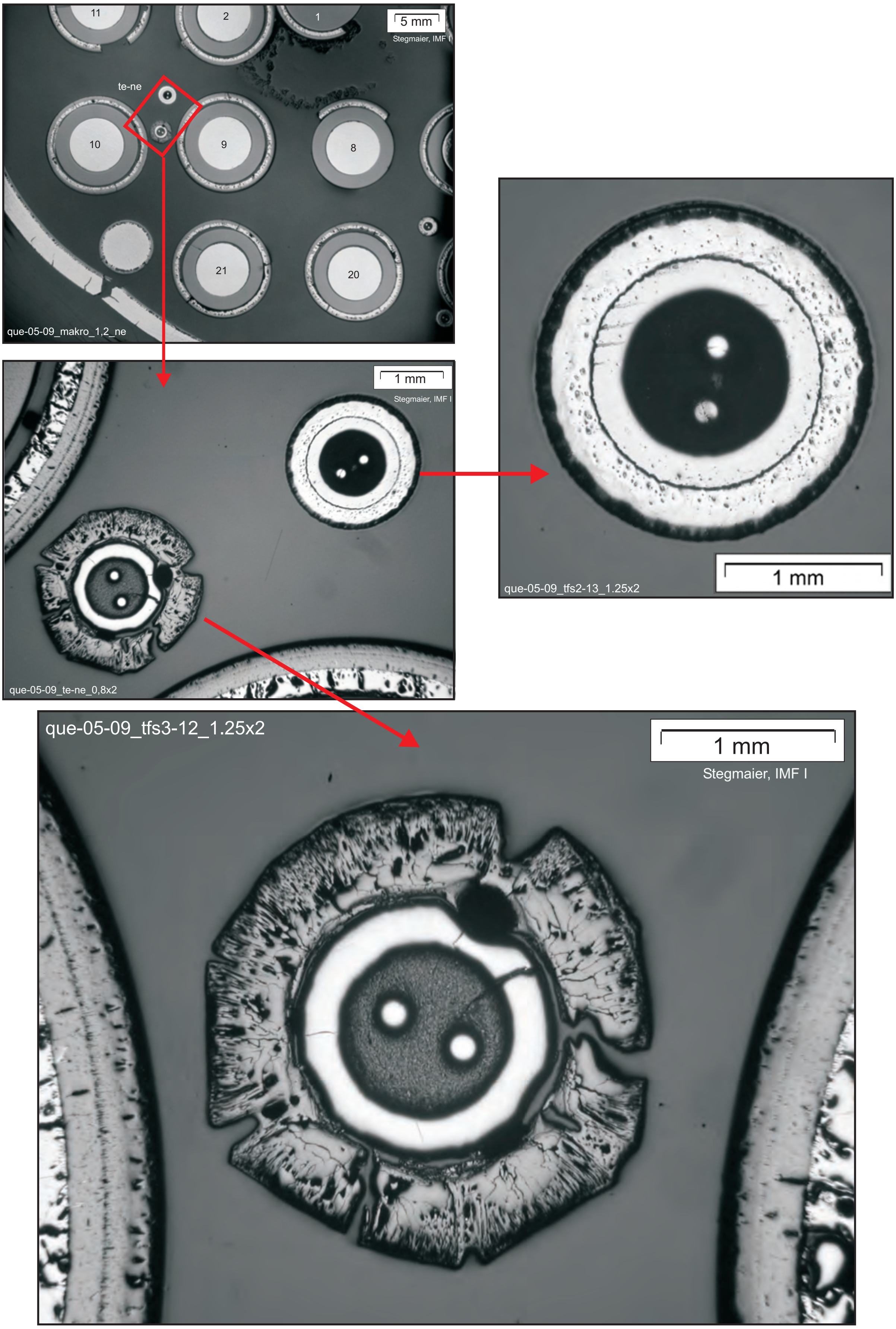

Fig74:QUE05-09(1000mm)F1000-4.cdr
23.04.02 - IMF

Fig. 74: QUENCH-05; Cross section at bundle elevation 1000 mm (QUE-05-09, top); status of two thermocouples in close vicinity.

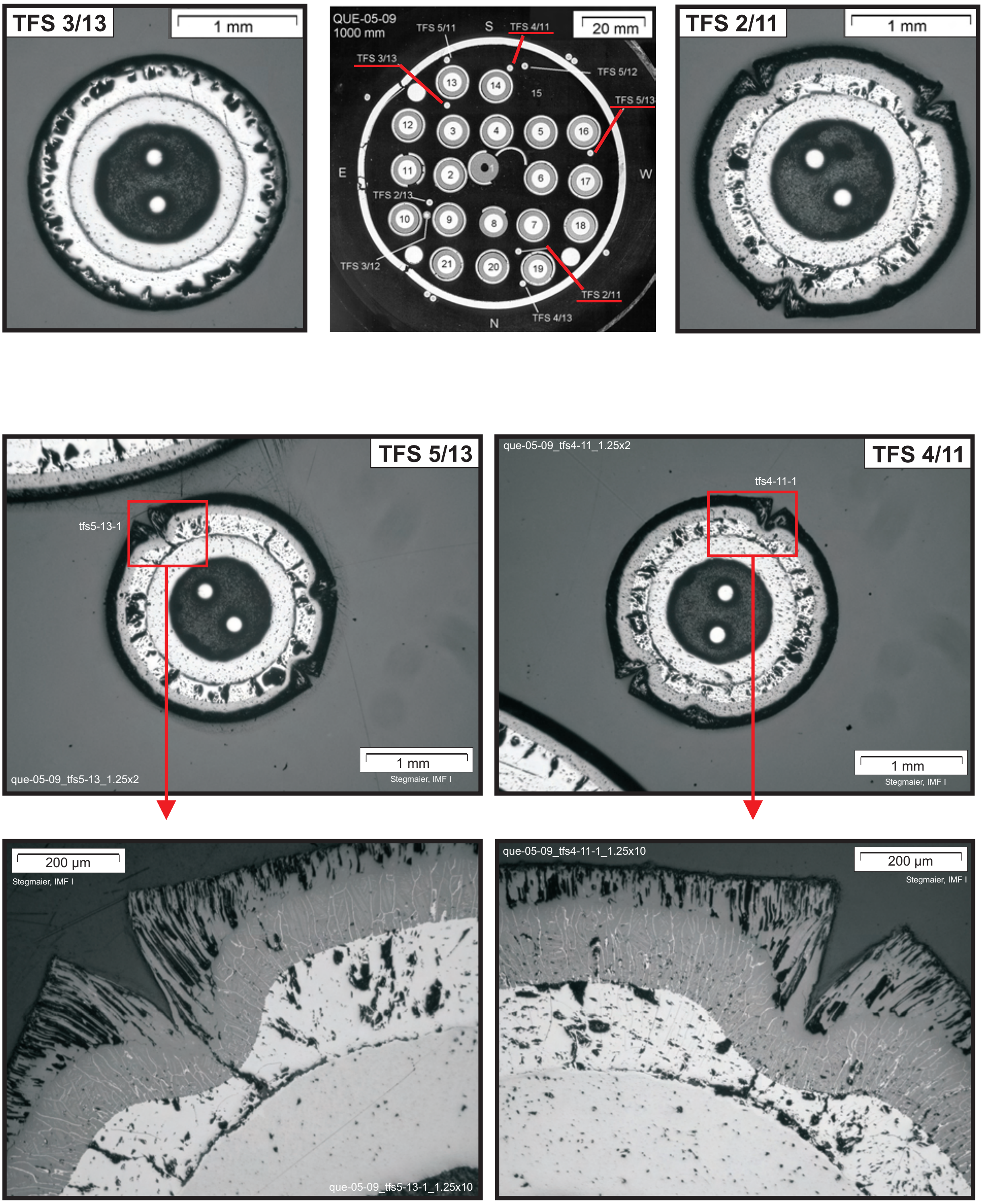

Fig75:QUE05-09(1000mm)F1000-5.cdr
23.04.02 - IMF

Fig. 75: QUENCH-05; Cross section at bundle elevation 1000 mm (QUE-05-09, top); thermocouple oxidation status.

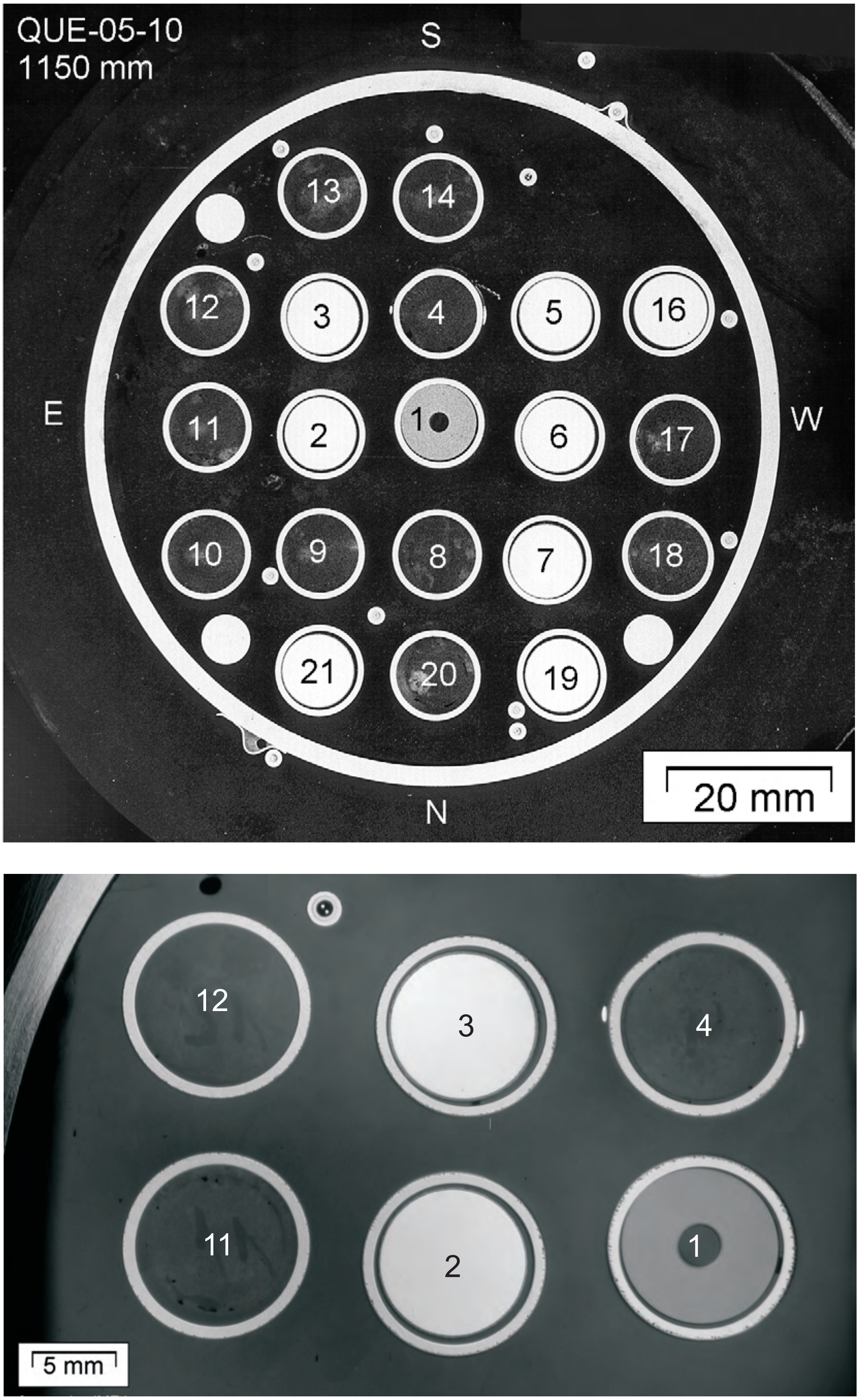

Fig76:QUE05-10(1150mm)F1150-1.cdr
23.04.02 - IMF

Fig. 76: QUENCH-05; Cross section at bundle elevation 1150 mm (QUE-05-10, top); overview.

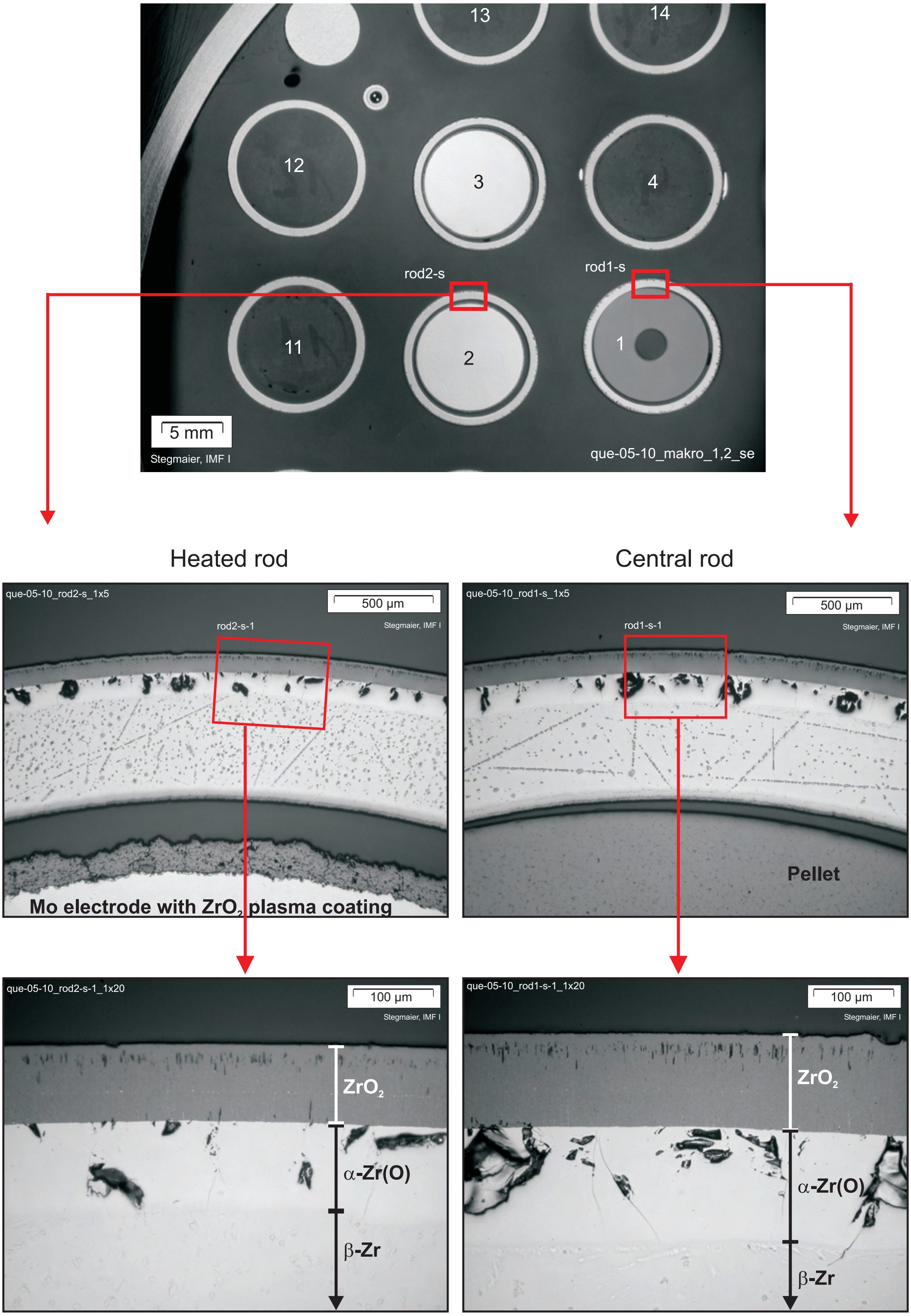

Fig77:QUE05-10(1150mm)F1150-2.cdr
24.04.02 - IMF

Fig. 77: QUENCH-05; Cross section at bundle elevation 1150 mm (QUE-05-10, top); rod oxidation status.

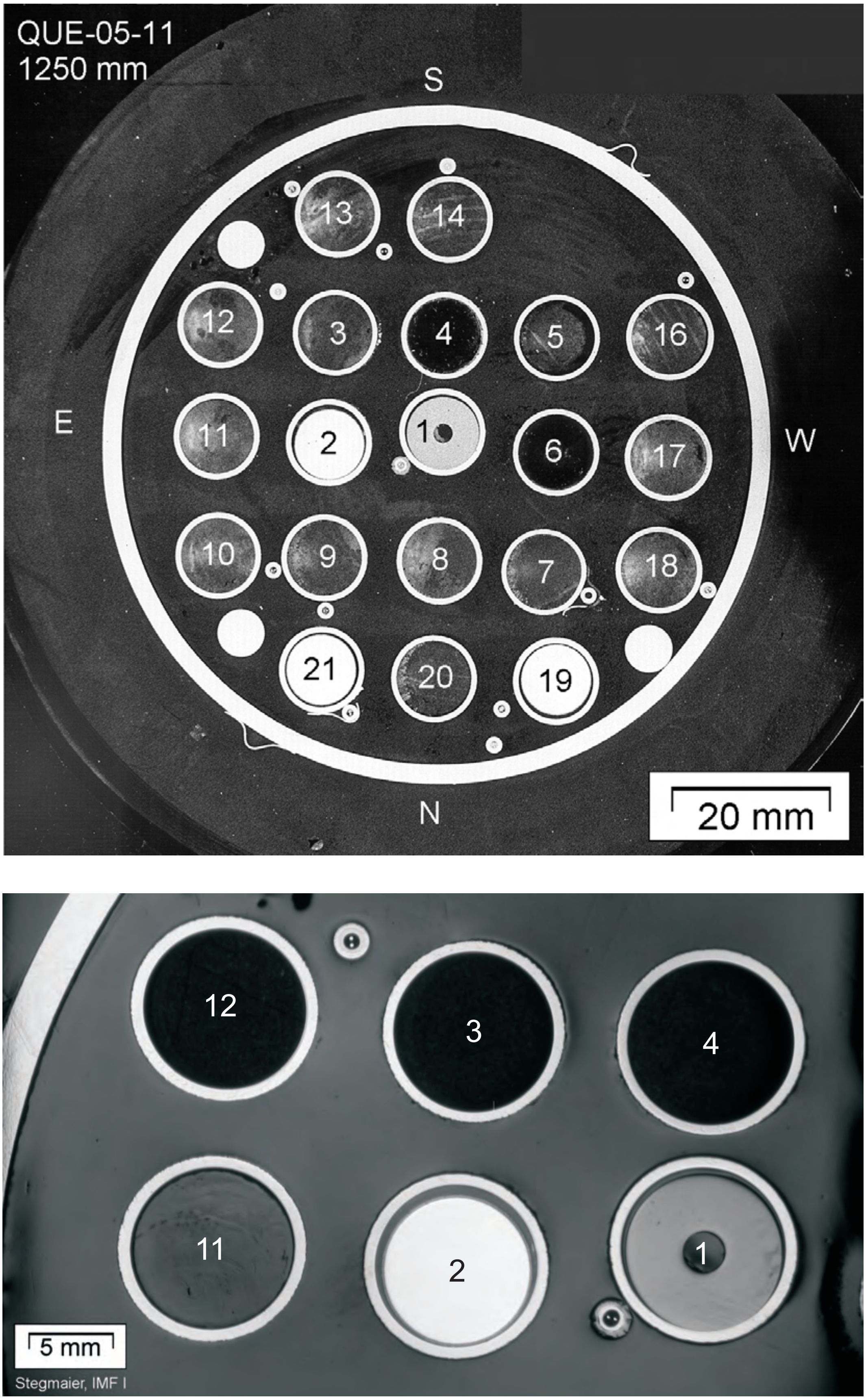

Fig78:QUE05-11(1250mm)F1250-1.cdr
23.04.02 - IMF

Fig. 78: QUENCH-05; Cross section at bundle elevation 1250 mm (QUE-05-11, top); overview.

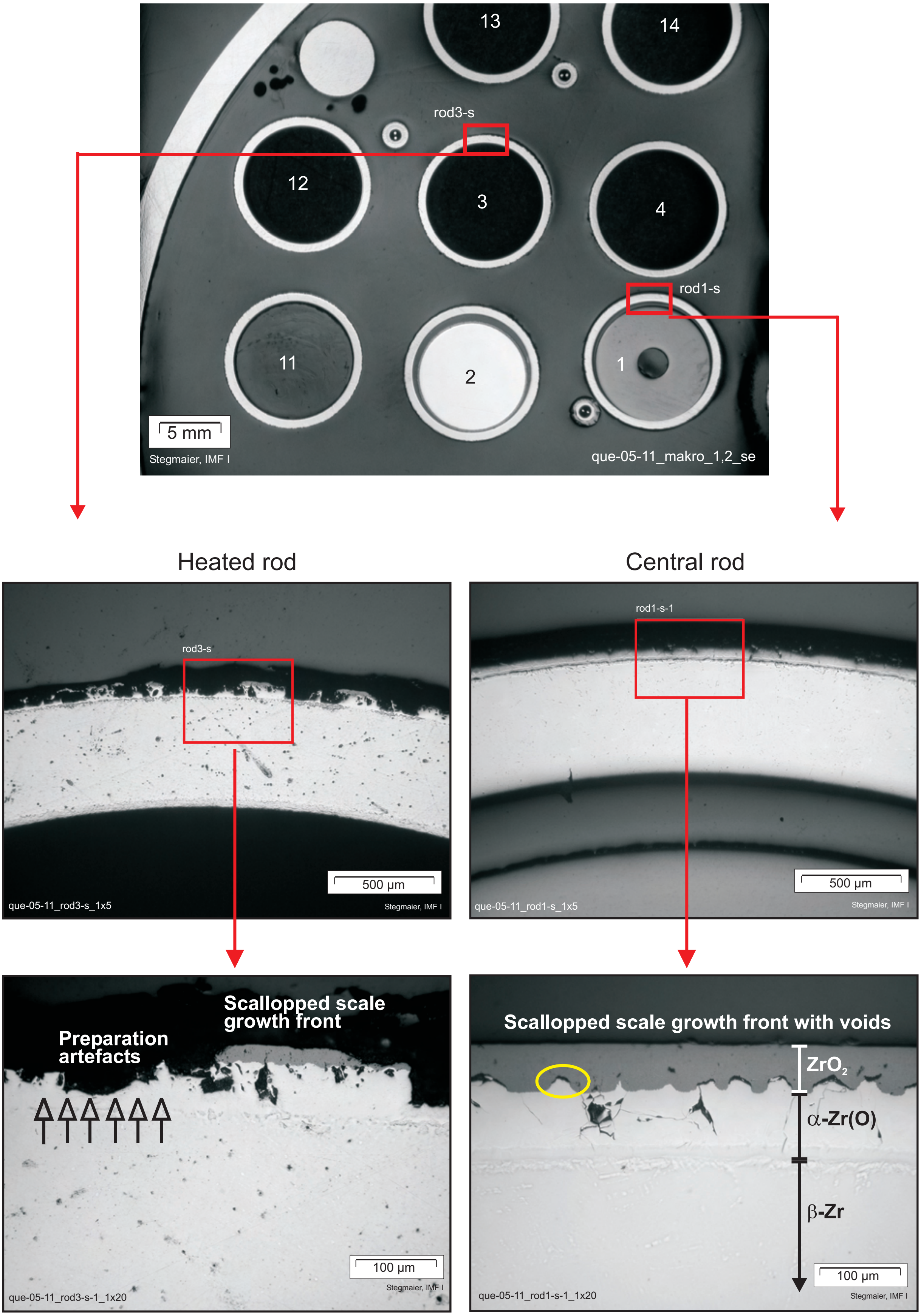

Fig79:QUE05-11(1250mm)F1250-2.cdr
23.04.02 - IMF

Fig. 79: QUENCH-05; Cross section at bundle elevation 1250 mm (QUE-05-11, top); rod oxidation status indicating pretransition phase of breakaway phenomenon.

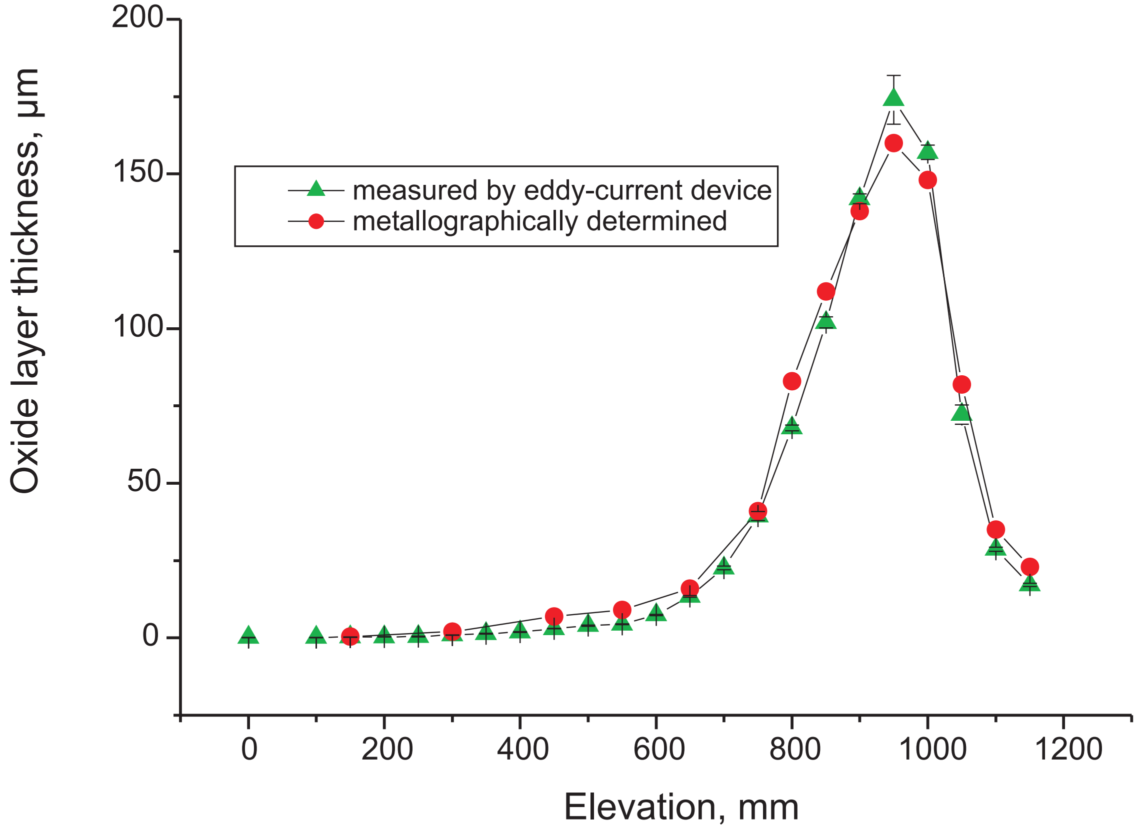

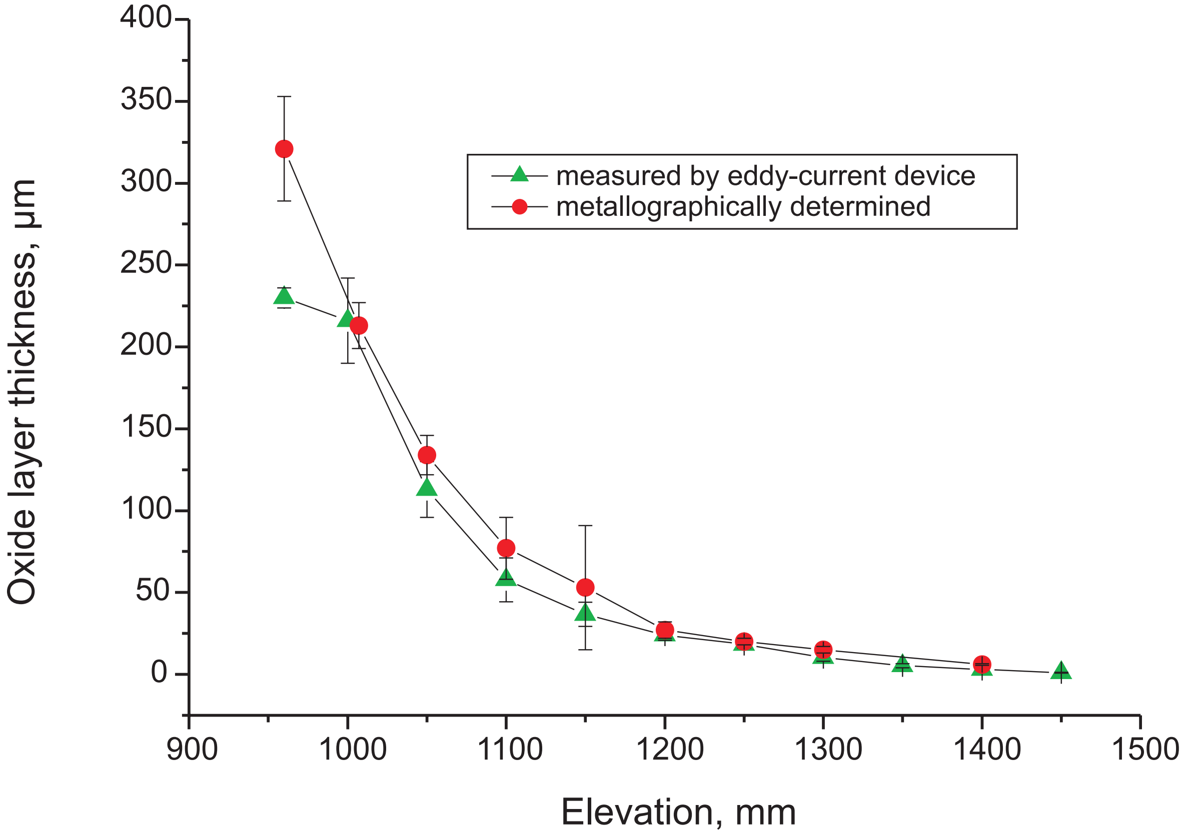

Fig 80-QUE05 eckstab oxid.cdr
24.04.02 - IMF

Fig. 80: QUENCH-05; Oxide layer thickness of corner rod B (withdrawn from bundle during transient), top, and of rod 15, bottom

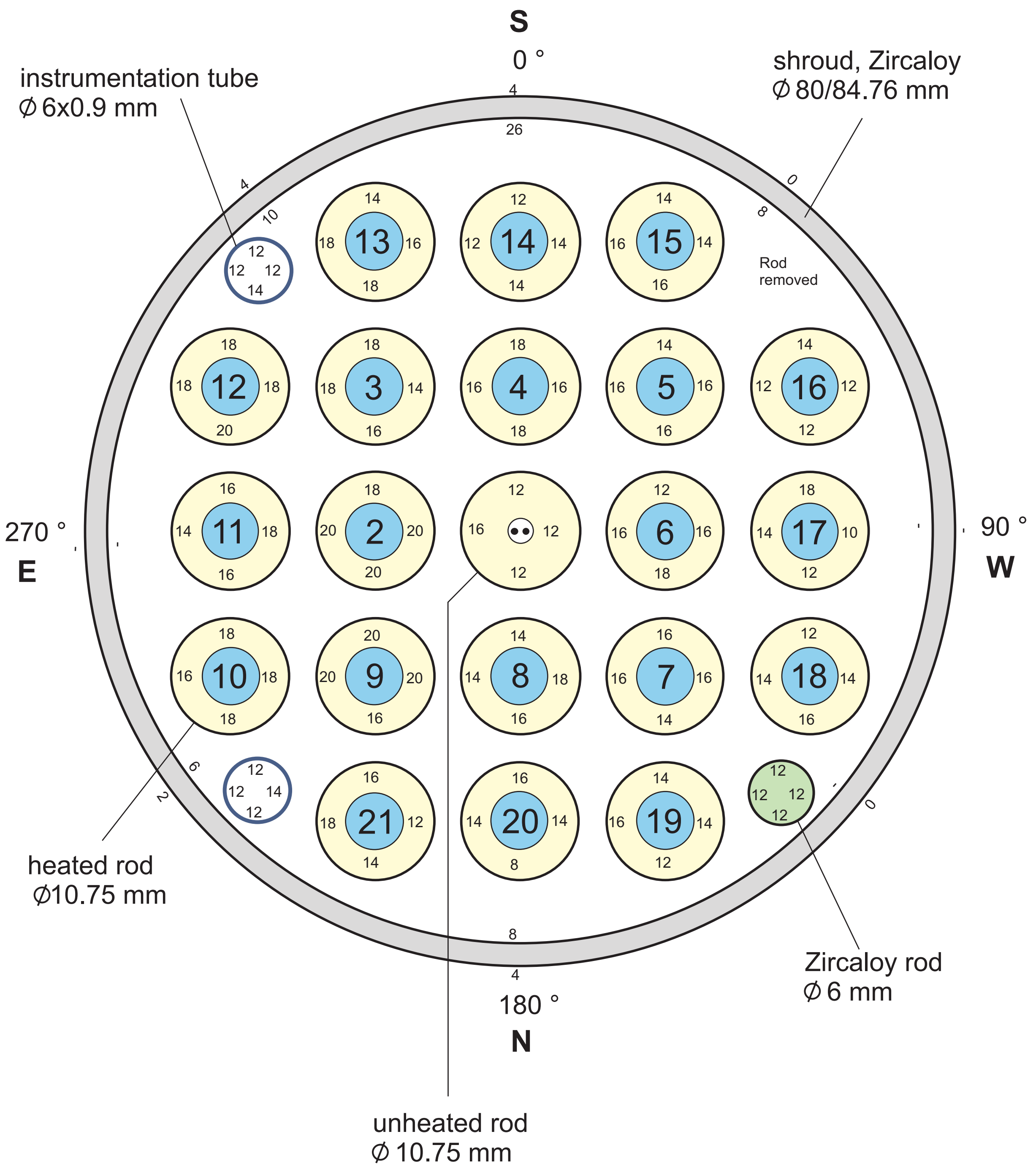

Fig 81-QUE05 cross section QUE-05-3.cdr
24.04.02 - IMF

Fig. 81: QUENCH-05; Oxide layer thicknesses at bundle elevation 550 mm

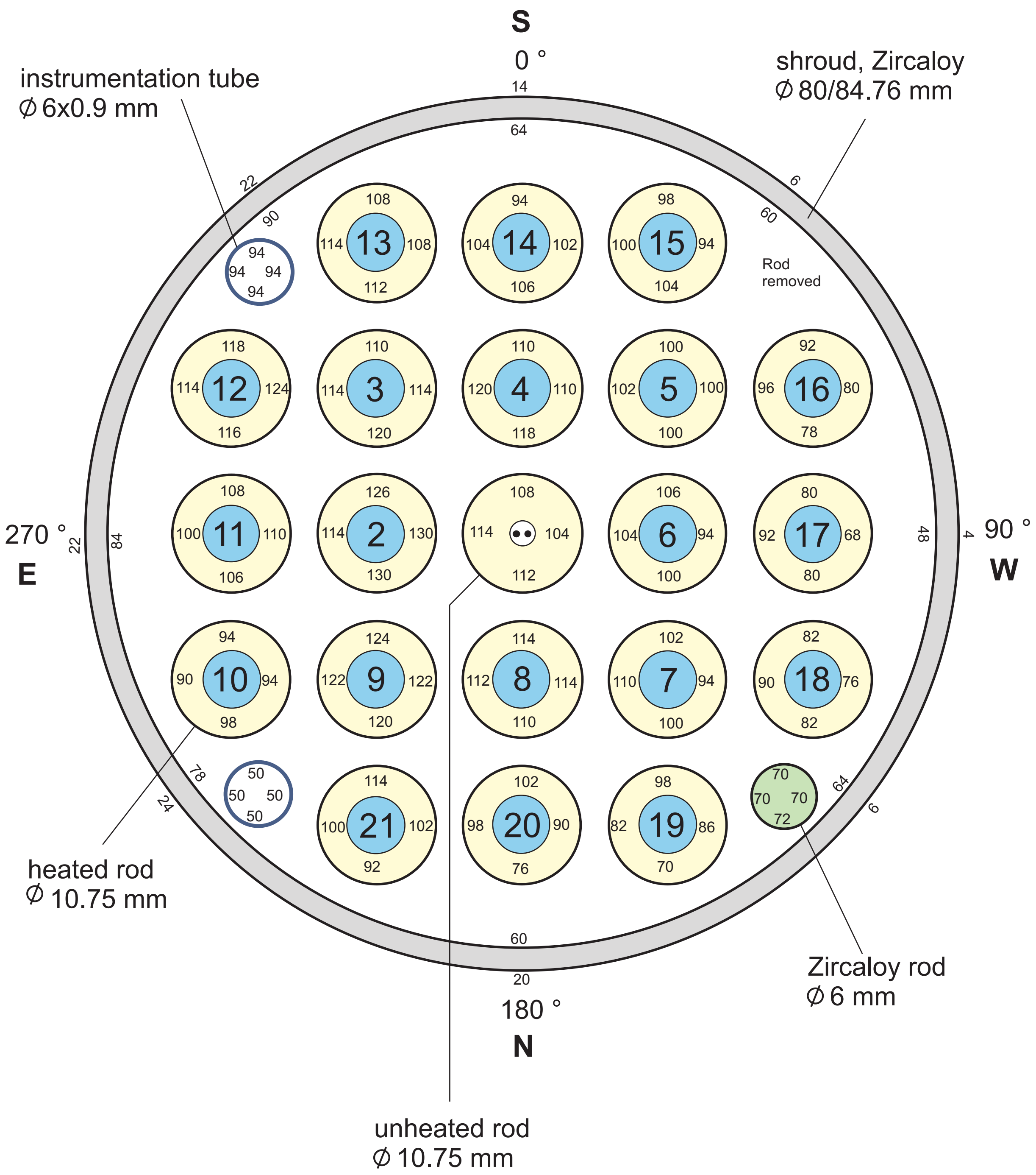

Fig 82-QUE05 cross section QUE-05-4.cdr
24.04.02 - IMF

Fig. 82: QUENCH-05; Oxide layer thicknesses at bundle elevation 750 mm

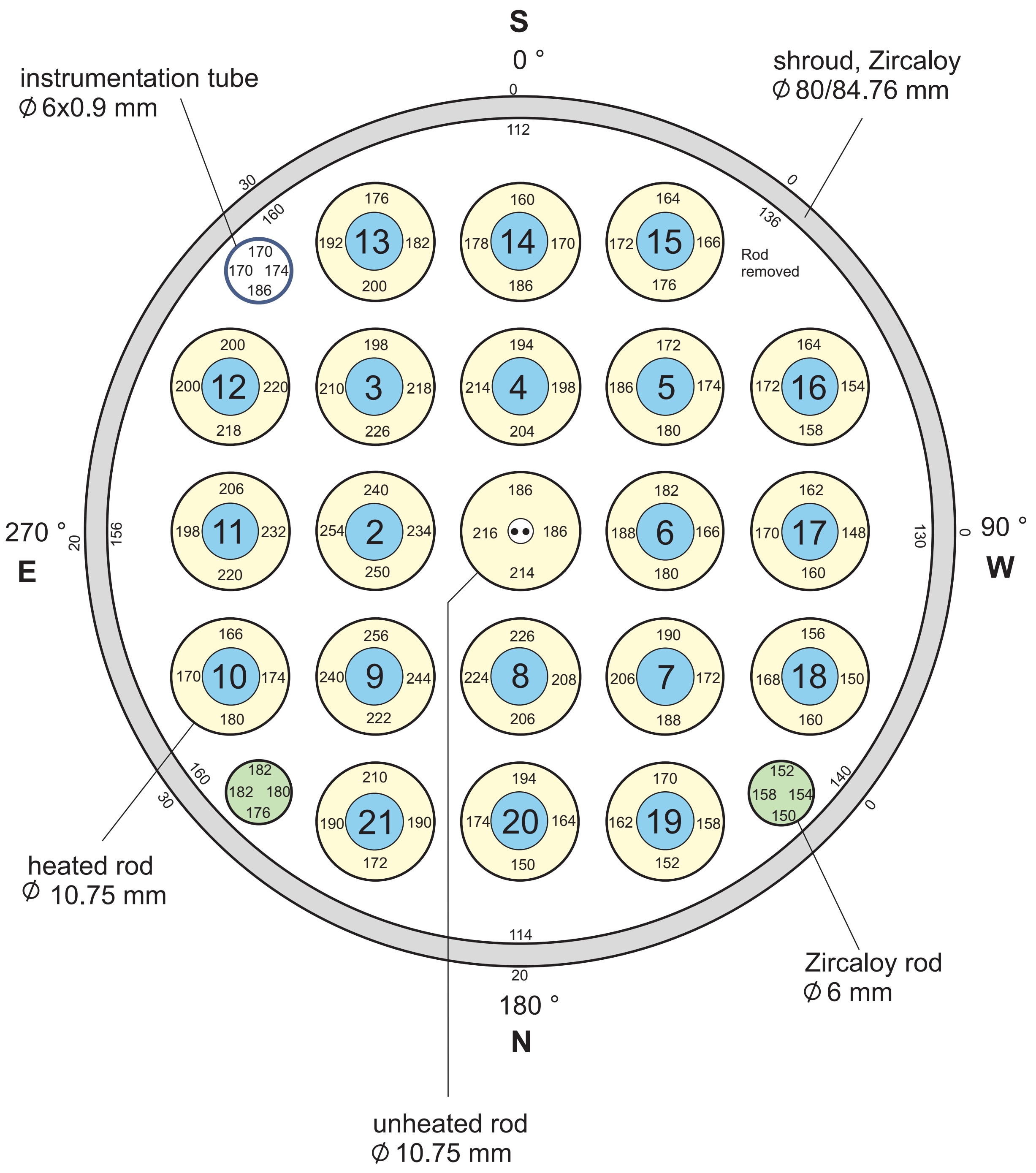

Fig 83-QUE05 cross section QUE-05-5.cdr
24.04.02 - IMF

Fig. 83: QUENCH-05; Oxide layer thicknesses at bundle elevation 850 mm

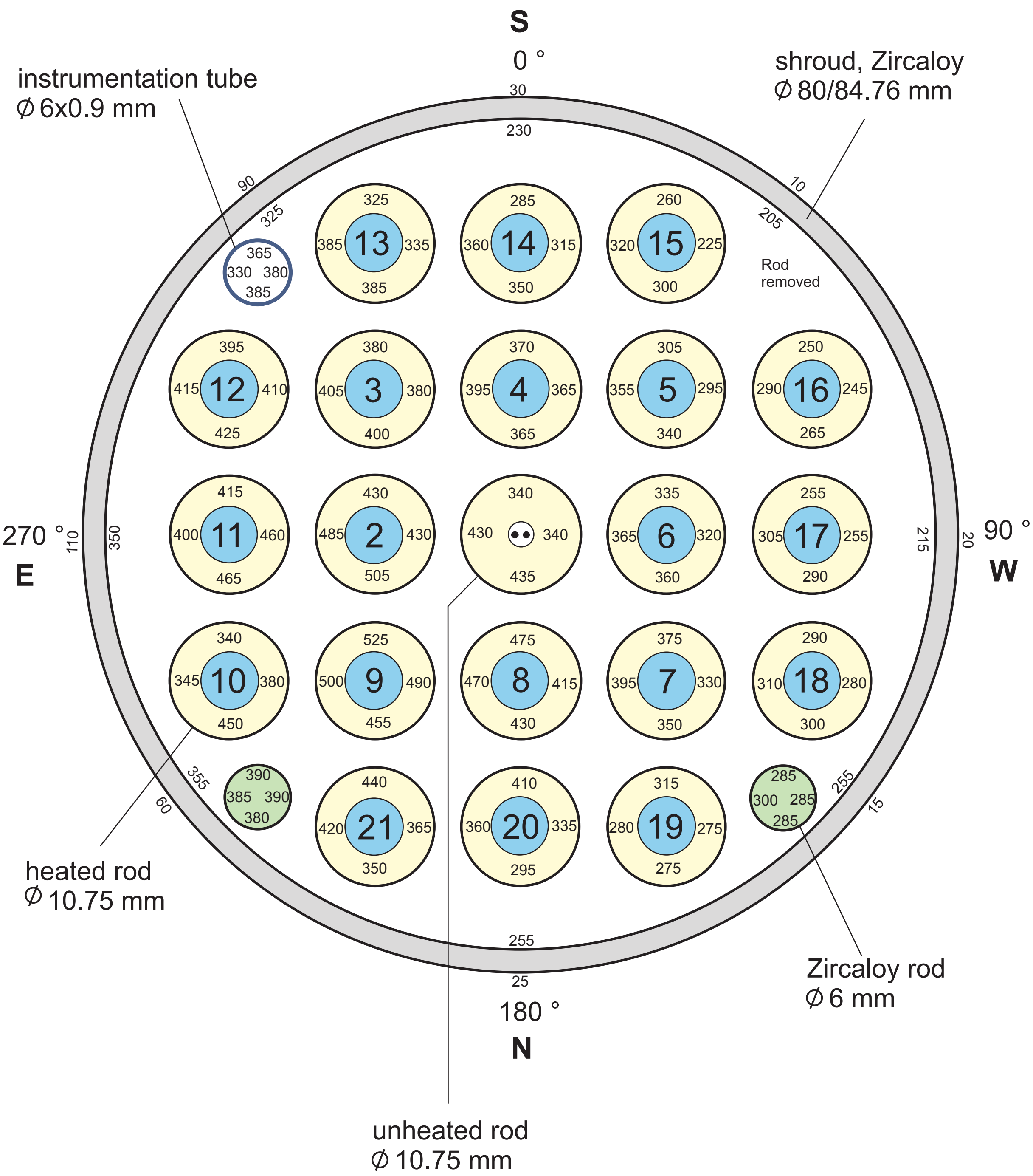

Fig 84-QUE05 cross section QUE-05-6.cdr
24.04.02 - IMF

Fig. 84: QUENCH-05; Oxide layer thicknesses at bundle elevation 920 mm

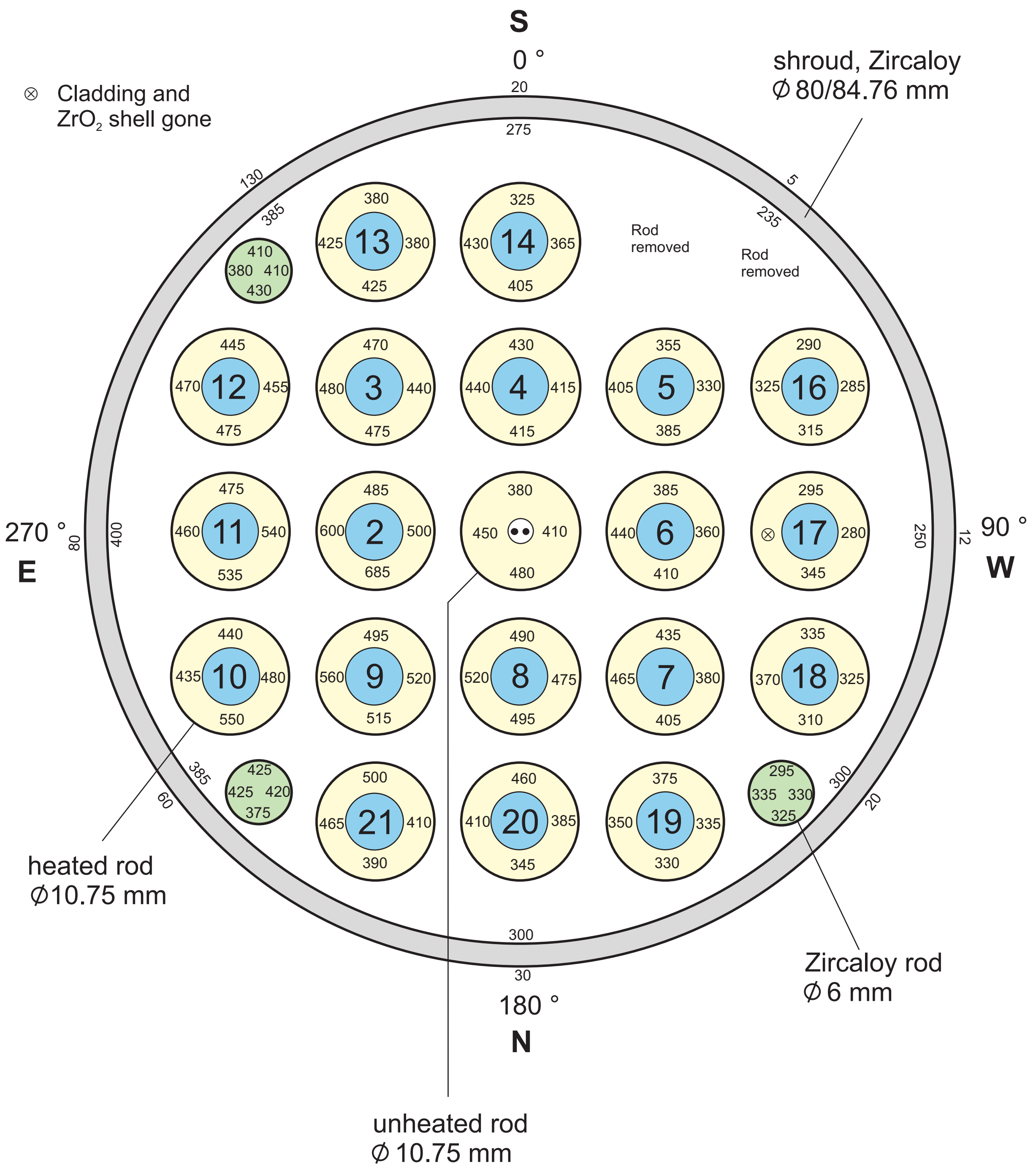

Fig 85-QUE05 cross section QUE-05-7.cdr
24.04.02 - IMF

Fig. 85: QUENCH-05; Oxide layer thicknesses at bundle elevation 950 mm

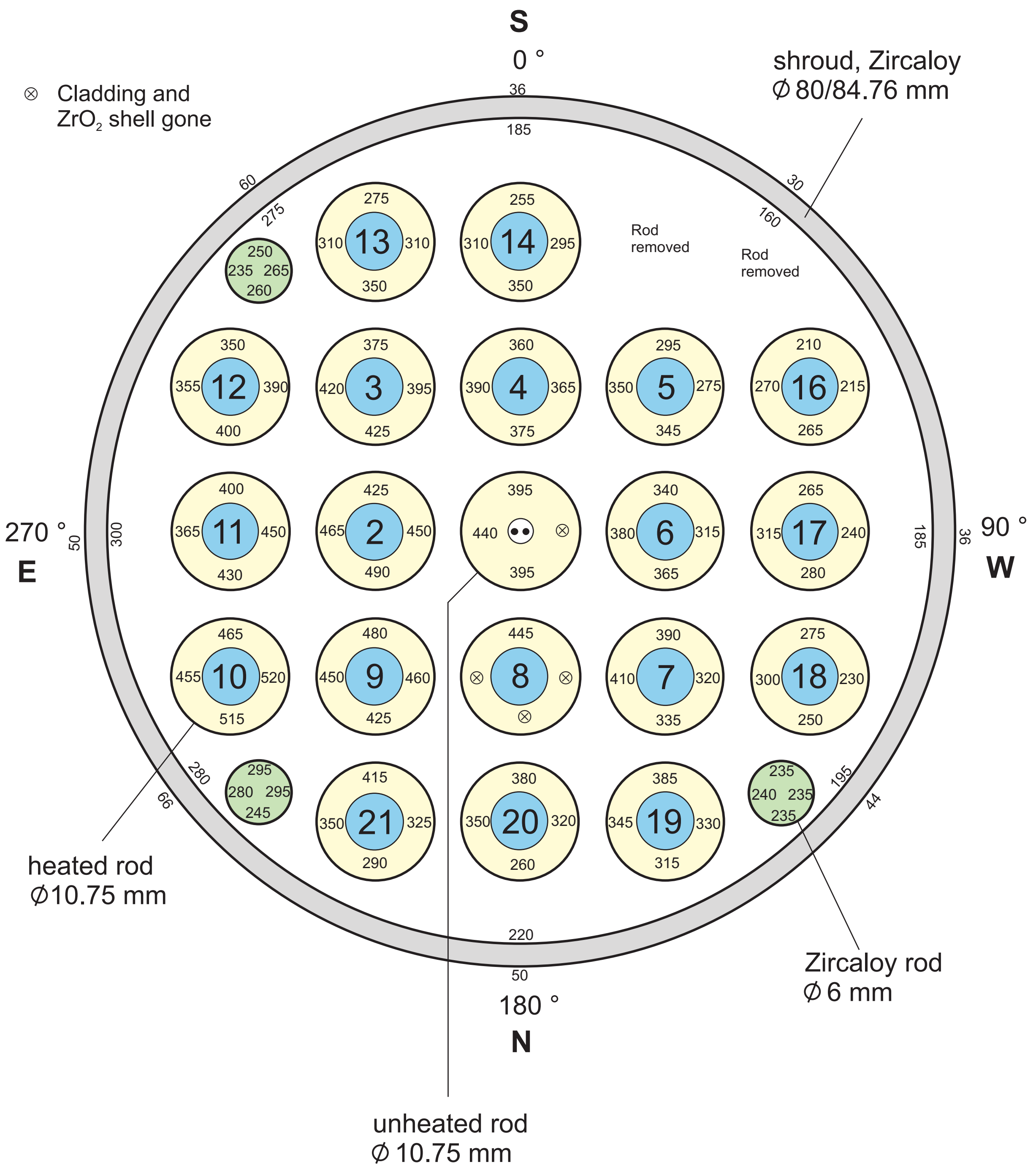

Fig 86-QUE05 cross section QUE-05-9.cdr
24.04.02 - IMF

Fig. 86: QUENCH-05; Oxide layer thicknesses at bundle elevation 1000 mm

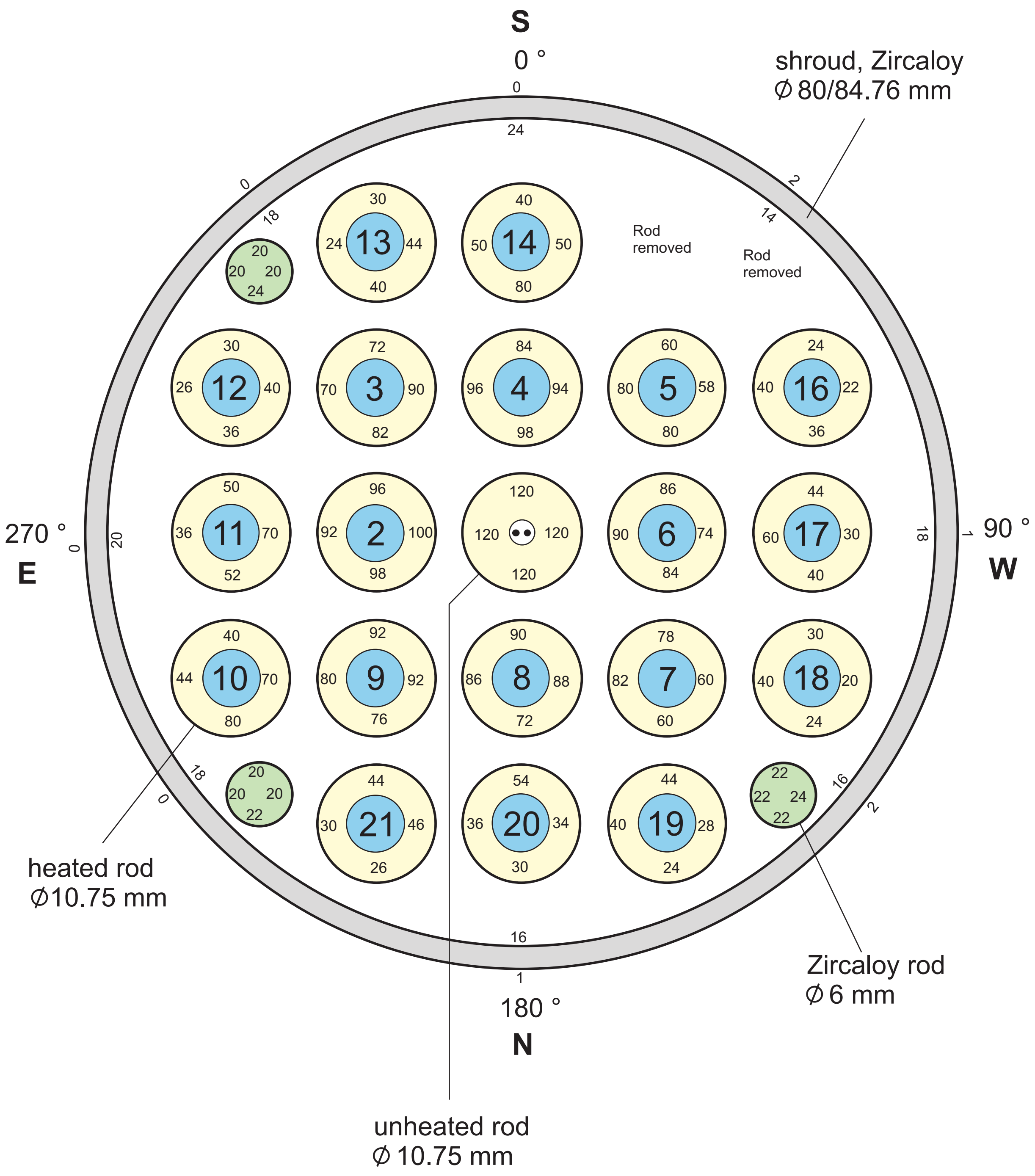

Fig 87-QUE05 cross section QUE-05-10.cdr
24.04.02 - IMF

Fig. 87: QUENCH-05; Oxide layer thicknesses at bundle elevation 1150 mm

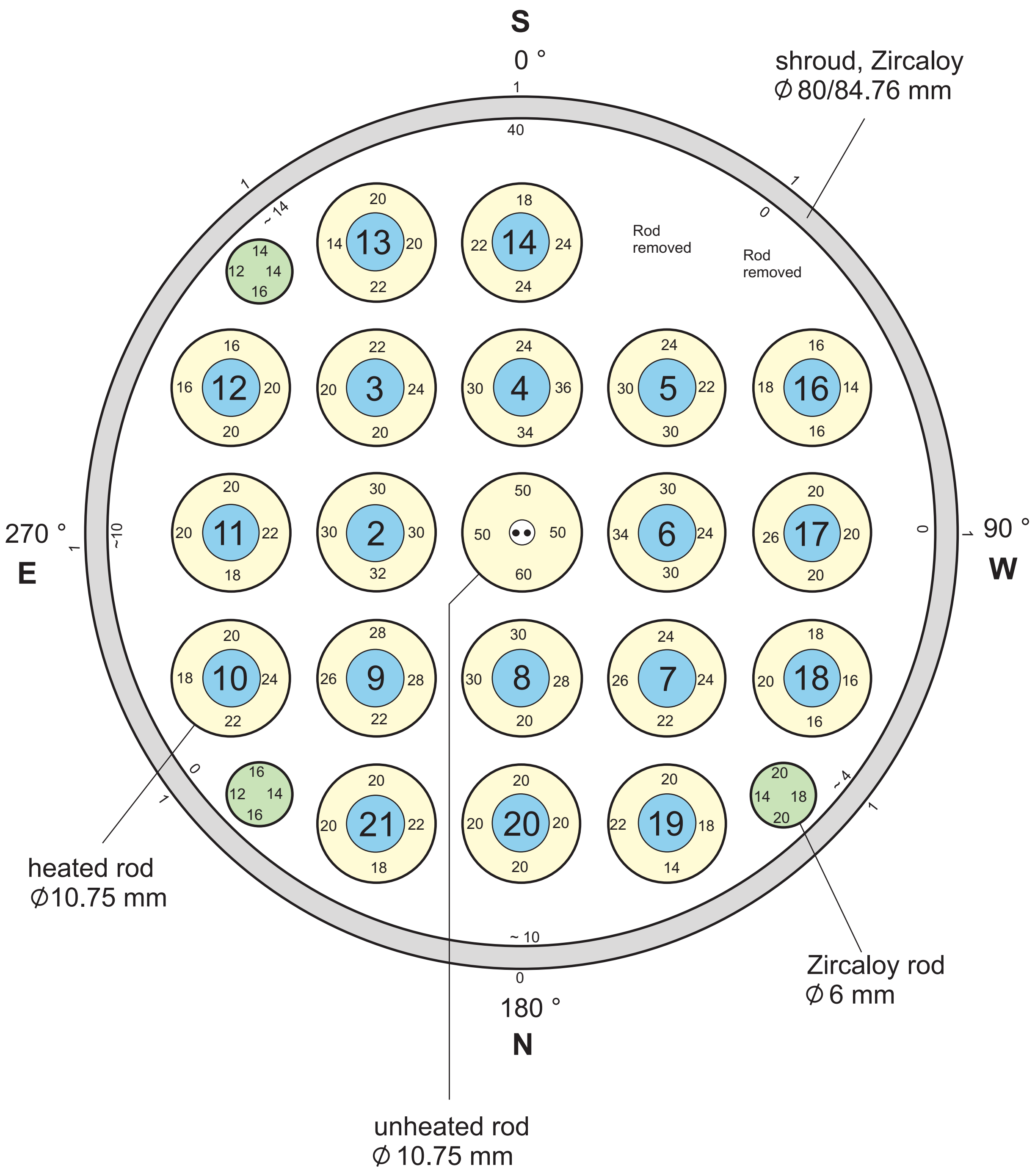

Fig 88-QUE05 cross section QUE-05-11.cdr
24.04.02 - IMF

Fig. 88: QUENCH-05; Oxide layer thicknesses at bundle elevation 1250 mm

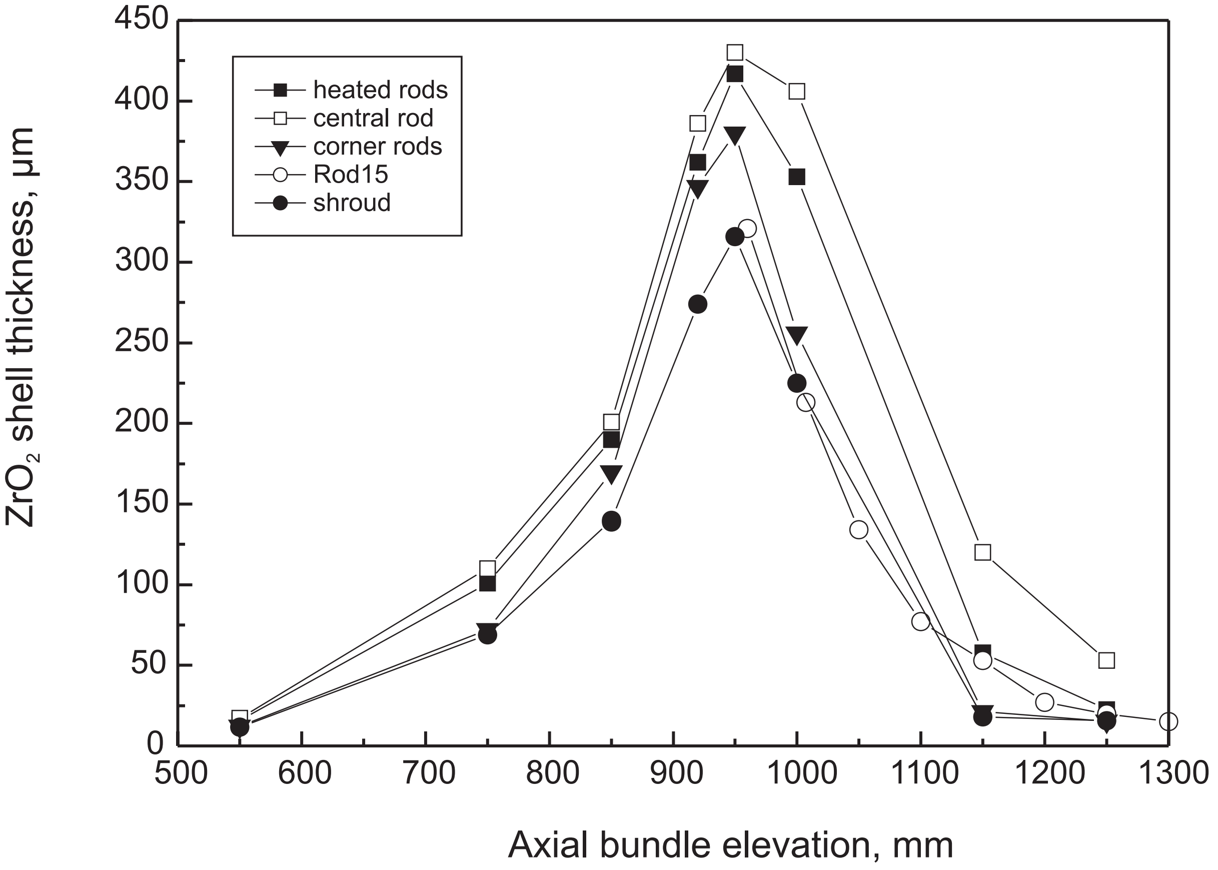

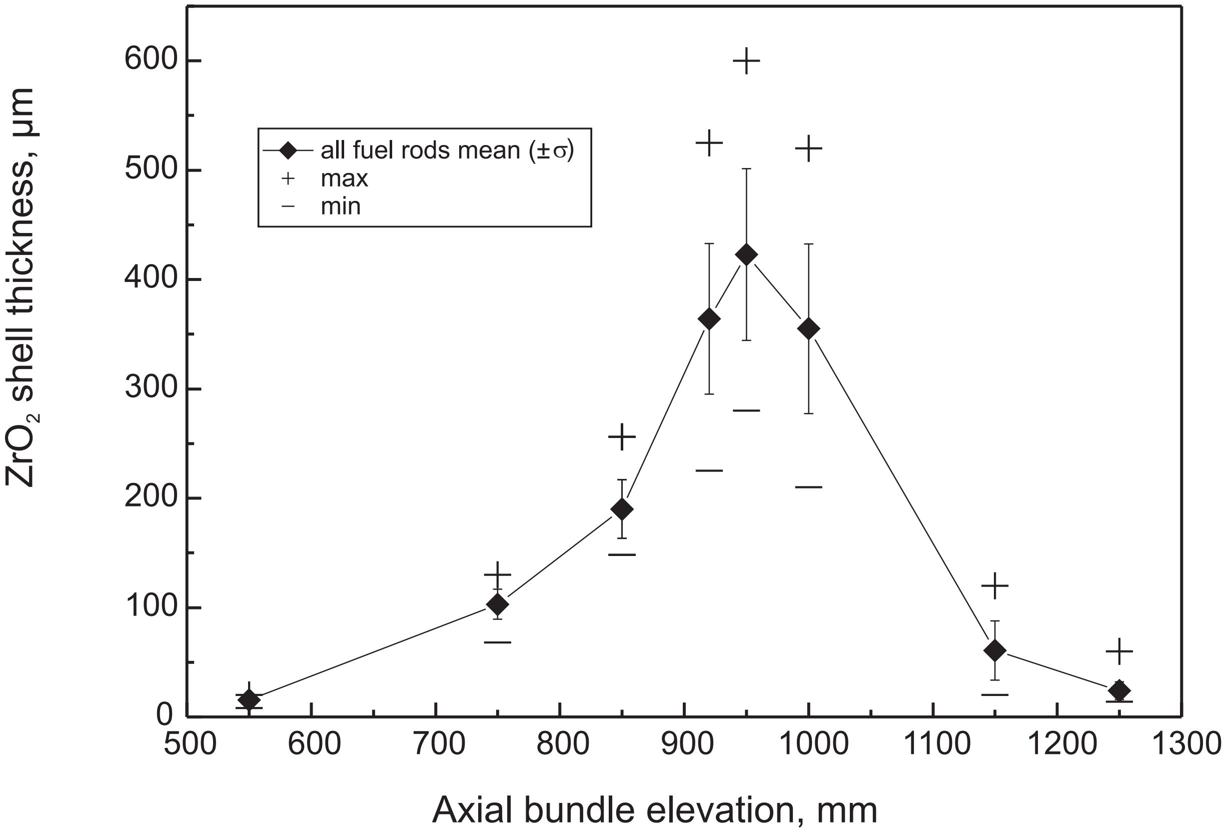

Fig 89-QUE05 Axial oxide layer.cdr
12.03.02 - IMF

Fig. 89: QUENCH-05; Axial oxide layer thickness distribution

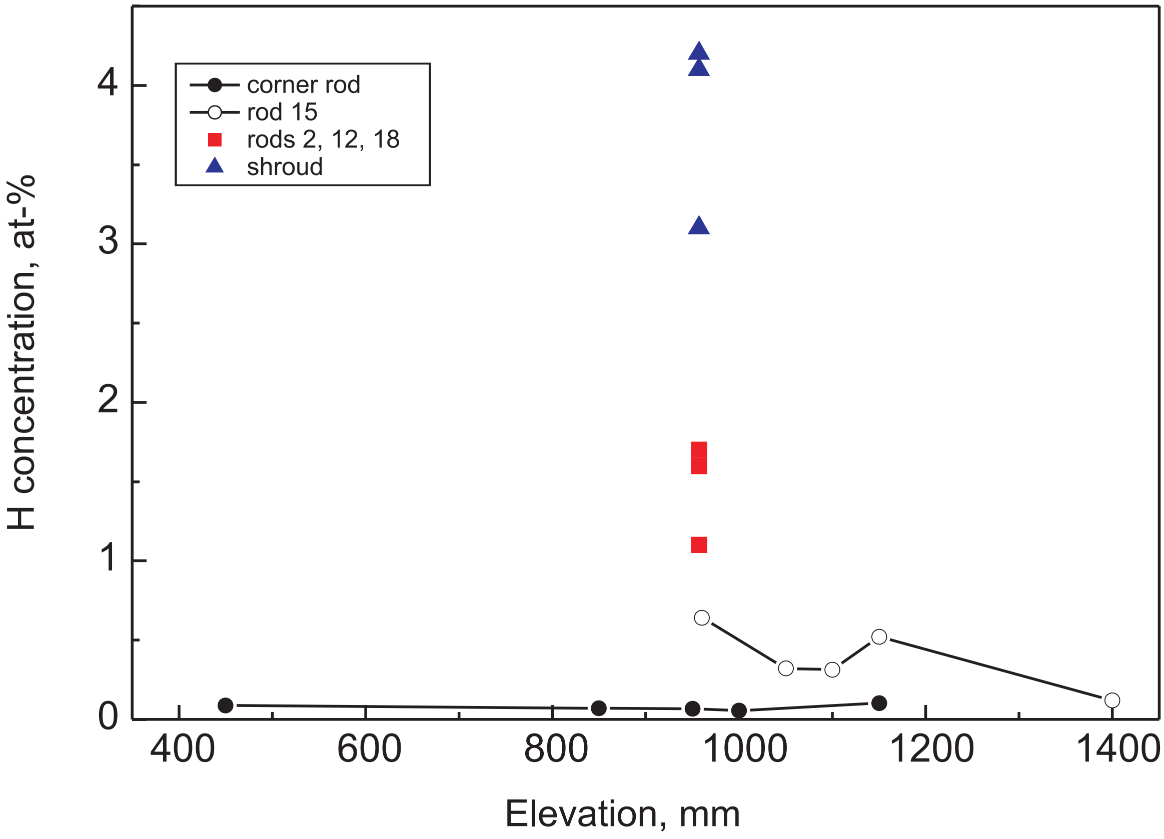

Fig 90-QUE05 H2 analyse.cdr
24.04.02 - IMF

Fig. 90: QUENCH-05; Hydrogen absorbed by the remaining Zry(O) metal phases

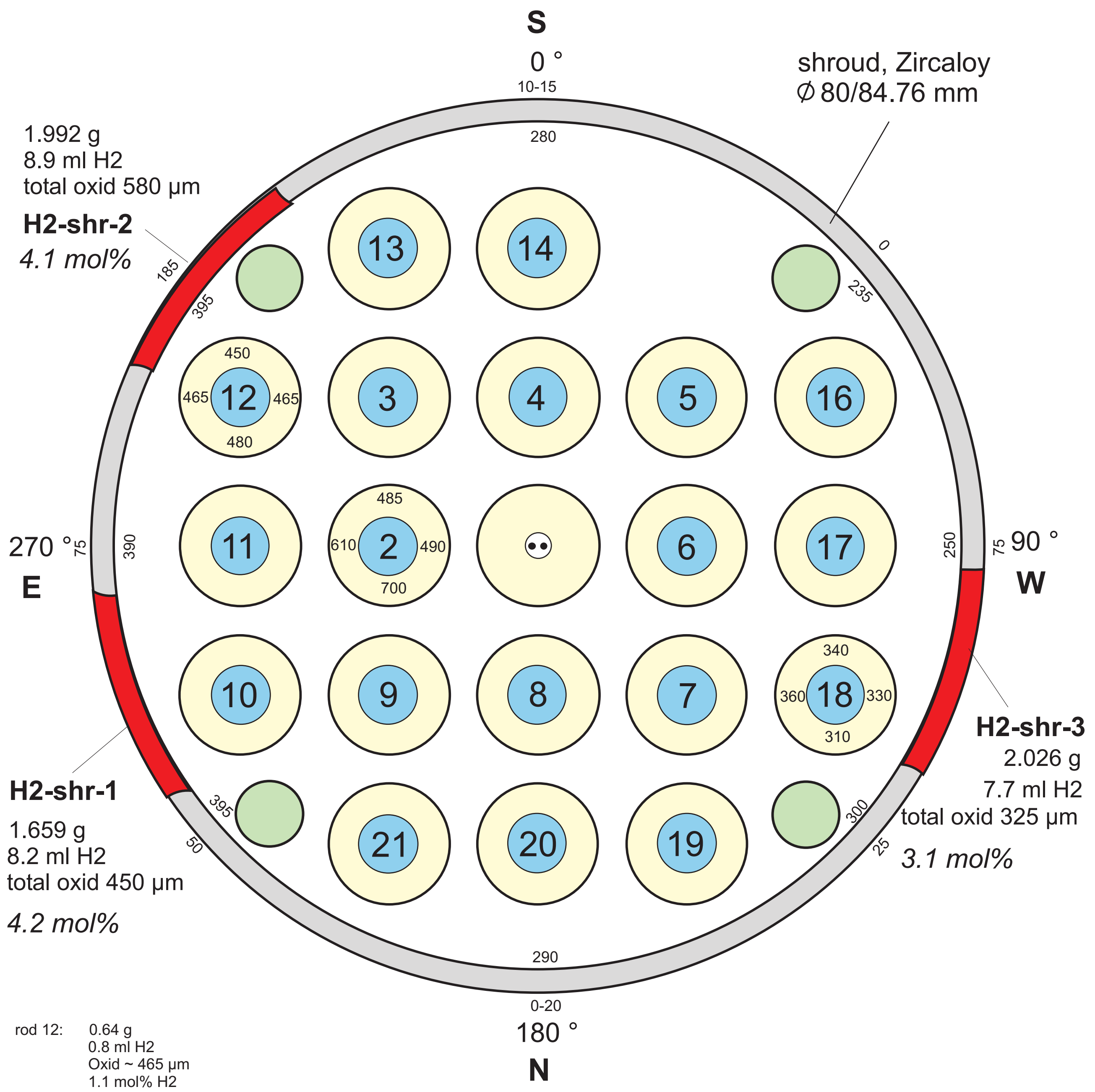

1.992 g
8.9 ml H2
total oxid 580 µm

H2-shr-2
4.1 mol%

H2-shr-3
2.026 g
7.7 ml H2
total oxid 325 µm
3.1 mol%

H2-shr-1
1.659 g
8.2 ml H2
total oxid 450 µm
4.2 mol%

rod 12: 0.64 g
0.8 ml H2
Oxid ~ 465 µm
1.1 mol% H2

rod 1.3 ml H2
oxid ~ 570 µm
1.7 mol% H2

rod 18: 0.41 g
0.8 ml H2
oxid ~ 335 µm
1.6 mol% H2

QUE-05-02, h2-shr-4: 2.338 g
0.5 ml H2
oxid 1µm
0.2 mol% H2

Fig 91-QUE05 H2 analyse 05-08.cdr
12.03.02 - IMF

Fig. 91: QUENCH-05; H_2 analysis of cross section QUE-05-08 (957 mm)

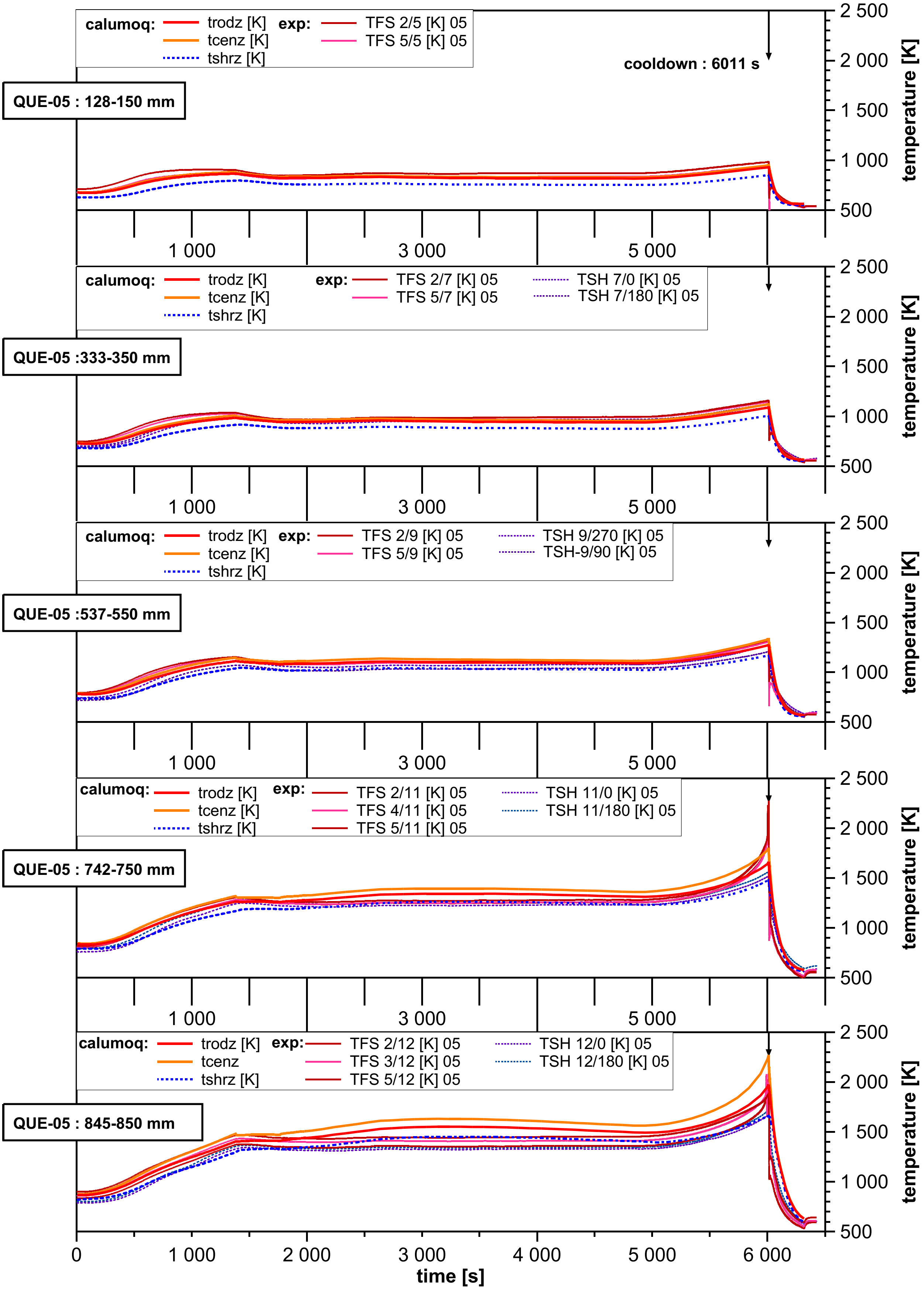

Fig. 92: QUENCH-05; Evolution of rod and shroud temperatures

Fig 92-QUE05 Evolution.cdr
12.03.02 - IMF

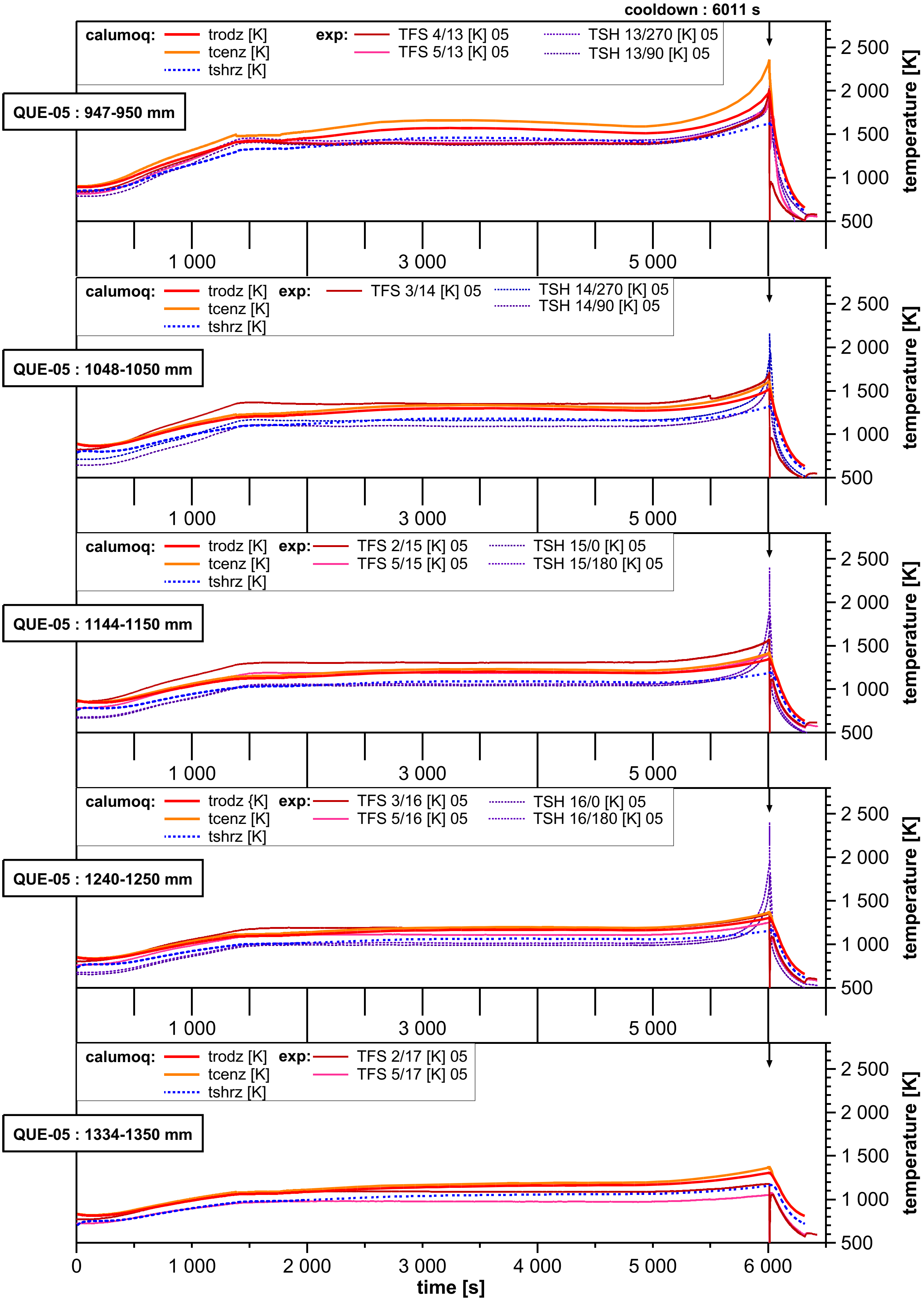

Fig. 93: QUENCH-05; Evolution of rod and shroud temperatures

Fig 93-QUE05 Evolution.cdr
12.03.02 - IMF

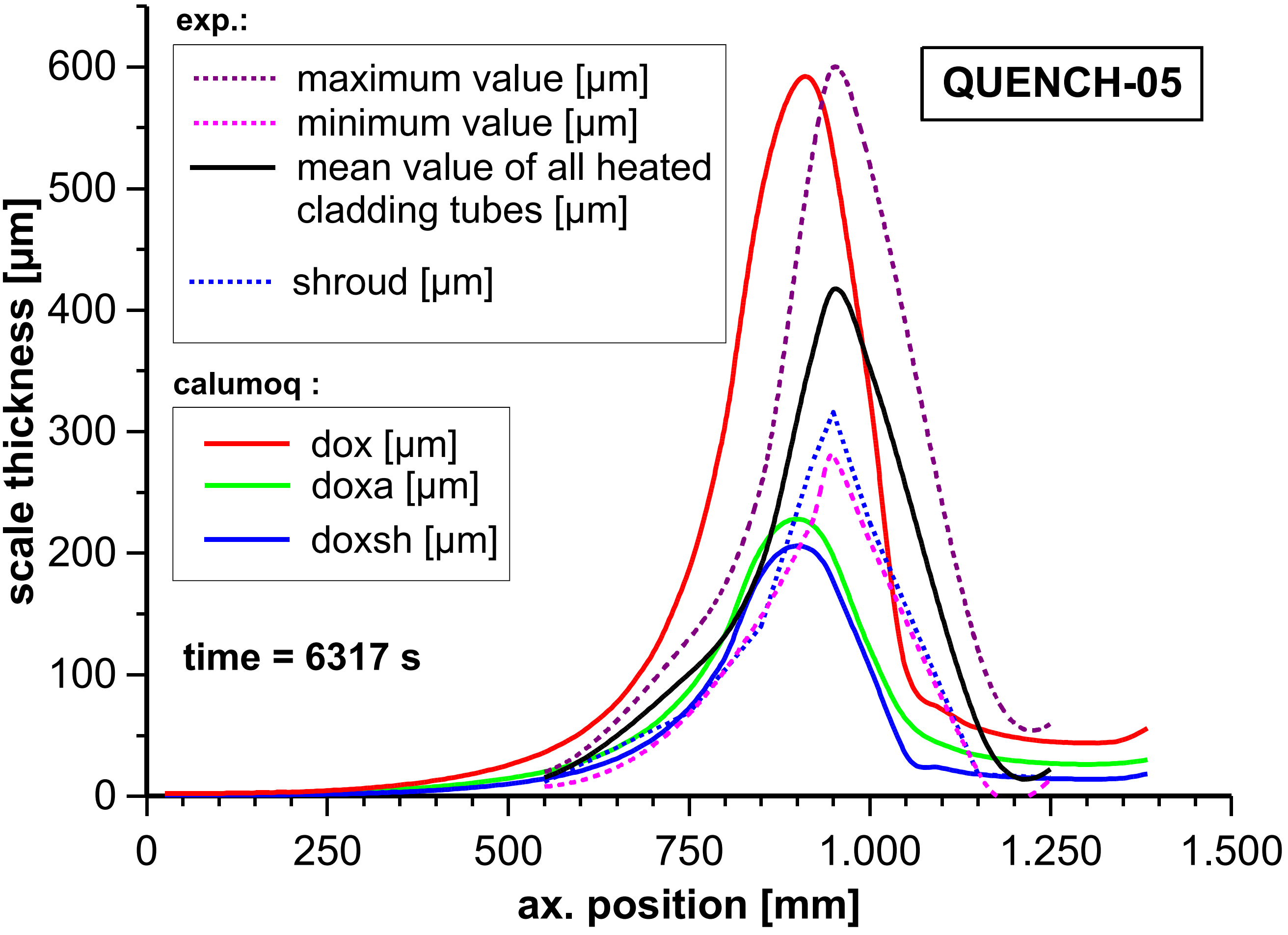

Fig. 94: QUENCH-05; Axial distributions of the oxide scale thickness at the end of the experiment

Fig 94-QUE05 Axial distr.cdr
12.03.02 - IMF

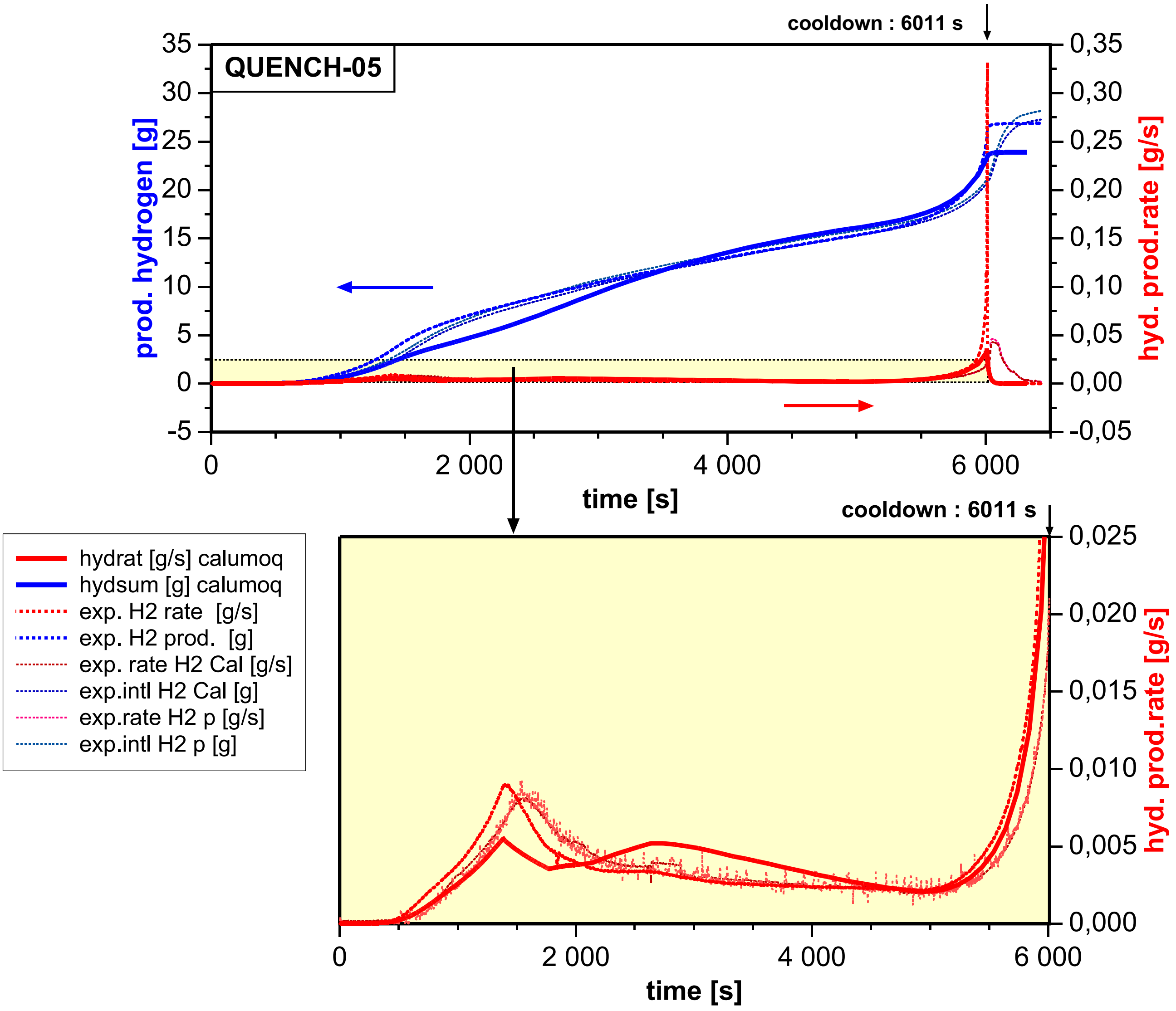

Fig. 95: QUENCH-05; Evolution of the hydrogen production rate and the overall produced hydrogen

Fig 95-QUE05 Evolution.cdr
12.03.02 - IMF

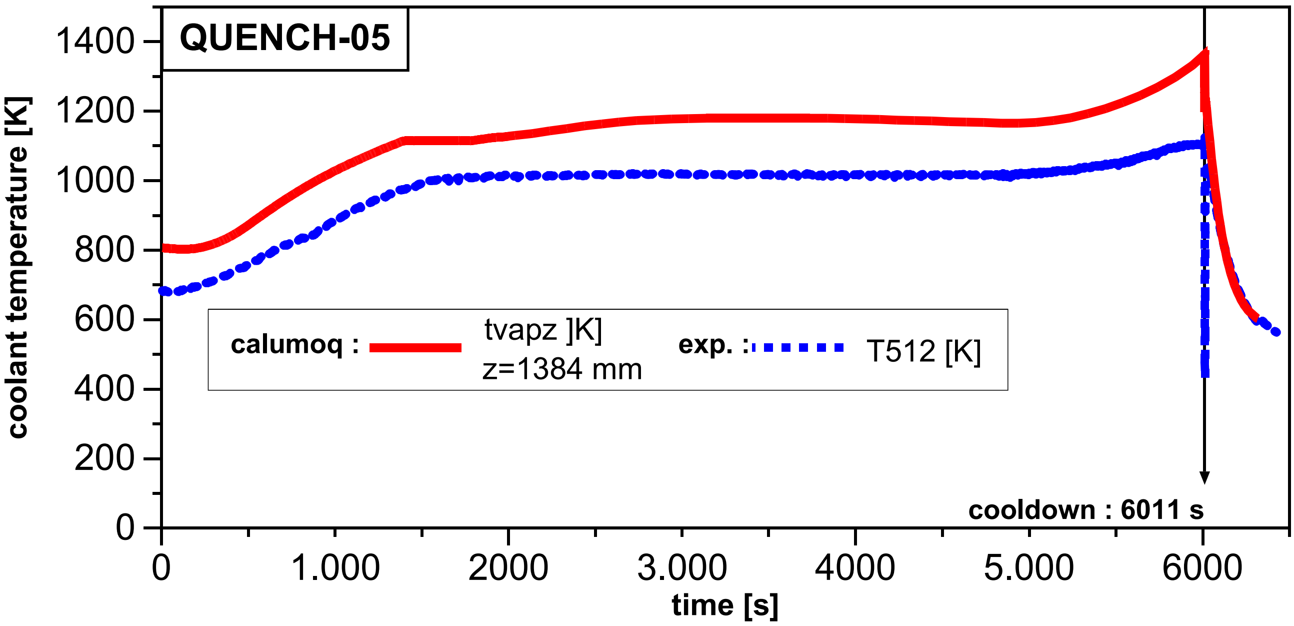

Fig. 96: QUENCH-05; Evolution of outlet coolant temperatures

Fig 96-QUE05 Evolution.cdr
12.03.02 - IMF